Fluid Inclusion Study of Drill Core and Outcrop Samples from the Bruce Nuclear Site, Southern Ontario

NWMO-TR-2015-24 December 2015

Larryn W. Diamond

Lukas Aschwanden

Rita Caldas

Rock-Water Interaction Group, Institute of Geological Sciences,
University of Bern, Switzerland

nwmo
NUCLEAR WASTE MANAGEMENT ORGANIZATION
SOCIÉTÉ DE GESTION DES DÉCHETS NUCLÉAIRES

Nuclear Waste Management Organization
22 St. Clair Avenue East, 6th Floor
Toronto, Ontario
M4T 2S3
Canada

Tel: 416-934-9814
Web: www.nwmo.ca

Fluid Inclusion Study of Drill Core and Outcrop Samples from the Bruce Nuclear Site, Southern Ontario

NWMO-TR-2015-24

December 2015

Larryn W. Diamond
Lukas Aschwanden
Rita Caldas

Rock-Water Interaction Group, Institute of Geological Sciences, University of Bern, Switzerland

This report has been prepared under contract to NWMO. The report has been reviewed by NWMO, but the views and conclusions are those of the authors and do not necessarily represent those of the NWMO.

All copyright and intellectual property rights belong to NWMO.

Document History

Title:	Fluid Inclusion Study of Drill Core and Outcrop Samples from the Bruce Nuclear Site, Southern Ontario		
Report Number:	**NWMO-TR-2015-24**		
Revision:	R000	Date:	December 2015
Rock-Water Interaction Group, Institute of Geological Sciences, University of Bern, Switzerland			
Authored by:	L. W. Diamond, L. Aschwanden, R. Caldas		
Verified by:	M. Mazurek		
Approved by:	M. Mazurek		
Nuclear Waste Management Organization			
Reviewed by:	A. Parmenter		
Accepted by:	M. Jensen		

ABSTRACT

Title: **Fluid Inclusion Study of Drill Core and Outcrop Samples from the Bruce Nuclear Site, Southern Ontario**
Report No.: **NWMO-TR-2015-24**
Author(s): L. W. Diamond, L. Aschwanden, R. Caldas
Company: Rock-Water Interaction Group, Institute of Geological Sciences, University of Bern, Switzerland
Date: December 2015

Abstract
Fluid inclusions were investigated in carbonate vugs and veinlets in fifteen drill core samples from beneath the Bruce nuclear site, including samples from Cambrian, Ordovician and Devonian formations. Six samples of calcite veins from an outcrop of the Lucas Formation were also investigated. The inclusions were analysed petrographically in visible and UV light and by laser Raman spectroscopy and crushing-stage experiments. The inclusions in calcite proved difficult to analyse, owing to the widely known phenomenon of stretching upon heating. Accordingly, the analytical workflow included a procedure to sort valid data from artefacts. The interpretation of the results involved thermodynamic modelling to estimate salinities and trapping temperatures.

The fluid inclusion record is highly consistent between the 15 samples, supporting the idea that geological features within the DGR site are predictable from the acquired evidence. The results show that the deep Cambrian to Mid-Ordovician vugs and veins share the same history of fluid evolution, and are thus genetically related, whereas the veinlets in the shallow Devonian Lucas Formation formed from very different fluids.

In the Cambrian to Mid-Ordovician carbonates, five "paleofluids" have been recognized which are similar to diagenetic fluids reported in the same units in the regional literature. Each paleofluid precipitated minerals or was present during microfracturing in the vugs and veins. Paleofluid 1 was a mixture of halite-saturated brine + free methane±CO_2 gas that precipitated saddle- and rhombic-habit dolomite. The saddle dolomites precipitated at 122–128 °C. Paleofluid 2, a similar halite-saturated, two-phase mixture (brine + free methane gas), infiltrated the vugs and veins in pulses at temperatures between 42 and 85 °C. Paleofluid 3 was a halite-saturated brine without an accompanying gas phase. It healed microfractures in the previously precipitated minerals after infiltrating in pulses at temperatures between 71 and 120 °C. Paleofluid 4 was a simple halite-undersaturated brine, without free gas, that entered the sediments at some temperature below 70 °C. Paleofluid 5 consisted of light petroleum oil accompanied by free methane gas that was trapped in microfractures at 50–60 °C. No indication has been found in the Cambrian to Mid-Ordovician samples for a fluid that could have originated by influx of glacial melt-water.

The Devonian Lucas limestone contains a record of three additional paleofluids. Paleofluid 6 was a low-salinity aqueous solution accompanied by free methane gas, which precipitated calcite and minor ankerite in veinlets at ~60 °C. Paleofluid 7 was a slightly diluted version of Paleofluid 6 but without free gas in the aqueous solution. Paleofluid 8 consisted of light petroleum oil accompanied by free methane gas. Overall, the low salinity fluids in the Devonian Lucas Formation contrast strongly with the brines in the underlying Cambrian to Mid-Ordovician rocks, ruling out a common fluid origin.

TABLE OF CONTENTS

Page

ABSTRACT ..... **iii**

1. INTRODUCTION **1**

2. SAMPLES ANALYSED **1**

3. ANALYTICAL APPROACH AND METHODS **1**

3.1 PETROGRAPHY IN VISIBLE AND UV LIGHT **1**
3.1.1 Identification of Assemblages of Primary and Secondary Inclusions 4
3.1.2 Identification of Homogeneous Versus Heterogeneous Entrapment 4
3.1.3 Identification of Paleofluid Generations 5
3.2 MICROTHERMOMETRY **6**
3.2.1 Microthermometric Determination of Homogenization Temperatures 6
3.2.2 Deduction of Trapping Temperatures from True Homogenization Temperatures 8
3.2.3 Microthermometric Determination of Ice Melting Temperatures 9
3.3 LASER RAMAN SPECTROSCOPY **10**
3.4 CRUSHING-STAGE ANALYSIS **11**

4. RESULTS **11**

4.1 PETROGRAPHIC RESULTS **11**
4.1.1 Solid Phases within Fluid Inclusions at Room Temperature 11
4.1.2 Paragenetic Diagrams 13
4.2 MICROTHERMOMETRIC RESULTS **14**
4.2.1 Phase Behaviour of Fluid Inclusions Below Room Temperature 14
4.2.2 Microthermometric Data 18
4.2.3 Crushing-Stage Data 18
4.2.4 Brine compositions in the Model H_2O–NaCl–$CaCl_2$ Ternary System 18
4.2.5 Pressure Correction for T_h Values of Homogeneously Entrapped Inclusions 26
4.3 SEQUENCE OF MINERAL PRECIPITATION, FLUID ENTRAPMENT AND FLUID PROPERTIES **29**

5. DISCUSSION OF FLUID INCLUSION RESULTS AND PALEOFLUID EVOLUTION **37**

5.1 PALEOFLUIDS IN THE CAMBRIAN AND MID-ORDOVICIAN VUGS AND VEINS **37**
5.2 PALEOFLUIDS IN THE DEVONIAN LUCAS FORMATION VEINLETS **39**

6. IMPLICATIONS OF FLUID INCLUSION RESULTS FOR UNDERSTANDING THE GEOLOGICAL EVOLUTION OF THE BRUCE NUCLEAR SITE **40**

6.1 REGIONAL OCCURRENCE OF BRINES **40**
6.2 OCCURRENCE OF HYDROTHERMAL DOLOMITE (HTD) **41**
6.3 MAXIMUM BURIAL TEMPERATURE **42**
6.4 HALITE DISTRIBUTION IN CORE SAMPLES **42**
6.5 PETROLEUM DISTRIBUTION IN CORE SAMPLES **43**

6.6 AGE OF METHANE 45
6.7 GAS SATURATION 45
6.8 ABSENCE OF GLACIAL WATER INFILTRATION 47

7. SUMMARY OF RESULTS 48

REFERENCES 51

APPENDIX A: PETROGRAPHIC OBSERVATIONS (ANNOTATED PHOTOGRAPHIC RECORD) 53

APPENDIX B: PHASE BEHAVIOUR OF FLUID INCLUSIONS BELOW ROOM TEMPERATURE 117

APPENDIX C: ELECTRON MICROPROBE ANALYSES OF DOLOMITES 123

LIST OF TABLES

Page

Table 1: Rock Samples and Methods Used to Analyse Their Fluid Inclusions 2
Table 2: Microthermometric Results. Outcrop Samples are Listed First, Followed by Borehole Samples in Order of Borehole Number and Then Depth.....19
Table 3: Crushing-Stage Results 25

LIST OF FIGURES

Page

Figure 1: Key to Locations of Fluid Inclusion Samples from DGR Boreholes at the Bruce Nuclear Site 3
Figure 2: Illustration of How the Relative Ages of Fractures and Their Fluid Inclusion Generations Can be Determined from Petrographic Observations (For a Real Example, See Figure A67).....4
Figure 3: Illustration of How the Original Phase-State of Paleofluids Can be Deduced from Observations of Fluid Inclusions Under the Microscope. Examples are of Fluid Inclusions Trapped in a Healed Fracture in a Calcite Crystal, as in the DGR Samples. (a) If the Volume Fractions of the Fluid Phases are Uniform Within the Same Set of Coeval Inclusions (i.e., Within the Same "Assemblage") at Room Temperature, Then (a') the Paleofluid is Interpreted to Have Been Trapped from One Homogeneous Fluid. (b) The Same Principle Applies Even if the Assemblage Contains no Vapour Bubbles. In this case the Paleofluid (b') is Interpreted to Have Been a Homogeneous Liquid at T < 70 °C. (c) If the Volume Fractions of the Fluid Phases are Variable Within the Same Inclusion Assemblage at Room Temperature, then (c') the Paleofluid is Interpreted to Have Been Trapped from two Heterogeneous Fluids (e.g., Water and Coexisting Bubbles of Immiscible Gas) 7
Figure 4: Liquid + Vapour Inclusions in Calcite Photographed in Transmitted Light at Room Temperature. Left: Before Heating. Right: After Heating to 57 °C, at Which Temperature the Inclusions Homogenized Via Progressive Bubble Contraction and Disappearance. The Vapour Bubble Reappeared at 46 °C During Cooling. The Marked Increase in Volume Fraction of the Vapour Bubble Proves That the Inclusions Irreversibly Increased Their Volumes ("Stretched") During the Heating Experiment. [Primary Fluid Inclusions in Sample DGR 6-886.91] 8
Figure 5: Various Primary and Secondary Fluid Inclusions in the DGR Samples From the Cambrian and Mid-Ordovician Contain Halite Crystallites. Within Individual Fluid Inclusion Assemblages the Volume Fractions of Halite are Strongly Variable, as Visible in a) to e) [Microphotographs in Transmitted, Polarized Light; DGR-6-886.91] 12
Figure 6: Left) Numerous Primary Fluid Inclusions in the DD-Calcite Samples Contain Accidentally Captured Rhombohedral Crystallites of Ankerite. Right) Acquired Raman Spectrum of the Calcite Host-Crystal and of an Ankerite Crystallite Within a Fluid Inclusion.....13

Figure 7: Paragenetic Diagrams Summarising Petrographic Observations, Interpreted Paleofluids, Micro-Thermometry, Trapping Temperatures and Salinities in the Bruce Nuclear Site Samples. This Set of Diagrams Covers Time Stages IX–XI in the Vugs and Veins, and Pertains Only to the Samples from the Shallow Lucas Formation. See Diagrams Below For Deeper Borehole Samples.....15
Figure 8: Compositions of Brines in Cambrian and Mid-Ordovician Samples, in Terms of the Model H_2O–NaCl–$CaCl_2$ Ternary System. (a) Black Curves and Squares: Stable Phase Equilibria; Red Curve: Metastable Cotectic, as Modelled for this Study From Data Generated by the Correlations of Steele-Macinnis et al. (2011); See Figure 9 for Temperatures Along Curve. Blue Curves: Example Isotherms of Ice Melting in the Absence of Halite (Upper Field) and Halite Melting in the Absence of Ice (Lower Field). Grey Field: Stability of Hydrohalite. Green Arrow: Example of Halite Melting Trend from the Cotectic (See Text). (b) Same Diagram as (A) Without Hydrohalite Field and Isotherms. Compositions of Assemblages of Brines in Paleofluids 1–3 at the Temperature of Their Entrapment are Shown by the Symbols. HTD: Brines that Deposited Hydrothermal Saddle Dolomite. The Compositions of Brines in Paleofluid 4 are Only Broadly Constrained to Fall Within the Relevant T_m(Ice) Isotherms (Uncertainty Indicated By Question Marks). Data from Table 2. Paleofluids are as Given in Figure 10.....27
Figure 9: Compositions of the Liquid Phase (Brine) in the Model H_2O–NaCl–$CaCl_2$ Ternary System as a Function of Temperature on the Metastable Cotectic Ice + Halite + Liquid + Vapour (Same as Red Curve in Figure 8). Calculated as Described in Text 28
Figure 10: Principle of Derivation of Pressure Corrections for T_h Measurements of Homogeneously Entrapped Fluid Inclusions in this Study. See Section 4.2.5 for Explanation.....29
Figure 11: Synthesis of Paragenetic Diagrams in Figure 7. The Indicated Salinities of the Lucas Formation Inclusions Correspond to Their Bulk Salinities in Equivalent Wt% NaCl. Salinities Shown for the Mid-Ordovician and Cambrian Samples Refer to the Model Ternary H_2O–NaCl–$CaCl_2$. Trapping Temperatures (T_{trap}) for Paleofluid 3 are Corrected for Paleo-Hydrostatic Pressure (Cambrian Samples) or an Average of Paleo-Hydrostatic and Paleo-Lithostatic Pressures (Ordovician Samples) - See Text Section 4.2.5 for Explanation. * Calcite Dated to 51 ±2 – 109 ±4 Ma by Davis (2013). ** Calcite Dated to 445 ±42 Ma by Davis (2013).....30
Figure 12: Histograms of Final Ice-Melting Temperatures in Equilibrium with Vapour in Cambrian to Mid-Ordovician Samples. Ice Melting in Stages II–V is Metastable; Stable Hydrohalite Nucleates Only Rarely (T_m(Hydrohalite) Not Shown). Data from Table 2. Paleofluids are as Given in Figure 8 31
Figure 13: (a) Subhedral, Fluid Inclusion-Poor Dolomite Lining the Walls of a Vein in Sample DGR 2-844.31. (B) Euhedral, Fluid Inclusion-Rich Saddle Dolomite Lining the Walls of a Vug in Sample DGR 4-829.53. The Dolomite Is Overgrown By and Thus Predates Anhydrite. (C) Calcite-Celestine Vein in Sample DGR 4-769.57. The Celestine is Aligned Along the Central Axis of the Vein and Overgrows the Calcite Which Lines the Walls of the Vein 32
Figure 14: Raman Vibrational Spectra of Methane (Left) and CO_2 (Right; Two Peaks Belonging to Fermi Diad) Measured in the Vapour Bubble of Primary Fluid Inclusions in Stage II Saddle Dolomite of Sample DGR-4-829.53.....33
Figure 15: Relationship Between Paleofluid Salinities and Trapping Temperatures. For Definitions of Numbered Paleofluids, Refer to Figure 11. HTD: Hydrothermal

Dolomite with Saddle Texture. RD: Rhombic Dolomite. Paleofluids 1, 2, 5 and 8 Coexisted with Free Methane Gas (Not Shown) and Paleofluids 1–3 were Saturated with Respect to Halite (Not Shown). Arrows Mark Uncertainty in Trapping Temperatures of Paleofluids 4, 7 and 8. Paleofluids 1–5 Occur in Vugs and Veins in the Mid-Ordovician and Cambrian Formations; Paleofluids 6–8 Occur in Veinlets in the Devonian Lucas Formation.....38

Figure 16: Distribution of Halite at the Bruce Nuclear Site (Modified from Figure 5 in Al et al., 2015), Based on XRD, SEM, Petrography and Core Logging in the DGR Boreholes. These Observations Show that Halite is Present Essentially Continuously from the Upper Salina Group Down to the Sherman Fall Formation. It Appears Again in the Shadow Lake and Cambrian Formations. Overlain on the Borehole Columns are the Occurrences of Halite-Saturated Paleo-Fluids Derived from this Fluid Inclusion Study (Red Symbols). These New Observations Confirm the Presence of Halite in the Sherman Fall and Cambrian Formations and Show that it is also Present in the Coboconk and Gull River Formations, Thereby Filling an Information Gap. Thus, Halite-Saturated Paleofluids were Present Throughout the Entire Stratigraphic Sequence Between the Cambrian and Upper Salina Group 44

Figure 17: Distribution of Hydrocarbons in Borehole Cores at the Bruce Nuclear Site, From Figure 2.32 in NWMO (2011). Overlain with Blue Symbols are the Occurrences of Oil-Bearing Fluid Inclusions (This Study). The 7 Deep Samples that Contain Oil Inclusions Come from the Coboconk, Gull River and Cambrian Formations. All Correlate Well with Horizons in Which Oil Seeps Were Logged in the Cores. Lucas Formation Samples Also Contain Oil Inclusions 46

1. INTRODUCTION

The Paleozoic bedrock at the Bruce Nuclear Site, situated near Tiverton in Southern Ontario, has been proposed for a Deep Geologic Repository (DGR) for the low- and intermediate-level radioactive waste produced by the Ontario Power Generation Corporation. The Nuclear Waste Management Organization (NWMO, Toronto) is currently conducting a broad geoscientific investigation of the bedrock at the site. In support of this investigation, NWMO has commissioned the present study of fluid inclusions in selected drill-core and outcrop samples.

Downhole sampling of groundwaters and laboratory extraction of pore water from core samples have provided information on recent and present-day fluids in the bedrock (e.g., NWMO, 2011). In contrast, analysis of fluid inclusions trapped within mineral grains provides insight into the properties and evolution of deep groundwaters active in the distant geological past. In this report, these ancient fluids (often mixtures of brine and gas) are referred to as "paleofluids".

The aims of the present study are: (1) to identify any paleofluids that were at one time present in the sampled rocks; (2) to identify the relative ages of these fluids with respect to each other and with respect to episodes of mineral growth and deformation; (3) to provide basic information on the chemical composition (e.g., salinity, contents of carbon-dioxide, methane and higher-order hydrocarbons) and density of the fluids; (4) to place constraints on the range of temperatures that the rocks experienced during paleofluid activity. Besides presenting the results, this report discusses their implications for understanding the geological evolution of the Bruce nuclear site.

This report incorporates and updates all the information presented in a preliminary report (Diamond & Caldas, 2013) that deals with a subset of the samples treated herein. The present document therefore supersedes that preliminary report.

2. SAMPLES ANALYSED

Fluid inclusions were investigated in vug- and veinlet-filling minerals in 15 core samples from the DGR boreholes and in 6 samples of calcite veins from an outcrop of the Lucas Formation at the Bruce nuclear site (Table 1). All the samples were provided by NWMO. The locations of the core samples are shown schematically with respect to the Bruce nuclear site stratigraphy in Figure 1.

3. ANALYTICAL APPROACH AND METHODS

Selected dolomites were analysed by electron microprobe (Appendix 3) but all other analyses addressed the petrographic setting and properties of the fluid inclusions, as detailed below.

3.1 PETROGRAPHY IN VISIBLE AND UV LIGHT

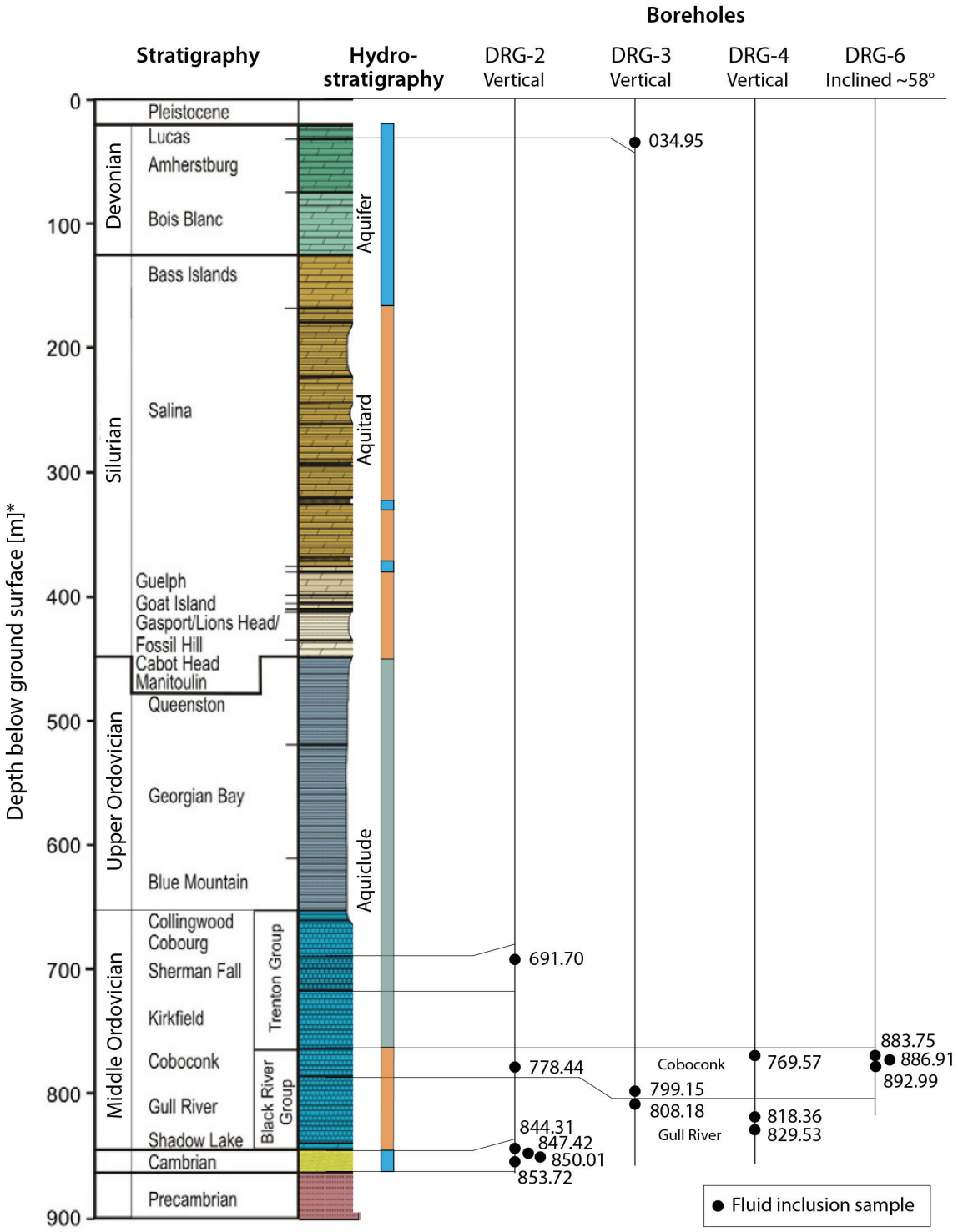
The present investigation follows the general principles and practice of fluid inclusion studies outlined by Roedder (1984), Goldstein and Reynolds (1994) and Samson et al. (2003).

Petrographic examination of the samples was performed at high magnification (objectives between 4x and 100x) using an Olympus BX51 polarizing microscope. To facilitate this, a ~150 µm thick section was cut from each sample and polished on both sides to provide good transparency. Observations were made in normal transmitted light and in UV epi-illumination (to identify fluorescence, i.e., aromatic, hydrocarbons).

Table 1: Rock Samples and Methods Used to Analyse Their Fluid Inclusions

Sample	Depth (m)	Feature & Mineralogy	Formation	VisTr	UV	µTherm	Raman	Crushing
DD 12-11	Outcrop	NE-trending surface vein	Lucas	X	X	X	X	X
DD 12-12_1	Outcrop	SE-trending surface vein	Lucas	X	X	X	X	–
DD 12-12_2	Outcrop	SE-trending surface vein	Lucas	X	X	–	X	X
DD 12-12 FV	Outcrop	Subhorizontal (flat) surface vein	Lucas	X	X	–	X	–
DD 12-13_1	Outcrop	N-trending surface vein	Lucas	X	X	X	X	X
DD 12-13_2	Outcrop	N-trending surface vein	Lucas	X	X	X	X	X
DGR2-691.70	691.70	Calcite vein in argillaceous limestone	Sherman Fall	X	X	X	X	–
DGR2-778.44	778.44	Dolomite vein in dolostone	Coboconk	X	X	X	X	–
DGR2-844.31	844.31	Coarse calcite vein in dolostone	Cambrian	X	X	X	X	X
DGR2-847.42	847.42	Calcite vug in sandstone	Cambrian	X	X	X	X	X
DGR2-850.01	850.01	Calcite vug in sandstone	Cambrian	X	X	X	X	X
DGR2-853.72	853.72	Calcite vein in sandstone	Cambrian	X	X	X	X	–
DGR3-034.95*	34.95	Calcite vein in limestone	Lucas	X	X	X	X	X
DGR3-799.15	799.15	Calcite vug in limestone	Coboconk	X	X	X	X	X
DGR3-808.18	808.18	Calcite vein in argillaceous limestone	Gull River	X	X	X	X	–
DGR4-818.36	818.36	Calcite vug and vein in dolostone	Gull River	X	X	X	X	X
DGR4-769.57	769.57	Calcite vein in argillaceous limestone	Coboconk	X	X	X	X	–
DGR4-829.53	829.53	Vug lined by coarse-grained dolomite with anhydrite infill	Gull River	X	X	X	X	X
DGR6-883.75	883.75	Calcite vug in limestone	Coboconk	X	X	X	X	X
DGR6-886.91*	886.91	Calcite vug and vein in dolostone	Coboconk	X	X	X	X	X
DGR6-892.99	892.99	Calcite vugs and veins in dolostone	Coboconk	X	X	X	X	–

VisTr: Transmitted, visible-light microscopy
UV: Reflected, ultraviolet-light microscopy
µTherm: Microthermometry
Raman: Laser Raman microspectroscopy
Crushing: Crushing-stage analyses to detect presence of CO_2 and CH_4
* Samples dated radiometrically (Davis, 2013).



Notes: Stratigraphic column from NWMO (2011). Numbers next to black dots represent depths (in metres) along the respective boreholes, and these serve as sample numbers. *Borehole DGR-6 was inclined and therefore the indicated sample depths for this hole do not correspond to vertical depths below surface.

Figure 1: Key to Locations of Fluid Inclusion Samples from DGR Boreholes at the Bruce Nuclear Site

Petrography was performed in three steps:

3.1.1 Identification of Assemblages of Primary and Secondary Inclusions

First, groups of cogenetic inclusions (hereafter termed "fluid inclusion assemblages") were identified based on their geometric relationships with respect to their host mineral, in this case calcite. These petrographic criteria allowed the ages of the assemblages to be recognized with respect to events of mineral growth and brittle fracturing. Thus, assemblages of inclusions arrayed on crystal growth horizons were obviously trapped during growth of the host mineral and are therefore termed primary. Inclusions trapped in healed fractures were obviously trapped at some time after crystal growth and are therefore termed secondary. The relative ages of different secondary assemblages could be recognized from cross-cutting relationships, as illustrated in Figure 2.

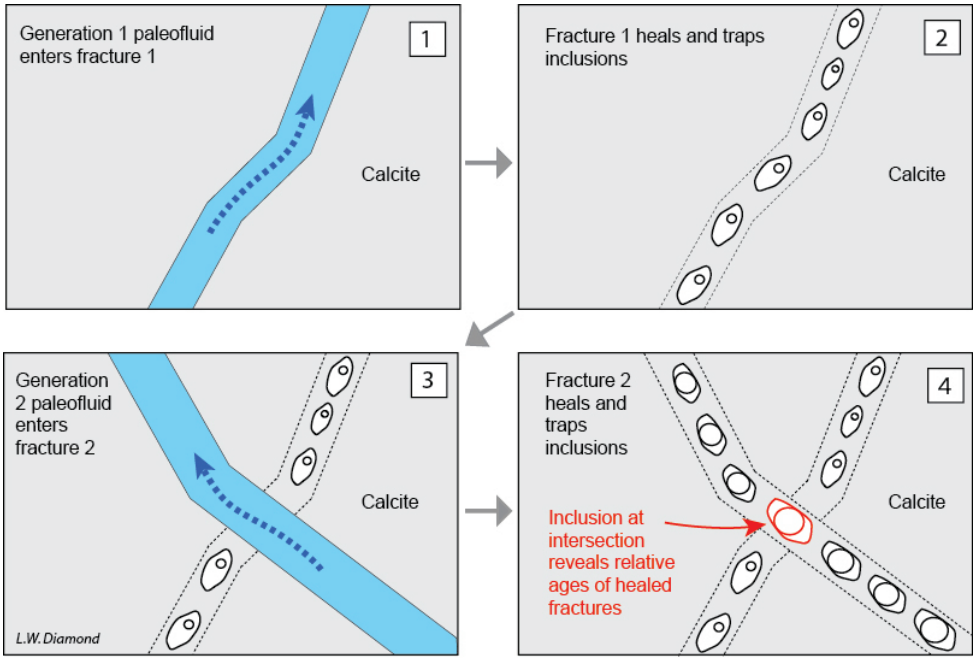


Figure 2: Illustration of How the Relative Ages of Fractures and Their Fluid Inclusion Generations Can be Determined from Petrographic Observations (For a Real Example, See Figure A67)

3.1.2 Identification of Homogeneous Versus Heterogeneous Entrapment

In a second step, still under the microscope at room temperature, the fluid phases within individual inclusions were identified and their volumetric proportions were estimated by eye (e.g., "80 vol% liquid + 20 vol% vapour"). Such phase volume fractions are independent of inclusion shape and size. In particular, the variation of the volume fractions within each assemblage was determined (e.g., "uniformly 20 vol% vapour", or "variable between 10 and 90 vol% vapour"). These variations, or lack thereof, can be interpreted within the theoretical

framework of modern fluid inclusion studies (e.g., Diamond, 2003a) to identify the original phase-state of the free paleofluids in the rocks. Thus, assemblages with uniform phase-volume fractions indicate that just one, homogeneous, paleofluid was present in the rock at the time of inclusion entrapment (e.g., "saline water" or "methane gas"). The volume fraction of vapour is uniform in this case, because all the inclusions, regardless of their shape or size, exsolve the same relative amount of vapour upon post-entrapment cooling to room temperature. In contrast, assemblages with variable phase-volume fractions indicate that two or more paleofluids were present in the rock at the time of inclusion entrapment (e.g., "saline water + immiscible, coexisting methane gas"). In this case, the variable volume fractions arise from trapping of the coexisting phases (e.g., liquid and gas) in random proportions from the heterogeneous mixture. Figure 3 illustrates this key principle.

Although the above principle relies on recognition of phase volume proportions, these are difficult to estimate from two-dimensional microscope images, as the thickness of the inclusions in the third (depth) dimension cannot be viewed directly. Changing the focal depth of the microscope helps determine whether the inclusion is flat or thick, but, in fact, one usually must rely on area fractions rather than volume fractions. Though there can be significant differences between the two (Bakker and Diamond, 2006), with experience one can reliably distinguish whether the inclusions in a given assemblage have uniform or variable phase proportions. Thus, the values of "vol%" given for fluid phases in this report are approximate but sufficient for the present needs.

In the DGR calcite crystals one of the identified generations of fluid inclusions consists of liquid water only, without any vapour bubbles (as shown in Figure 3b). Normally a vapour bubble forms as an inclusion cools down from its geological environment of trapping. If the inclusions are small or flat (i.e., with relatively high surface free energy) and if the contained water is dense (from entrapment at low, diagenetic temperature), then bubble nucleation is inhibited and the result is a metastable liquid state. This phenomenon is well known and understood in the literature (e.g., Diamond, 2003a), and so the monophase DGR samples are in no way exceptional. Empirically it has been found that liquid-only inclusions form at temperatures below about 70 °C (e.g., Goldstein and Reynolds, 1994). The point here is that if an assemblage consists of liquid-only inclusions (possibly including some larger inclusions with small bubbles, in which nucleation was successful), then it must have been trapped from a homogeneous (i.e., single-phase) fluid (Figures 3b and b'). Thus, such assemblages are described during petrographic studies as having "uniformly 0 vol% vapour", and they have the same significance as other assemblages of liquid + vapour inclusions with uniform phase proportions.

3.1.3 Identification of Paleofluid Generations

Finally, the various inclusion assemblages were compared and, based on their relative ages, grouped into paleofluid generations. Organizing these generations along a time line reveals a paragenetic sequence in which the history of fluid evolution in the samples with respect to mineral growth and fracturing can be visualized (see Results - Section 4).

Once the above petrographic study using transmitted-light microscopy was completed, selected inclusions from each paleofluid generation were analysed by the following instrumental techniques.

3.2 MICROTHERMOMETRY

Heating and cooling experiments were performed to determine temperatures of equilibrium phase transitions within individual fluid inclusions, from which bulk salinity can be estimated and constraints placed on fluid trapping temperatures. In this study, only two phase transitions were measured, according to the methodology outlined in the following sections: (1) the homogenization temperature (between 50 and 125 °C) and (2) the temperature at which ice or hydrohalite melts (between –53 and –0.1 °C). Hydrohalite was observed only rarely. No reliable eutectic temperatures could be determined, due either to the small size of the inclusions or to their metastable behaviour at very low temperatures.

Measurements were made with a Linkam MSD-600 heating-cooling stage at the Institute of Geological Sciences, University of Bern. The stage was mounted on an Olympus BX51 microscope and the inclusions were viewed during measurements through an Olympus 100x/0.80 LM PlanFI objective lens. The stage was calibrated against phase transitions in synthetic fluid inclusions of known composition and density. Measurements below room temperature are thus accurate to ±0.1 °C and those above room temperature are accurate to ±1 °C.

3.2.1 Microthermometric Determination of Homogenization Temperatures

The homogenization temperature, abbreviated T_h, is the equilibrium temperature at which a fluid inclusion transforms from a heterogeneous (multiphase) state (e.g., liquid + vapour) to a homogeneous state (e.g., liquid) upon gradual heating. In inclusions with liquid-like bulk densities (the case of most of the Bruce nuclear site fluid inclusions) the homogenization transition is preceded by gradual shrinkage of the vapour bubble and the transition itself is defined at the moment when the bubble disappears completely. Reproducible equilibrium measurements were performed in this study at a heating rate of ~0.5 °C/min.

Because fluid inclusions are essentially constant-volume (i.e., isochoric) systems, heating them automatically increases their internal pressure. Hard host minerals such as quartz and dolomite withstand this pressure increase, behaving as rigid isochoric containers under atmospheric confining pressure. However, when inclusions are hosted by softer minerals, such as calcite and anhydrite, the increase in internal pressure upon heating in the laboratory may cause the inclusion walls to deform ("stretch") irreversibly. This usually occurs without any leakage of the fluid contents. Such stretching increases the size of the vapour bubble, hence elevating and therefore falsifying the homogenization temperature. That is to say, the observed T_h value measured in the laboratory is higher than the "true" value which would reflect the density of the inclusion at the time of its entrapment.

Although stretching cannot be avoided with a conventional microthermometric apparatus, it can be recognized after the fact by comparing the area fraction of the vapour bubble before and after heating. Accordingly, in this study, all the inclusions in calcite were photographed before and after heating to check for stretching. For many of the fluid inclusions hosted by calcite, comparison of these photographs revealed notable increases in area% of the vapour bubbles (e.g., Figure 4). Moreover, repeated heating and cooling cycles showed ever increasing vapour fractions. For inclusions with such clear evidence of volume expansion, the measured T_h values can be treated as maximum values, i.e., T_h(true) < T_h(observed).

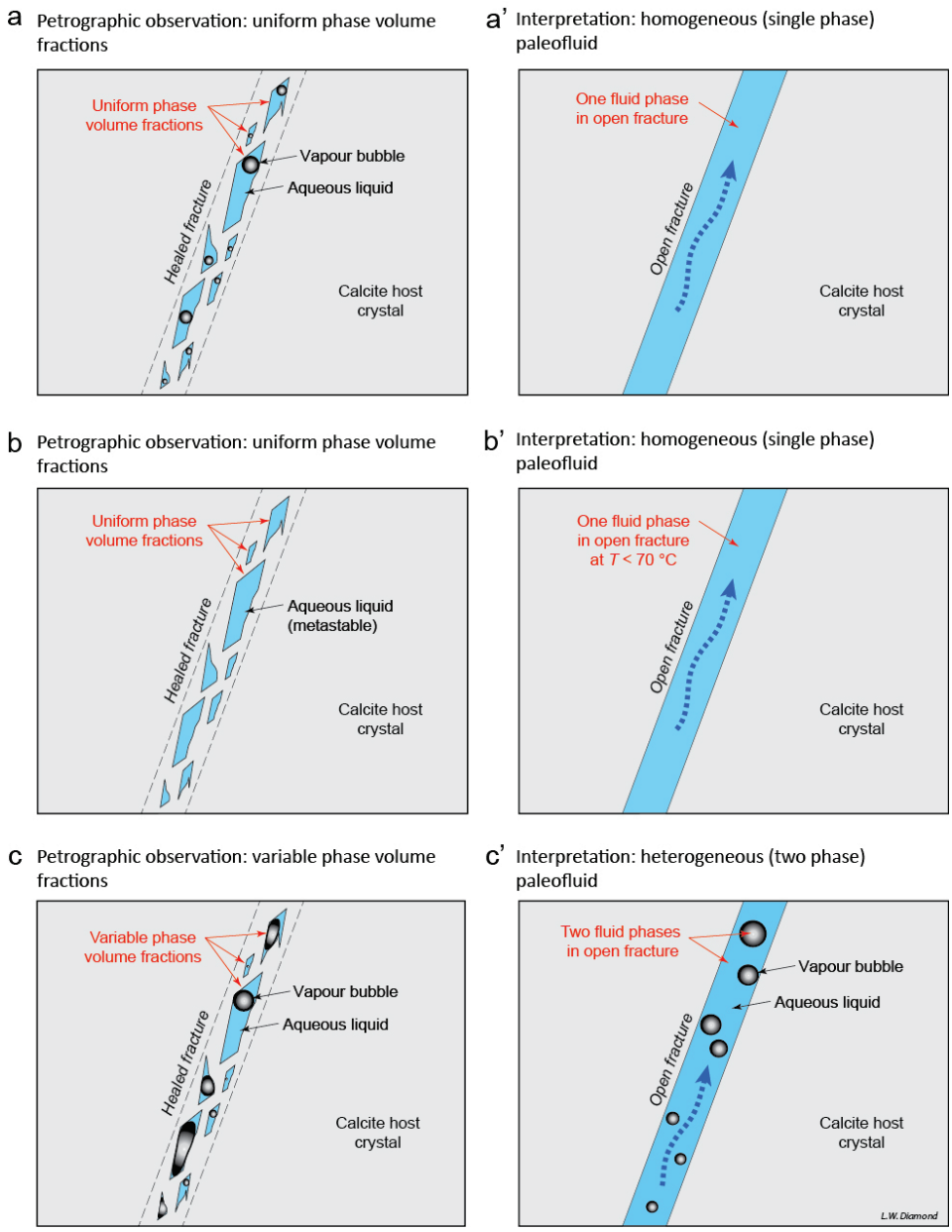


Figure 3: Illustration of How the Original Phase-State of Paleofluids Can be Deduced from Observations of Fluid Inclusions Under the Microscope. Examples are of Fluid Inclusions Trapped in a Healed Fracture in a Calcite Crystal, as in the DGR Samples. (a) If the Volume Fractions of the Fluid Phases are Uniform Within the Same Set of Coeval Inclusions (i.e., Within the Same "Assemblage") at Room Temperature, Then (a') the Paleofluid is Interpreted to Have Been Trapped from One Homogeneous Fluid. (b) The Same Principle Applies Even if the Assemblage Contains no Vapour Bubbles. In this case the Paleofluid (b') is Interpreted to Have Been a Homogeneous Liquid at T < 70 °C. (c) If the Volume Fractions of the Fluid Phases are Variable Within the Same Inclusion Assemblage at Room Temperature, then (c') the Paleofluid is Interpreted to Have Been Trapped from two Heterogeneous Fluids (e.g., Water and Coexisting Bubbles of Immiscible Gas)

The extent of calcite stretching and volume expansion of the inclusions depends on numerous factors, including inclusion size, shape, density and depth in the sample. Therefore, the observed T_h values typically vary widely, even in assemblages which prior to heating showed perfectly uniform volume fractions of vapour. Hence, in assemblages where all the inclusions have stretched, the lowest homogenization temperature among those measured is taken as the closest upper limit on T_h(true).

In contrast to fluid inclusions hosted by calcite, inclusions in dolomite are generally known to behave robustly during heating experiments; in the Bruce nuclear site samples, no anomalous behaviour was observed. Therefore, T_h(observed) in dolomite can be taken as equal to T_h(true).

By definition, inclusions which at room temperature consist only of metastable liquid water are already homogeneous. Experience shows that cooling of such inclusions almost never induces vapour nucleation before ice nucleates and therefore no T_h values can be measured in such inclusions by conventional microthermometry. The only constraint on trapping temperature that these inclusions provide is the empirical rule that they were trapped below about 70 °C.

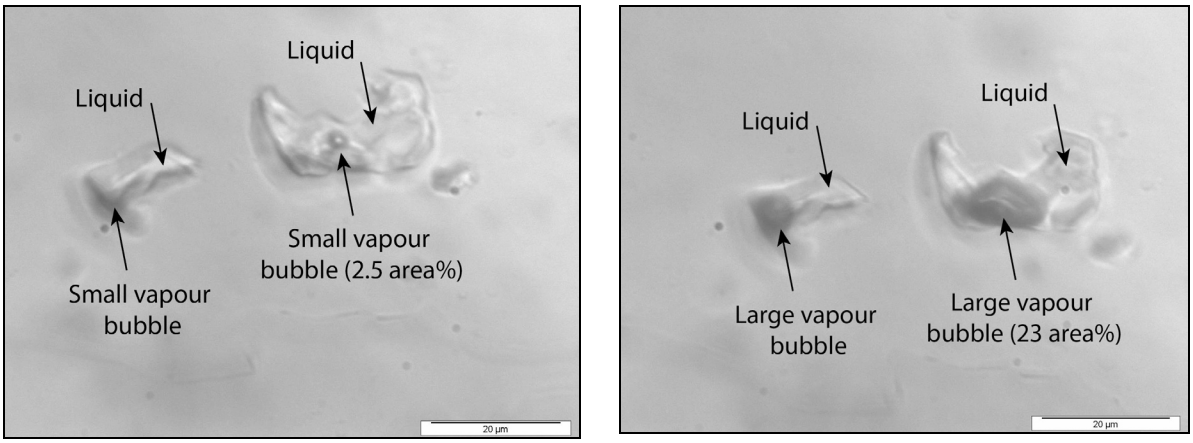


Figure 4: Liquid + Vapour Inclusions in Calcite Photographed in Transmitted Light at Room Temperature. Left: Before Heating. Right: After Heating to 57 °C, at Which Temperature the Inclusions Homogenized Via Progressive Bubble Contraction and Disappearance. The Vapour Bubble Reappeared at 46 °C During Cooling. The Marked Increase in Volume Fraction of the Vapour Bubble Proves That the Inclusions Irreversibly Increased Their Volumes ("Stretched") During the Heating Experiment. [Primary Fluid Inclusions in Sample DGR 6-886.91]

3.2.2 Deduction of Trapping Temperatures from True Homogenization Temperatures

In general, values of T_h are used to estimate fluid trapping temperatures in two ways (Diamond, 2003a):

(1) For inclusion assemblages trapped homogeneously (i.e., from one paleofluid phase, as shown in Figure 3a'), T_h provides a minimum constraint on the temperature at which the

fluid was trapped by the host mineral. Most assemblages of homogeneously trapped fluid inclusions display a range of T_h values of ~10–15 °C, presumably owing to fluctuations in density, P or T during trapping. Thus, the highest value of the range can be used as the tightest constraint on the trapping temperature, i.e., $T_{trap} > T_{h,max}$. In cases where aqueous fluids are trapped at shallow depths (less than ~2 km), such as in the DGR samples, the difference between T_{trap} and T_h is only a few degrees (i.e., the P/T slope of the relevant isochores is very steep). The correction is quantified for the present study in Section 4.2.5 below.

(2) Fluid inclusions that are trapped heterogeneously contain essentially random mechanical mixtures of the two or more fluids present in the rock pores (e.g., Figure 3c'). For reasons not explained here in detail (see Diamond, 2003a and 2003b), the T_h value of the inclusion with the smallest fraction of vapour is assumed to be equal to T_{trap}. In general, this T_h value corresponds to the lowest in the assemblage, i.e., $T_{trap} = T_{h,min}$. Likewise, all the inclusions with higher fractions of vapour will homogenize at temperatures above T_{trap}. The maximum T_h that can be observed is equal to the critical temperature of the fluid mixture. It is important to appreciate that, although T_h values up to several hundred degrees can be measured readily (and reproducibly, providing no host-mineral stretching occurs), none of the values higher than the lowest in the assemblage have any relevance for real temperatures attained in nature. They are simply artefacts of the random mixture of liquid and vapour initially enclosed in the inclusions at T_{trap} (Diamond, 2003a, 2003b).

3.2.3 Microthermometric Determination of Ice Melting Temperatures

In the present study, microthermometry at sub-zero temperatures was performed *after* the homogenization temperatures of the fluid inclusions had been measured. This sequence was followed to avoid yet another artefact related to the host-mineral "stretching" phenomenon. In the case of calcite-hosted inclusions, cooling below the freezing point of water may cause the inclusion walls to deform irreversibly in response to the volume increase upon crystallization of ice. This can effectively increase the volume of the inclusion without leaking any of its contents. The consequence is that the vapour bubble increases in size and hence any subsequent measurement of the homogenisation temperature would yield an artificially elevated, false value. Conversely, although heating to high temperatures may also stretch inclusions in calcite, this has no effect on the validity of subsequent measurements at sub-zero temperatures, as these transitions are independent of the volume fraction of vapour present (so long as *some* vapour is present). Anhydrite is notably weaker than calcite, and in the Bruce nuclear site samples all of the aqueous fluid inclusions observed in the present study ruptured upon freezing, leaking their contents and precluding ice-melting measurements.

As is the case for T_h measurements, any determinations of equilibrium phase transitions at sub-zero temperatures must be performed upon gradual heating rather than upon cooling, owing to the sluggish nucleation kinetics of solid phases at low temperatures. In contrast, equilibrium melting occurs at slow heating rates (e.g., 2 °C / min).

In the present study, the fluid inclusion samples were first cooled to –190 °C to promote nucleation of solid salt-hydrates and/or ice. The normal procedure of microthermometry at sub-zero temperatures is to heat slowly and determine the sequence of equilibrium transitions that defines the major components and bulk salinity of the inclusion uniquely; first, the eutectic temperature is determined, followed by any peritectics, and then the final melting temperature of the most stable solid phase. However, most of the saline inclusions encountered in the

Bruce nuclear site samples did not follow full equilibrium sequences. This is a well-known phenomenon in $CaCl_2$- and $MgCl_2$-rich brines (e.g., Oakes et al., 1990; Bakker and Baumgartner, 2012), caused by the strong hydration of the aqueous electrolytes, which inhibits crystallization of equilibrium phases at low temperatures.

By experiment, it was found in the saline inclusions from the Bruce nuclear site that ice behaves as a metastable *equilibrium* phase. That is, it nucleates fairly reliably, it melts in a gradual and reproducible manner within individual inclusions, and inclusions within the same assemblage of homogeneously-trapped inclusions yield essentially the same melting temperatures. The final melting temperature of ice in the presence of vapour, denoted T_m(ice), therefore provides a useful indicator in this study for other phase transitions which are kinetically inhibited (e.g., the melting of hydrohalite or antarcticite). For example, T_m(ice) varies systematically between different generations of fluid inclusions and hence it can be used to correlate generations between different samples. Moreover, comparison of the measured T_m(ice) values with laboratory calibrations in synthetic chemical systems (Hall et al., 1988; Oakes et al., 1990) allows the bulk salinity of the inclusions to be calculated in terms of *equivalent* wt% NaCl or $CaCl_2$+NaCl mixtures (denoted $NaCl_{eq}$ and $CaCl_2$+$NaCl_{eq}$). This value can be taken as a proxy for the mass of total dissolved solids (TDS). For inclusions saturated in halite, their bulk composition can be modelled within the H_2O–NaCl–$CaCl_2$ system (the stability of the metastable equilibrium assemblage ice + halite + liquid + vapour was quantitatively modelled for this purpose as part of this study).

Ice melting is easily measured in large inclusions containing liquid and vapour. However, in tiny, high density inclusions that contain only metastable liquid water, useful measurements are precluded. In these inclusions ice typically melts several degrees above 0 °C in the absence of vapour via a *disequilibrium* transition. The disequilibrium behaviour is easily recognized as such because, at a certain temperature, relatively large ice crystals disappear almost instantaneously, whereas equilibrium transitions below 0 °C are characterized by gradual reduction in crystal size. Because such *disequilibrium* transitions are not reproducible they cannot be quantitatively calibrated by experimental studies, and hence they cannot be used to calculate the bulk salinity of the inclusion. In some of the Bruce nuclear site fluid inclusions hosted by calcite crystals, vapour bubbles could be nucleated by heating the inclusions above room temperature until they stretched irreversibly. Thus, reproducible, equilibrium values of T_m(ice) could be determined after such intentional stretching.

3.3 LASER RAMAN SPECTROSCOPY

This method was used to identify gases and certain minerals within the fluid inclusions. Only compounds with dominantly covalent bonding yield Raman signals (e.g., methane, calcite, ice, solid CO_2), and so strong electrolytes such as NaCl cannot be detected when present in dissolved or anhydrous solid form. However, the various halide salts can at least be qualitatively identified when present in hydrated form at very low temperatures (e.g. hydrohalite, $NaCl{\cdot}2H_2O$; antarcticite, $CaCl_2{\cdot}6H_2O$). The samples need to be cooled well below room temperature to nucleate such hydrates.

This method is normally non-destructive but occasionally metastable components such as certain hydrocarbons may break down under the laser beam. Details of the method are given in Burke (2001). In practice, fluid inclusions hosted by calcite cannot always be analysed by

Raman spectroscopy. This is due to the strong birefringence of calcite, which makes it difficult to aim the laser into small inclusions.

A Horiba Jobin-Yvon LabRam HR-800 confocal instrument at the Institute of Geological Sciences, University of Bern, was used in this study. Red (632.8 nm) He-Ne and green (532.12 nm) Nd-YAG lasers were used for signal excitation, focussed through an Olympus BX41 microscope with an Olympus 100/0.95 UM PlanFI objective lens.

3.4 CRUSHING-STAGE ANALYSIS

Crushing-stage analysis is a destructive, qualitative means of determining whether the vapour fraction of an inclusion consists of water vapour or of other gases such as methane or carbon dioxide under elevated pressure. A fragment of the crystal containing fluid inclusions is placed in a transparent crushing stage and immersed in a droplet of oil. The crushing stage is then compressed to fracture the mineral fragment and to open the inclusions to atmospheric pressure, while simultaneously observing the inclusions under the microscope through a 20X objective.

When glycerine is used as the immersion oil, in which both CH_4 and CO_2 are insoluble, the appearance of expanding bubbles upon crushing the sample indicates the presence of pressurized gas within the inclusions. The absence of bubbles is typical for aqueous inclusions in which the bubbles consist only of H_2O vapour, which are normally below atmospheric pressure at room temperature.

When naphtha is used as the immersion oil, in which CH_4 is soluble but CO_2 is not, it is possible to distinguish between these two gases. In both cases the gas liberated by crushing typically expands rapidly, but bubbles dominated by CH_4 quickly dissolve into the naphtha, whereas bubbles dominated by CO_2 remain stable for long periods.

Details of the method are given in Roedder (1984), Diamond and Marshall (1990) and Goldstein and Reynolds (1994).

4. RESULTS

4.1 PETROGRAPHIC RESULTS

4.1.1 Solid Phases within Fluid Inclusions at Room Temperature

Two solid phases were identified in the fluid inclusions at room temperature. They occur exclusively of one another, as detailed in Section 4.2 below:

1) Halite was identified by its cubic habit, its isotropic optical properties, its lack of optical relief where it contacts calcite (due to the similarity in refractive indexes, at least with one of the optical axes of calcite; Figure 5c and 5e), its failure to yield a Raman spectrum (as an archetypal ionically-bonded solid), and its occasional conversion to hydrohalite during low-temperature microthermometry (see Section 4.2.1 below). Within individual fluid inclusion assemblages the volume fractions of halite are strongly variable (e.g., Figure 5).

2) Ankerite was identified by its rhombohedral habit, its high birefringence and its characteristic Raman spectrum. Within individual fluid inclusion assemblages the volume fractions of ankerite are strongly variable (see Figure 6).

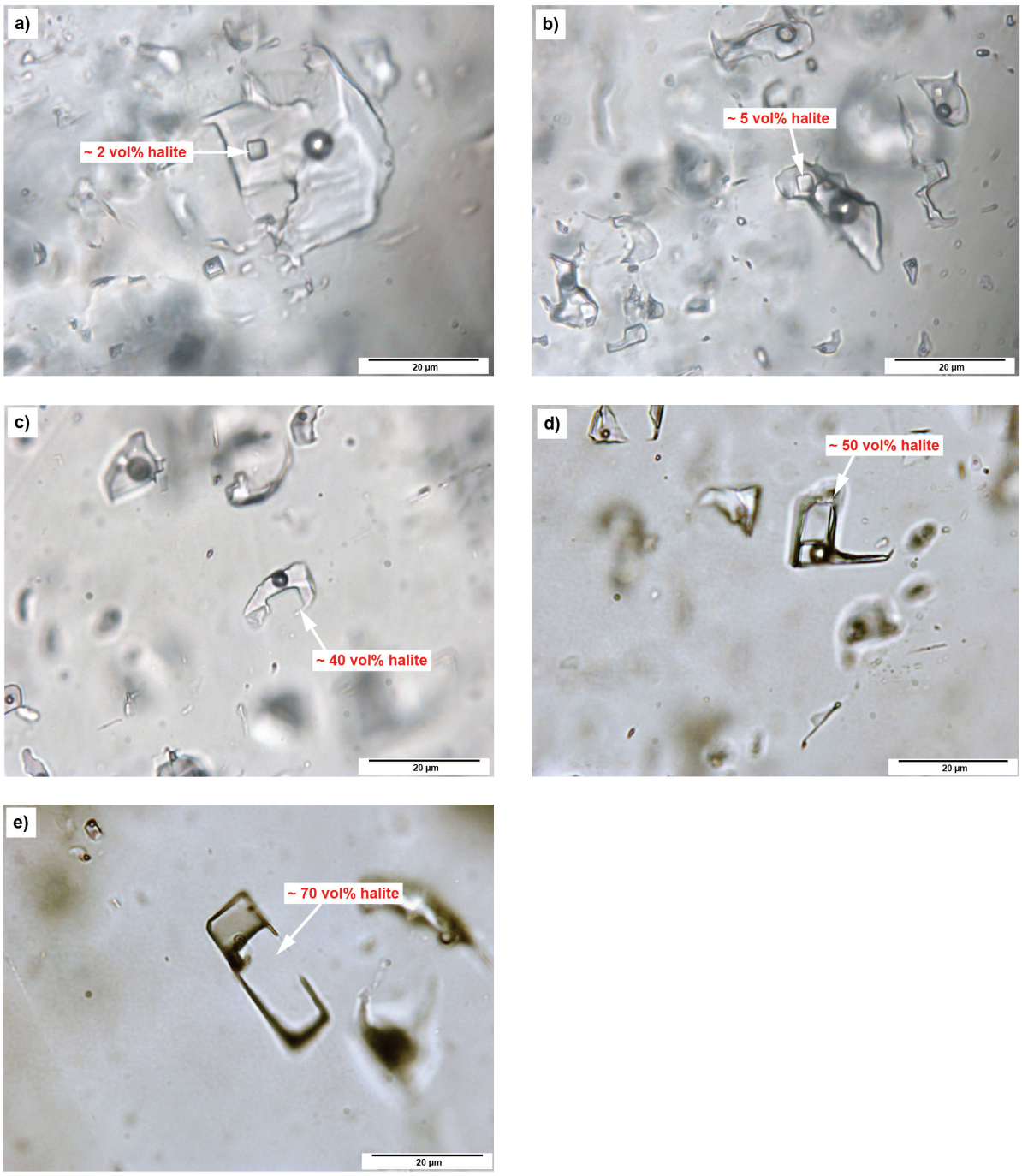


Figure 5: Various Primary and Secondary Fluid Inclusions in the DGR Samples From the Cambrian and Mid-Ordovician Contain Halite Crystallites. Within Individual Fluid Inclusion Assemblages the Volume Fractions of Halite are Strongly Variable, as Visible in a) to e) [Microphotographs in Transmitted, Polarized Light; DGR-6-886.91]

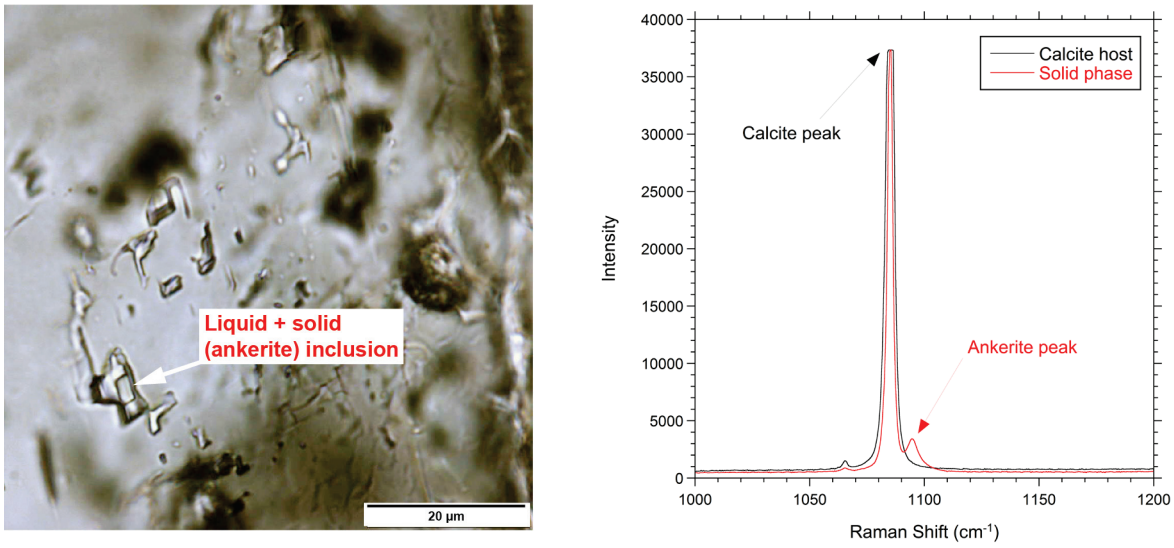


Figure 6: Left) Numerous Primary Fluid Inclusions in the DD-Calcite Samples Contain Accidentally Captured Rhombohedral Crystallites of Ankerite. Right) Acquired Raman Spectrum of the Calcite Host-Crystal and of an Ankerite Crystallite Within a Fluid Inclusion

4.1.2 Paragenetic Diagrams

Key petrographic observations for each of the samples have been documented in 225 labelled photographs in Appendix 1 (Figures A1–A102). The caption to each of these figures identifies the relative timing of the illustrated inclusion assemblages with respect to the host mineral and to other inclusion generations, plus their volume fractions of vapour.

All of the petrographic information in Appendix 1 is summarised in the form of paragenetic diagrams in Figure 7. A diagram is presented for each sample, ranked vertically in Figure 7 according to stratigraphic position (cf. Figure 1). The diagrams consist of 9 columns (numbered in blue at top), as follows:

Column 1 lists the identified generations of minerals and fluid inclusions. The phases coexisting in the inclusions at room temperature are also identified.

Column 2 lists the numbers of the relevant figures in Appendix 1 that show the specific evidence (e.g., mineral zonation, cross-cutting relations, etc.) upon which the interpretations of relative timing and mode of fluid inclusion trapping are based.

Column 3 lists the room-temperature values of vol% vapour within individual fluid inclusion assemblages. A uniform volume fraction of vapour, as indicated by a unique vol%-value for a given assemblage, implies homogeneous (i.e., single fluid phase) entrapment whereas variable volume fractions for the assemblage implies heterogeneous (i.e., multi-fluid phase) entrapment.

Column 4 lists the room-temperature values of vol% halite within individual fluid inclusion assemblages. A uniform volume fraction of halite, in the present case indicated by 0 vol% for a given assemblage, implies homogeneous (i.e., single fluid phase) entrapment of a halite-undersaturated fluid, whereas variable volume fractions for the assemblage implies heterogeneous entrapment (i.e., the fluid(s) were trapped in the presence of excess solid halite).

Column 5 shows successive time stages of mineral and fluid inclusion generations in the investigated wall rocks, vugs and veins. For example, the first diagram (sample DGR 3-034.95 Lucas Formation) shows coloured bands for "Calcite" and "Primary Liq + Vap" inclusions arranged below each other within Stage IX. This means that the indicated inclusions are of the same age as the calcite, and thus the calcite in fact precipitated from the paleofluid represented by the "Primary Liq + Vap" generation of fluid inclusions. The diagram has no implications for the absolute duration of the time stages, nor for the duration of the transitions between the stages. Question marks show where petrographic evidence to constrain the relative timing of fluid generations is missing or ambiguous. For example, in the third diagram (sample DD 12-12-1 Lucas Formation) the "Secondary metastable-Liq" generation of fluid inclusions is drawn with question marks across Stages X to XI, because its timing relative to the "Secondary Oil+Vap" generation is unknown (see discussion in Section 4.3). The stages are correlated between all the samples. For some samples certain stages have been left empty where the corresponding mineral or fluid inclusion generation was not observed.

Column 6 shows the interpreted phase-state of each paleofluid generation at the time of its entrapment, based on the principles in Section 3.1.2 and Figure 3. For example, the label "Aqueous solution + gas" means that these two immiscible, mutually saturated fluid phases were simultaneously present in the vugs and veins of the host rock at the time the fluid inclusions were trapped.

Column 7 shows the interpreted temperature of entrapment of the paleofluid generations, based on the principles in Section 3.2.2. Values in square brackets (which pertain to homogeneously-trapped inclusions) are pressure-corrected, as explained in Section 4.2.5.

Column 8 shows the range of melting temperatures of ice (or hydrohalite in blue) in the presence of vapour for the investigated assemblages (from data in Table 2).

4.2 MICROTHERMOMETRIC RESULTS

4.2.1 Phase Behaviour of Fluid Inclusions Below Room Temperature

Examples of the low-temperature behaviour of high-salinity and low-salinity inclusions from the Bruce nuclear site samples are documented with photographs and text in Appendix 2.

Few of the high-salinity inclusions show stable equilibrium phase transitions at sub-zero temperatures, i.e., hydrohalite is rarely observed as the last solid to melt upon heating. Instead, most undergo metastable transitions owing to kinetic inhibition of hydrohalite nucleation. Therefore, the metastable equilibrium melting of ice is used in the present study to derive the salinity of the inclusions, as explained in Section 4.2.4.

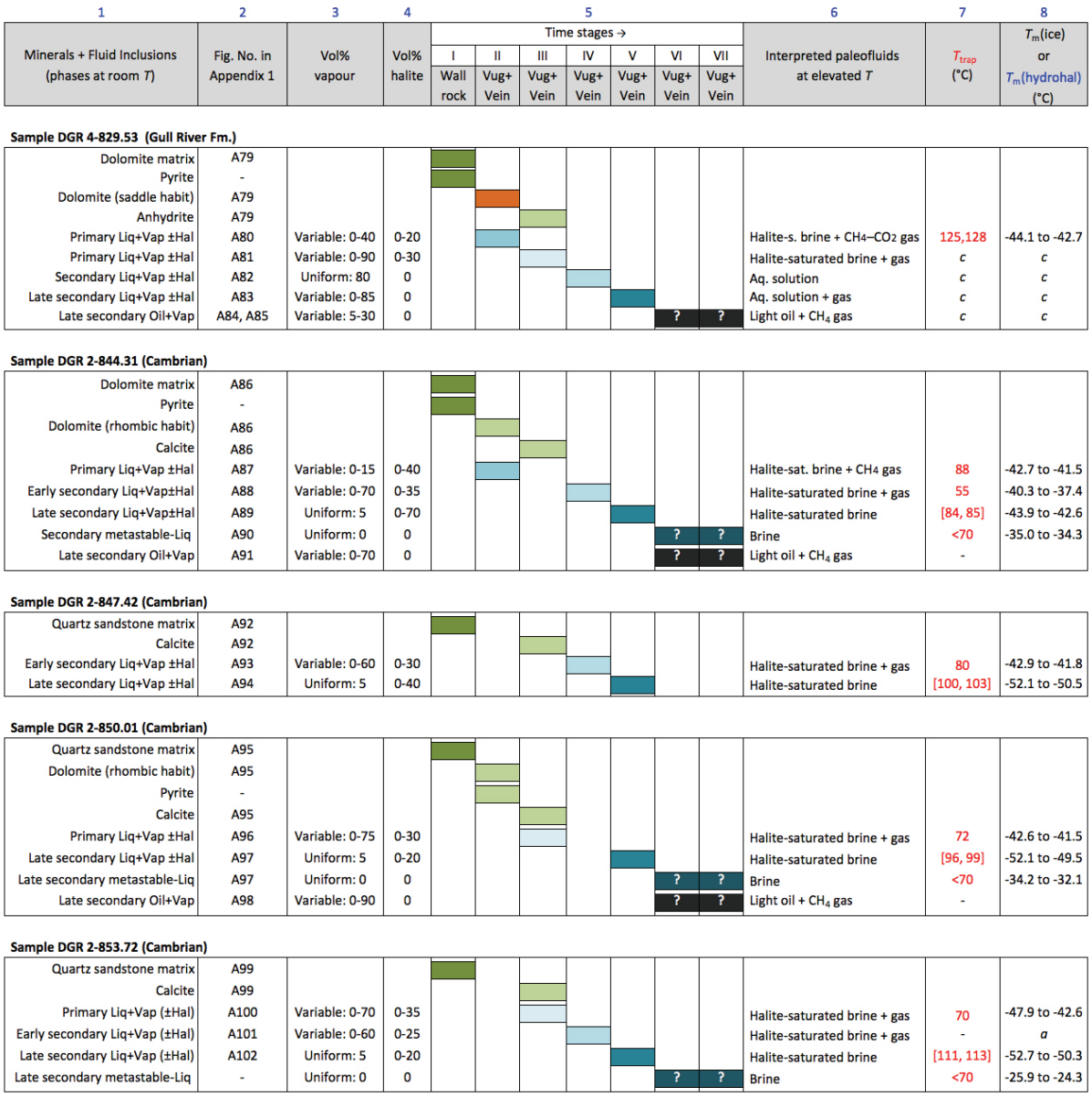
1	2	3	4	5				6	7	8
				Time stages →						
Minerals + Fluid Inclusions (phases at room *T*)	Fig. No. in Appendix 1	Vol% vapour	Vol% halite	VIII Wall rock	IX Vug+ Vein	X Vug+ Vein	XI Vug+ Vein	Interpreted paleofluids at elevated *T*	T_{trap} (°C)	T_m(ice) (°C)
Sample DGR 3-034.95 (Lucas Fm.)										
Dolomite matrix	-									
Calcite	A1-A3									
Primary Liq+Vap	A2-A7	Variable: 0-70	0					Aq. soln. + gas	-	-0.9 to -0.1
Secondary metastable-Liq	A6	Uniform: 0	0			?	?	Aq. solution	<70	-0.6 to -0.3
Sample DD 12-11 (Lucas Fm.)										
Dolomite matrix	A8									
Calcite	A8									
Primary Liq+Vap±Ankerite	A9	Variable: 0-90	0					Aq. soln. + gas	<75.9	-0.7 to -0.4
Secondary metastable-Liq	A10	Uniform: 0	0			?	?	Aq. solution	-	-0.5 to -0.3
Sample DD 12-12-1 (Lucas Fm.)										
Dolomite matrix	A11									
Calcite	A11									
Primary Liq+Vap±Ankerite	A12	Variable: 0-70	0					Aq. soln. + gas	-	-1.6 to -0.2
Secondary metastable-Liq	A13	Uniform: 0	0			?	?	Aq. solution	<70	-0.6 to -0.2
Secondary Oil+Vap	A14	Variable: 0-90	0			?	?	Light oil + CH_4 gas	-	-
Sample DD 12-12-2 (Lucas Fm.)										
Dolomite matrix	A11									
Calcite	A11									
Primary Liq+Vap±Ankerite	A12	Variable: 0-70	0					Aq. soln. + gas		
Sec. metastable-Liq±Ankerite	A13	Uniform: 0	0			?	?	Aq. solution		
Secondary Oil+Vap	A14	Variable: 0-90	0			?	?	Light oil + CH_4 gas		
Sample DD 12-12-Fv (Lucas Fm.)										
Dolomite matrix	A11									
Calcite	A11									
Primary Liq+Vap±Ankerite	A12	Variable: 0-60	0					Aq. soln. + gas		
Sec. metastable-Liq±Ankerite	A13	Uniform: 0	0			?	?	Aq. solution		
Secondary Oil+Vap	A14	Variable: 0-70	0			?	?	Light oil + CH_4 gas		
SAMPLE DD 12-13-1 (Lucas Fm.)										
Dolomite matrix	A15									
Calcite	A15									
Primary Liq+Vap±Ankerite	A16	Variable: 0-90	0					Aq. soln. + gas	<83.4	
Sec. metastable-Liq±Ankerite	A17	Uniform: 0	0			?	?	Aq. solution		
Secondary Oil+Vap	A16	Variable: 0-80	0			?	?	Light oil + CH_4 gas		
SAMPLE DD 12-13-2 (Lucas Fm.)										
Dolomite matrix	A15									
Calcite	A15									
Primary Liq+Vap±Ankerite	A16	Variable: 0-65	0					Aq. soln. + gas	62	-0.3 to -0.1
Secondary metastable-Liq	A17	Uniform: 0	0			?	?	Aq. solution	<70	-0.4 to -0.1
Secondary Oil+Vap	A16	Variable: 20-60	0			?	?	Light oil + CH_4 gas	-	-

Figure 7: Paragenetic Diagrams Summarising Petrographic Observations, Interpreted Paleofluids, Micro-Thermometry, Trapping Temperatures and Salinities in the Bruce Nuclear Site Samples. This Set of Diagrams Covers Time Stages IX–XI in the Vugs and Veins, and Pertains Only to the Samples from the Shallow Lucas Formation. See Diagrams Below For Deeper Borehole Samples

1	2	3	4	5							6	7	8
Minerals + Fluid Inclusions (phases at room *T*)	Fig. No. in Appendix 1	Vol% vapour	Vol% halite	Time stages → I	II	III	IV	V	VI	VII	Interpreted paleofluids at elevated *T*	T_{trap} (°C)	T_m(ice) or T_m(hydrohal) (°C)
				Wall rock	Vug+ Vein	Vug+ Vein	Vug+ Vein	Vug+ Vein	Vug+ Vein	Vug+ Vein			
Sample DGR 2-691.70 (Sherman Fall Fm.)													
Calcite matrix	A18												
Pyrite	-												
Calcite	A18												
Primary Liq+Vap ±Hal	A19	Variable: 0-60	0-30								Halite-saturated brine + gas	65,78	-46.9 to -40.9
Secondary Liq+Vap ±Hal	A20	Uniform: 5	0-40								Halite-saturated brine	[89, 120]	-45.2 to -44.7
Late secondary metastable-Liq	A21	Uniform: 0	0						?	?	Aq. solution	<70	*a*
Sample DGR 4-769.57 (Coboconk Fm.)													
Calcite matrix	A22												
Pyrite	-												
Calcite	A22												
Celestine	A22												
Primary Liq+Vap ±Hal	A23	Variable: 0-70	0-30								Halite-saturated brine + gas	54	-44.2 to -35.9
Early secondary Liq+Vap ±Hal	A24	Variable: 0-90	0-70								Halite-saturated brine + gas	71	-46.5 to -35.2
Late secondary Liq+Vap ±Hal	A25	Uniform: 5	0-40								Halite-saturated brine	[94]	*b*
Late secondary metastable-Liq	A26	Uniform: 0	0						?	?	Aq. solution	<70	*a*
Late secondary Oil+Vap	A27	Variable: 0-50	0						?	?	Light oil + CH_4 gas	-	
Sample DGR 2-778.44 (Coboconk Fm.)													
Dolomite matrix	A28												
Pyrite	-												
Dolomite (saddle habit)	A28												
Primary Liq+Vap ±Hal	A29	Variable: 0-60	0-20								Halite-saturated brine + gas	122	*a,b*
Late secondary Oil+Vap	A30	Uniform: 10	0						?	?	Light oil	-	
Sample DGR 3.799.15 (Coboconk Fm.)													
Calcite matrix	-												
Calcite	A31, A32												
Primary Liq+Vap ±Hal	A33-A36	Variable: 0-60	0-30								Halite-saturated brine + gas	-	-22.9 to -16.5
Secondary Liq+Vap ±Hal	A37-A41, A43	Uniform: 10	0-30								Halite-saturated brine	[101]	-45.3 to -27.1
Late secondary metastable-Liq	A42	Uniform: 0	0						?	?	Aq. solution	<70	*a*
Sampld DGR 6.883.75 (Coboconk Fm.)													
Dolomite matrix	-												
Calcite	A45												
Primary Liq+Vap ±Hal	A46	Variable: 0-85	0-50								} Halite-saturated brine + gas	} 61	-21.5 to -18.2
Secondary Liq+Vap ±Hal	-	Variable: 0-80	0-20				?						-40.7 to -39.0
Secondary Liq+Vap ±Hal	-	Variable: 0-80	0-20				?				Halite-saturated brine + gas	-	-36.4 to -33.2
Late secondary Liq+Vap ±Hal	A47, A48	Uniform: 5	0-30								Halite-saturated brine	-	-40.7 to -36.3
Sample DGR 6.886.91 (Coboconk Fm.)													
Dolomite matrix	-												
Calcite	A49												
Primary Liq+Vap	A50	Variable: 0-85	0-70								} Halite-saturated brine + gas	} 57	-
Secondary Liq+Vap+Hal	A53, A54	Variable: 0-90	0-50										-46 to -34
Late secondary Liq+Vap	A51, A52	Uniform: 5	0-15								Halite-saturated brine	[71]	-47 to -42
Late secondary metastable-Liq	A53	Uniform: 0	0						?	?	Aq. solution	<70	*a*
Sample DGR 6-892.99 (Coboconk Fm.)													
Dolomite matrix	A55, A56												
Calcite	A55, A56												
Primary Liq+Vap ±Hal	A57-A61	Variable: 0-95									} Halite-saturated brine + gas	-	
Secondary Liq+Vap ±Hal	A65	Variable: 0-90	0-40										-46.8 to -42.1
Late secondary Liq+Vap ±Hal	A62B, A64	Uniform: 10	0-10								Halite-saturated brine	[72]	-42.3 to -40.8
Late secondary metast.-Liq	A62C, A63	Uniform: 0	0						?	?	Aq. solution	<70	*a*
Late secondary Oil+Vap	A66, A67	Uniform: 10	0						?	?	Light oil	50	
Sample DGR 4-818.36 (Gull River Fm.)													
Dolomite matrix	A68, A69, A72												
Pyrite	A69												
Primary, unknown phases	A69												
Calcite	A68, A69, A72												-
Primary Liq+Vap ±Hal	A74A,B	Variable: 0-90									} Halite-sat. brine + CH_4 gas	} 42	
Early secondary Liq+Vap ±Hal	A71	Variable: 10-90	0-20										-43.1 to -40.2
Late secondary Liq+Vap ±Hal	A74C, A75	Uniform: 10	0-50								Halite-saturated brine	[109]	-44.1 to -38.8
Late secondary metast.-Liq	A70, A77	Uniform: 0	0						?	?	Aq. solution	<70	*a*
Late secondary Oil+Vap	A72, A73, A76	Variable: 5-80	0						?	?	Light oil + CH_4 gas	60	

a Inclusions too small to analyse
b Ice did not nucleate

Figure 7 *continued*: DGR Borehole Samples From the Cambrian and Mid-Ordovician, With Vugs and Veins Resolved Into Time Stages II–VII



1	2	3	4	5							6	7	8
Minerals + Fluid Inclusions (phases at room *T*)	Fig. No. in Appendix 1	Vol% vapour	Vol% halite	Time stages → I	II	III	IV	V	VI	VII	Interpreted paleofluids at elevated *T*	T_{trap} (°C)	T_m(ice) or T_m(hydrohal) (°C)
				Wall rock	Vug+ Vein	Vug+ Vein	Vug+ Vein	Vug+ Vein	Vug+ Vein	Vug+ Vein			
Sample DGR 4-829.53 (Gull River Fm.)													
Dolomite matrix	A79												
Pyrite	-												
Dolomite (saddle habit)	A79												
Anhydrite	A79												
Primary Liq+Vap ±Hal	A80	Variable: 0-40	0-20								Halite-s. brine + CH_4–CO_2 gas	125,128	-44.1 to -42.7
Primary Liq+Vap ±Hal	A81	Variable: 0-90	0-30								Halite-saturated brine + gas	*c*	*c*
Secondary Liq+Vap ±Hal	A82	Uniform: 80	0								Aq. solution	*c*	*c*
Late secondary Liq+Vap ±Hal	A83	Variable: 0-85	0								Aq. solution + gas	*c*	*c*
Late secondary Oil+Vap	A84, A85	Variable: 5-30	0						?	?	Light oil + CH_4 gas	*c*	*c*
Sample DGR 2-844.31 (Cambrian)													
Dolomite matrix	A86												
Pyrite	-												
Dolomite (rhombic habit)	A86												
Calcite	A86												
Primary Liq+Vap ±Hal	A87	Variable: 0-15	0-40								Halite-sat. brine + CH_4 gas	88	-42.7 to -41.5
Early secondary Liq+Vap±Hal	A88	Variable: 0-70	0-35								Halite-saturated brine + gas	55	-40.3 to -37.4
Late secondary Liq+Vap±Hal	A89	Uniform: 5	0-70								Halite-saturated brine	[84, 85]	-43.9 to -42.6
Secondary metastable-Liq	A90	Uniform: 0	0						?	?	Brine	<70	-35.0 to -34.3
Late secondary Oil+Vap	A91	Variable: 0-70	0						?	?	Light oil + CH_4 gas	-	
Sample DGR 2-847.42 (Cambrian)													
Quartz sandstone matrix	A92												
Calcite	A92												
Early secondary Liq+Vap ±Hal	A93	Variable: 0-60	0-30								Halite-saturated brine + gas	80	-42.9 to -41.8
Late secondary Liq+Vap ±Hal	A94	Uniform: 5	0-40								Halite-saturated brine	[100, 103]	-52.1 to -50.5
Sample DGR 2-850.01 (Cambrian)													
Quartz sandstone matrix	A95												
Dolomite (rhombic habit)	A95												
Pyrite	-												
Calcite	A95												
Primary Liq+Vap ±Hal	A96	Variable: 0-75	0-30								Halite-saturated brine + gas	72	-42.6 to -41.5
Late secondary Liq+Vap ±Hal	A97	Uniform: 5	0-20								Halite-saturated brine	[96, 99]	-52.1 to -49.5
Late secondary metastable-Liq	A97	Uniform: 0	0						?	?	Brine	<70	-34.2 to -32.1
Late secondary Oil+Vap	A98	Variable: 0-90	0						?	?	Light oil + CH_4 gas	-	
Sample DGR 2-853.72 (Cambrian)													
Quartz sandstone matrix	A99												
Calcite	A99												
Primary Liq+Vap (±Hal)	A100	Variable: 0-70	0-35								Halite-saturated brine + gas	70	-47.9 to -42.6
Early secondary Liq+Vap (±Hal)	A101	Variable: 0-60	0-25								Halite-saturated brine + gas	-	*a*
Late secondary Liq+Vap (±Hal)	A102	Uniform: 5	0-20								Halite-saturated brine	[111, 113]	-52.7 to -50.3
Late secondary metastable-Liq	-	Uniform: 0	0						?	?	Brine	<70	-25.9 to -24.3

a Inclusions too small to analyse
c Inclusions in anhydrite ruptured upon heating and freezing

Figure 7 *continued*: DGR Borehole Samples From the Cambrian and Mid-Ordovician, With Vugs and Veins Resolved Into Time Stages II–VII

An important feature of the observed assemblages of high-salinity inclusions is that their volume fractions of halite are highly variable. Although inhibition of halite nucleation could perhaps explain the absence of halite in some inclusions (despite the extensive geological time available for nucleation), all the observed assemblages also show a range in the relative fractions of halite where it is present, as visible in Figure 5. The validity of the deduction that this texture indicates halite-saturation at the time of fluid entrapment is therefore unaffected by the phenomenon of nucleation inhibition.

In contrast to the high-salinity inclusions, the low-salinity inclusions behave as equilibrium systems (Appendix B.2), characteristic of very dilute aqueous solutions.

4.2.2 Microthermometric Data

Table 2 shows all the microthermometric measurements. The column labelled "Interpretation of T_h" specifies the significance of each T_h measurement according to the principles and strategy outlined in Sections 3.2.1 and 3.2.2, taking into account any evidence found for stretching. Red numbers in column 3 show the true or most constraining values on T_h(true). The same values are also listed in column 8 of Figure 7.

4.2.3 Crushing-Stage Data

Table 3 shows all the crushing-stage results. All 4 analysed Lucas Formation samples liberated abundant gas upon crushing under glycerine. Of the 9 analysed samples from the Cambrian and Mid-Ordovician, four released abundant gas (DGR 2-844.31 Cambrian, DGR 2-850.01 Cambrian, DGR 4-818.36 Gull River, DGR 4-829.53 Gull River), corroborating the detection by Raman analysis of $CH_4 \pm CO_2$ in their primary Liq + Vap ± Hal inclusions. The other Cambrian and Mid-Ordovician samples liberated sparse amounts of gas. Nevertheless, the crushing-stage confirmed that all the analysed samples contain gas under elevated pressure (i.e., considerably in excess of atmospheric pressure).

Additional crushing tests on 4 samples (DD 12-11 Lucas, DD 12-12 Lucas, DGR 2-844.31 Cambrian and DGR 2-850.01 Cambrian) under naphtha revealed that in all cases, the released gas is dominantly CH_4 and not CO_2.

4.2.4 Brine compositions in the Model H_2O–NaCl–$CaCl_2$ Ternary System

The brines belonging to Paleofluids 1-4 (as defined in Figure 8 below) in the Cambrian and Mid-Ordovician samples are undoubtedly complex mixtures of various salts besides NaCl. The presence of Ca, Mg and Fe in host minerals suggests the presence of $CaCl_2$, $MgCl_2$, $FeCl_2$. Presumably KCl and others are also present, as is typical for basinal brines. The very low measured T_m(ice) values, far below the eutectic temperature for H_2O–NaCl at –21 °C, are consistent with the dominance of 2:1 electrolytes. For example, the H_2O–$CaCl_2$–$MgCl_2$ system has its stable eutectic at –55 °C. This implies that ice could melt at any temperature above this value. In the investigated samples, T_m(ice) values are as low as –53 °C.

With the data at hand, it is possible to express the bulk composition of the brines only in terms of simplified ternary model systems. Considering that many of the brines are saturated with respect to halite, the appropriate model system is the H_2O–NaCl–$CaCl_2$ ternary. Figure 8a shows the stable phase relations in this system, based on Oakes et al. (1990) and Steele-MacInnis et al. (2011). Blue lines in this diagram show selected isotherms of ice melting along the Ice + Liquid + Vapour liquidus and of halite melting along the Halite + Liquid + Vapour liquidus. The stable hydrohalite liquidus is shaded grey.

Table 2: Microthermometric Results. Outcrop Samples are Listed First, Followed by Borehole Samples in Order of Borehole Number and Then Depth

Sample/ Strat. Formation Inclusion generation	Assemblage number	T_h (LV→L) [°C]	Interpretation of T_h	T_n (L→LV) [°C]	T_{trap} [°C]	T_m(ice) (LVS→LV) [°C]
DD 12-11 Devonian						
Prim. Liq+Vap±Ankerite	1	125.3	Artifact (stretching)	96.4		-0.4
in calcite	4	109.1 stretched	Artifact (stretching)	No bubble		-0.7
	4	106.9 stretched	Artifact (stretching)	No bubble		-
Heterogeneous trapping	6	-		-		-0.7
	8	Stretched		-		-0.5
	9	Stretched		-		-0.4
	10	-		-		-0.5
	10	Stretched		-		-0.6
	13	Stretched		-		-0.5
	15	-		-		-0.4
	15	-		-		-0.7
	Isolated	75.9	T_h(min) > T_h(true)	No bubble	<75.9	–
DD 12-12-1 Devonian						
Prim. Liq+Vap±Ankerite	1	-		-		0.3 (metast.)
in calcite	1	-		-		0.2 (metast.)
	2	-		-		-0.2
Heterogeneous trapping	3	-		-		-0.9
	3	-		-		-0.7
	3	-		-		-1.3
	4	-		-		-1.6
	5	-		-		-0.7
	6	-		-		-1.4
	7	-		-		-0.5
Late second. metast. Liq	1	-		-	<70	-0.6 artif. stretched
in calcite	1	-		-		-0.3 artif. stretched
	1	-		-		-0.2 artif. stretched
Homogeneous trapping	1	-		-		-0.4 artif. stretched
	1	-		-		-0.3 artif. stretched
	1	-		-		-0.4 artif. stretched
DD 12-13-1 Devonian						
Prim. Liq+Vap±Ankerite	Isolated	83.7	Artifact (het. trapping)	No bubble		-
in calcite	Isolated	83.4	T_h(min) > T_h(true)	No bubble	<83.4	-
Heterogeneous trapping	Isolated	160.5 stretched	Artifact (stretching)	131.1		-
DD 12-13-2 Devonian						
Prim. Liq+Vap±Ankerite	1	130.8	Artifact (stretching)	57.5		-0.3
in calcite	2	-		-		-0.2
	3	Stretched		-		0.1 (metastable)
Heterogeneous trapping	3	122.2	Artifact (stretching)	No bubble		-0.2
	3	104.7 stretched	Artifact (stretching)	54.3		-
	3	Stretched		-		-0.1
	4	136.1	Artifact (stretching)	51.9		-0.2
	5	Stretched		-		0.2 (metastable)
	7	-		-		-0.2
	9	-		-		0.2 (metastable)
	10	Stretched		-		-0.1
	10	-		-		-0.1
	Isolated	151.7 stretched	Artifact (stretching)	97.8		-
	Isolated	62.1	T_h(min) = T_h(true)	No bubble	62.1	-
	Isolated	65.8	Artifact (het. trapping)	No bubble		-
	Isolated	78.7	Artifact (het. trapping)	No bubble		-
	Isolated	78.1	Artifact (het. trapping)	No bubble		-

T_n(L→LV): Nucleation temperature of vapour bubble upon cooling from T_h
Isolated: Inclusions not recognizably part of an assemblage

Table 2: ***Continued***

Sample/ Strat. Formation Inclusion generation	Assemblage number	T_h (LV→L) [°C]	Interpretation of T_h	T_n (L→LV) [°C]	T_{trap} [°C]	T_m(ice) (LVS→LV) [°C]
DGR 2-691.70 Sherman Fall						
Primary Liq+Vap±Hal	1	78.1	T_h(min) = T_h(true)	75.4	78	-46.9
in calcite	1	93.7	Artifact (het. trapping)	91.8		-46.0
	1	96.7	Artifact (het. trapping)	92.1		-46.6
Heterogeneous trapping	1	97.5	Artifact (het. trapping)	94.3		-
therefore T_{trap}=T_h(min)	3	64.7	T_h(min) = T_h(true)	54.5	65	-43.5
	3	81.9	Artifact (het. trapping)	76.6		-42.7
	3	84.1	Artifact (het. trapping)	79.8		-41.6
	3	-		-		-40.9
Secondary Liq+Vap±Hal	2	76.5	T_h(true); no stretching	73.1	>76 [89]	-
in calcite	2	77.1	T_h(true); no stretching	71.3		-
	2	72.1	T_h(true); no stretching	67.8		-
Homogeneous trapping	2	73.5	T_h(true); no stretching	68.6		-
therefore T_{trap}>T_h(max)	3	105.8	T_h(true); no stretching	101.3		-45.2
	3	106.1	T_h(true); no stretching	102.2	>106 [120]	-44.7
	3	104.6	T_h(true); no stretching	100.6		-
	3	101.7	T_h(true); no stretching	97.5		-
DGR 2-778.44 Coboconk						
Primary Liq+Vap ±Hal	1	124.6	Artifact (het. trapping)	115.6		-
in dolomite	1	133.4	Artifact (het. trapping)	123.1		-
	2	125.2	Artifact (het. trapping)	112.4		-
Heterogeneous trapping	3	149.6	Artifact (het. trapping)	92.1		-
therefore T_{trap}=T_h(min)	3	146.7	Artifact (het. trapping)	139.2		-
	4	123.7	Artifact (het. trapping)	No bubble		-
	4	128.3	Artifact (het. trapping)	86.2		-
	4	132.9	Artifact (het. trapping)	82.7		-
	5	122.1	T_h(min) = T_h(true)	51.6	122	-
	5	130.1	Artifact (het. trapping)	78.1		-
DGR 2-844.31 Cambrian						
Primary Liq+Vap±Hal	1	87.8	T_h(min) = T_h(true)	43.5	88	-
in dolomite	1	129.7	Artifact (het. trapping)	97.1		-
	3	105.7	Artifact (het. trapping)	96.3		-41.5
Heterogeneous trapping	3	116.1	Artifact (het. trapping)	64.3		-42.7
therefore T_{trap}=T_h(min)	3	96.6	Artifact (het. trapping)	59.2		-
	4	89.2	Artifact (het. trapping)	26.8		-
	4	88.7	Artifact (het. trapping)	No bubble		-
	4	118.9	Artifact (het. trapping)	68.5		-
Early sec. Liq+Vap±Hal	1	56.8	Artifact (het. trapping)	49.8		-
in calcite	1	54.8	T_h(min) = T_h(true)	45.2	55	-40.3
Heterogeneous trapping	1	61.2	Artifact (het. trapping)	40.1		-37.4
therefore T_{trap}=T_h(min)	1	65.4	Artifact (het. trapping)	58.2		-38.9
Late second. Liq+Vap±Hal	1	76.8	T_h(true); no stretching	28.1	>77 [85]	-43.0
in calcite	1	73.1	T_h(true); no stretching	52.3		-42.6
	1	74.3	T_h(true); no stretching	36.3		-
Homogeneous trapping	3	69.8	T_h(true); no stretching	51.0		-43.2
therefore T_{trap}>T_h(max)	3	74.9	T_h(true); no stretching	72.3	>75 [84]	-43.9
	3	74.1	T_h(true); no stretching	68.6		-42.7
	3	74.5	T_h(true); no stretching	50.6		-43.8
	3	70.2	T_h(true); no stretching	56.1		-43.4
Late second. metast. Liq	1	-		-		-35.0 artif. stretched
in calcite	1	-		-		-34.3 artif. stretched
Homogeneous trapping	1	-		-		-34.4 artif. stretched

T_n(L→LV): Nucleation temperature of vapour bubble upon cooling from T_h
[Blue]: Pressure-corrected trapping temperatures according to Section 4.2.5 in text.

Table 2: ***Continued***

Sample/ Strat. Formation Inclusion generation	Assemblage number	T_h (LV→L) [°C]	Interpretation of T_h	T_n (L→LV) [°C]	T_{trap} [°C]	T_m(ice) (LVS→LV) [°C]
DGR 2-847.42 Cambrian						
Early sec. Liq+Vap±Hal	1	79.8	T_h(min) = T_h(true)	34.7	80	-42.1
in calcite	1	88.9	Artifact (het. trapping)	58.3		-42.9
Heterogeneous trapping	1	97.6	Artifact (het. trapping)	92.9		-41.8
therefore T_{trap}=T_h(min)	1	99.1	Artifact (het. trapping)	96.2		-
Late second. Liq+Vap±Hal	1	87.1	T_h(true); no stretching	80.2		-52.1
in calcite	1	89.2	T_h(true); no stretching	84.8		-50.7
	1	93.7	T_h(true); no stretching	88.3	>94 [103]	-
Homogeneous trapping	1	87.5	T_h(true); no stretching	82.3		-
therefore T_{trap}>T_h(max)	2	83.6	T_h(true); no stretching	79.2		-50.9
	2	85.4	T_h(true); no stretching	78.5		-50.5
	2	90.9	T_h(true); no stretching	88.1	>91 [100]	-
DGR 2-850.01 Cambrian						
Primary Liq+Vap±Hal	1	71.8	T_h(min) = T_h(true)	No bubble	72	-41.6
in calcite	1	87.5	Artifact (het. trapping)	No bubble		-42.6
Heterogeneous trapping	1	91.3	Artifact (het. trapping)	84.7		-41.5
therefore T_{trap}=T_h(min)	1	120.3	Artifact (het. trapping)	88.1		-42.1
Secondary Liq+Vap±Hal	1	91.1	T_h(true); no stretching	86.4	>91 [99]	-52.1
in calcite	1	89.7	T_h(true); no stretching	84.8		-49.5
	1	80.5	T_h(true); no stretching	73.4		-51.9
Homogeneous trapping	1	85.4	T_h(true); no stretching	80.1		-51.7
therefore T_{trap}>T_h(max)	2	83.1	T_h(true); no stretching	74.3		-
	2	86.8	T_h(true); no stretching	79.4		-51.3
	2	88.4	T_h(true); no stretching	83.3	>88 [96]	-
Late second. metast. Liq	1	-		-	<70	-32.1 artif. stretched
in calcite	1	-		-		-32.8 artif. stretched
Homogeneous trapping	1	-		-		-34.2 artif. stretched
DGR 2-853.72 Cambrian						
Primary Liq+Vap±Hal	2	-		-		-42.7
in calcite	2	-		-		-42.6
	3	101.9	Artifact (het. trapping)	No bubble		-43.1
Heterogeneous trapping	3	101.7	Artifact (het. trapping)	47.7		-42.9
therefore T_{trap}=T_h(min)	5	70.3	T_h(min) = T_h(true)	No bubble	70	-
	5	71.5	Artifact (het. trapping)	No bubble		-
	5	78.7	Artifact (het. trapping)	No bubble		-
	5	81.6	Artifact (het. trapping)	No bubble		-
	5	87.4	Artifact (het. trapping)	No bubble		-
	5	92.7	Artifact (het. trapping)	30.5		-47.2
	5	95.4	Artifact (het. trapping)	No bubble		-47.9
	5	135.3	Artifact (het. trapping)	56.3		-
Late second. Liq+Vap±Hal	2	92.1	T_h(true); no stretching	61.1		-51.3
in calcite	2	96.3	T_h(true); no stretching	89.3		-50.3
	2	104.3	T_h(true); no stretching	96.3	>104 [113]	-51.7
Homogeneous trapping	3	94.1	T_h(true); no stretching	No bubble		-
therefore T_{trap}>T_h(max)	3	97.4	T_h(true); no stretching	93.2		-52.7
	3	98.7	T_h(true); no stretching	96.1		-
	3	102.1	T_h(true); no stretching	No bubble	>102 [111]	-
Late second. metast. Liq	1	-		-	<70	-25.2 artif. stretched
in calcite	1	-		-		-24.3 artif. stretched
Homogeneous trapping	1	-		-		-24.8 artif. stretched
	1	-		-		-25.9 artif. stretched

T_n(L→LV): Nucleation temperature of vapour bubble upon cooling from T_h
[Blue]: Pressure-corrected trapping temperatures according to Section 4.2.5 in text.

Table 2: ***Continued***

Sample/ Strat. Formation Inclusion generation	Assemblage number	T_h (LV→L) [°C]	Interpretation of T_h	T_n (L→LV) [°C]	T_{trap} [°C]	T_m(ice) (LVS→LV) [°C]
DGR 3-034.95 Lucas						
Prim. Liq+Vap±Ankerite	1	-		-		-0.4
in calcite	1	-		-		-0.4
	1	-		-		-0.5
Heterogeneous trapping	2	-		-		-0.1
	2	-		-		-0.9
	2	-		-		-0.5
	2	-		-		-0.5
	3	-		-		-0.6
	3	-		-		-0.4
	3	-		-		-0.4
	4	-		-		-0.4
	4	-		-		-0.2
Late second. metast. Liq	1	-		-	<70	-0.3 artif. stretched
in calcite	1	-		-		-0.5 artif. stretched
	1	-		-		-0.4 artif. stretched
Homogeneous trapping	1	-		-		-0.6 artif. stretched
	1	-		-		-0.5 artif. stretched
	1	-		-		-0.3 artif. stretched
DGR 3-799.15 Coboconk						
Primary Liq+Vap±Hal	1	-		-	-	Hydrohalite -20.1
in calcite	2	-		-		Hydrohalite -19.9
	3	-		-		Hydrohalite -16.5
Heterogeneous trapping	4	-		-		Hydrohalite -22.8
	5	-		-		Hydrohalite -22.0
	6	-		-		Hydrohalite -22.9
	7	-		-		Hydrohalite -18.4
Secondary Liq+Vap±Hal	1	85.6	T_h(true); no stretching	No bubble	>86 [101]	-
in calcite	1	83	T_h(true); no stretching	73.8		-
	1	102.9	Artifact (stretching)	-		-
Homogeneous trapping	1	110.5	Artifact (stretching)	103.5		-
therefore T_{trap}>T_h(max)	1	124.5	Artifact (stretching)	122.2		-
	1	134.5	Artifact (stretching)	80		-
	1	154.5	Artifact (stretching)	107.8		-
DGR 3-808.18 Gull River						
Primary L+V (in Cal)	1	-		-	-	T_m(cla) = 15.2
DGR 4-818.36 Gull River						
Primary Liq+Vap±Hal	1	-		-	-	-41.8
in calcite	1	-		-		-40.2
	1	-		-		-41.3
Heterogeneous trapping	1	-		-		-41.7
therefore T_{trap}=T_h(min)	1	-		-		-41.1
	2	-		-		-43.1
	2	-		-		-42.7
Secondary Liq+Vap±Hal	1	42.1	T_h(min) = T_h(true)	31.2	42	-
in calcite	1	51.6	Artifact (het. trapping)	Decrep.		-
Heterogeneous trapping	1	98.8	Artifact (het. trapping)	94.7		-
therefore T_{trap}=T_h(min)						
Late second. Liq+Vap±Hal	1	-		-		-43.7 (artif. stretched)
in calcite	1	-		-		-42.8 (artif. stretched)
	2	-		-		-39.9 (artif. stretched)
Homogeneous trapping	2	-		-		-38.8 (artif. stretched)
therefore T_{trap}>T_h(max)	3	-		-		-44.1 (artif. stretched)
	4	-		-		-42.8 (artif. stretched)
	5	-		-		-41.8 (artif. stretched)
	6	89	T_h(true); no stretching	82.7		-
	6	93.5	T_h(true); no stretching	85.8	>94 [109]	-
Late second. Oil+CH4	1	59.1	T_h(min) = T_h(true)	39.8	60	-
in calcite	1	64.5	Artifact (het. trapping)	51.1		-
	1	89	Artifact (het. trapping)	82.7		-
Heterogeneous trapping	1	93.5	Artifact (het. trapping)	85.8		-
therefore T_{trap}=T_h(min)	1	94.1	Artifact (het. trapping)	79.5		-
	1	94.1	Artifact (het. trapping)	79.5		-
	1	126.8	Artifact (het. trapping)	114.6		-

T_n(L→LV): Nucleation temperature of vapour bubble upon cooling from T_h
[Blue]: Pressure-corrected trapping temperatures according to Section 4.2.5 in text.
Hydrohalite: Last solid to melt upon heating below 0 °C is hydrohalite, not ice.

Table 2: ***Continued***

Sample/ Strat. Formation Inclusion generation	Assemblage number	T_h (LV→L) [°C]	Interpretation of T_h	T_n (L→LV) [°C]	T_{trap} [°C]	T_m(ice) (LVS→LV) [°C]
DGR 4-769.57 Coboconk						
Primary Liq+Vap±Hal	1	54.1	T_h(min) = T_h(true)	No bubble	54	-35.9
in calcite	1	63.9	Artifact (het. trapping)	No bubble		-40.9
	1	73.2	Artifact (het. trapping)	No bubble		-44.2
Heterogeneous trapping	1	92.8	Artifact (het. trapping)	88.1		-44.1
therefore T_{trap}=T_h(min)	1	-		-		-37.1
Secondary Liq+Vap±Hal	1	72.3	Artifact (het. trapping)	67.1	71	-44.2
in calcite	1	70.5	T_h(min) = T_h(true)	64.2		-35.2
Heterogeneous trapping	1	76.1	Artifact (het. trapping)	70.8		-46.2
therefore T_{trap}=T_h(min)	2	-		-		-46.5
Late second. Liq+Vap±Hal	1	80.4	T_h(true); no stretching	77.3	>80 [94]	*
in calcite	1	79.3	T_h(true); no stretching	75.7		*
Homogeneous trapping	1	74.7	T_h(true); no stretching	71.2		*
therefore T_{trap}>T_h(max)	1	75.8	T_h(true); no stretching	71.1		*
DGR 4-829.53 Gull River						
Primary Liq+Vap ±Hal	1	125.3	T_h(min) = T_h(true)	119.8	125	-42.9
in dolomite	1	127.6	Artifact (het. trapping)	110.6		-43.4
	1	132.2	Artifact (het. trapping)	90.1		-44.1
Heterogeneous trapping	1	134.8	Artifact (het. trapping)	74.3		-43.6
therefore T_{trap}=T_h(min)	1	137.8	Artifact (het. trapping)	94.7		-44.1
	2	127.9	T_h(min) = T_h(true)	79.1	128	-
	2	128.7	Artifact (het. trapping)	104.6		-
	2	132.9	Artifact (het. trapping)	102.2		-43.2
	2	134.2	Artifact (het. trapping)	64.5		-
	2	134.5	Artifact (het. trapping)	131.7		-42.7
DGR 6-883.75 Coboconk						
Primary Liq+Vap±Hal	1	-		-	-	Hydrohalite -20.6
in calcite	1	-		-		Hydrohalite -21.5
	1	-		-		Hydrohalite -18.2
Heterogeneous trapping	1	-		-		Hydrohalite -20.5
therefore T_{trap}=T_h(min)	2	60.9	T_h(min) = T_h(true)	Decrep.	61	-
	2	140.9	Artifact (het. trapping)	138.4		-
	2	259.6	Artifact (het. trapping)	231.4		-
	2	298	Artifact (het. trapping)	270.4		-
Secondary Liq+Vap±Hal	1	-		-		-36.4
in calcite	1	-		-		-33.2
Heterogeneous trapping	1	-		-		-35.2
	1	-		-		-34.8
Late second. Liq+Vap±Hal	1	-		-	-	-39.0
in calcite	1	-		-		-39.9
	1	-		-		-40.7
Homogeneous trapping	2	-		-		-26.7
	2	-		-		-36.3
	2	-		-		-26.4
	3	-		-		-39.2
	3	-		-		-40.3
	4	235	Artifact (stretching)	218.7		-
	4	243.7	Artifact (stretching)	229.3		-
	4	328.4	Artifact (stretching)	317.2		-
	4	363.7	Artifact (stretching)	350.5		-

* No nucleation of ice or hydrohalite

T_n(L→LV): Nucleation temperature of vapour bubble upon cooling from T_h

[Blue]: Pressure-corrected trapping temperatures according to Section 4.2.5 in text.

Hydrohalite: Last solid to melt upon heating below 0 °C is hydrohalite, not ice.

Table 2: ***Continued***

Sample/ Strat. Formation Inclusion generation	Assemblage number	T_h (LV→L) [°C]	Interpretation of T_h	T_n (L→LV) [°C]	T_{trap} [°C]	T_m(ice) (LVS→LV) [°C]
DGR 6-886.91 Coboconk						
Primary Liq+Vap±Hal	1	56.9	T_h(min) = T_h(true)	45.9	57	-
in calcite	1	99.5	Artifact (het. trapping)	-		-
Heterogeneous trapping	1	165.2	Artifact (het. trapping)	-		-
therefore T_{trap}=T_h(min)	1	193.5	Artifact (het. trapping)	187.1		-
Secondary Liq+Vap±Hal	1	-		-		-34
in calcite	1	-		-		-34
	1	-		-		-45
Heterogeneous trapping	1	-		-		-44
	1	-		-		-43
	1	-		-		-40
	2	-		-		-41
	2	-		-		-46
	2	-		-		-40
	2	-		-		-38
	2	-		-		-43
	2	-		-		-42
	3	160.8	Artifact (stretch+het.trap.)	153.4	-	-
	3	188.8	Artifact (stretch+het.trap.)	178.9		-
	3	208.7	Artifact (stretch+het.trap.)	200.6		-
	3	293.2	Artifact (stretch+het.trap.)	277.8		-
Late second. Liq+Vap±Hal	1	-		-		-42
in calcite	1	-		-		-46
	1	-		-		-47
Homogeneous trapping	1	-		-		-47
therefore T_{trap}>T_h(max)	2	56.9	T_h(true); no stretching	53.4	>57 [71]	-
	2	72.6	Artifact (stretching)	63.7		-
	2	75.9	Artifact (stretching)	52.5		-
	2	80.5	Artifact (stretching)	67.5		-
	2	85.9	Artifact (stretching)	83.2		-
DGR 6-892.99 Coboconk						
Primary Liq+Vap±Hal	1	-		-	-	-46.8
in calcite	1	-		-		-45.4
	1	-		-		-42.1
Heterogeneous trapping	2	-		-		-45.1
	2	-		-		-44.5
Late second. Liq+Vap±Hal	1	-		-		-42.3 (artif. stretch)
in calcite	1	-		-		-40.8 (artif. stretch)
Homogeneous trapping	2	57.6	T_h(true); no stretching	44.2	>58 [72]	-
therefore T_{trap}>T_h(max)	2	61.1	T_h(true); no stretching	35.4		-
Late second. Oil+Vap	1	48.3	T_h(true); no stretching	-		-
in calcite	1	49.9	T_h(true); no stretching	33.1	50	-
Heterogeneous trapping	1	139.8	T_h(true); no stretching	31		-
therefore T_{trap}=T_h(min)						

T_n(L→LV): Nucleation temperature of vapour bubble upon cooling from T_h
[Blue]: Pressure-corrected trapping temperatures according to Section 4.2.5 in text.

Table 3: Crushing-Stage Results

Sample	Formation	Run	Gas detected by crushing (Y/N)? Brackets: minor amounts of gas		*Comments*
DD 12-11	Lucas				
		1	Y	CH_4	*Additional crushing in naphtha*
		2	Y	CH_4	*Additional crushing in naphtha*
		3	Y	CH_4	*Additional crushing in naphtha*
DD 12-12	Lucas				
		1	Y	CH_4	*Additional crushing in naphtha*
		2	Y	CH_4	*Additional crushing in naphtha*
		3	Y	CH_4	*Additional crushing in naphtha*
DD 12-13	Lucas				
		1	Y		
		2	Y		
		3	Y		
DGR 2-691.71	Sherman Fall				
			Not analyzed		*Vein too small to be sampled for crushing*
DGR 2-778.44	Coboconk				
			Not analyzed		*Dolomite too dark to see inclusions*
DGR 2-844.31	Cambrian				
		1	Y	CH_4	*Additional crushing in naphtha*
		2	Y	CH_4	*Additional crushing in naphtha*
		3	Y	CH_4	*Additional crushing in naphtha*
DGR 2-847.42	Cambrian				
		1	N		
		2	(Y)		
		3	(Y)		
DGR 2-850.01	Cambrian				
		1	Y	CH_4	*Additional crushing in naphtha*
		2	(Y)	CH_4	*Additional crushing in naphtha*
		3	Y	CH_4	*Additional crushing in naphtha*
DGR 2-853.72	Cambrian				
			Not analyzed		*Vein too small to be sampled for crushing*
DGR 3-034.95	Lucas				
		1	Y		
		2	Y		
		3	Y		
DGR 3.799.15	Coboconk				
		1	N		
		2	N		
		3	(Y)		
DGR 3-808.18	Gull River				
			Not analyzed		*Sample contains no inclusions*
DGR 4-818.36	Gull River				
		1	Y		
		2	(Y)		
		3	Y		
DGR 4-769.57	Coboconk				
			Not analyzed		*No sample left*
DGR 4-829.53	Gull River				
		1	Y		
		2	Y		
		3	Y		
DGR 6.883.75	Coboconk				
		1	N		
		2	(Y)		
		3	(Y)		
DGR 6.886.91	Coboconk				
		1	(Y)		
		2	N		
		3	(Y)		
DGR 6-892.99	Coboconk				
			Not analyzed		*Vein too small to be sampled for crushing*

All Samples were tested while immersed in glycerine and some were also tested while immersed in naphtha.

Different approaches are used here to estimate the composition of the halite-saturated brines versus the undersaturated brines. In the vast majority of halite-saturated brine inclusions, ice was observed to melt in metastable equilibrium with halite, rather than stable hydrohalite. To model this behaviour, the metastable cotectic has been constructed for this study by extrapolating the ice and halite liquidi beneath the hydrohalite field, based on calculations using the correlations in MacInnis et al. (2011). The red curve in Figure 8 marks the locus of this metastable equilibrium. Figure 9 shows temperatures and total salinity along this curve. To determine the bulk composition of a given halite-saturated fluid inclusion, T_m(ice) is first plotted on the metastable cotectic. Consider the example at –42 °C, indicated by the green circle. From this point the green arrow shows the change in the composition of the liquid as halite melts upon further heating (the arrow points to the NaCl apex of the diagram). The green arrow terminates at the isotherm on the halite liquidus, which corresponds to the independently-determined trapping temperature of the fluid inclusion. The example is for a trapping temperature of 128 °C. At this point the composition of the halite-saturated brine is defined within the ternary system. The example orange box indicates a bulk salinity ($CaCl_2$+$NaCl_{eq}$) of 34 wt% and a $CaCl_2$/($CaCl_2$+NaCl) ratio of 46 mol%.

In the rare halite-saturated inclusions where hydrohalite nucleates, its melting temperature was used to fix its position on the cotectic curve involving hydrohalite+halite+liquid+vapour (lower bounding curve of grey shaded field in Figure 8a; temperatures along this cotectic are not shown in Figure 8 but were obtained from MacInnis et al., 2011). From that point a melting trend (similar to the green arrow in Figure 8a) was constructed towards halite to determine the bulk composition at the trapping temperature of the inclusion.

For the halite-undersaturated inclusions (belonging to Paleofluid 4 in Figure 8), the lack of an observable melting transition in addition to T_m(ice) renders an exact solution impossible. Such inclusions can only be broadly constrained to lie along the relevant isotherm on the ice liquidus. For example, an inclusion that shows T_m(ice) at –42 °C lies somewhere along a rather short isotherm, such that the possible range of bulk compositions is small. In contrast, an inclusion with T_m(ice) = –14 °C could have any conceivable $CaCl_2$/($CaCl_2$+NaCl) ratio, while the bulk salinity is narrowly constrained at ~23–26 wt% $CaCl_2$+$NaCl_{eq}$. Figure 8b shows the results of applying these two approaches to the studied inclusions, based on the microthermometric data in Table 2.

4.2.5 Pressure Correction for T_h Values of Homogeneously Entrapped Inclusions

As explained in Section 3.2.2, the T_h values of homogeneously entrapped inclusions yield only lower limits on the true trapping temperatures. Thus the T_{trap} values listed in Table 2 are given as, e.g., >80 °C. The true trapping temperature can be estimated if (1) sufficient experimental or theoretical equations-of-state are available to calculate the P/T slope of the isochore of the fluid inclusions, and (2) the pressure of the fluid at the time of trapping (P_{trap}) is known. Then T_{trap} can be derived by intersection of the isochore with P_{trap}. The difference between T_h and T_{trap} is known as the "pressure correction" in the fluid inclusion literature.

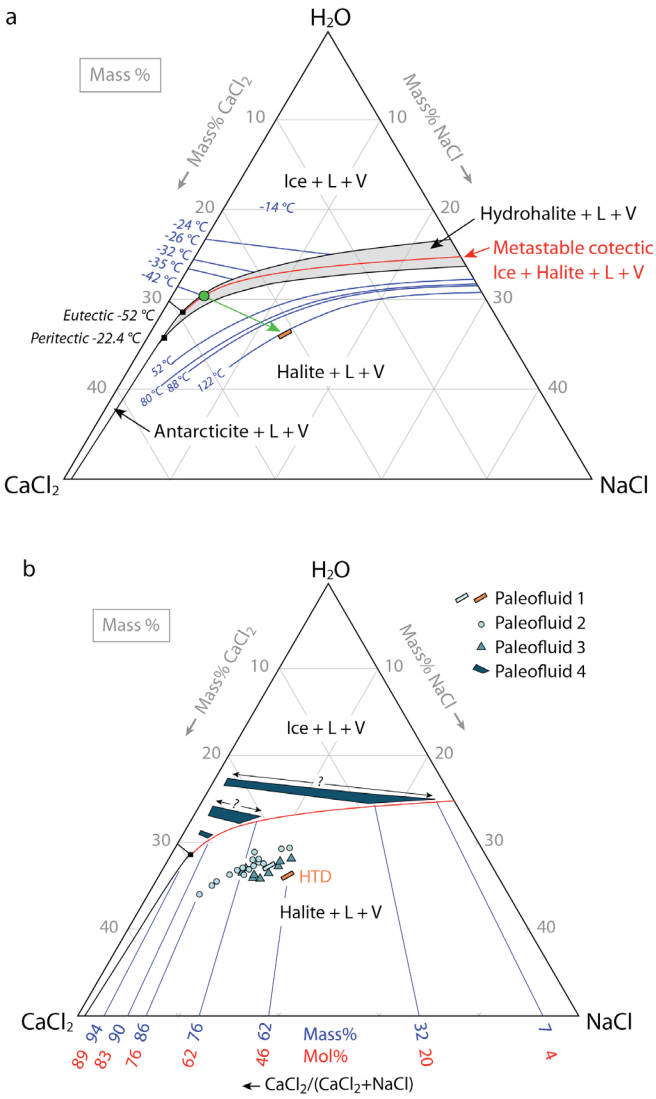


Figure 8: Compositions of Brines in Cambrian and Mid-Ordovician Samples, in Terms of the Model H_2O–NaCl–$CaCl_2$ Ternary System. (a) Black Curves and Squares: Stable Phase Equilibria; Red Curve: Metastable Cotectic, as Modelled for this Study From Data Generated by the Correlations of Steele-Macinnis et al. (2011); See Figure 9 for Temperatures Along Curve. Blue Curves: Example Isotherms of Ice Melting in the Absence of Halite (Upper Field) and Halite Melting in the Absence of Ice (Lower Field). Grey Field: Stability of Hydrohalite. Green Arrow: Example of Halite Melting Trend from the Cotectic (See Text). (b) Same Diagram as (A) Without Hydrohalite Field and Isotherms. Compositions of Assemblages of Brines in Paleofluids 1–3 at the Temperature of Their Entrapment are Shown by the Symbols. HTD: Brines that Deposited Hydrothermal Saddle Dolomite. The Compositions of Brines in Paleofluid 4 are Only Broadly Constrained to Fall Within the Relevant T_m(Ice) Isotherms (Uncertainty Indicated By Question Marks). Data from Table 2. Paleofluids are as Given in Figure 10

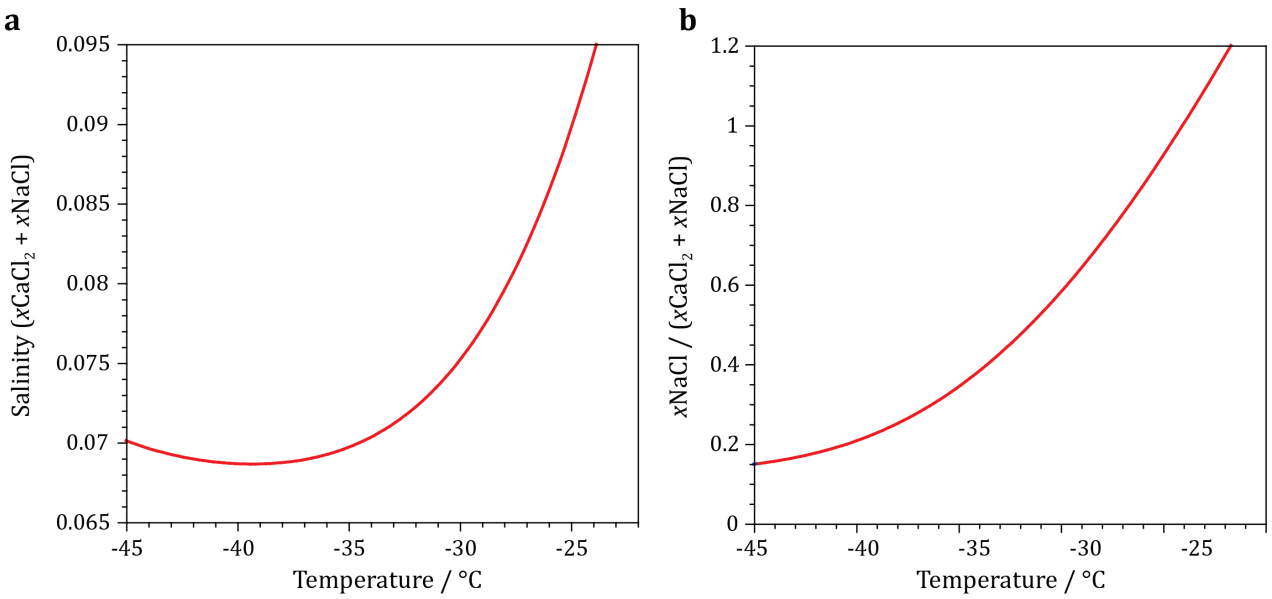


Figure 9: Compositions of the Liquid Phase (Brine) in the Model H_2O–NaCl–$CaCl_2$ Ternary System as a Function of Temperature on the Metastable Cotectic Ice + Halite + Liquid + Vapour (Same as Red Curve in Figure 8). Calculated as Described in Text

Pressure corrections for the homogeneously entrapped inclusions were therefore calculated as follows (examples are given in Figure 10):

1) The composition of the inclusions was taken from Figure 9, i.e., the inclusions are treated as ternary H_2O–NaCl–$CaCl_2$ mixtures. Although the brines are certainly more complex than this ternary system, this treatment is reasonable for the purpose, as the slopes of isochores are essentially determined by the concentration of 1:1 versus 1:2 salts. The identity of the salts (e.g., NaCl versus KCl or $CaCl_2$ versus $MgCl_2$) has only a very minor effect. The equation-of-state of Zhang and Frantz (1987) was used to calculate the position of isochores in P–T space, anchored by the observed T_h values. Figure 10 shows isochores for the lowest and highest measured T_h values in this study, calculated for an equi-molar mixture summing to 30 wt% $CaCl_2$+NaCl.

2) The pressure at fluid trapping was estimated from the stratigraphic depth of the samples (700–860 m) plus 1 km of additional sediment overburden (value from NWMO 2011, p.30). The pressure on the fluid could, in principle, have varied anywhere between lithostatic and hydrostatic, thus both constraints are shown as horizontal lines in Figure 10 (the density of the brine was used to calculate the hydrostat).

3) Intersection of the isochores with the hydrostatic and lithostatic pressures leads to a range of possible trapping temperatures, labelled a, a', b and b' in Figure 10. Reading off these temperatures via dotted lines 1–4 yields pressure corrections (labelled ΔT in Figure 10) between 8 and 22 °C. The Cambrian is and presumably always was an aquifer. Therefore, the pressure correction applied to fluid inclusions in the Cambrian samples is taken from the paleo-hydrostat calculated for 1860 m paleo-depth (8-9 °C). The Black River Group is an aquiclude (Figure 1), so the pressure corrections for inclusions in the Coboconk and Gull River formations are taken from the average of the

paleo-hydrostatic and paleo-lithostatic values for the relevant sample depths (and 14–15.5 °C). The Trenton Group is an aquitard today, but it was likely more permeable during the paleofluid activity recorded by the fluid inclusions. Accordingly, an average pressure correction for 1700 m paleodepth is also applied to inclusions in the Sherman Fall Formation (12.5–14 °C).

The resulting pressure-corrected trapping temperatures are listed in Table 2 in blue brackets.

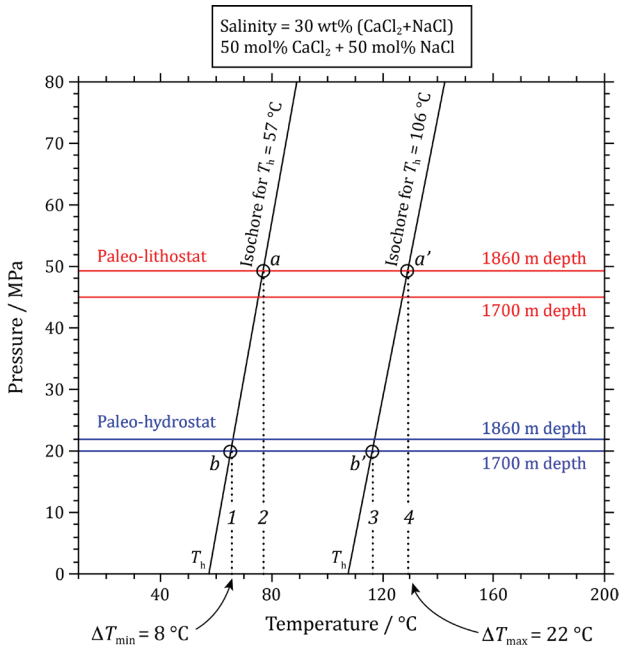


Figure 10: Principle of Derivation of Pressure Corrections for T_h Measurements of Homogeneously Entrapped Fluid Inclusions in this Study. See Section 4.2.5 for Explanation

4.3 SEQUENCE OF MINERAL PRECIPITATION, FLUID ENTRAPMENT AND FLUID PROPERTIES

The paragenetic sequence diagrams in Figure 7 are so consistent throughout the Cambrian, Ordovician, and Devonian samples, respectively, that they permit 3 summary diagrams to be constructed without loss of significant details, as shown in Figure 11. This synthetic figure is used as a basis to describe, in the following paragraphs, the sequence of mineral precipitation and fluid entrapment events, and to summarize the properties of the paleofluids recorded by the fluid inclusions in the vugs and veins. Histograms of the T_m(ice) data for the brine inclusions are given in Figure 12, sorted according to the four paleofluids and the corresponding stages identified in Figure 11.

Stage I

The main minerals making up the host rocks of the investigated vugs and veins in the Cambrian–Ordovician samples have been assigned to Stage I in Figure 7. The host-rock

dolomite contains fluid inclusions of ≤ 2 µm diameter, but these are too small to be tractable with the available analytical techniques.

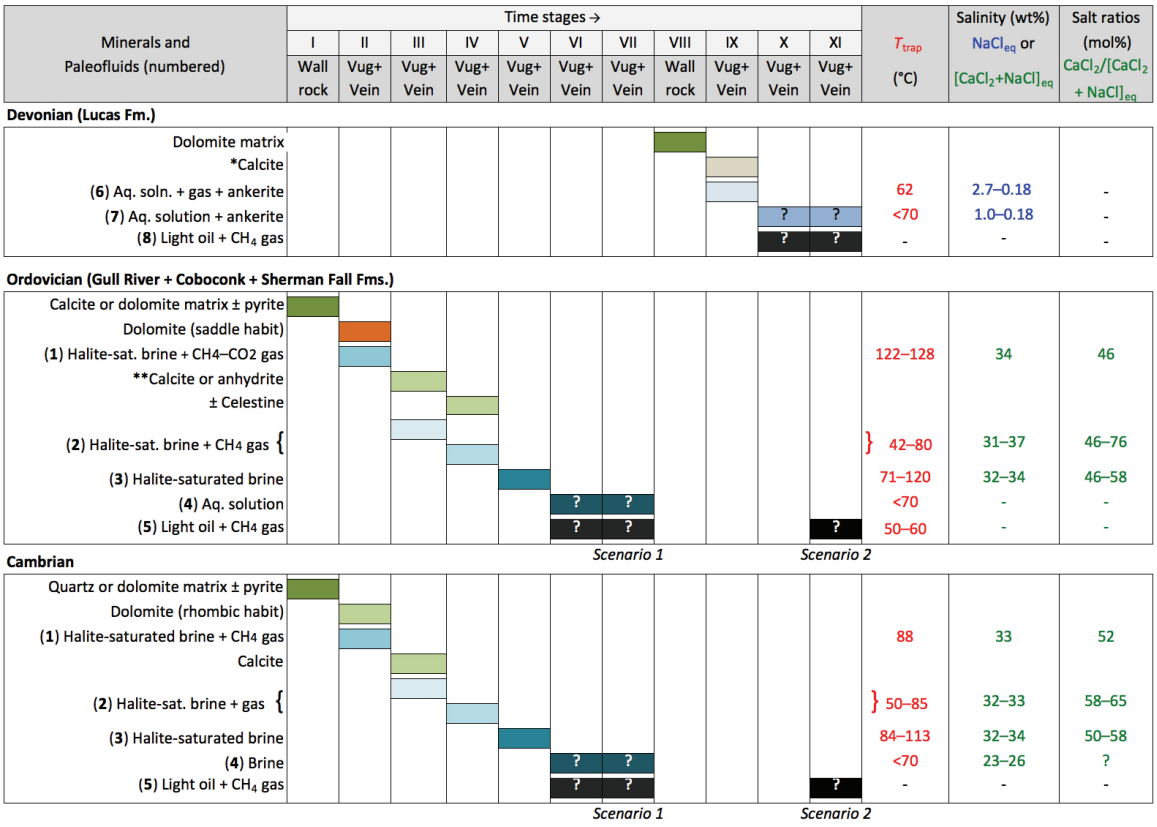
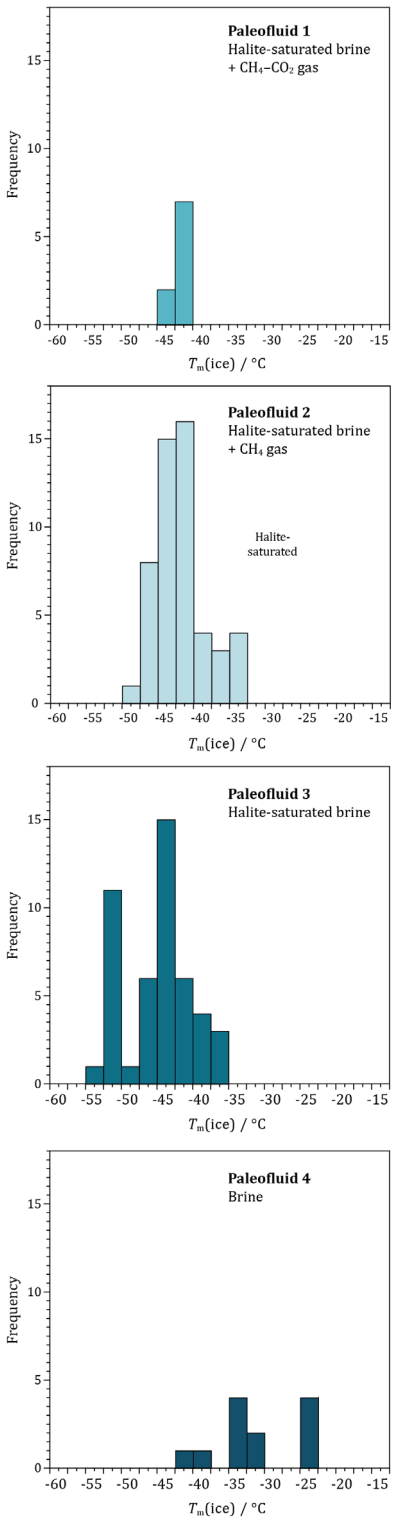


Figure 11: Synthesis of Paragenetic Diagrams in Figure 7. The Indicated Salinities of the Lucas Formation Inclusions Correspond to Their Bulk Salinities in Equivalent Wt% NaCl. Salinities Shown for the Mid-Ordovician and Cambrian Samples Refer to the Model Ternary H_2O–NaCl–$CaCl_2$. Trapping Temperatures (T_{trap}) for Paleofluid 3 are Corrected for Paleo-Hydrostatic Pressure (Cambrian Samples) or an Average of Paleo-Hydrostatic and Paleo-Lithostatic Pressures (Ordovician Samples) - See Text Section 4.2.5 for Explanation. * Calcite Dated to 51 ±2 – 109 ±4 Ma by Davis (2013). ** Calcite Dated to 445 ±42 Ma by Davis (2013)

Stage II

The earliest mineral assemblage within the investigated vugs and veins is dolomite + pyrite, although it occurs in only 4 of the samples (Figure 7). Two of these samples from the Cambrian contain dolomite that is subhedral or rhombic with straight crystal faces and that contain primary fluid inclusions decorating crystal growth zones (Figures 9a and A86, A87). In contrast, the other two samples from the Coboconk and Gull River formations contain saddle dolomites that are so rich in primary fluid inclusions that they appear cloudy (Figures 9b and A79, A80). The latter dolomites are highlighted in orange in Figures 7 and 11. These dolomites show notable elevated Fe- and Mn-contents compared to the matrix dolomites, as determined in this study by electron microprobe analysis (Appendix 3).



Stage II

Stage III-IV

Stage V

Stage VI or VII

Figure 12: Histograms of Final Ice-Melting Temperatures in Equilibrium with Vapour in Cambrian to Mid-Ordovician Samples. Ice Melting in Stages II–V is Metastable; Stable Hydrohalite Nucleates Only Rarely (T_m(Hydrohalite) Not Shown). Data from Table 2. Paleofluids are as Given in Figure 8

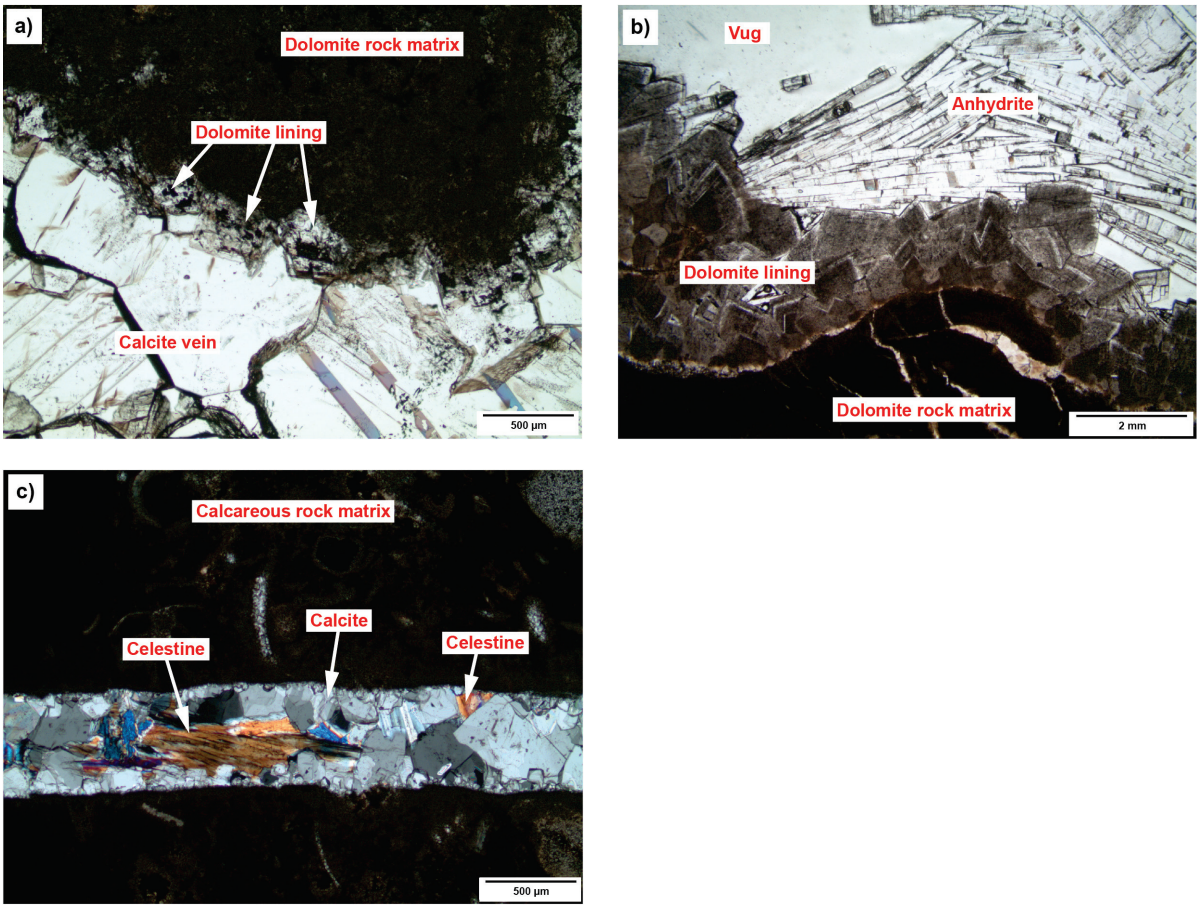


Figure 13: (a) Subhedral, Fluid Inclusion-Poor Dolomite Lining the Walls of a Vein in Sample DGR 2-844.31. (B) Euhedral, Fluid Inclusion-Rich Saddle Dolomite Lining the Walls of a Vug in Sample DGR 4-829.53. The Dolomite Is Overgrown By and Thus Predates Anhydrite. (C) Calcite-Celestine Vein in Sample DGR 4-769.57. The Celestine is Aligned Along the Central Axis of the Vein and Overgrows the Calcite Which Lines the Walls of the Vein

All the dolomites examined in this study (whether with subhedral or saddle habits) appear to contain the same types of heterogeneously trapped fluid inclusions. These indicate that the dolomites precipitated from chemically-complex, halite-saturated brines that coexisted with immiscible gas. Raman spectroscopy showed that the gas is a CO_2–CH_4 mixture (Figure 14). The peak position of the CH_4 in the Raman spectrum, the presence of gas-hydrate-clathrate at low temperatures (Appendix B, Figure B2) and the abundance of expandable methane gas in the crushing-stage experiments (Table 3) all point to high internal gas pressures.

Since the mutually saturated brine and gas phases in this generation were trapped simultaneously, the lowest homogenization temperatures among the brine inclusions are equal to their trapping temperatures. The one rhombic dolomite for which data are available yields a precipitation temperature of 88 °C (Cambrian DGR 2-844.31), whereas the saddle dolomites precipitated at 122 °C (Coboconk) and 125–128 °C (Gull River).

The salinities of the brines (Figures 8 and 12) are very similar in the two dolomite types: 33 wt% $CaCl_2$+$NaCl_{eq}$ and 52 mol% $CaCl_2$/($CaCl_2$+NaCl) in the rhombic type and 34 wt% $CaCl_2$+$NaCl_{eq}$ and 46 mol% $CaCl_2$/($CaCl_2$+NaCl) in the saddle dolomite.

Stages III–IV

The dolomite in the Gull River sample DGR 4-829.53 is unique in the sample set, in that it is overgrown by anhydrite rather than by calcite (Figure 7). Otherwise, in all the remaining 12 deep DGR samples, Stage III consists of clear, euhedral calcite crystals. However, the anhydrite contains the same primary and secondary fluid inclusions as in all the other samples (compare paragenetic diagrams for Stages III–VII in Figure 7). The Stage III calcite contains primary liq+vap-gas±halite fluid inclusions with variable phase-volume fractions, which are essentially indistinguishable from those that precipitated the Stage II dolomite. The primary inclusions in vug calcite are identical in appearance and properties to those in veinlet calcite, hence these two textural kinds of calcite are lumped together in the definition of "Stage III" in Figure 7.

The heterogeneous entrapment textures of the inclusions indicate that the calcite precipitated from a halite-saturated brine coexisting with a free methane gas phase. Methane was detected in a few of the largest gas bubbles in one sample but its detection was precluded by the small size of the inclusions in the other samples.

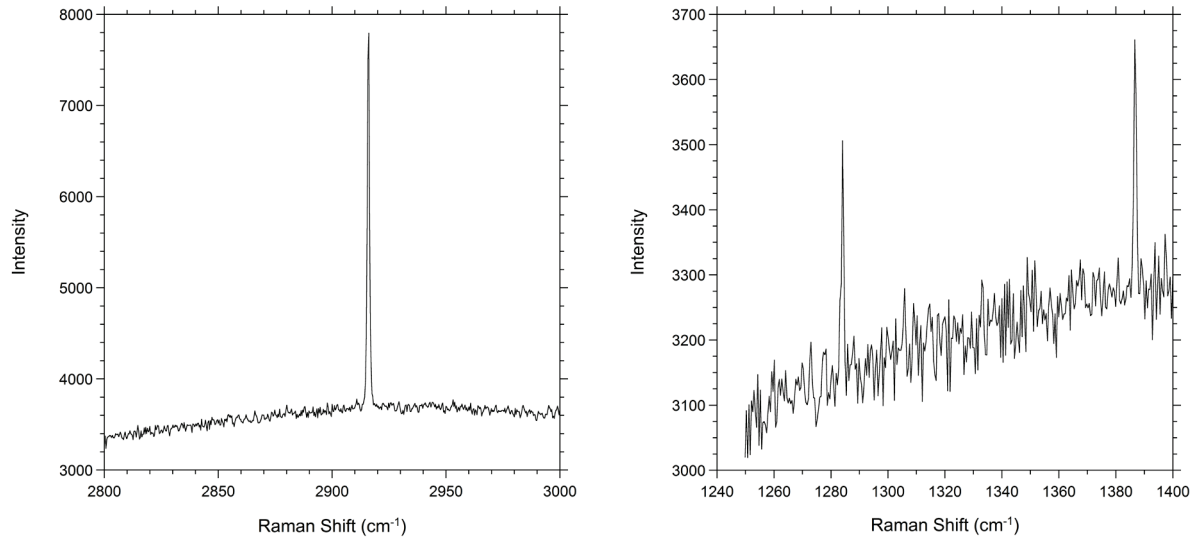


Figure 14: Raman Vibrational Spectra of Methane (Left) and CO_2 (Right; Two Peaks Belonging to Fermi Diad) Measured in the Vapour Bubble of Primary Fluid Inclusions in Stage II Saddle Dolomite of Sample DGR-4-829.53

Exactly the same kinds of fluid inclusion assemblages are also found in healed microfractures (macroscopically invisible) cross-cutting Stage III calcite in both vugs and veinlets. This demonstrates that the same mixture of halite-saturated brine and methane gas was present in the vugs and veins after calcite had ceased precipitating.

The minimum homogenization temperatures of the primary inclusions in calcite yield a range of temperatures for calcite precipitation and for the subsequent entrapment of the secondary inclusions from 42 °C to 80 °C. No clear stratigraphic or other control on the temperatures is apparent within this range (column 7 in Figure 7).

The salinities of the brines vary from 31 to 37 wt% $CaCl_2$+$NaCl_{eq}$ with $CaCl_2$/($CaCl_2$+NaCl) ratios of 46–76 mol%.

Stage V

This stage in Figure 7 is defined by the ubiquitous presence, in 12 of the 13 Cambrian and Mid-Ordovician samples, of late secondary fluid inclusions in healed microfractures in calcite (e.g., Figure A97). Clear cross-cutting textures demonstrate that they post-date the early secondary inclusions assigned to Stage IV. The assemblages consist of homogeneously trapped brine + vapour (uniformly with 5–10 vol% vapour). The brines show a tight cluster of salinities between 32 and 34 wt% $(CaCl_2+NaCl)_{eq}$ with $CaCl_2$/($CaCl_2$+NaCl) ratios of 46–58 mol%.

For this case of homogeneous entrapment, the homogenization temperatures set only a lower limit on trapping temperatures. The maximum T_h values show a wide range of values across the samples, between 57 °C and 106 °C, without any significant modes within this range. There is no robust correlation between T_h(max) and salinity or between T_h(max) and stratigraphic depth. For instance, the Sherman Fall sample DGR 2-691.70 contains inclusion assemblages with T_h(max) of 76 °C and 106 °C, both with the same salinity.

Stages VI and VII

Two compositional types of secondary fluid inclusion assemblages (aqueous and hydrocarbon) have been assigned to Stages VI and VII in Figure 7. They each occur in healed microfractures in calcite. While clear cross-cutting relationships were found proving that both types are younger than the Stage V secondary brine inclusions (e.g., Figure A67), no mutual cross-cutting relationships between these latest secondary aqueous and hydrocarbon assemblages were found. Moreover, no individual assemblages were found in which aqueous and hydrocarbon inclusions were trapped simultaneously within the same healed fracture (this would have been obvious evidence for the contemporaneity of the two fluids). Therefore, the relative timing between these two inclusion types remains unresolved. Despite the lack of mixed assemblages, the idea that fracture healing in calcite (via dissolution–reprecipitation processes) requires water, suggests that the hydrocarbons were accompanied by an aqueous phase that facilitated their entrapment as inclusions. Hence the two inclusion types could indeed have been coeval and so Stage VI in Figure 7 is drawn to illustrate this possibility, with questions marks indicating the timing ambiguity. Stage VII is included in Figure 7 simply to accommodate the possibility that the aqueous inclusions are younger than the hydrocarbon inclusions, or vice versa, the uncertainty again being indicated by question marks. The scenario in which the hydrocarbon inclusions are in Stage VII is labelled "scenario 1" in Figure 11. Yet another possibility is that they belong to Stage XI ("scenario 2"), as discussed further below.

The aqueous fluid inclusions assigned to Stages VI or VII consist of metastable liquid water (without vapour bubbles). As such, their entrapment temperature is assumed to be <70 °C (see explanation of general principle in Section 3.1.2). The inclusions of this generation in the Mid-Ordovician rocks were generally too small to attempt salinity measurements, but the inclusions

in the four Cambrian samples could be artificially stretched to generate bubbles, which allowed T_m(ice) to be measured successfully. However, as mentioned in Section 4.2.4, the lack of a second measureable melting transition in addition to ice-melting makes it difficult to estimate the bulk salinity and Ca/Na ratio precisely. The inclusions plot in three bands in Figure 8, constrained by their T_m(ice) isotherms. These correspond to salinities from about 23 to 26 wt% $CaCl_2$+$NaCl_{eq}$. The most saline assemblages have $CaCl_2$/($CaCl_2$+NaCl) ratios of 58–89 mol% (lower two bands in Figure 8) but the ratios of the other inclusions are not definable.

The hydrocarbon inclusions assigned to Stages VI or VII consist of liquid oil (petroleum) + vapour bubbles, mostly in variable volume proportions. Mostly the oil is colourless in normal transmitted light but in some inclusions it shows a characteristic brownish tinge (e.g., Figure A76C). The consistent bluish-white fluorescence of the oil under UV epi-illumination in all Mid-Ordovician and Cambrian samples (Figures B7C, A30D, A66, A72A, A76B,D,F, A84D, A85D, A91D and A98D) suggests that it is a thermally mature, light oil of high API gravity (McLimans, 1991), although effects such as interaction with trapped water and biodegradation may also produce similar colours (Oxtoby, 2002; George et al., 2002). The high fluorescence from the oil swamped the Raman vibrational spectrum from the vapour bubbles and so the composition of the vapour could not be determined directly. However, as vapour in equilibrium with oil is essentially always dominated by methane, Figure 7 shows CH_4 as the interpreted gas species. Since there is no direct evidence that the hydrocarbon inclusions contain exsolved water, the lowest T_h values in individual assemblages can be taken as equal to trapping temperatures. Samples from the Gull River and Coboconk thus yield trapping temperatures of 60 and 50 °C, respectively. Should evidence be found for water saturation, then these temperatures would represent lower limits on the true trapping temperatures.

Stage VIII

The dolomitic matrix of the host rocks of the vugs and veins in the Devonian samples has been assigned to Stage VIII in Figure 7. This temporal assignment is somewhat arbitrary, as it is not known if the Devonian host rocks were dolomitized before or after cessation of Stage VII fluid activity in the underlying Cambrian–Ordovician formations.

Stage IX

Seven samples from the shallow Lucas Formation were examined petrographically (Figure 7) and fluid inclusions were analysed in five of these. The inclusions are identical in all the samples and therefore no analyses were performed on the remaining two samples.

The Lucas Formation samples consist of calcite vein fillings, at first sight comparable to Stage II calcite in the Mid-Ordovician and Cambrian samples. However, a direct temporal correlation with the deeper-seated calcites is ruled out for the following reasons. First, the salinity of the primary fluid inclusions it contains are dramatically different to those in the Mid-Ordovician and Cambrian samples (very low salinity versus hypersaline brines; see below), so it is clear that the parent fluids of the two calcites were unrelated. Second, radiometric age dating by Davis (2013) has shown that vein calcite in the Mid-Ordovician Coboconk Formation is 445 ±42 Ma whereas the Lucas Formation calcite veinlets formed over a range of ages from 51±2 Ma to 109 ±4 Ma. Accordingly, the calcite in the Lucas formation has been assigned to Stage IX in the overall paragenetic sequence in Figure 7. The primary fluid inclusions in the calcite consist of aqueous liquid + vapour in variable proportions within individual assemblages, demonstrating heterogeneous entrapment. Recognizable assemblages are rather rare and many of the calcite

crystals contain only relatively large, isolated primary inclusions (labelled "isolated" in Table 2). They have variable volume fractions of vapour and are in all respects identical to the inclusions in bonafide assemblages. No Raman spectra could be obtained from the vapour bubbles, owing to their small sizes and strong double refraction of the host calcite. However, crushing-stage tests (Table 3) revealed abundant high-pressure CH_4 in all the examined samples. In each of the samples taken from the outcrops (DD samples), some of the primary fluid inclusions contain rhombs of ankerite. The occurrence of the ankerite within the inclusions of a given assemblage is sporadic. The large size of the crystallites compared to the host inclusions rules out their precipitation from the small amount of trapped liquid. These two observations indicate that the ankerite is not a daughter phase that precipitated after entrapment of the inclusions, but that it was accidentally captured during calcite growth. This implies that the parent fluid that precipitated calcite was also saturated with respect to ankerite.

All of the inclusions in recognizable primary assemblages stretched irreversibly upon microthermometric heating, thereby precluding determination of T_h(true). However, the larger isolated inclusions occasionally yielded reproducible homogenization temperatures between 62 °C and 84 °C, without displaying any evidence of stretching. As all the isolated inclusions in the various analysed crystals appear to be petrographically equivalent, they are interpreted as being coeval. This allows their T_h values to be treated as if they belonged to one heterogeneously-trapped assemblage. Accordingly, the lowest T_h value (62 °C) is taken as the trapping temperature (Table 2 and Figure 7). It is not clear why the Lucas Formation calcites are so prone to stretching, and indeed why some calcites are more robust than others is in general not well understood in the fluid inclusion literature.

Temperatures of ice melting at equilibrium reveal very low salinities between 0.18 and 2.7 wt% $NaCl_{eq}$. These are thus vastly more dilute than all the fluid inclusions in the Cambrian and Mid-Ordovician samples.

Stages X to XI

Two secondary generations of fluid inclusions are present in the Lucas Formation vein calcites, one aqueous and the other hydrocarbon-bearing. Unfortunately, their timing relative to each other is unclear. Neither conclusive cross-cutting textures (e.g., as in Figure A67) nor coexisting aqueous and hydrocarbon inclusions within the same healed microfractures have been found. The uncertainty in relative timing is the same as that between the two latest secondary generations assigned to Stages VI and VII in the Cambrian and Mid-Ordovician samples. Accordingly, the two secondary generations in the Lucas Formation have been assigned to Stages X and XI in Figure 7, with question marks indicating the timing ambiguity. The comparable salinity of the aqueous secondary inclusions (see below) to the primary inclusions in calcite could be taken as an argument that there is no significant fluid evolution between growth of calcite and entrapment of the secondary aqueous fluid in microfractures. Therefore, the aqueous inclusions would belong to Stage X whereas the hydrocarbon inclusions would follow in Stage XI. However, the presumed need for water to permit entrapment of hydrocarbon inclusions in water-soluble calcite leaves the possibility open that the two generations were instead coeval. Finally, there is no strong objective argument against placing the hydrocarbon inclusions in Stage X and the aqueous inclusions in Stage XI.
The secondary aqueous inclusions consist of metastable liquid and hence they were trapped at some temperature below ~70 °C. Their stable ice-melting temperatures indicate salinities even lower than those of the primary inclusions in calcite, in the range 0.18–1.0 wt% $NaCl_{eq}$. The late secondary hydrocarbon inclusions consist of liquid oil (petroleum) + methane vapour

bubbles in variable volume proportions. The inclusions display bluish-white fluorescence under UV epi-illumination (Figures A14C and A16E). According to the simple methods applied in this study, these inclusions look identical to the hydrocarbon inclusions in the Cambrian and Mid-Ordovician samples (Stage VI or VII). The same conclusions are therefore drawn from their fluorescence colour, i.e., they are probably a thermally mature, light oil of high API gravity, barring other effects such as interaction with trapped water or biodegradation.

Although the hydrocarbon inclusions in the Lucas Formation and those in the Cambrian and Mid-Ordovician samples are similar, the presence of the thick Blue Mountain – Georgian Bay – Queenston shale succession, which would have acted as seal to such cross-formational flow, argues against all of the observed hydrocarbons being coeval (i.e., "scenario 2" in Figure 11). As in the case of scenario 1, this scenario suffers from the lack of a demonstrably coeval aqueous fluid in the Mid-Ordovician and Cambrian formations to heal the water-soluble walls of the microfractures in which the hydrocarbon inclusions are trapped. However, there could be traces of water in the hydrocarbon inclusions themselves that we have not detected.

5. DISCUSSION OF FLUID INCLUSION RESULTS AND PALEOFLUID EVOLUTION

5.1 PALEOFLUIDS IN THE CAMBRIAN AND MID-ORDOVICIAN VUGS AND VEINS

As mentioned in Section 4.3, the sequence of fluid inclusion generations in the studied Cambrian and Mid-Ordovician samples is so consistent that they can be summarized into two paragenetic diagrams (Figure 11) without loss of significant information. The two diagrams could in fact be merged into one unified diagram except for one difference in Stage II: high-T saddle-dolomite is present in the Mid-Ordovician whereas lower-T, rhombic-habit dolomite occurs in the Cambrian. This difference is discussed further below. As the phase-state of the fluids at their time of trapping has been reconstructed (according to principles in Section 3.1.2), Figure 11 lists the deduced "paleofluids" (i.e., free mono-phase or multi-phase fluid mixtures) that existed in the vugs and veins and that were sampled by the fluid inclusion assemblages. A sequence of 5 paleofluids can be recognized, as follows. Their salinities and trapping temperatures are shown in Figure 15.

Paleofluid 1: Halite-saturated brine + $CH_4 \pm CO_2$ gas

During Stage II (Figure 11), a mixture of immiscible (mutually saturated) hypersaline brine and $CH_4 \pm CO_2$ gas was responsible for precipitating saddle-dolomite at 122–128 °C in the vugs and veins of the Mid-Ordovician, while apparently the same fluid mixture (according to the rather coarse analytical methods applied) precipitated rhombic dolomite at 88 °C in the Cambrian. In both cases the brine was saturated with respect to halite, meaning halite was present as a solid mineral in the vugs and veins during dolomite growth.

Paleofluid 2: Halite-saturated brine + $CH_4 \pm CO_2$ gas

Essentially the same fluid mixture as Paleofluid 1 was responsible for later precipitation of most of the Stage III calcite ± anhydrite ± celestite and for healing of microfractures in these minerals in Stage IV, but at temperatures from 85 °C down to 42 °C (Figure 15). The calcite has been dated by Davis (2013) at 445 ± 42 Ma (i.e., broadly Paleozoic). Again, the composition of these brines was buffered by the presence of solid halite throughout Stages III and IV, with salinities

of 31–37 wt% $CaCl_{2eq}$+$NaCl_{eq}$. Thus, it is possible that the calcite ± anhydrite ± celestite assemblage precipitated from a stagnant remnant of the void-filling fluid present in Stage I.

Paleofluid 3: Halite-saturated brine

Stage V in Figure 11 is characterized by the presence of a halite-saturated brine, which healed microfractures in the pre-existing vug and vein minerals at various temperatures between 70 and 120 °C. Individual assemblages of inclusions record T_{trap} of 71, 72, 84, 85, 89, 94, 96, 99, 100, 101, 103, 109, 111, 120 °C, as indicated by the set of bands in Figure 15. This brine was also hypersaline, clearly saturated by solid halite in the vugs and veins and with a narrow range of total salinity of 32–34 wt% $CaCl_{2eq}$+$NaCl_{eq}$. The notable difference with respect to Paleofluids 1 and 2 is the absence of any free gas phase. In other words, the brine was undersaturated with respect to gas (e.g., CH_4–CO_2 gas) at this stage. One can imagine the vugs and veins being completely filled with hypersaline brine, without any gas bubbles. We note that this interpretation is based on a consistent pattern found in 12 samples (Figure 7) and it is therefore not an artefact of sampling.

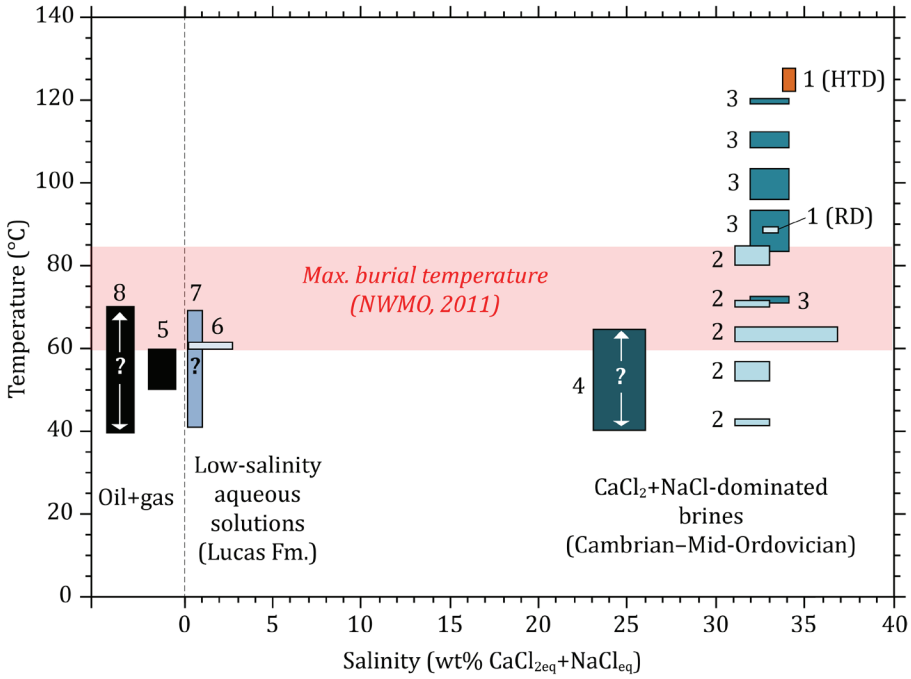


Figure 15: Relationship Between Paleofluid Salinities and Trapping Temperatures. For Definitions of Numbered Paleofluids, Refer to Figure 11. HTD: Hydrothermal Dolomite with Saddle Texture. RD: Rhombic Dolomite. Paleofluids 1, 2, 5 and 8 Coexisted with Free Methane Gas (Not Shown) and Paleofluids 1–3 were Saturated with Respect to Halite (Not Shown). Arrows Mark Uncertainty in Trapping Temperatures of Paleofluids 4, 7 and 8. Paleofluids 1–5 Occur in Vugs and Veins in the Mid-Ordovician and Cambrian Formations; Paleofluids 6–8 Occur in Veinlets in the Devonian Lucas Formation

The wide range in T_{trap} values is remarkable (Figure 15). Inclusion assemblages within the same samples were mostly trapped within a few degrees of each other (Table 2), but the Sherman Fall sample (DGR2-691.70) shows a difference of 31 °C between the entrapment temperatures of individual assemblages. Although the approach used to calculate pressure

corrections for these inclusions is based on simplified assumptions (Section 4.2.5), the range of temperatures appears to be robust. It seems unlikely that this spread of temperatures, all of which occurred during the same Stage V fracture-healing event, could represent temperature fluctuations of the immediately adjacent host-rocks. A more probable interpretation is that pulses of relatively hot brine, of external origin, infiltrated the vugs and veins (each band in Figure 15 may represent such a pulse). The highest temperatures may thus represent pulses of brine that had cooled only slightly against their wall rocks during migration through the sedimentary sequence. High flux rates are one way to explain such "hydrothermal" anomalies. The lower-temperature fluid pulses (~71–85 °C) had presumably cooled more efficiently during their flow through the surrounding rocks, suggesting lower flux rates or longer and more tortuous flow-paths into the vugs and veins.

Paleofluid 4: Brine

Stage VI and/or VII in Figure 11 records a brine that healed microfractures in the pre-existing minerals within the vugs and veins at some unknown temperature below ~70 °C. This paleofluid differs from Paleofluid 3 in that it was clearly not saturated with respect to halite. Its overall salinity is also lower, at 23–26 wt% $CaCl_{2eq}$+$NaCl_{eq}$. This suggests that the solid halite, which was previously in contact with the vug/vein fluids in the earlier stages, had been dissolved by the time Stage VI inclusions were trapped. Again, this pattern is visible in all the analysed samples. The source of this paleofluid, which is also evidently of external origin, must therefore have been different to that of Paleofluid 3.

Paleofluid 5: Light oil + methane gas

Stage VII and/or Stage VI in Figure 11 marks the migration of light hydrocarbon oil plus free methane gas through microfractures in the vugs and veins. As mentioned in Section 4.3 "Stages VI and VII", it is not clear if this hydrocarbon mixture pre-dated, coexisted with, or post-dated Paleofluid 4 (brine). Entrapment was between 50 and 60 °C.

5.2 PALEOFLUIDS IN THE DEVONIAN LUCAS FORMATION VEINLETS

The discordant calcite veinlets in the outcrops and shallow borehole samples from the Lucas Formation record the influx of three paleofluids, as follows.

Paleofluid 6: Low-salinity aqueous solution + CH_4 gas

As explained in Section 4.3 "Stage IX", the calcite veinlets in the Lucas Formation are assigned to a much younger stage than the ostensibly equivalent calcite in the Mid-Ordovician and Cambrian samples. The calcite yields younger radiometric ages and the parent solution from which it precipitated was geochemically unrelated to the brines in the deeper formations, having a salinity of only 0.18–2.7 wt% $NaCl_{eq}$. This aqueous solution was saturated in free methane gas and, in addition to calcite, it was also saturated with respect to ankerite. The temperature of calcite precipitation was around 60 °C.

Paleofluid 7: Low-salinity aqueous solution

Microfractures in the Lucas Formation calcites are healed by essentially the same low-salinity aqueous solution (Stage X or XI in Figure 10) as in Paleofluid 6, with salinity of 0.18–1.0 wt%

$NaCl_{eq}$. The only difference is that the solution was no longer accompanied by a free gas phase. As evident in Figure 7, this conclusion is robust, the same result having been seen in all 7 examined samples. One can imagine that the gas, originally accompanying the aqueous solution in Stage IX, had migrated out of the veinlets, leaving only the aqueous solution wetting the mineral surfaces when the microfracturing event marked by Stage X or XI occurred. The temperature of entrapment is constrained to have been below ~70 °C, therefore it could have been the same as in Stage IX (60 °C).

Paleofluid 8: Light oil + methane gas

As is the case for Stages VI and VII in the Mid-Ordovician and Cambrian samples (Figure 10), the relative timing between Paleofluids 7 and 8 remains ambiguous (see discussion in Section 4.3, "Stage XI"). However, there is no doubt that a mutually saturated mixture of light oil (high API gravity) and CH_4-dominated gas migrated through the veinlets after calcite growth had ceased.

Scenario 2 – Paleofluids 5 + 8 combined: Light oil + methane gas

The available evidence allows that Paleofluids 5 and 8 are one and the same, as shown by "scenario 2" in Figure 10. This would imply (implies) that both the Cambrian–Black River units and the Devonian Lucas Formation were open to infiltration by hydrocarbons very late in the paragenetic history (later than the ~50–110 Ma age of the Lucas Formation calcite). It is highly unlikely that these units could have been linked by cross-formational flow across the thick Blue Mountain – Georgian Bay – Queenston shale succession, which has excellent sealing properties. In line with this expectation, core-logging observations (Figure 17) show no trace of hydrocarbon seeps or petroliferous odours, except within a thin zone at the base of the (this) shale sequence. Therefore, any infiltration of hydrocarbons would have been lateral: confined within the Cambrian–Black River units in the lower part of the stratigraphic section and confined, perhaps simultaneously, within the Lucas Formation in the upper part. However, there are no known drivers for such migration through the Cambrian–Black River at or later than 100 Ma. In view of this, and considering that the hydrocarbon inclusions are correlated only by fluorescence colour and homogenization temperature, "scenario 2" appears improbable.

6. IMPLICATIONS OF FLUID INCLUSION RESULTS FOR UNDERSTANDING THE GEOLOGICAL EVOLUTION OF THE BRUCE NUCLEAR SITE

In the following section a number of themes are discussed which have been addressed in the NWMO Geosynthesis (2011) and into which the present fluid inclusion results provide additional insight.

6.1 REGIONAL OCCURRENCE OF BRINES

The series of brines recorded in Paleofluids 1–4 in the Cambrian and Mid-Ordovician samples appear to be very similar to brines reported throughout Southern Ontario and Manitoulin Island in the dolomitized Black River and Trenton Groups (Coniglio and Williams-Jones, 1992; Coniglio et al., 1994; Haeri-Ardakani et al., 2013). Final melting temperatures of ice are observed over the same wide range (e.g., –45 to –20 °C in Coniglio et al., 1994), implying similar high salinities and $CaCl_2$-dominated compositions within the H_2O–NaCl–$CaCl_2$ model system, as observed in the present study. The brine inclusions were heterogeneously trapped

along with gas-rich inclusions on Manitoulin Island, pointing to a paleofluid involving brine + immiscible gas. Paleofluids 1 and 2 in the present study involved the same two fluids, but they were also saturated with respect to halite. Coniglio et al. (1994) reported a stage of early calcite that pre-dates saddle dolomite, but this is missing from the studied vugs and veins at the Bruce nuclear site.

Low-salinity aqueous solutions were also noted by Coniglio et al. (1994). They report a range of ice melting temperatures for inclusions in "late calcite", some of which lie within the interval –5° and 0 °C (their Figure 12f). In the present study, no such weakly saline inclusions were found in the Cambrian and Mid-Ordovician samples, but similar low-salinity inclusions are present in the Devonian Lucas Formation (Paleofluids 6 and 7).

Despite the differences mentioned above, it can be concluded that the paleofluids reconstructed from the inclusions in the studied samples from the Bruce nuclear site are neither unusual nor unexpected, when viewed in the context of regional studies.

6.2 OCCURRENCE OF HYDROTHERMAL DOLOMITE (HTD)

Hydrothermal dolomite (HTD), i.e., dolomite that precipitated from fluid that was perceptibly hotter than the surrounding host rock, is known to be widespread in the sedimentary sequence of southern Ontario and the Michigan Basin (Coniglio and Williams-Jones, 1992; Davies and Smith, 2006; Haeri-Ardakani et al., 2013). The hot dolomitising fluids are thought to have migrated laterally towards the margin of the Basin along the Cambrian sandstone, from where they ascended into the overlying carbonate sequence (Davies and Smith, 2006). The dissolution caused by these fluids generated enough pore space to act as oil and gas reservoirs in the Black River and Trenton Groups in southern Ontario. As well as being characterized by anomalous temperatures, individual hydrothermal dolomite crystals typically have a saddle habit, are often enriched in iron and have radiogenic Sr and depleted $\delta^{18}O$ isotopic signatures, and they contain primary inclusions of $CaCl_2$–NaCl brine with salinities of 20–30 wt% (Coniglio and Williams-Jones, 1992; Davies and Smith, 2006; Haeri-Ardakani et al., 2013).

At the Bruce nuclear site, INTERA (2011) suggested that thin, planar, strata-bound dolomite horizons within the Upper Ordovician shales may have formed from HTD-type fluids. The strata-bound dolomites were not investigated in this study but two of the 12 investigated Cambrian and Mid-Ordovician samples contain saddle dolomites (Stage II in Figures 7 and 8; marked orange in Figures 11 and 15) with formation temperatures (deduced from primary fluid inclusions of Paleofluid 1; i.e., halite-saturated brine + immiscible CH_4–CO_2 gas) of 122–128 °C, the highest of all paleofluids in the present study. The combination of their high temperatures, their saddle habit, their elevated Fe- and Mn-contents compared to rock-matrix dolomites (Appendix 3), and the known regional abundance of such dolomites, leads us to conclude they are hydrothermal dolomites in the sense of Coniglio and Williams-Jones (1992) and Davies and Smith (2006). In contrast, the Cambrian samples contain rhombic dolomites which formed from the same Paleofluid 1, but at 88 °C. The salinity of the primary brine inclusions in the two dolomites is compatible with the descriptions of the regional HTD occurrences, but this cannot be a diagnostic criterion in the present case, as all Stage II–IV fluids are similar in this respect.

One of the identified hydrothermal dolomites sits within a vug that is only half the diameter of the core sample (DGR 4-829.53 Gull River; Figure A79) whereas the other is in a very small vein within a banded dolomitic host rock (DGR 2-778.44 Coboconk; Figure A28). From these

drill core observations it is not possible to estimate the distribution of the HTD mineralization at the Bruce nuclear site. However, it should be borne in mind that sufficient amounts of fluid must have infiltrated the vug and vein network in order for the fluid to maintain its temperature above that of the wall rocks along its flow path.

6.3 MAXIMUM BURIAL TEMPERATURE

NWMO (2011, p. 30) reviewed regional constraints on paleo-geothermal gradients and burial depths and calculated peak burial temperatures at the top of the Trenton Group (Collingwood Mbr.) at the Bruce nuclear site of 69 ± 6 °C. They also cited conodont alteration data (Legall et al., 1981) suggesting a maximum temperature of 75 °C ± 15 °C. The latter range is shown in pink in Figure 15. The thermal peak is thought to have been attained in Carboniferous–Permian time (NWMO, 2011, pp. 78–79).

The fluid trapping temperatures obtained in the present study for the Trenton and Black River Groups overlap only partly with the maximum burial temperature estimated by NWMO (2011). Paleofluids 1–3 are notable for their wide ranges in trapping temperatures despite their well-constrained timing stages. In Sections 5.2 and 6.2 it is argued that their temperature ranges represent various pulses of externally-derived "hydrothermal" fluid. It follows that the lowest temperatures recorded by these paleofluids must lie closest to the temperature of the host rocks, which represent the low-temperature heat-sink against which the fluids cooled. This suggests ambient rock temperatures ≤ 88 °C during stage II, ≤ 42 °C during stages III–IV and ≤ 71 °C during stage V. Stages II and III are of Paleozoic age, based on the 445 ± 42 Ma age of as Stage-III calcite obtained by Davis (2013), and therefore they predate the thermal peak of the host formations. The exact trapping temperature of Paleofluid 4 is not known, although it must have been below ~70 °C, whereas Paleofluid 5 was trapped between 50 and 60 °C. Because both paleofluids are recorded in secondary inclusions, their timing relationships with respect to the thermal peak are unknown: they could be pre-, syn- or post-peak.

Thus, while the fluid inclusion results do not set any definitive constraints on the maximum burial temperature of the Trenton and Black River Groups, they are not inconsistent with the NWMO (2011) estimate of 75 °C ± 15 °C.

6.4 HALITE DISTRIBUTION IN CORE SAMPLES

Examination of drill core samples by visual logging, petrography, SEM and XRD (NWMO, 2011) has shown that halite is present more or less continuously from the upper Salina Group down to the Sherman Fall Formation. Halite is apparently missing in the Kirkfield, Coboconk and Shadow Lake Formations and only two occurrences were found by SEM in the Gull River and the Cambrian (Figure 16). The present study has shown that Paleofluids 1–3 were saturated with respect to solid halite at the time they were trapped in fluid inclusions. The stratigraphic distribution of these paleofluids therefore constitutes an additional source of information on the distribution of halite.

Figure 16 compares the stratigraphic distribution of the halite-saturated inclusions with the NMWO (2011) results. The fluid inclusion data (large red symbols) confirm the presence of halite in the Sherman Fall, Gull River and Cambrian, and they additionally show that halite was present in the Coboconk, thereby filling an information gap.

It follows that halite, and hence halite-saturated fluids, were present throughout the entire stratigraphic sequence between the Cambrian and Upper Ordovician formations, at least up to the time corresponding to Stage V in Figure 10. Thereafter in the presently investigated formations it appears that halite was dissolved, at least in the immediate vicinity of the studied vugs and veins, by infiltration of Paleofluid 4 (halite-undersaturated brine). The suite of samples in the present study does not reach above the Sherman Fall Formation and so it is not clear if Paleofluid 4 also flushed the vugs and veins in those units. However, the preservation of halite in those stratigraphically higher rocks (Figure 16) argues against infiltration of a fluid equivalent to Paleofluid 4.

In Sections 5.2, 6.2 and 6.3 it is argued that the three halite-saturated Paleofluids 1–3 entered the sedimentary sequence as pulses, many with temperatures higher than the surrounding host rocks (Figure 15). Since the solubility of halite depends very strongly on temperature, cooling of these hypersaline brines against their wall rocks during fluid infiltration is an obvious mechanism to explain the precipitation of halite.

6.5 PETROLEUM DISTRIBUTION IN CORE SAMPLES

Figure 17 shows the stratigraphic distribution of heavy hydrocarbons (bituminous layering, oil seeps and petroliferous odours) logged in core samples from the Bruce nuclear site (from Figure 2.32 in NWMO, 2011). Overlain with blue symbols are the occurrences of oil inclusions in vugs and veins, as found in this study. The seven deep samples that contain oil inclusions come from the Coboconk, Gull River and Cambrian Formations. All correlate well with horizons in which oil seeps were logged in the cores. In addition, oil is present in the fluid inclusions within the Devonian Lucas Formation, although in this case no oil seeps were detected in the core.

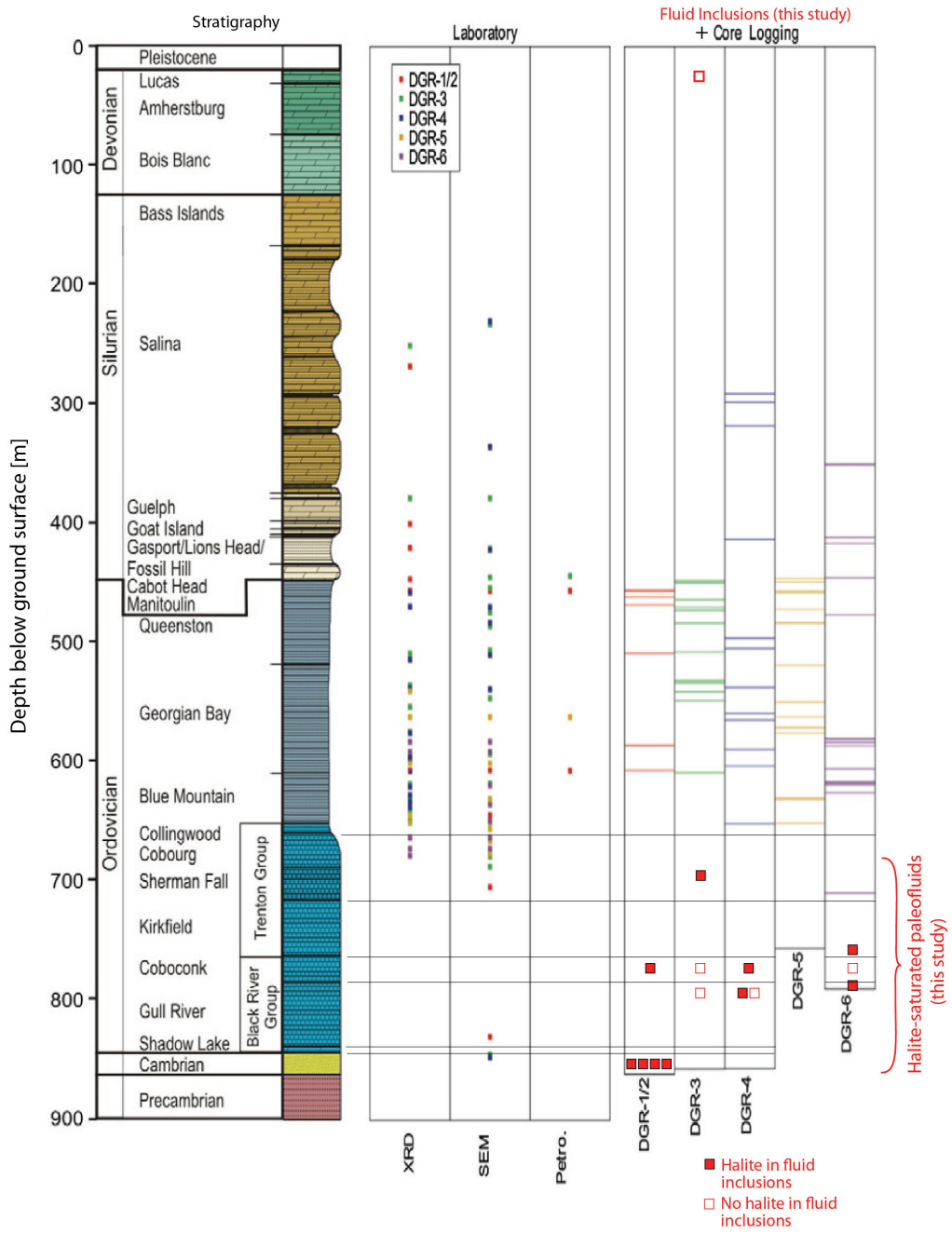


Figure 16: Distribution of Halite at the Bruce Nuclear Site (Modified from Figure 5 in Al et al., 2015), Based on XRD, SEM, Petrography and Core Logging in the DGR Boreholes. These Observations Show that Halite is Present Essentially Continuously from the Upper Salina Group Down to the Sherman Fall Formation. It Appears Again in the Shadow Lake and Cambrian Formations. Overlain on the Borehole Columns are the Occurrences of Halite-Saturated Paleo-Fluids Derived from this Fluid Inclusion Study (Red Symbols). These New Observations Confirm the Presence of Halite in the Sherman Fall and Cambrian Formations and Show that it is also Present in the Coboconk and Gull River Formations, Thereby Filling an Information Gap. Thus, Halite-Saturated Paleofluids were Present Throughout the Entire Stratigraphic Sequence Between the Cambrian and Upper Salina Group

The striking result of the paragenetic studies (Figure 11) is that the oil inclusions are either the latest or second-latest paleofluids in the investigated vug and vein samples. The spatial correlation in Figure 17 between oil inclusions and core-logging occurrences of oil in the Middle Ordovician formations seems strong enough to conclude that all hydrocarbons in these formations are of the same age, i.e., post-calcite precipitation. The low measured trapping temperatures of the oil inclusions (40–60 °C) imply that the ambient rock temperatures were comparatively low at this stage. This renders in-situ generation of the oil very unlikely. Instead, the low temperature and the post-calcite timing suggest that the hydrocarbons are all of external origin to the host formations, i.e., they infiltrated from a distant source, rather than having formed within the Cambrian, Coboconk or Gull River formations.

6.6 AGE OF METHANE

NWMO (2011) cites the isotopic and compositional indicators published by Sherwood-Lollar et al. (1994), which show that methane in the formations below the Cobourg is dominantly thermogenic. Further, NWMO (2011) noted that thermogenic generation requires T > 70 °C (Hunt, 1996), and therefore it is likely the gas was produced near the maximum burial temperature, which is thought to have been in Permian–Carboniferous time. They concluded the gas must be very old and that it could be of in-situ or external origin.

This fluid inclusion study has detected methane in hypersaline Paleofluids 1 and 2 and also accompanying oil in Paleofluids 5, 7 and 8, the latter two in the Devonian Lucas Formation. The age of at least some of the methane is therefore fixed to be as old as the earliest vein- and vug-filling dolomite (whether rhombic or hydrothermal saddle dolomite). According to the radiometric dating of Stage-III calcite by Davis (2013), the methane in Paleofluids 1 and 2 is of Paleozoic age. However, the methane in the Lucas Formation calcite may be as young as the calcite in which it is trapped as primary inclusions (i.e., 50–110 Ma; Davis 2013), while the methane associated with the post-calcite oil inclusions in the Lucas veinlets could be even younger.

6.7 GAS SATURATION

The question of whether free methane gas is currently present in the stratigraphic sequence at the Bruce nuclear site has been raised by several workers (e.g., INTERA, 2011; Al et al., 2015). The fluid inclusion record in the vugs and veins provides insight into the evolution of gas saturation through time in the largest pore spaces (vugs and veins) of the investigated formations.

In the Mid-Ordovician and Cambrian formations, Paleofluids 1 and 2 included free methane gas but it disappeared from the fluid phase assemblage during influx of Paleofluids 3 and 4 when the dissolution of halite began. However, free methane appeared again in the youngest fluid generations in equilibrium with light hydrocarbon oil. As discussed in Section 4.3 and as shown by the labels "scenario 1" and "scenario 2" in Figure 11, it is not clear whether this petroleum-related methane entered the vugs and veins during Stage VI/VII or X/XI.

As far as the present-day, in-situ state of gas-saturation is concerned, the following arguments can be made. We first assume that no fluids infiltrated the vugs and veins other than those recorded as fluid inclusions. In particular, this means that the latest fluids to enter the rocks were those assigned to Stages VI/VII and X/XI.

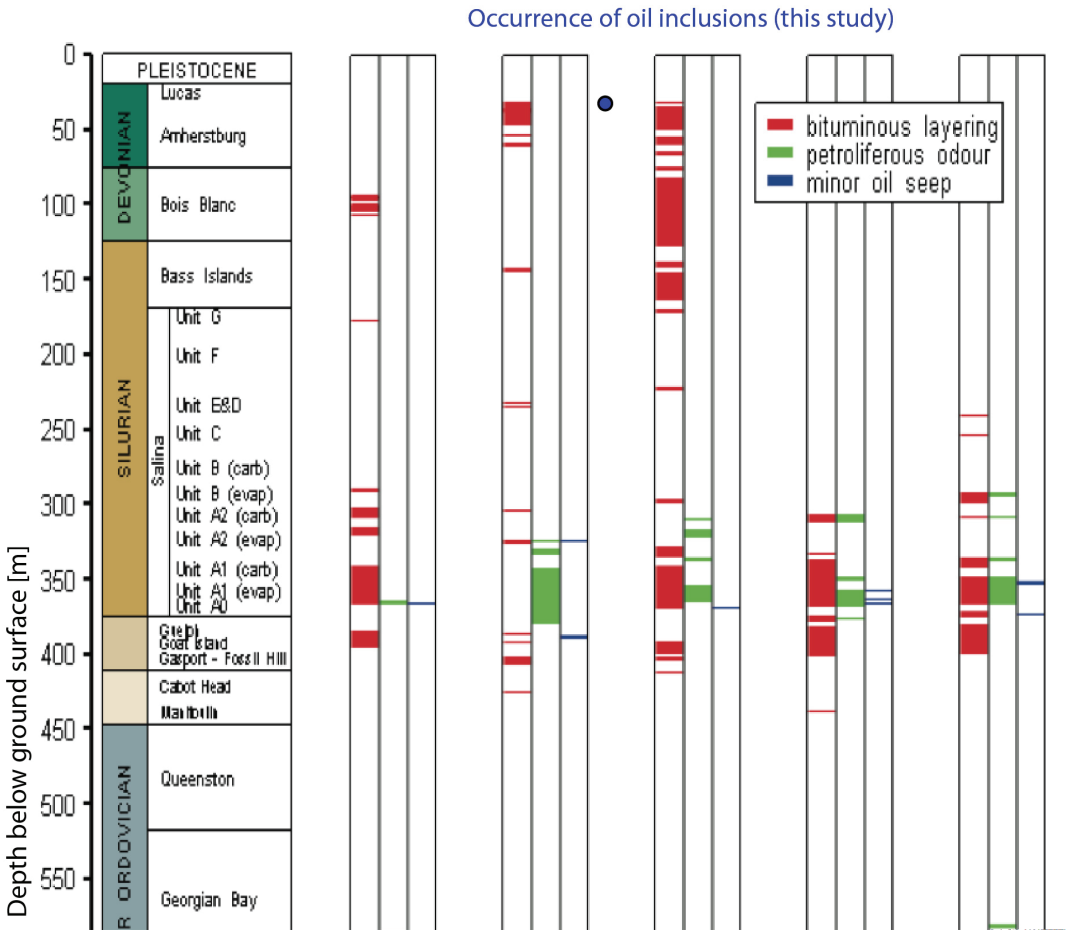


Figure 17: Distribution of Hydrocarbons in Borehole Cores at the Bruce Nuclear Site, From Figure 2.32 in NWMO (2011). Overlain with Blue Symbols are the Occurrences of Oil-Bearing Fluid Inclusions (This Study). The 7 Deep Samples that Contain Oil Inclusions Come from the Coboconk, Gull River and Cambrian Formations. All Correlate Well with Horizons in Which Oil Seeps Were Logged in the Cores. Lucas Formation Samples Also Contain Oil Inclusions

Two possible interpretations follow:

(1) if the oil+gas mixture was the latest of all fluid generations (as is permitted by the available evidence), then it seems likely that the free methane is still locked in the void space of the vugs and veins;
(2) alternatively, if Paleofluid 4 (methane-undersaturated brine) infiltrated the vugs and veins after the oil+gas mixture, then there is no reason from the fluid inclusion record to expect gas saturation in the vugs and veins today.

Thus, while interpretation (1) supports the tentative conclusions of INTERA (2011, p.236), that free methane gas may be widespread, the lack of conclusive petrographic evidence for the relative timing of the last two paleofluids renders a definitive answer impossible.

6.8 ABSENCE OF GLACIAL WATER INFILTRATION

Considerable effort was expended in the present study on the petrographic search for various fluid inclusion types (summarized in Figure 7). This effort revealed a series of hypersaline brines in the Mid-Ordovician and Cambrian formations, the lowest salinity being 23 wt% $CaCl_{2eq}$+$NaCl_{eq}$. There is therefore no hint of fresh-water influx in the fluid inclusion record that could be attributed to a glacial origin.

Despite the thorough petrographic search, it is valid to question whether water of glacial origin could have infiltrated the sampled rocks without leaving its trace as secondary fluid inclusions in healed fractures or as dissolution textures. We consider this scenario very unlikely. The sampled vugs and veins contain easily deformable and relatively soluble minerals (especially calcite and anhydrite). Easily deformable minerals tend to fracture readily and thus trap secondary fluid inclusions, even when the pore fluid is undersaturated with respect to the host mineral (reduction in surface free energy is usually strong enough to drive fracture-healing even when the free pore fluid is undersaturated). Post-formation dissolution can be ruled out in the present samples because the calcites and anhydrites have sharp edges and smooth faces.

A counterproof supporting these arguments is provided by the findings of Coniglio et al. (1994) in outcrop samples from the dolomitized Black River and Trenton Groups on Manitoulin Island. Since those rocks have been uplifted through the depth realm into which meteoric waters commonly penetrate, it is to be expected that they contain low-salinity fluid inclusions in late fractures. In line with this expectation, fluid inclusions with ice-melting temperatures near 0 °C are indeed present in the latest generation of calcite on Manitoulin Island (Figure 12f in Coniglio et al., 1994).

In contrast to the vug- and vein-filling minerals in the Cambrian and Mid-Ordovician samples, the calcites in the Lucas Formation veinlets precipitated from low-salinity fluids (0.18–2.7 wt% $NaCl_{eq}$) and they contain secondary inclusions of similar salinity (Paleofluids 6 and 7). Again, this is consistent with the fact that these outcrop samples were uplifted through the realm of shallow groundwater activity.

7. SUMMARY OF RESULTS

Fluid inclusions were investigated in carbonate vugs and veinlets in fifteen core samples from beneath the Bruce nuclear site, including samples from Cambrian, Ordovician and Devonian formations. Six samples of calcite veins from an outcrop of the Lucas Formation were also investigated. The inclusions were analysed petrographically in visible and UV light and by laser Raman spectroscopy and crushing-stage experiments. The inclusions in calcite proved difficult to analyse, owing to the widely known phenomenon of stretching upon heating. Accordingly, the analytical workflow included a procedure to sort valid data from artefacts. The interpretation of the results involved thermodynamic modelling to estimate salinities and trapping temperatures.

The fluid inclusion record is highly consistent between the 15 samples, supporting the idea that geological features within the DGR site are predictable from the acquired evidence. The results show that the deep Cambrian to Mid-Ordovician vugs and veins share the same history of fluid evolution, and are thus genetically related with each other, whereas the veinlets in the shallow Devonian Lucas Formation formed from very different fluids.

In the Cambrian to Mid-Ordovician carbonates, five "paleofluids" have been recognized which are similar to diagenetic fluids reported in the same units in the regional literature. Each paleofluid precipitated minerals or was present during microfracturing in the vugs and veins, in the following sequence:

- Paleofluid 1 was a mixture of halite-saturated brine + free methane±CO_2 gas that precipitated saddle- and rhombic-habit dolomite. The saddle dolomites precipitated at 122–128 °C, well above the likely temperature of the wall rocks. Their morphology, high temperature origin and high Fe- and Mn-contents identify them as "hydrothermal" (HTD) dolomites, similar to those known elsewhere in the Michigan Basin. The spatial extent of the dissolution pathways associated with these fluids cannot be assessed from the fluid inclusion data. The rhombic dolomites have lower Fe contents and formed at 88 °C.

- Paleofluid 2 was a similar halite-saturated, two-phase mixture (brine + free methane gas) that precipitated calcite ± anhydrite ± celestite on the earlier dolomite and that later healed microfractures in the calcite. This mixture infiltrated the vugs and veins in pulses at temperatures between 42 and 85 °C, the lower values presumably representing the host-rock temperature. The calcite in a Coboconk sample has been dated radiometrically to 445 ±42 Ma (Davis 2013). This implies that hypersaline Paleofluids 1 and 2 entered the Black River and Trenton Groups during the Paleozoic.

- Paleofluid 3 was a halite-saturated brine without an accompanying gas phase. It healed microfractures in the previously precipitated minerals after infiltrating in pulses at temperatures between 71 and 120 °C. It can therefore be viewed as "hydrothermal" in the same sense as the saddle dolomite precipitated by Paleofluid 1.

The brines in Paleofluids 1–3 are complex mixtures of salts ($CaCl_2$+NaCl+$MgCl_2$ etc.). No significant differences in brine composition between the fluid generations are evident from the available data. Calculations for the model $CaCl_2$–NaCl–H_2O system indicate $CaCl_2$/($CaCl_2$+NaCl) ratios between 46 and 76 mol%. Their total salinities are likewise comparable, between 31 and 37 wt% $CaCl_{2eq}$+$NaCl_{eq}$.

- Paleofluid 4 was a simple halite-undersaturated brine, without free gas, that entered the sediments at some temperature below 70 °C (no tighter temperature constraint could be derived). As well as healing microfractures in the vug and vein minerals, this Paleofluid is deduced to have dissolved halite along its flow path. The paucity of macroscopic halite in the drill-core logs of the Cambrian and Gull River Formations and its apparent absence in the Coboconk Formation is likely due to this dissolution event. The salinity of the brine was between 23 and 26 wt% $CaCl_{2eq}$+$NaCl_{eq}$.

- Paleofluid 5 consisted of light petroleum oil accompanied by free methane gas, probably derived externally from the host-rock sequence. It was trapped in microfractures at 50–60 °C. The age of Paleofluid 5 relative to Paleofluid 4 is unclear.

As Paleofluids 3–5 are all represented by fluid inclusions in healed fractures of the Paleozoic Stage III calcite, their absolute ages are unconstrained. They could have entered the Cambrian to Mid-Ordovician units prior to, during or after the Permian-Carboniferous thermal peak.

No indication has been found in the Cambrian to Mid-Ordovician samples for a fluid that could have originated by influx of glacial melt-water.

The Devonian Lucas limestone contains a record of three additional paleofluids:

- Paleofluid 6 was a low-salinity aqueous solution (0.18–2.7 wt% $NaCl_{eq}$) accompanied by free methane gas, which precipitated calcite and minor ankerite in veinlets at ~60 °C. This calcite was dated by Davis (2013), yielding ages from 51 ±2 Ma to 109 ±4 Ma.

- Paleofluid 7 was a slightly diluted version of Paleofluid 6 (0.18–1.0 wt% $NaCl_{eq}$), which healed microfractures in the veinlet calcite and precipitated tiny amounts of ankerite. In contrast to Paleofluid 6, no free gas accompanied the aqueous solution.

- Paleofluid 8 was identical, according to simple UV petrography, to the mixture of light oil and free methane gas that characterizes Paleofluid 5. Its trapping temperature was not determined. The relative timing between Paleofluids 7 and 8 is unclear, but Paleofluid 6 definitely predates both.

The low salinity fluids in the Devonian Lucas Formation contrast strongly with the brines in the underlying Cambrian to Mid-Ordovician rocks, ruling out a common fluid origin. As the Lucas Formation samples derive from outcrops and from a shallow drill core, the low salinity Paleofluid 7 presumably represents groundwater containing a meteoric component.

The occurrence of petroleum-bearing inclusions in all Cambrian to Mid-Ordovician rocks is consistent with DGR core-logging observations. This study has shown that the petroleum is either the last or penultimate fluid to infiltrate the rocks. The occurrence of petroleum in the Lucas Formation is a new observation.

REFERENCES

Al, T.A., I.D. Clark, L. Kennell, M. Jensen and K.G. Raven. 2015. Geochemical evolution and residence time of porewater in low-permeability rocks of the Michigan Basin, Southwest Ontario. Chemical Geology 404, 1–17.

Bakker, R.J. and L.W. Diamond. 2006. Estimation of volume fractions of liquid and vapor phases in fluid inclusions, and definition of inclusion shapes. American Mineralogist, 91, 635-657.

Bakker, R.J. and M. Baumgartner. 2012. Unexpected phase assemblages in inclusions with ternary H2O-salt fluids at low temperatures. Central European Journal of Geosciences 4, 225–237.

Burke, E.A.J. 2001. Raman microspectrometry of fluid inclusions. Lithos, 55, 139-158.

Davis, D.W. 2013. Application of U-Pb Geochronology Methods to the Absolute Age Determination of Secondary Calcite. Nuclear Waste Management Organization Technical Report NWMO TR-2013-21. Toronto, Canada.

Diamond, L.W. 2003a. Systematics of H2O inclusions. *In:* I.M. Samson, A.J. Anderson, and D.D. Marshall, Eds. Short Course 32. Fluid Inclusions: Analysis and Interpretation, p. 55-79. Mineralogical Association of Canada.

Diamond, L.W. 2003b. Introduction to gas-bearing aqueous fluid inclusions. *In*: I.M. Samson, A.J. Anderson, and D.D. Marshall, Eds. Short Course 32. Fluid Inclusions: Analysis and Interpretation, p. 101–158. Mineralogical Association of Canada.

Diamond, L.W. and R. Caldas. 2013. Fluid Inclusion Study of DGR Drill Core. Report prepared for Nuclear Waste Management Organisation of Ontario (NMWO). Rock–Water Interaction, Institute of Geological Sciences, University of Bern, Switzerland. 46 p.

Diamond, L.W. and D.D. Marshall. 1990. Evaluation of the fluid inclusion crushing-stage as an aid in exploration for mesothermal gold-quartz deposits. Journal Geochem. Explor. 38, 285-297.

George, S.C., T.E. Ruble, A. Dutkiewicz and P.J. Eadington. 2001. Assessing the maturity of oil trapped in fluid inclusions using molecular geochemistry data and visually-determined fluorescence colours. Applied Geochemistry, 16, 451–473.

Goldstein, R.H. and T.J. Reynolds. 1994. Systematics of fluid inclusions in diagenetic minerals. 199 p. SEPM (Society for Sedimentary Geology), Tulsa.

Haeri-Ardakani, O., I. Al-Aasm and M. Coniglio. 2013. Petrologic and geochemical attributes of fracture-related dolomitization in Ordovician carbonates and their spatial distribution in southwestern Ontario, Canada. Marine and Petroleum Geology 43, 409-422.

Hall, D.L., S.M. Sterner and R.J. Bodnar. 1988. Freezing point depression of NaCl-KCl-H2O solutions. Econ. Geol., 83, 197-202.

Hunt, J.M. 1996. Petroleum Geochemistry and Geology. W. H. Freeman and Company, New York. 743 pp.

INTERA. 2011. Descriptive geosphere site model. Intera Engineering Ltd. report for the Nuclear Waste Management Organization NWMO DGR-TR-2011-24 R000. Toronto, Canada. http://www.opg.com/generating-power/nuclear/nuclear-waste-management/Deep-Geologic-Repository/Documents/GSR/4.1.17_Discriptive%20Geosphere%20Site%20Model.pdf.

Legall, F.D., C.R. Barnes and R.W. Macqueen. 1981. Thermal maturation, burial history and hotspot development, Paleozoic strata of southern Ontario-Quebec, from conodont acritarch colour alteration studies. Bulletin of Canadian Petroleum Geology 29, 492-539.

McLimans, R.K. 1991. Studies of reservoir diagenesis, burial history, and petroleum migration using luminescence microscopy. *In:* C.E. Barker, and O.C. Kopp, Eds. Luminescence microscopy and spectroscopy: Qualitative and quantitative applications, p. 97-106. Society for Economic Paleontologists and Mineralogists (SEPM), Tulsa, USA.

NWMO. 2011. Geosynthesis. OPG's Deep Geologic Repository for Low & Intermediate Level Waste. Nuclear Waste Management Organization (NWMO), Toronto, Canada. Report DGR-TR-2011-11, 418 pp.

Oakes, C.S., R.J. Bodnar and J.M. Simonson. 1990. The system NaCl-CaCl2-H2O. I. The ice liquidus at 1 atm total pressure. Geochimica et Cosmochimica Acta 54, 603-610.

Oxtoby, N.H. 2002. Comments on: Assessing the maturity of oil trapped in fluid inclusions using molecular geochemistry data and visually-determined fluorescence colours. Applied Geochemistry, 17, 1371–1374.

Roedder, E. 1984. Fluid inclusions. *In*: P.E. Ribbe, Ed. Reviews in Mineralogy, 12, p. 644. Mineralogical Society of America.

Samson, I.M., A.J. Anderson and D.D. Marshall. 2003. Fluid Inclusions: Analysis and Interpretation. Short Course 32, p. 1–374. Mineralogical Association of Canada.

Sherwood Lollar, B., S.M. Weise, S.K. Frape and J.F. Barker. 1994. Isotopic constraints on the migration of hydrocarbon and helium gases of Southwestern Ontario. Bulletin of Canadian Petroleum Geology 42(3), 283-295.

Steele-MacInnis, M., R.J. Bodnar and J. Naden. 2011. Numerical model to determine the composition of H2O–NaCl–CaCl2 fluid inclusions based on microthermometric and microanalytical data. Geochimica et Cosmochimica Acta 75, 21–40.

Zhang, Y.G. and J.D. Frantz. 1987. Determination of the homogenization temperatures and densities of supercritical fluids in the system NaCl-KCl-CaCl2-H2O using synthetic fluid inclusions. Chemical Geology 64, 335-350.

APPENDIX A: PETROGRAPHIC OBSERVATIONS (ANNOTATED PHOTOGRAPHIC RECORD)

SAMPLE DGR-3-034.95

Table A1. Paragenetic sequence and interpreted paleofluids in sample DGR-3.034.95. Column 2 lists the figures upon which the paragenetic sequence is based.

Sample DGR 3-034.95 (Lucas Fm.) Minerals + Fluid Inclusions (phases at room *T*)	Fig. No. in Appendix 1	Vol% vapour	Vol% halite	Time stages → VIII Wall rock	IX Vug+ Vein	X Vug+ Vein	XI Vug+ Vein
Dolomite matrix	-						
Calcite	A1-A3						
Primary Liq+Vap	A2-A7	Variable: 0-70	0				
Secondary metastable-Liq	A6	Uniform: 0	0			?	?

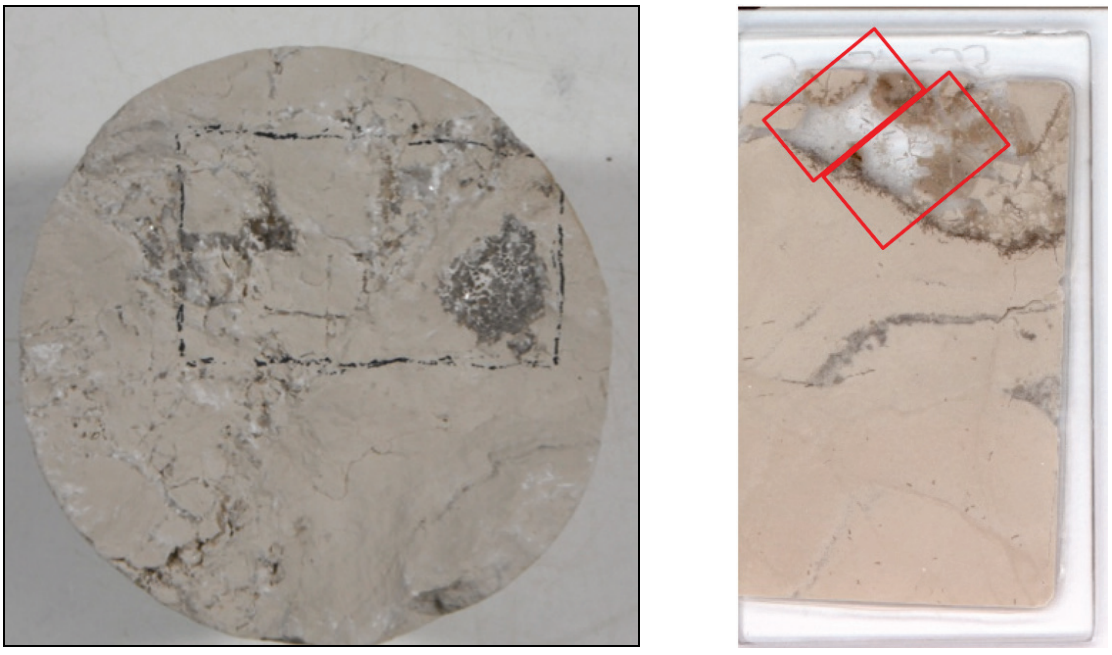


Figure A1. *Left:* Core sample showing area cut for petrographic section. *Right:* Areas of calcite-filled vug cut out for microthermometry. [Macrophotos in reflected light; DGR-3-034.95]

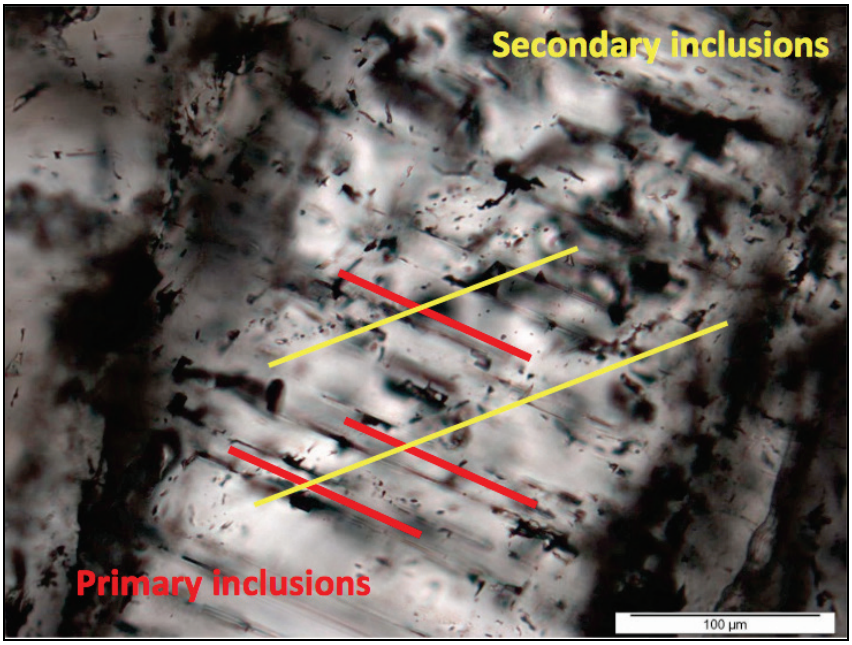


Figure A2. Petrographic relationships of primary and secondary fluid inclusions in sample 3-034.95. Planes of secondary fluid inclusions crosscut arrays of primary inclusions. [Transmitted, polarized light; DGR-3-034.95]

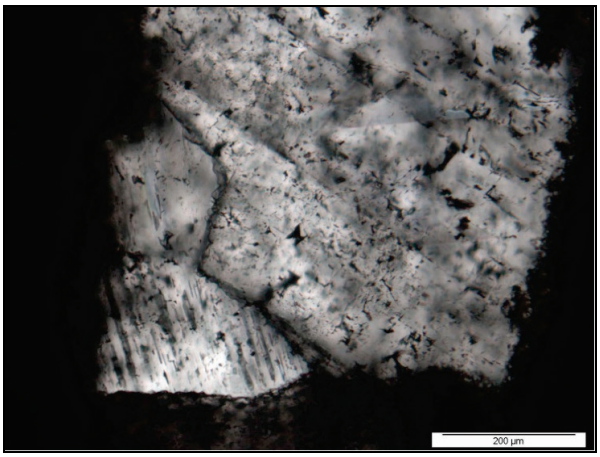


Figure A3. Petrographic relationships between the limestone host rock (opaque), the vug calcite and the primary fluid inclusions (dark specks) in sample 3-034.95 [Transmitted, polarized light; DGR-3-034.95]

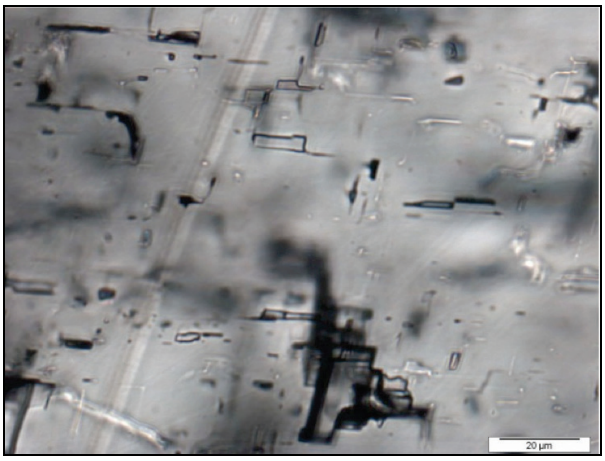


Figure A4. Euhedral to subhedral, primary inclusions containing metastable stretched water in vug calcite in sample 3-034.95 [Transmitted, polarized light; DGR-3-034.95]

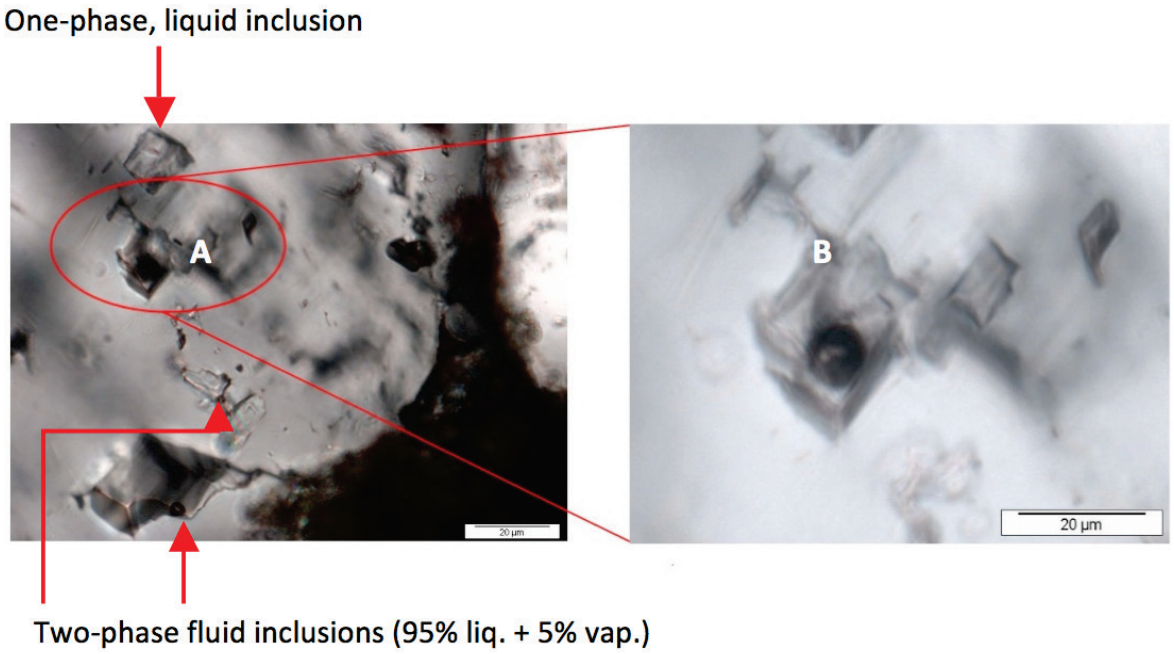
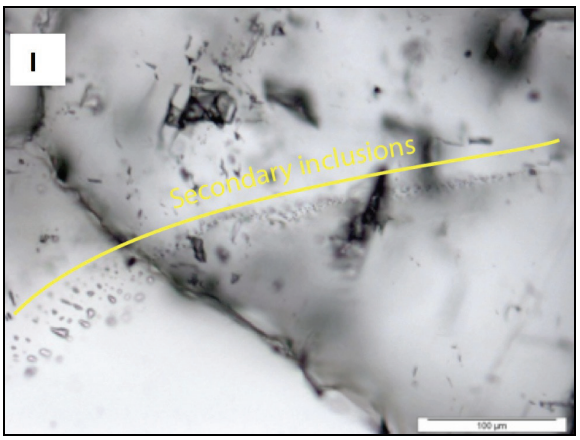
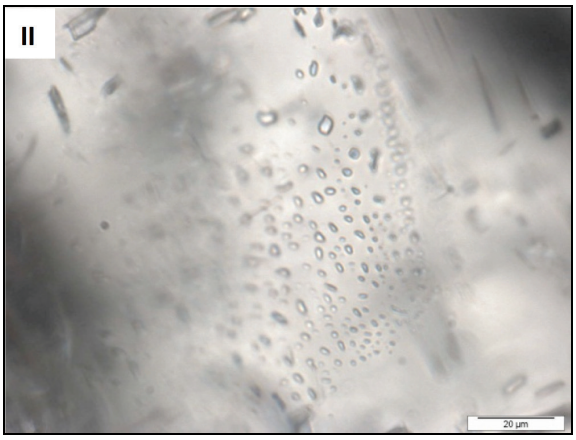


Figure A5. [A] Assemblage of primary, euhedral to subhedral fluid inclusions in vug calcite in sample 3-034.95. The volumetric proportions of liquid+vapour vary strongly within the same assemblage, indicating heterogeneous entrapment. [DGR-3-034.95] [B] Enlarged view of a liquid+vapour fluid inclusion with 70 vol.% liq. + 30 vol.% vap. [Transmitted, polarized light; DGR-3-034.95]





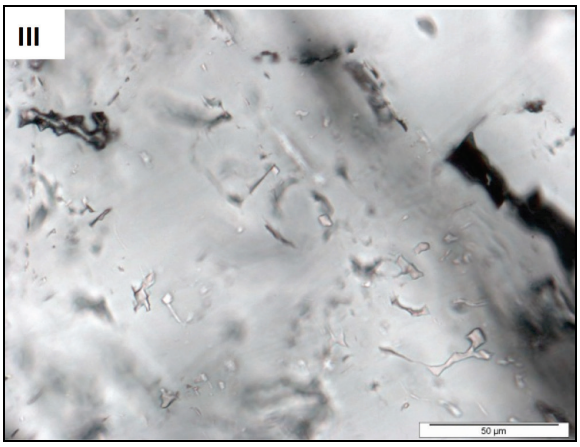


Figure A6. Secondary, liquid-only inclusions (metastable stretched water) in vug calcite in sample 3-034.95.
[I] Planar array of inclusions on a healed fracture cross-cutting a crystal grain boundary
[II] Planar array of subhedral to anhedral inclusions on a healed fracture.
[III] Planar array of anhedral inclusions on a healed fracture.
The uniformity of the phase contents in these examples is indicative of homogeneous entrapment.
[Transmitted, polarized light; DGR-3-034.95]

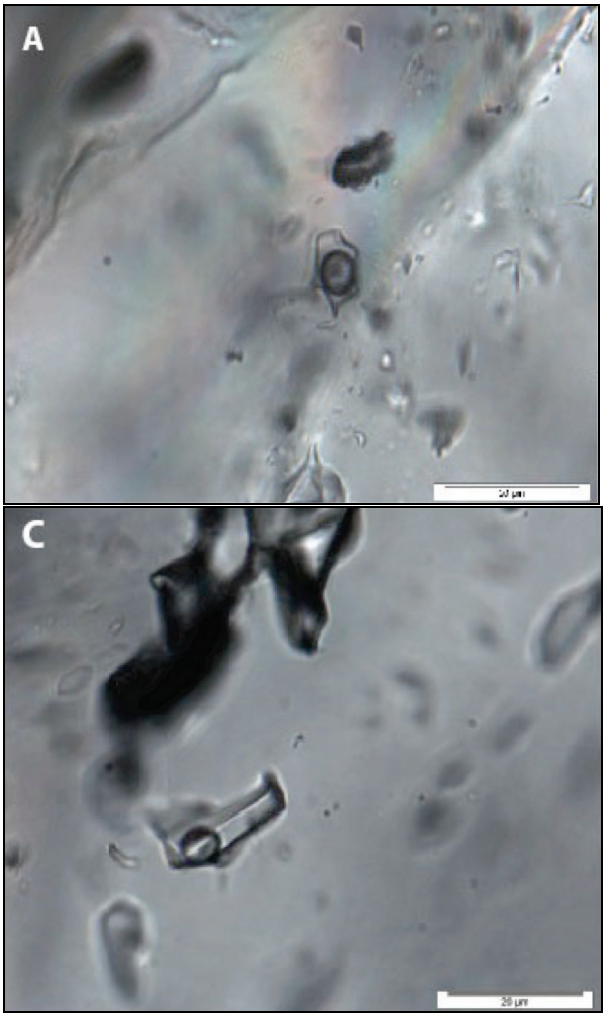


Figure A7. Examples of primary, isolated, liquid+vapour inclusions in sample 3-034.95, with variable volume fractions of vapour. Scale bars correspond to 20 µm.
[Transmitted, polarized light; DGR-3-034.95].

SAMPLE DD 12-11

Table A2. Paragenetic sequence and interpreted paleofluids in sample DD 12-11. Column 2 lists the figures upon which the paragenetic sequence is based.

Sample DD 12-11 (Lucas Fm.) Minerals + Fluid Inclusions (phases at room *T*)	Fig. No. in Appendix 1	Vol% vapour	Vol% halite	Time stages → VIII Wall rock	IX Vug+ Vein	X Vug+ Vein	XI Vug+ Vein
Dolomite matrix	A8						
Calcite	A8						
Primary Liq+Vap±Ankerite	A9	Variable: 0-90	0				
Secondary metastable-Liq	A10	Uniform: 0	0			?	?

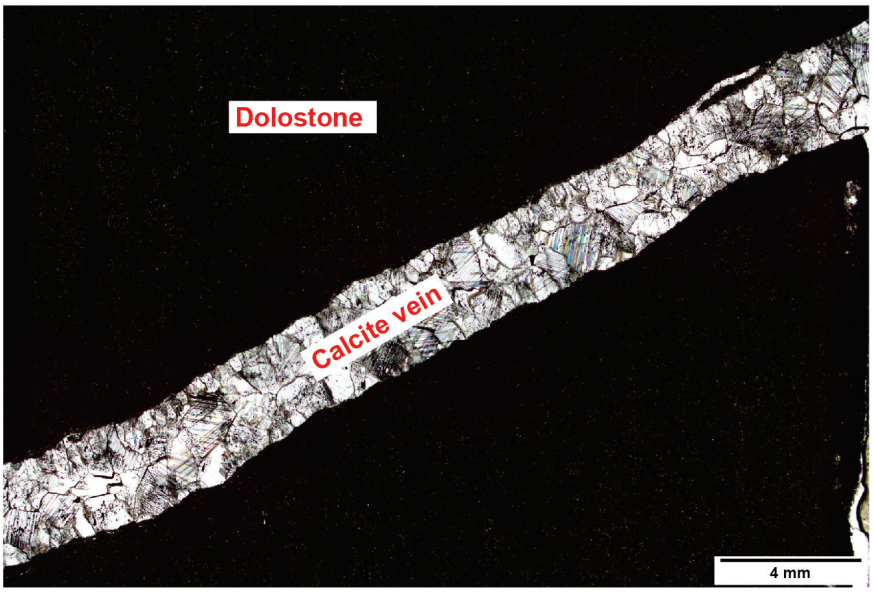


Figure A8. Calcite vein cut for microthermometry [Microphoto in transmitted, polarized light; DD 12-11].

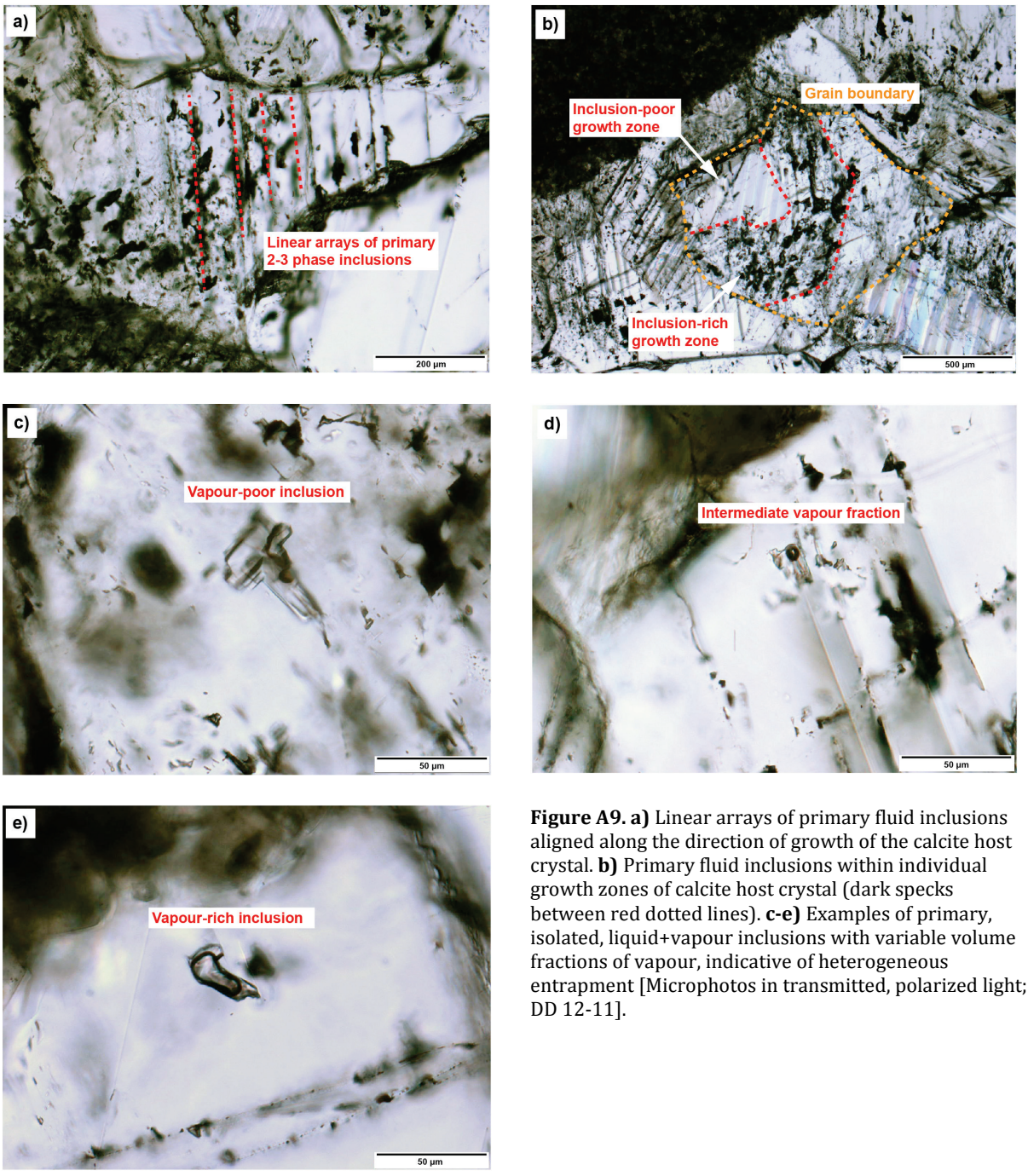


Figure A9. a) Linear arrays of primary fluid inclusions aligned along the direction of growth of the calcite host crystal. **b)** Primary fluid inclusions within individual growth zones of calcite host crystal (dark specks between red dotted lines). **c-e)** Examples of primary, isolated, liquid+vapour inclusions with variable volume fractions of vapour, indicative of heterogeneous entrapment [Microphotos in transmitted, polarized light; DD 12-11].

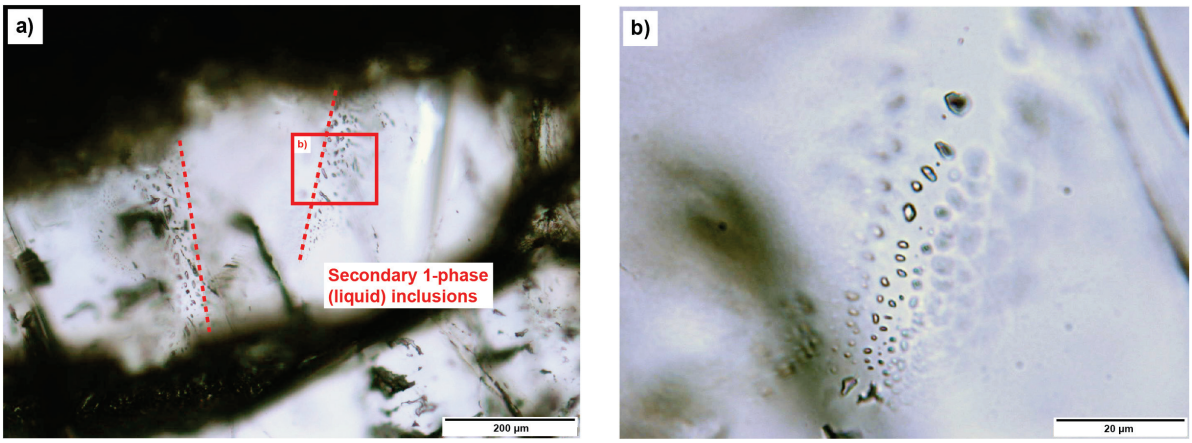


Figure A10. a,b) Planar arrays of secondary liquid-only inclusions (metastable stretched water) on healed fractures in vein calcite [Microphotos in transmitted, polarized light; DD 12-11].

SAMPLE DD 12-12

Table A3. Paragenetic sequence and interpreted paleofluids in sample DD 12-12. Column 2 lists the figures upon which the paragenetic sequence is based.

Sample DD 12-12 (Lucas Fm.) Minerals + Fluid Inclusions (phases at room *T*)	Fig. No. in Appendix 1	Vol% vapour	Vol% halite	Time stages → VIII Wall rock	IX Vug+ Vein	X Vug+ Vein	XI Vug+ Vein
Dolomite matrix	A11						
Calcite	A11						
Primary Liq+Vap±Ankerite	A12	Variable: 0-70	0				
Secondary metastable-Liq	A13	Uniform: 0	0			?	?
Secondary Oil+Vap	A14	Variable: 0-90	0			?	?

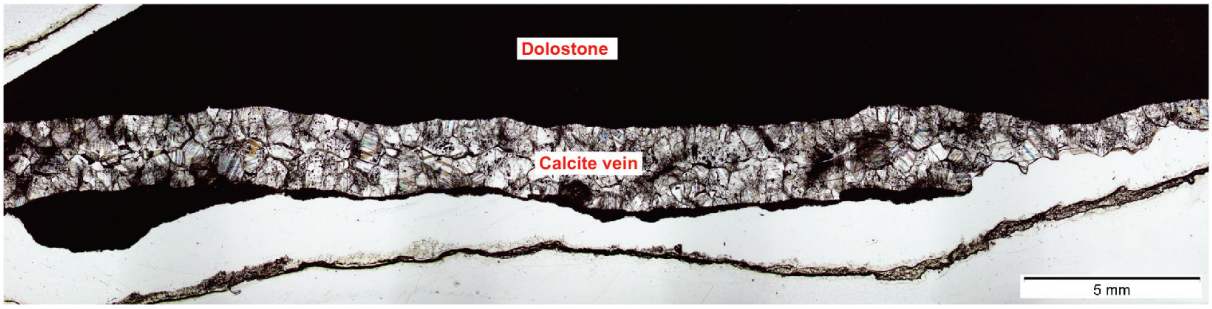
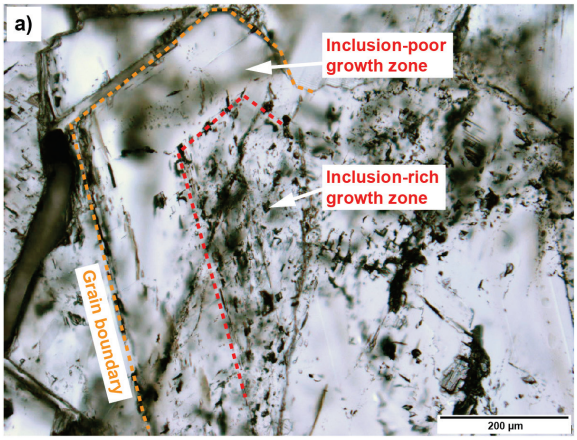
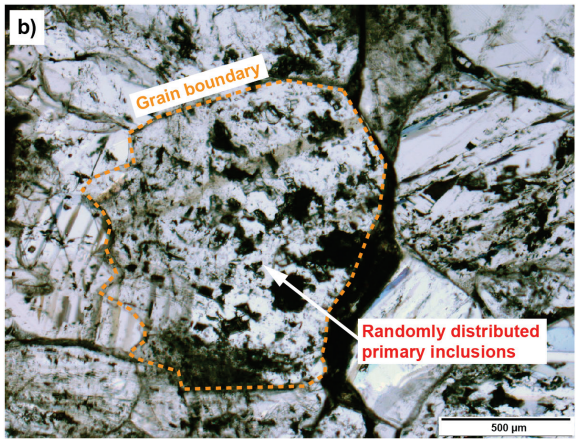


Figure A11. Calcite vein cut for microthermometry [Microphoto in transmitted, polarized light; DD 12-12].





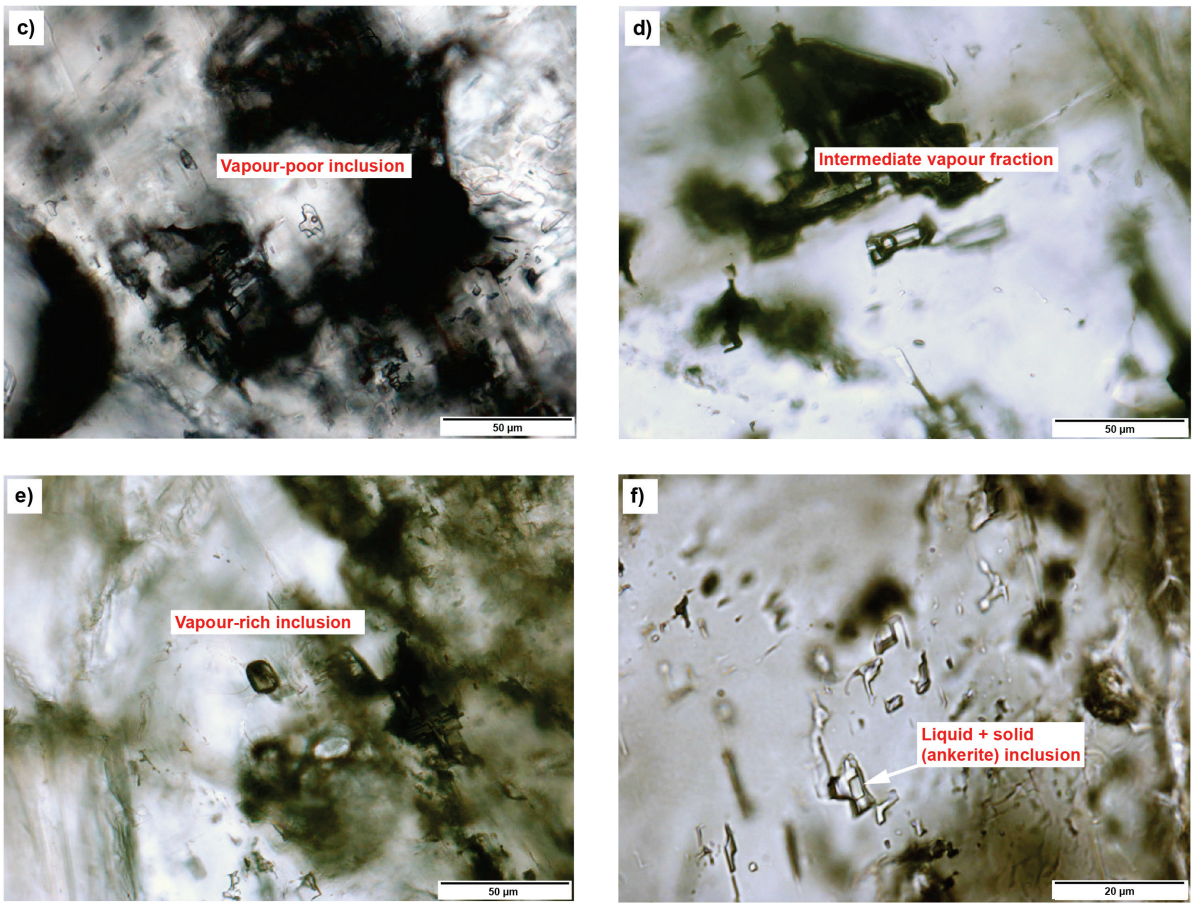


Figure A12. a) Primary fluid inclusions within an individual growth zone of the calcite host crystal (dark specks). The boundary between the inclusion-rich and the inclusion poor growth zone runs parallel to the grain boundary. **b)** Randomly distributed primary fluid inclusions (dark specks) within a calcite crystal. **c-e)** Examples of primary, isolated, liquid+vapour inclusions with variable volume fractions of vapour, indicative of heterogeneous entrapment. **f)** Primary liquid+vapour inclusion containing a rhombohedral solid phase. Raman spectroscopy identified the solid phase as ankerite [Microphotos in transmitted, polarized light; DD 12-12].

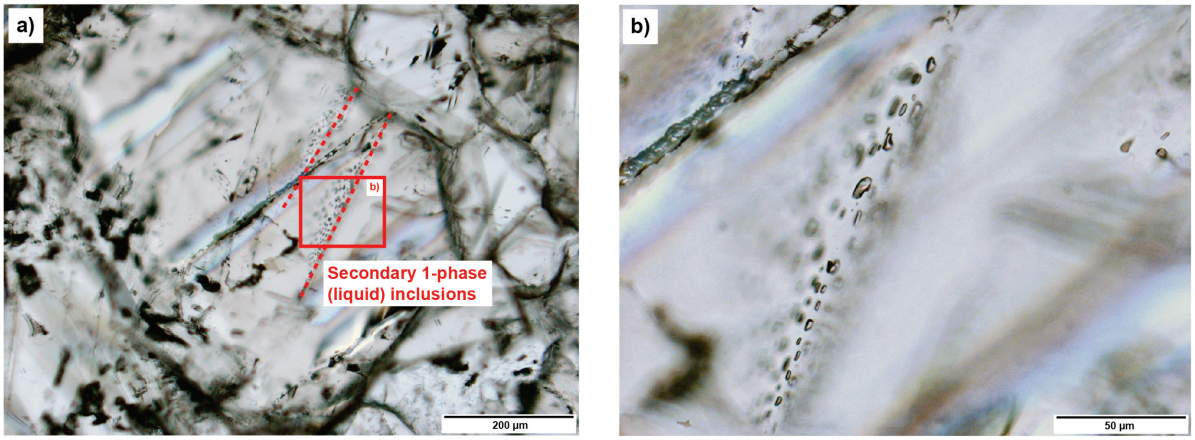


Figure A13. a,b) Planar arrays of secondary liquid-only inclusions (metastable stretched water) on healed fractures in vein calcite [Microphotos in transmitted, polarized light; DD 12-12].

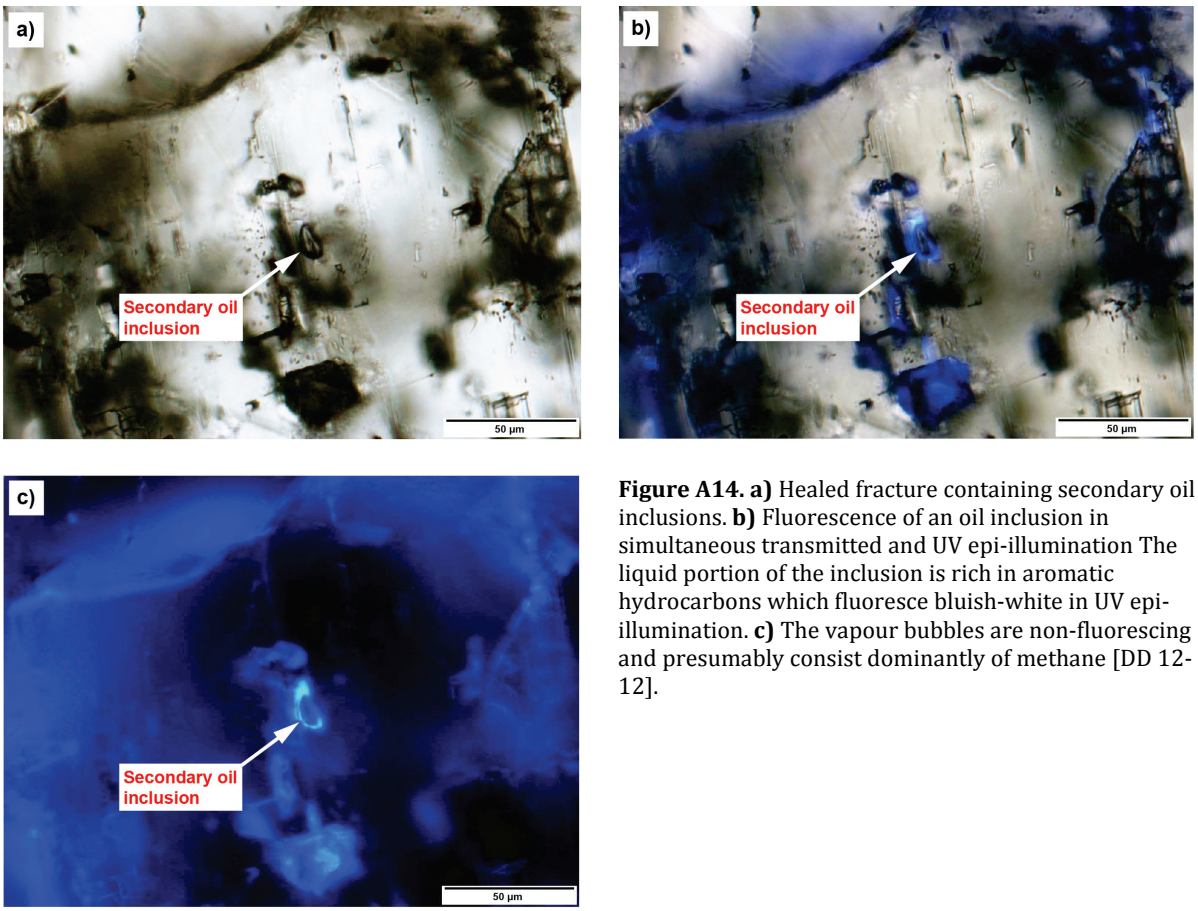


Figure A14. a) Healed fracture containing secondary oil inclusions. **b)** Fluorescence of an oil inclusion in simultaneous transmitted and UV epi-illumination The liquid portion of the inclusion is rich in aromatic hydrocarbons which fluoresce bluish-white in UV epi-illumination. **c)** The vapour bubbles are non-fluorescing and presumably consist dominantly of methane [DD 12-12].

SAMPLE DD 12-13

Table A4. Paragenetic sequence and interpreted paleofluids in sample DD 12-13. Column 2 lists the figures upon which the paragenetic sequence is based.

Sample DD 12-13 (Lucas Fm.) Minerals + Fluid Inclusions (phases at room *T*)	Fig. No. in Appendix 1	Vol% vapour	Vol% halite	Time stages → VIII Wall rock	IX Vug+ Vein	X Vug+ Vein	XI Vug+ Vein
Dolomite matrix	A15						
Calcite	A15						
Primary Liq+Vap±Ankerite	A16	Variable: 0-90	0				
Sec. metastable-Liq±Ankerite	A17	Uniform: 0	0			?	?
Secondary Oil+Vap	A16	Variable: 0-80	0			?	?

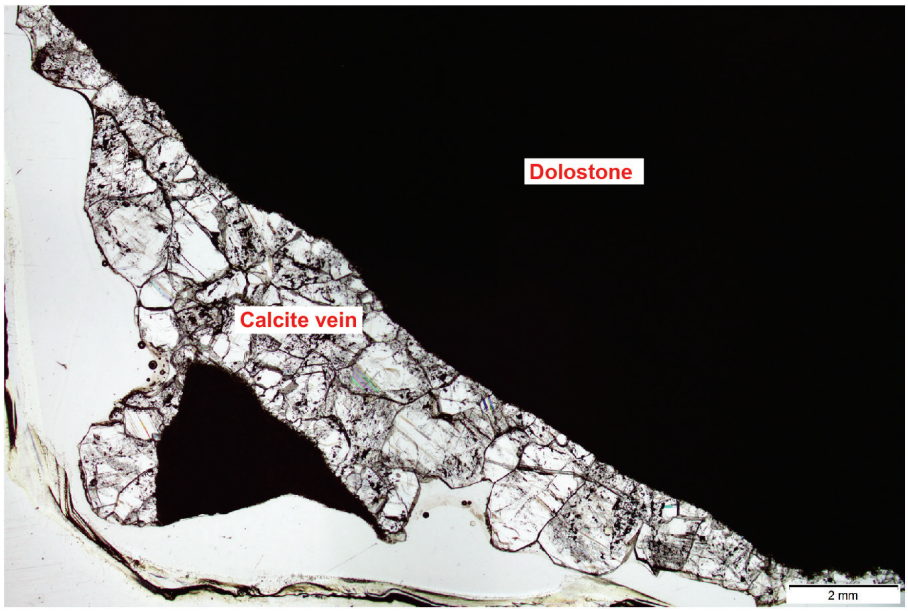


Figure A15. Calcite vein cut for microthermometry [Microphoto in transmitted, polarized light; DD 12-13].

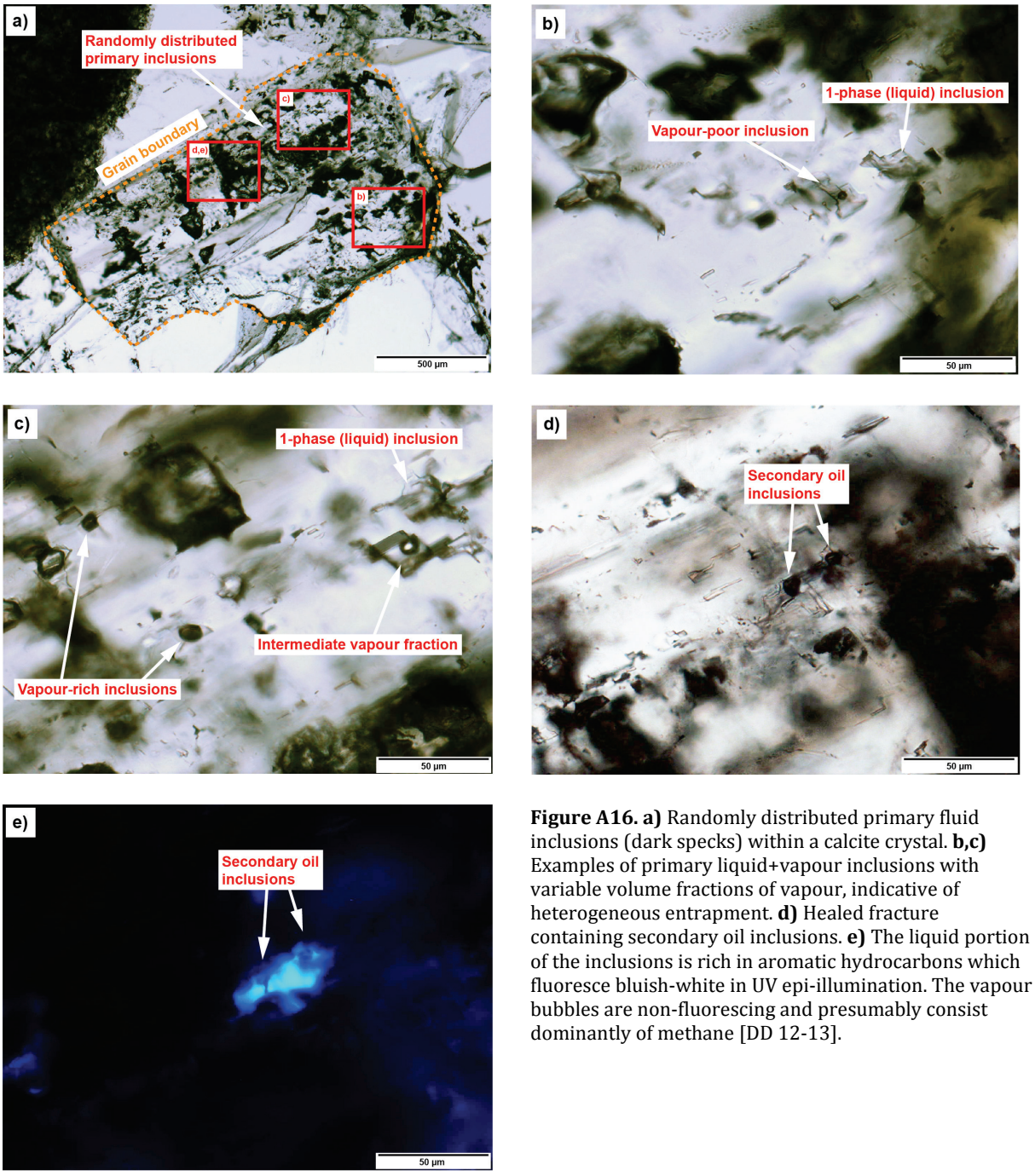


Figure A16. a) Randomly distributed primary fluid inclusions (dark specks) within a calcite crystal. **b,c)** Examples of primary liquid+vapour inclusions with variable volume fractions of vapour, indicative of heterogeneous entrapment. **d)** Healed fracture containing secondary oil inclusions. **e)** The liquid portion of the inclusions is rich in aromatic hydrocarbons which fluoresce bluish-white in UV epi-illumination. The vapour bubbles are non-fluorescing and presumably consist dominantly of methane [DD 12-13].

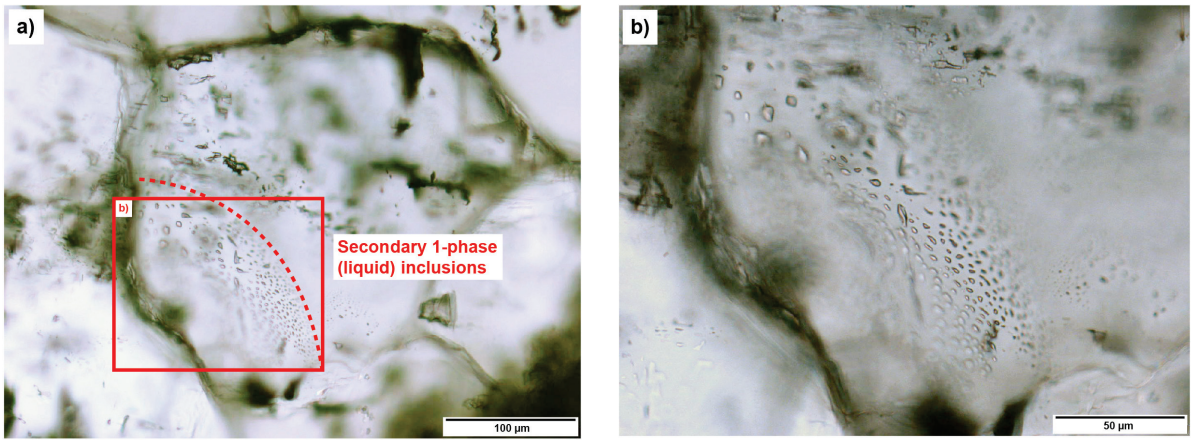


Figure A17. a,b) Planar arrays of secondary liquid-only inclusions (metastable stretched water) on a healed fracture in vein calcite [Microphotos in transmitted, polarized light; DD 12-13].

SAMPLE DGR-2-691.70

Table A5. Paragenetic sequence and interpreted paleofluids in sample DGR-2-691.70. Column 2 lists the figures upon which the paragenetic sequence is based.

Minerals + Fluid Inclusions (phases at room *T*)	Fig. No. in Appendix 1	Vol% vapour	Vol% halite	Time stages → I	II	III	IV	V	VI	VII
				Wall rock	Vug+ Vein	Vug+ Vein	Vug+ Vein	Vug+ Vein	Vug+ Vein	Vug+ Vein
Calcite matrix	A18									
Pyrite	-									
Calcite	A18									
Primary Liq+Vap ±Hal	A19	Variable: 0-60	0-30							
Secondary Liq+Vap ±Hal	A20	Uniform: 5	0-40							
Late secondary metastable-Liq	A21	Uniform: 0	0						?	?

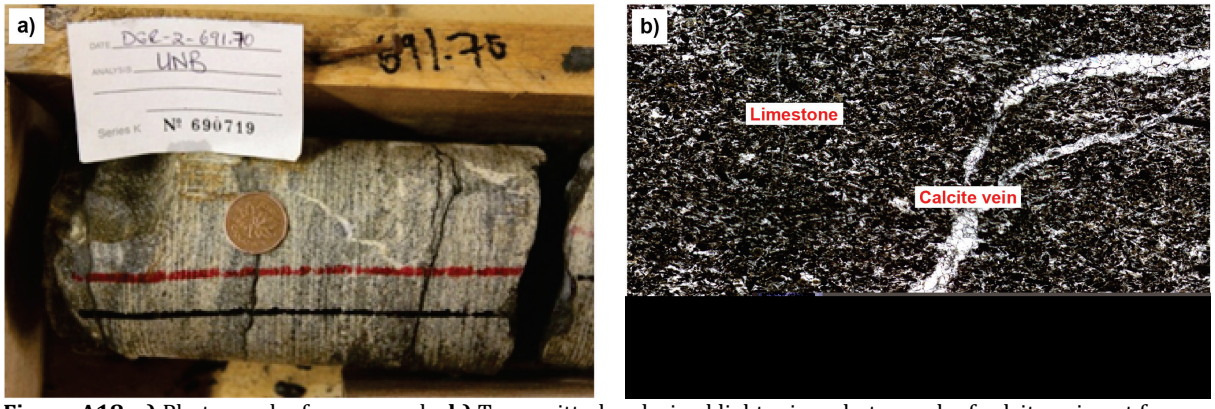
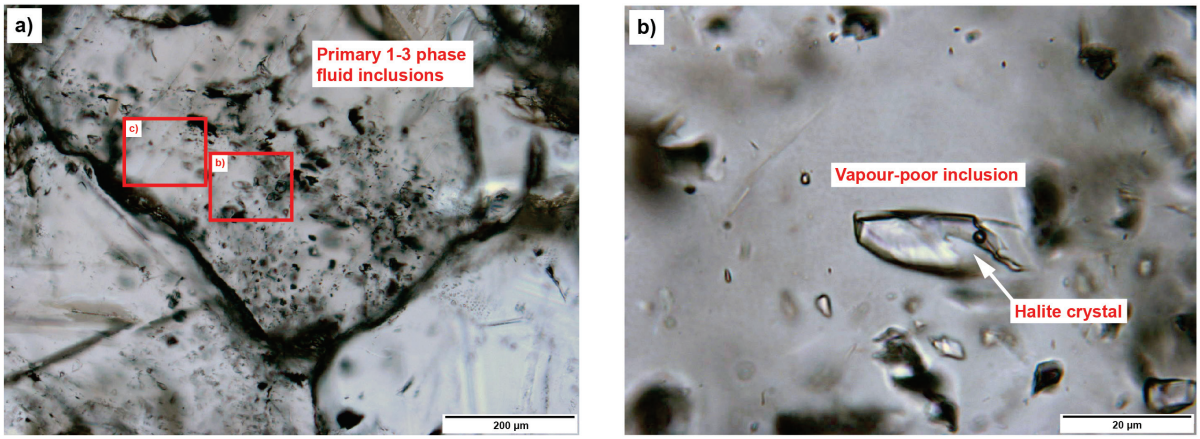


Figure A18. a) Photograph of core sample. **b)** Transmitted, polarized light microphotograph of calcite vein cut for microthermometry [DGR-2-691.70].



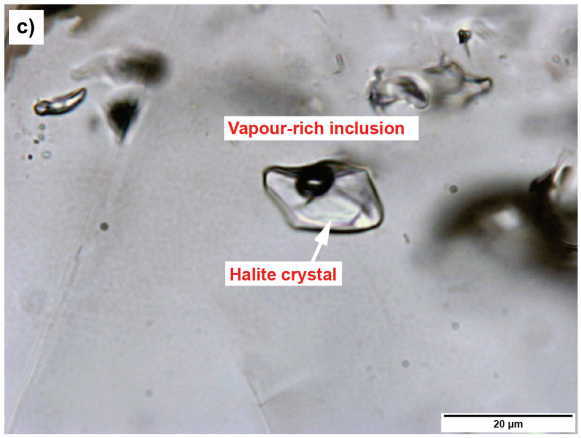


Figure A19. a) Randomly distributed primary fluid inclusions (dark specks) within a calcite crystal. **b,c)** Examples of primary liquid+vapour inclusions with variable volume fractions of vapour, indicative of heterogeneous entrapment. Some of the inclusions also contain variable-sized halite crystals [Microphotographs in transmitted, polarized light; DGR-2-691.70].

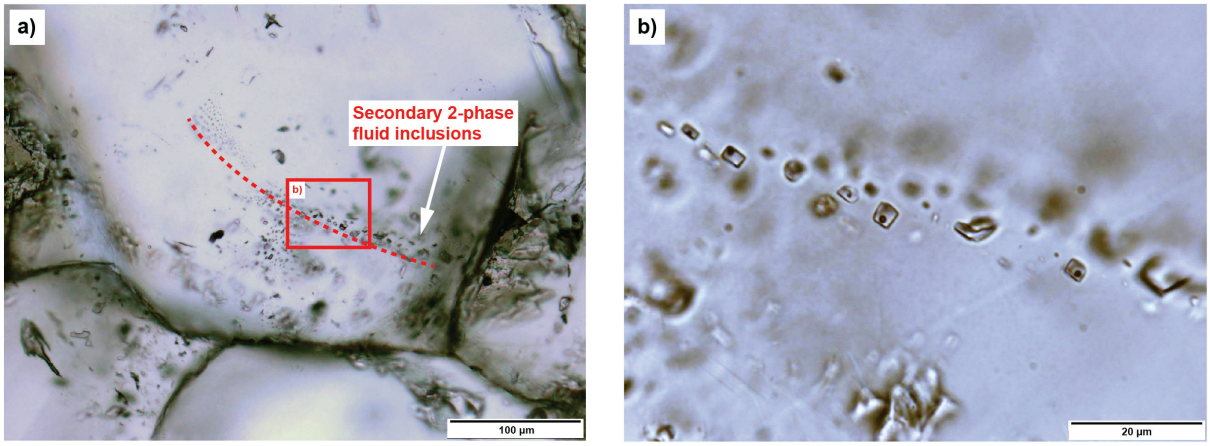


Figure A20. a) Planar array of secondary liquid+vapour inclusions on a healed fracture in vein calcite. **b)** The uniform phase proportions (~ 5 vol% vapour) indicate homogeneous entrapment [Microphotographs in transmitted, polarized light; DGR-2-691.70].

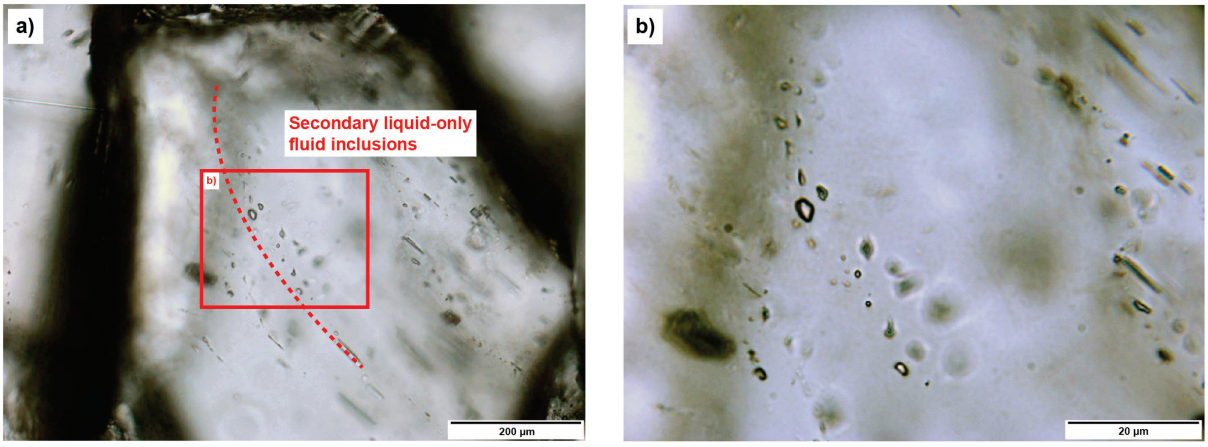


Figure A21. a,b) Planar arrays of secondary liquid-only inclusions (metastable stretched water) on a healed fracture in vein calcite [Microphotos in transmitted, polarized light; DGR-2-691.70].

SAMPLE DGR-4-769.57

Table A6. Paragenetic sequence and interpreted paleofluids in sample DGR-4-769.57. Column 2 lists the figures upon which the paragenetic sequence is based.

Minerals + Fluid Inclusions (phases at room *T*)	Fig. No. in Appendix 1	Vol% vapour	Vol% halite	Time stages → I Wall rock	II Vug+ Vein	III Vug+ Vein	IV Vug+ Vein	V Vug+ Vein	VI Vug+ Vein	VII Vug+ Vein
Calcite matrix	A22									
Pyrite	-									
Calcite	A22									
Celestine	A22									
Primary Liq+Vap ±Hal	A23	Variable: 0-70	0-30							
Early secondary Liq+Vap ±Hal	A24	Variable: 0-90	0-70							
Late secondary Liq+Vap ±Hal	A25	Uniform: 5	0-40							
Late secondary metastable-Liq	A26	Uniform: 0	0						?	?
Late secondary Oil+Vap	A27	Variable: 0-50	0						?	?

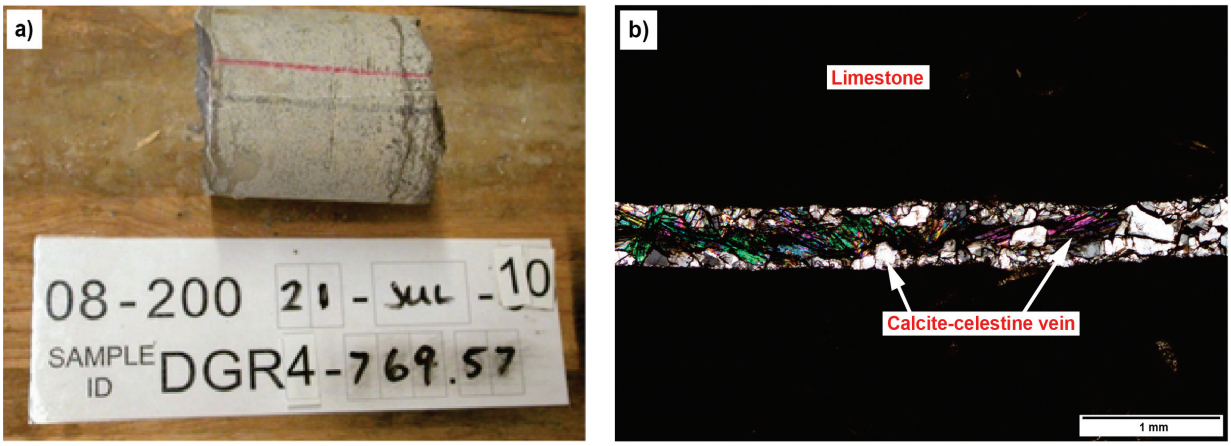
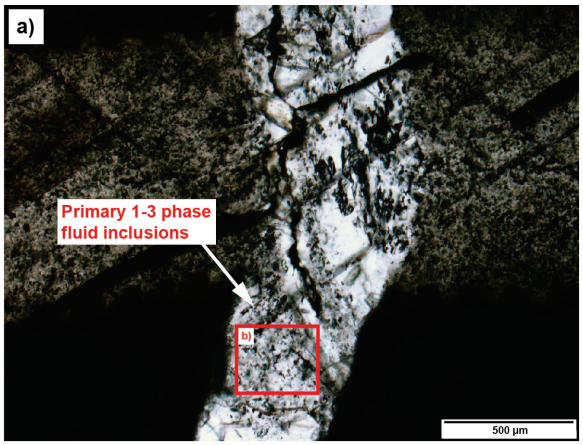
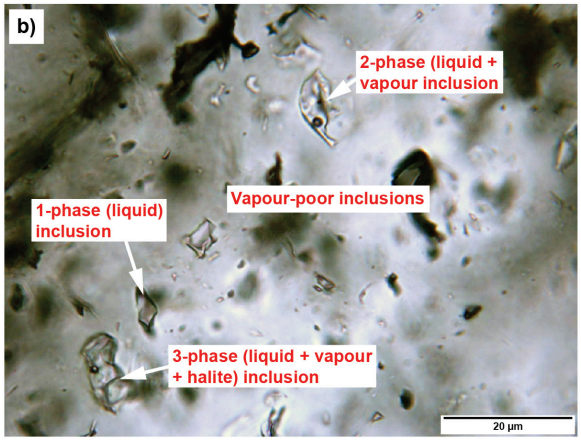


Figure A22. **a)** Photograph of core sample. **b)** Transmitted, polarized light microphotograph of calcite-celestine vein cut for microthermometry [DGR-4-769.57].





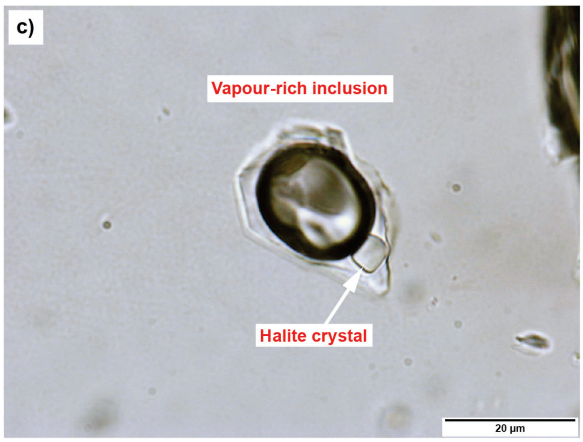
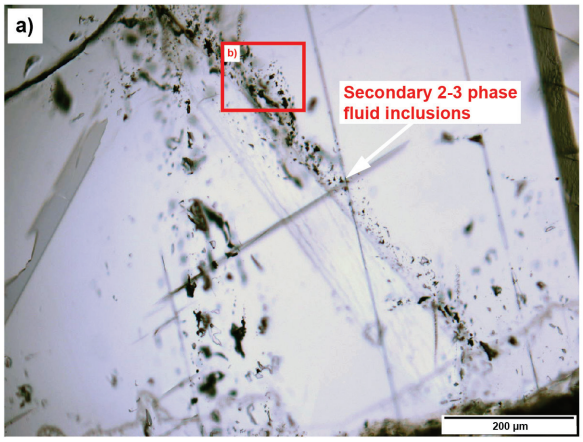


Figure A23. a) Randomly distributed primary fluid inclusions (dark specks) within vein calcite. **b,c)** Examples of primary liquid+vapour inclusions with variable volume fractions of vapour, indicative of heterogeneous entrapment. Some of the inclusions also contain variable-sized halite crystals [Microphotographs in transmitted, polarized light; DGR-4-769.57].



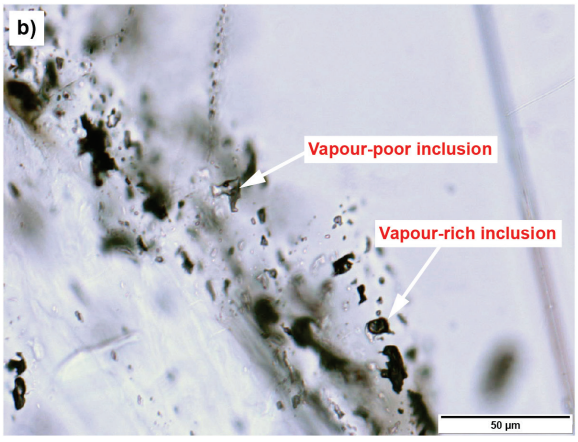


Figure A24. a) Trace of secondary, anhedral, liquid+vapour inclusions on healed fractures within vein calcite. **b)** The inclusions show variable phase proportions, indicative of heterogeneous entrapment [Microphotographs in transmitted, polarized light; DGR-4-769.57].

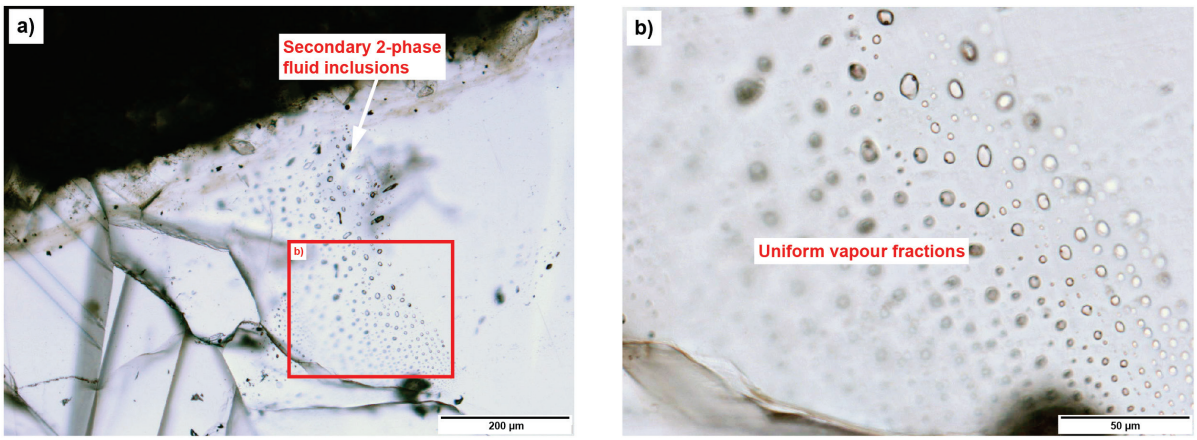


Figure A25. a) Trace of secondary, subhedral, liquid+vapour inclusions on healed fractures within vein calcite. **b)** The inclusions show uniform phase proportions (~5 vol% vapour), indicative of homogeneous entrapment [Microphotographs in transmitted, polarized light; DGR-4-769.57].

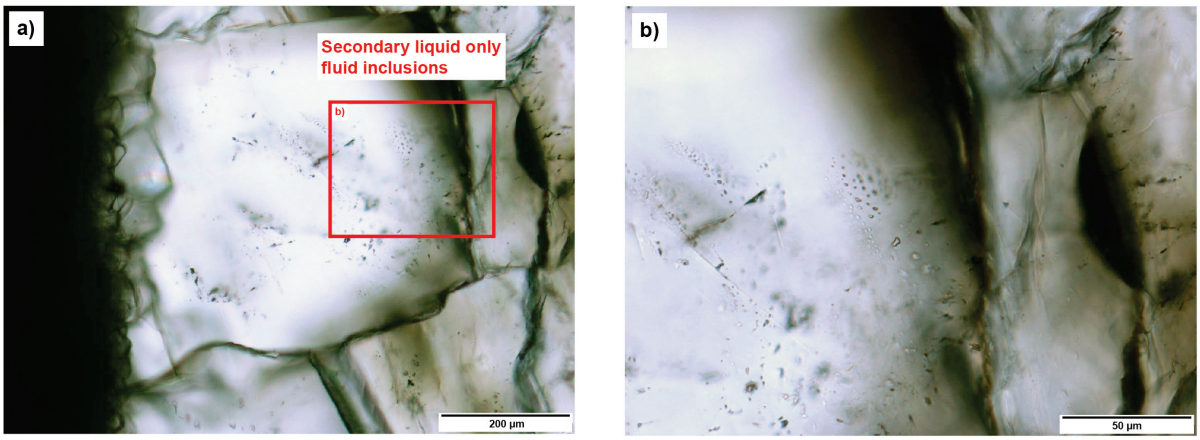
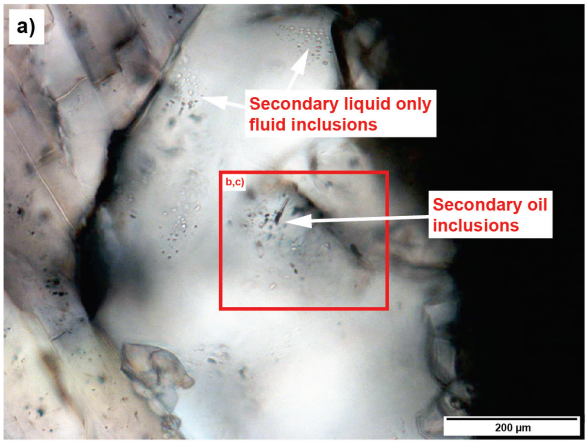
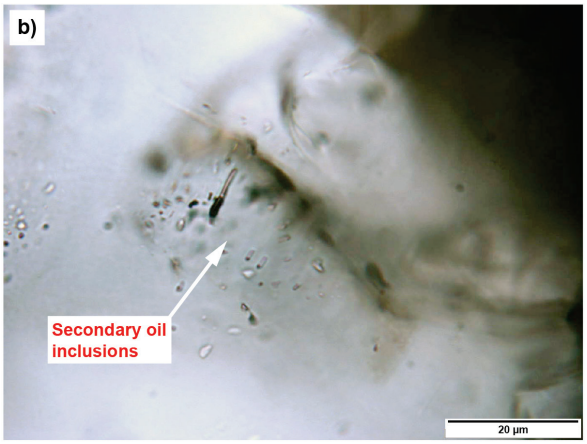


Figure A26. a) Planar array of secondary liquid-only inclusions (metastable stretched water) on a healed fracture in vein calcite [Microphotographs in transmitted, polarized light; DGR-4-769.57].





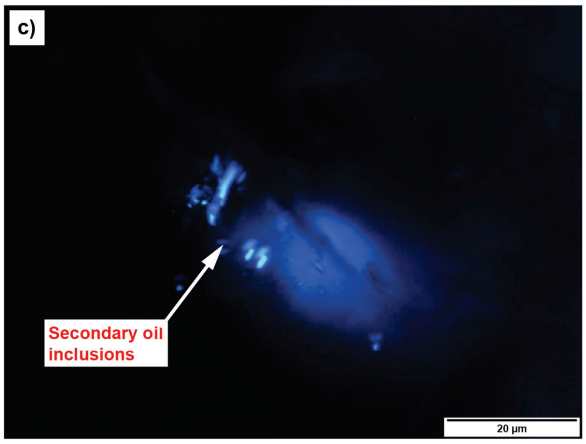


Figure A27. a,b) Healed fracture containing secondary oil inclusions showing variable phase proportions. The liquid portion has a distinct brownish tinge. **c)** The aromatic hydrocarbons show a bluish-white UV fluorescence colour [DGR-4-769.57].

SAMPLE DGR-2-778.44

Table A7. Paragenetic sequence and interpreted paleofluids in sample DGR-2-778.44. Column 2 lists the figures upon which the paragenetic sequence is based.

Minerals + Fluid Inclusions (phases at room *T*)	Fig. No. in Appendix 1	Vol% vapour	Vol% halite	Time stages → I	II	III	IV	V	VI	VII
				Wall rock	Vug+ Vein	Vug+ Vein	Vug+ Vein	Vug+ Vein	Vug+ Vein	Vug+ Vein
Dolomite matrix	A28									
Pyrite	-									
Dolomite (saddle habit)	A28									
Primary Liq+Vap ±Hal	A29	Variable: 0-60	0-20							
Late secondary Oil+Vap	A30	Uniform: 10	0						?	?

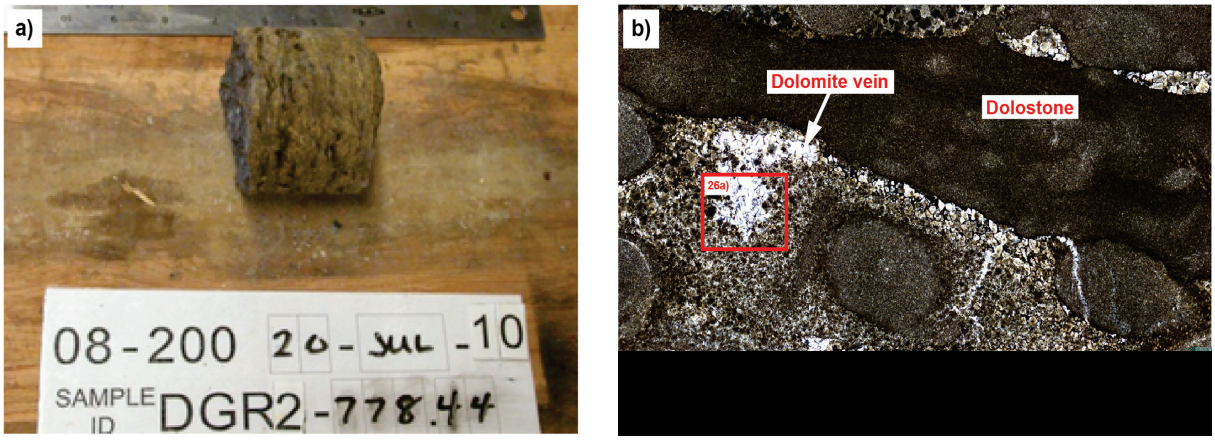
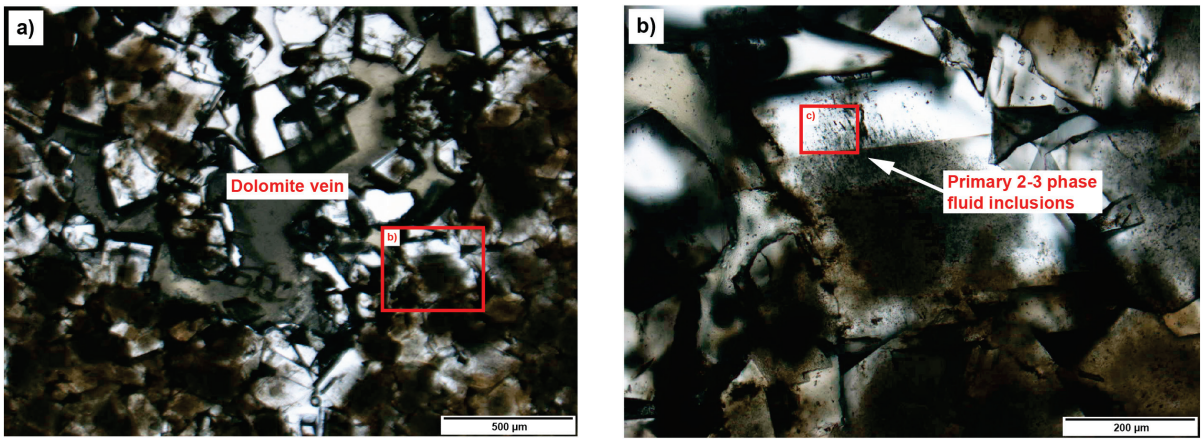


Figure A28. **a)** Photograph of core sample. **b)** Transmitted, polarized light microphotograph of dolomite vein cut for microthermometry [DGR-2-778.44].



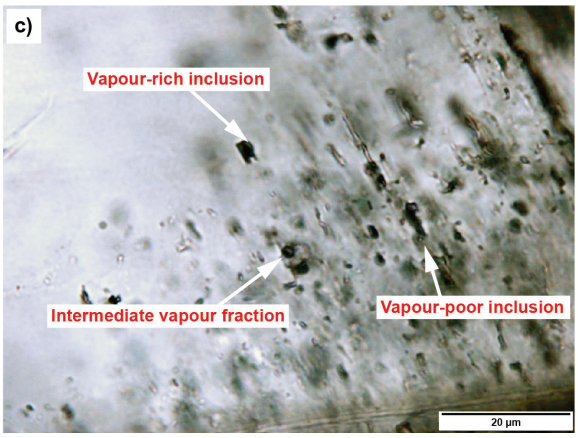


Figure A29. **a)** The walls of the vein are lined with coarse grained euhedral dolomite rhombs. **b)** Vein dolomite with linear arrays of primary inclusions radiating out from an inclusion-rich crystal core. **c)** The variable phase proportions of the primary inclusions indicate heterogeneous entrapment [Microphotographs in transmitted, polarized light; DGR-2-778.44].

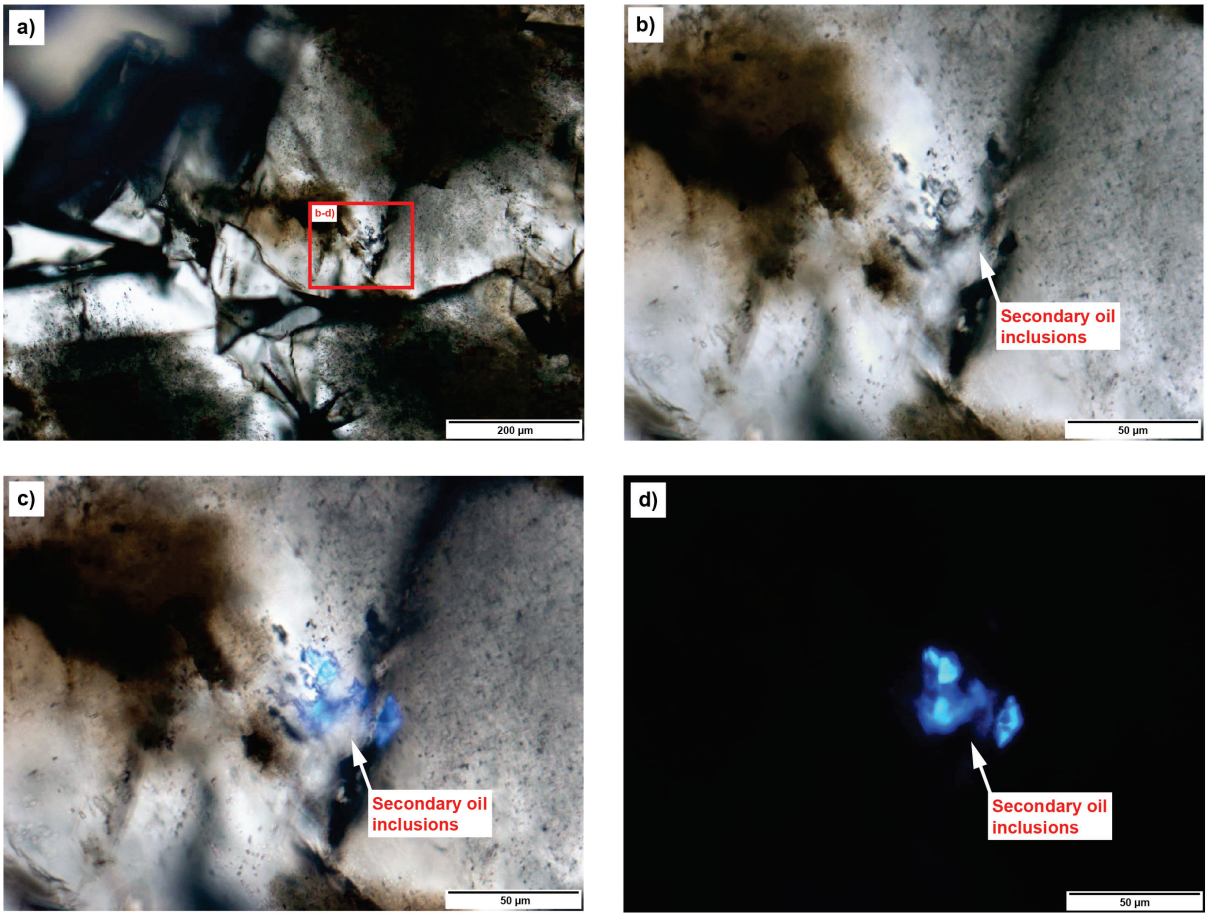


Figure A30. a,b) Healed fracture containing secondary oil inclusions. **c)** Fluorescence of the oil inclusions in simultaneous transmitted and UV epi-illumination. **d)** The hydrocarbons show a bluish-white UV fluorescence colour [DGR-2-778.44].

SAMPLE DGR-3-799.15

Table A8. Paragenetic sequence and interpreted paleofluids in sample DGR-3-799.15. Column 2 lists the figures upon which the paragenetic sequence is based.

Minerals + Fluid Inclusions (phases at room *T*)	Fig. No. in Appendix 1	Vol% vapour	Vol% halite	Time stages →						
				I	II	III	IV	V	VI	VII
				Wall rock	Vug+ Vein	Vug+ Vein	Vug+ Vein	Vug+ Vein	Vug+ Vein	Vug+ Vein
Calcite matrix	-									
Calcite	A31, A32									
Primary Liq+Vap ±Hal	A33-A36	Variable: 0-60	0-30							
Secondary Liq+Vap ±Hal	A37-A41, A43	Uniform: 10	0-30							
Late secondary metastable-Liq	A42	Uniform: 0	0						?	?

In addition to the features given in Table A8, some of the secondary Liq+Vap inclusions also enclose crystals (Figs. A40 and A41). No Raman signal was obtained owing to their small size and great depth within the thick-sections. The optical properties suggest anhydrite.

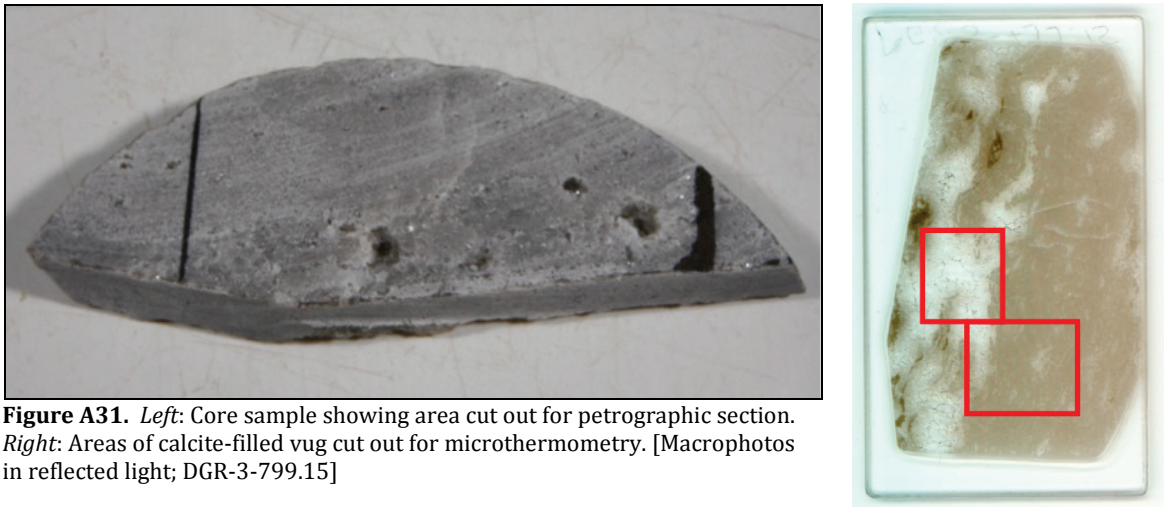


Figure A31. *Left*: Core sample showing area cut out for petrographic section. *Right*: Areas of calcite-filled vug cut out for microthermometry. [Macrophotos in reflected light; DGR-3-799.15]

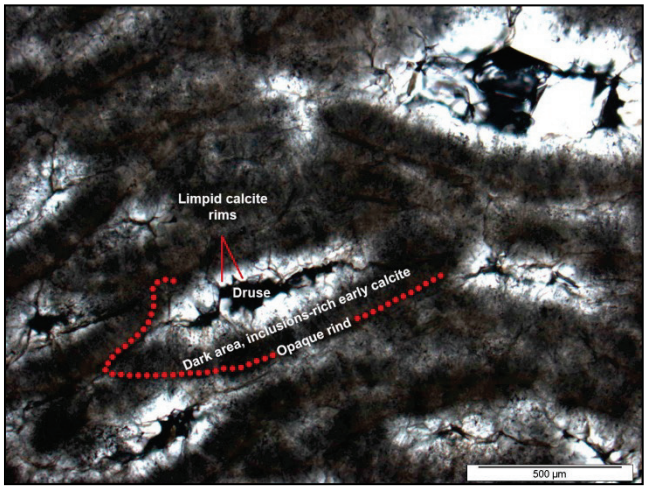


Figure A32. Petrographic relationship between vugs, euhedral calcite crystals and fluid inclusions. [Transmitted, polarized light; DGR-3-799.15]

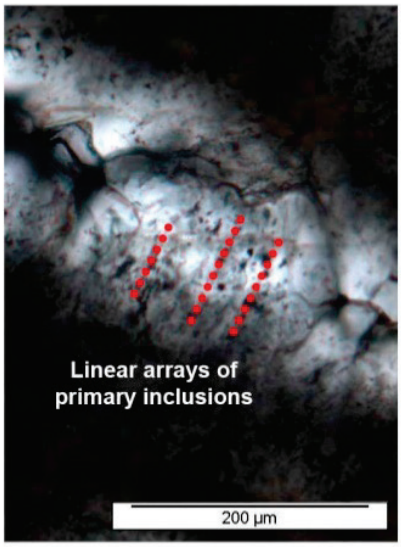


Figure A33. Linear arrays of primary inclusions aligned along the direction of growth of the host calcite (from opaque region towards the clear core of the vug). [Transmitted, polarized light; DGR-3-799.15]

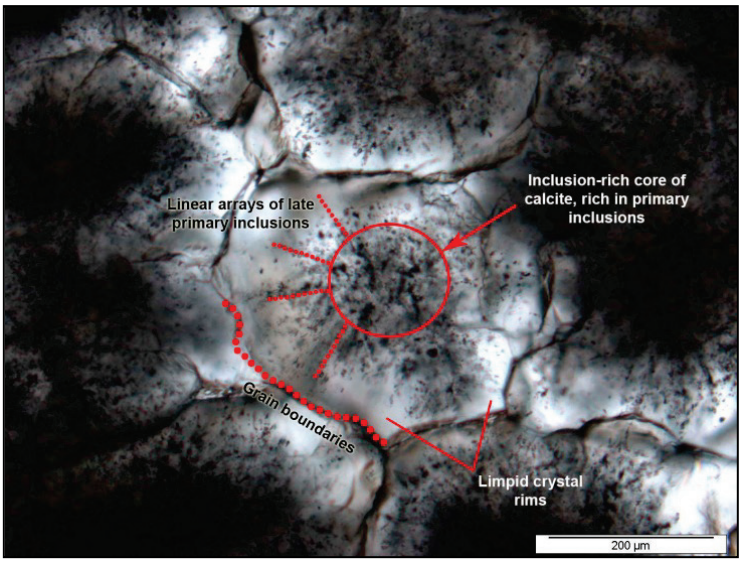


Figure A34. Calcite crystals near the cores of the vugs contain clouds three-dimensionally distribution primary fluid inclusions. The rims of these crystals contain linear arrays of fluid inclusions that radiate outwards, parallel to the growth direction of the crystal. Thus, these are also primary inclusions. [Transmitted, polarized light; DGR-3-799.15]

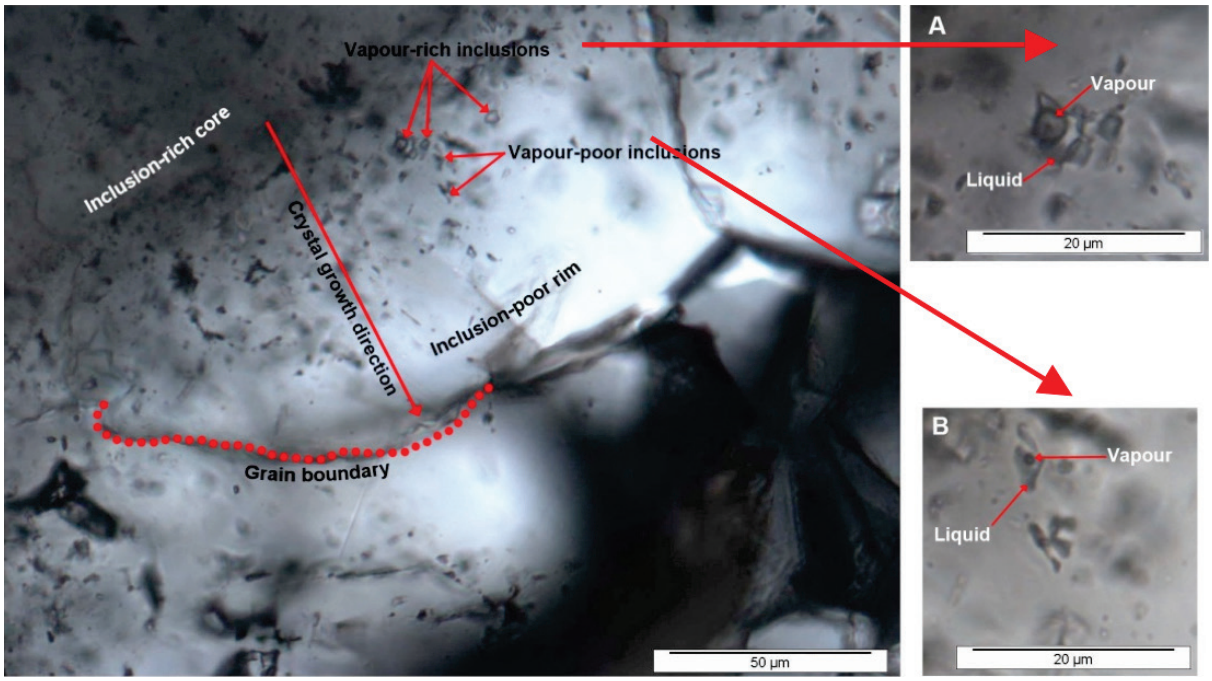


Figure A35. Primary, anhedral fluid inclusions showing the crystal growth direction. Petrographic relation between the core of the crystal and the grain boundary. [A] Vapour rich inclusion and [B] Liquid rich inclusion. [Transmitted, polarized light; DGR-3-799.15]

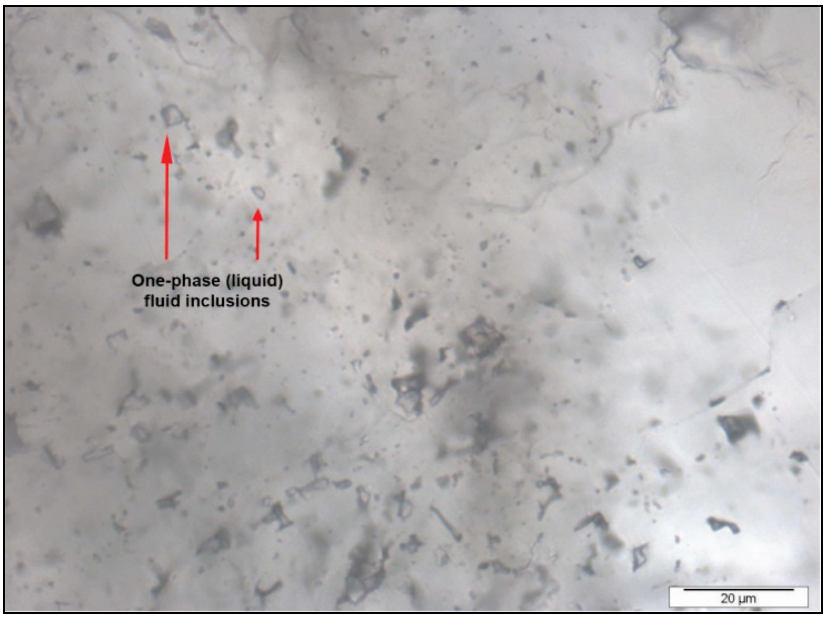


Figure A36. Primary, liquid-only inclusions. [Transmitted, polarized light; DGR-3-799.15]

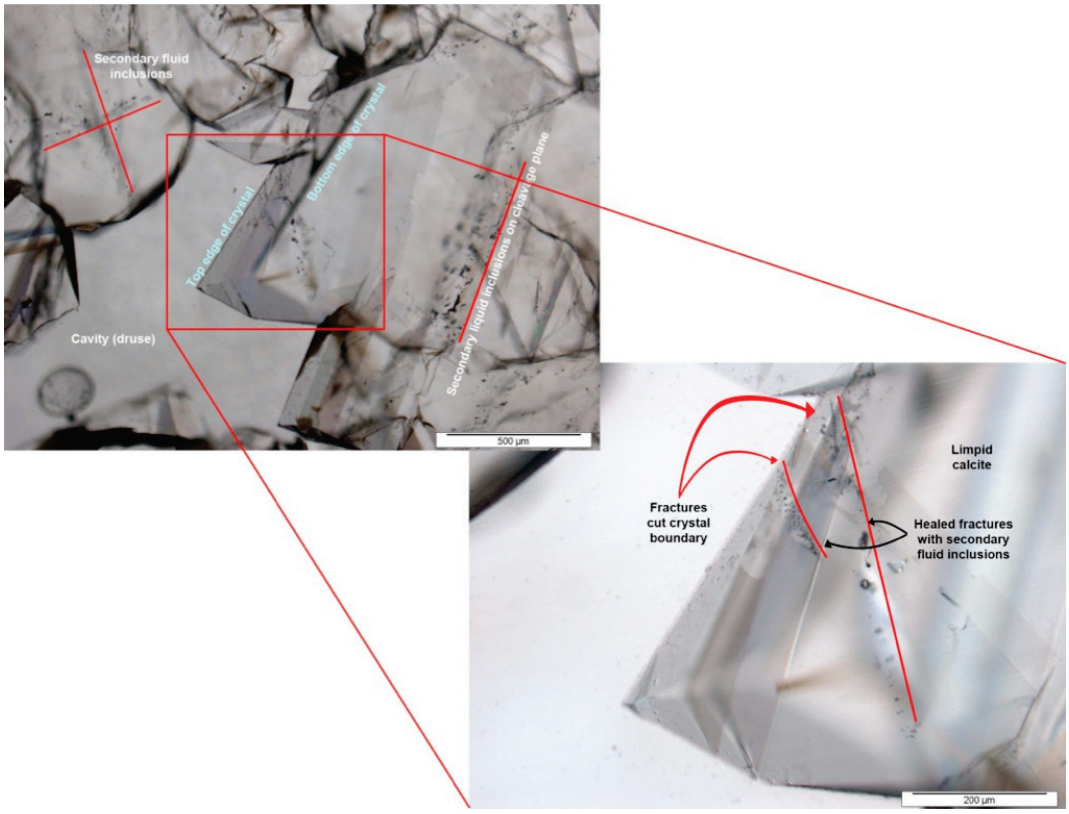


Figure A37. Calcite crystals cross-cut by healed fractures containing secondary, liquid+vapour inclusions. All the inclusions contain ~15 vol% vapour, indicating homogeneous entrapment. [Transmitted, polarized light; DGR-3-799.15]

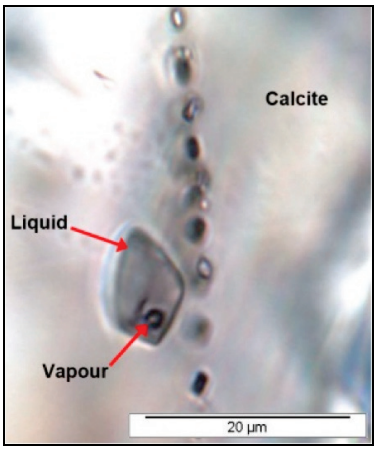


Figure A38. Two generations of equant, subhedral, secondary fluid inclusions, one generation with ≤2 µm diam. and the other with ≤10 µm diam. and ~5 vol% vapour. [Transmitted, polarized light; DGR-3-799.15]

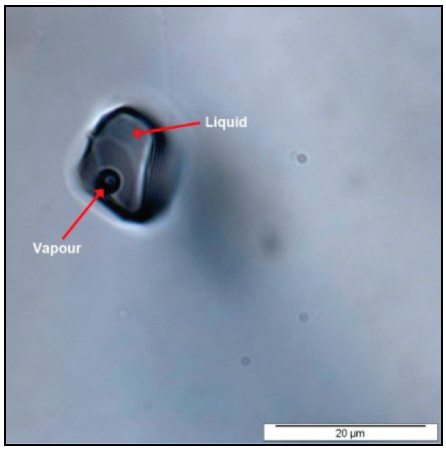


Figure A39. Subhedral secondary fluid inclusion (15 µm diam.) with ~10 vol% vapour. [Transmitted, polarized light; DGR-3-799.15]

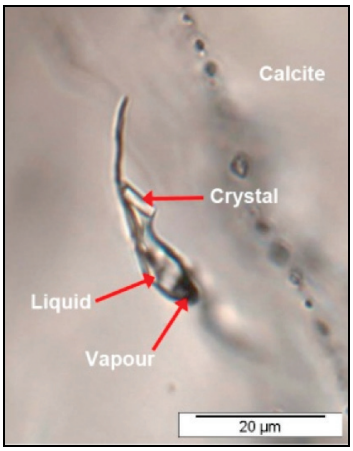


Figure A40. Elongated, irregular secondary fluid inclusion (25 µm long) containing liquid + vapour and a transparent, birefringent crystal, probably anhydrite. [Transmitted, polarized light; DGR-3-799.15]

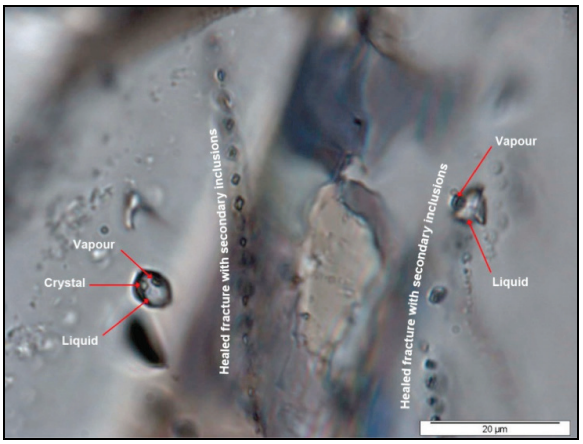


Figure A41. Two assemblages of equant, anhedral secondary fluid inclusions, one with ≤2 µm diam. and the other with ≤7 µm diam. Both contain liquid+vapour with uniform volume fractions of vapour (~10%), indicating homogeneous entrapment. One inclusion contains an unidentified solid phase. [Transmitted, polarized light; DGR-3-799.15]

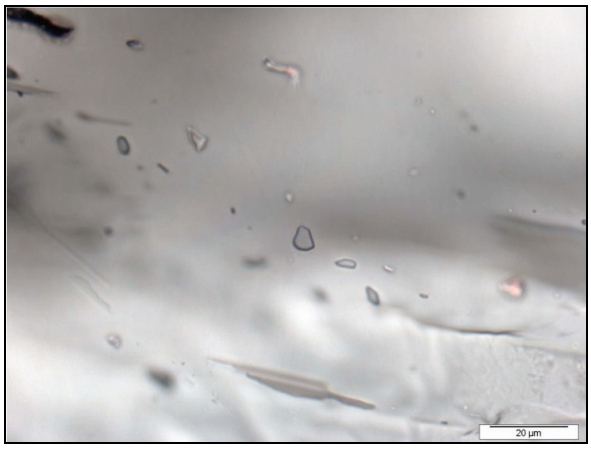


Figure A42. Secondary, anhedral, liquid-only inclusions with ≤4 µm diameter, formed by homogeneous entrapment. [Transmitted, polarized light; DGR-3-799.15]

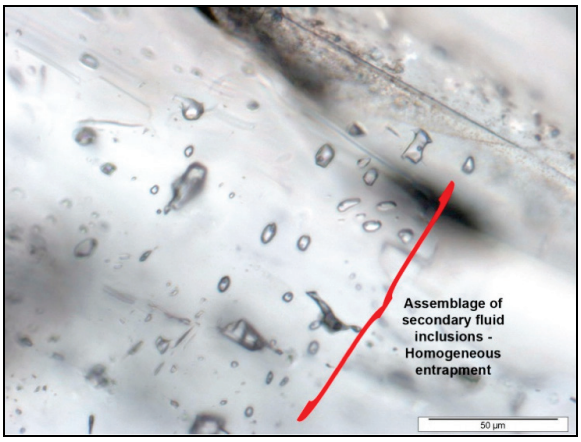


Figure A43. Assemblage of elongated and irregular secondary fluid inclusions with ≤25 µm diameter and ~5 vol% vapour. The uniform phase volume fractions indicate homogeneous entrapment. [Transmitted, polarized light; DGR-3-799.15]

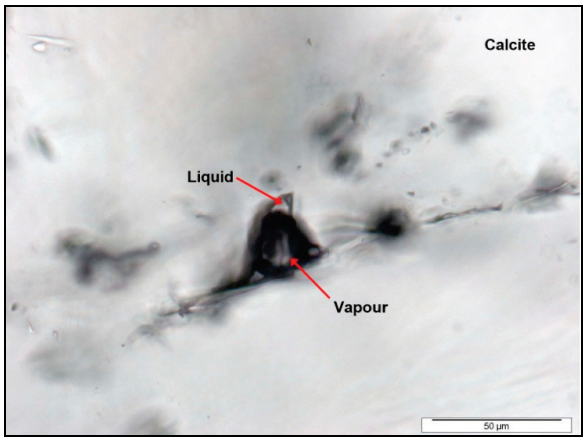


Figure A44. Secondary fluid inclusion with a diameter of 45 µm and vapour bubble (probably methane) making up about 90 vol%. [Transmitted, polarized light; DGR-3-799.15]

SAMPLE DGR-6-883.75

Table A9. Paragenetic sequence and interpreted paleofluids in sample DGR-6-883.75. Column 2 lists the figures upon which the paragenetic sequence is based.

Minerals + Fluid Inclusions (phases at room *T*)	Fig. No. in Appendix 1	Vol% vapour	Vol% halite	Time stages → I	II	III	IV	V	VI	VII
				Wall rock	Vug+ Vein	Vug+ Vein	Vug+ Vein	Vug+ Vein	Vug+ Vein	Vug+ Vein
Dolomite matrix	-									
Calcite	A45									
Primary Liq+Vap ±Hal	A46	Variable: 0-85	0-50							
Secondary Liq+Vap ±Hal	-	Variable: 0-80	0-20				?			
Secondary Liq+Vap ±Hal	-	Variable: 0-80	0-20				?			
Late secondary Liq+Vap ±Hal	A47, A48	Uniform: 5	0-30							

In addition to the features given in Table A9, some of the inclusions also enclose crystals. Figure A46D shows two different crystals within the inclusion. No Raman signal was obtained from the crystals owing to their small size and great depth within the thick-sections. The optical properties suggest anhydrite (elongated) and halite (rectangular).

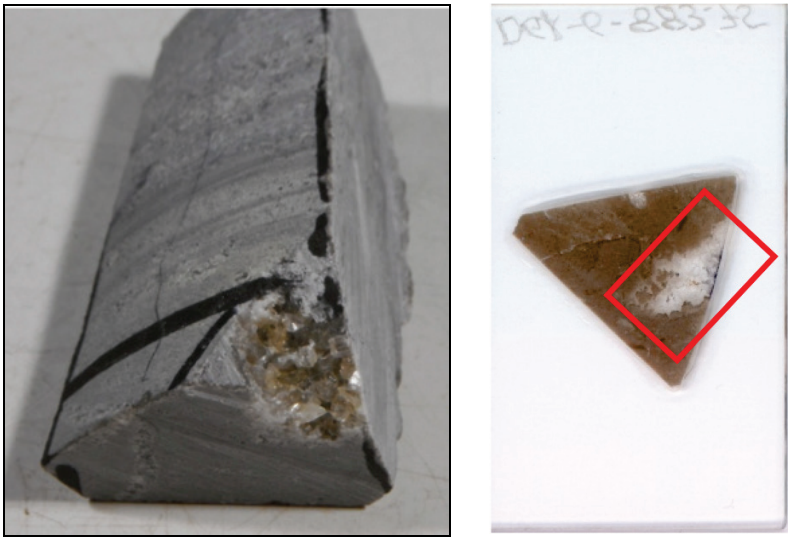


Figure A45. *Left*: Edge of core sample cut out for petrographic section. *Right*: Area of calcite-filled vug cut out for microthermometry. [Macrophotos in reflected light; DGR-6-883.75]

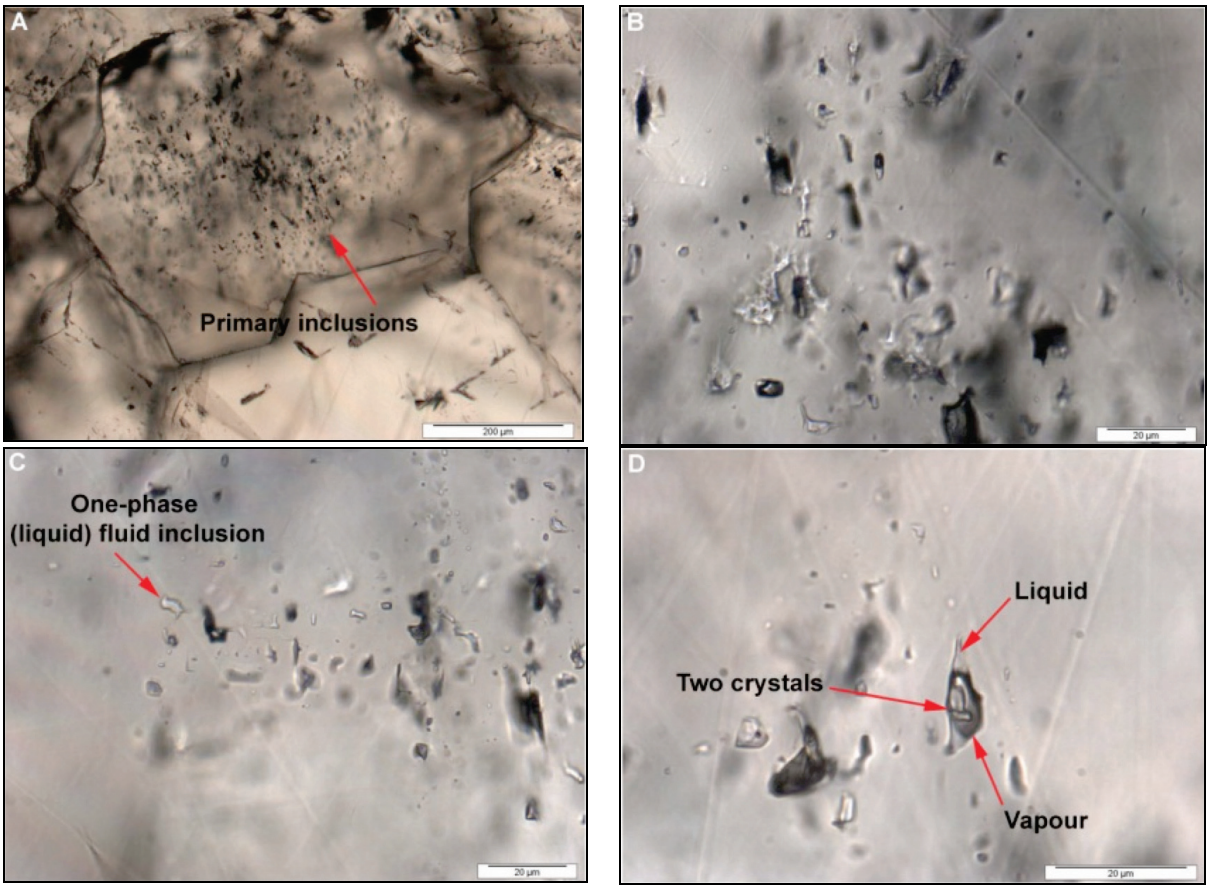


Figure A46. [A] Primary fluid inclusions in vug calcite. [B] Assemblage of primary fluid inclusions with variable content of vapour between 0 vol% and ~85 vol%, indicative of heterogeneous entrapment. [C] Anhedral liquid-only inclusions (metastable state), with ≤8 µm diameter, indicative of homogeneous entrapment [D] Elongated, liquid+vapour primary fluid inclusion with 70% vapour and 30% liquid and with two different crystals, most probably anhydrite (elongated) and possibly halite (rectangular). The crystals are too small and too deep to analyse by Raman spectroscopy. [Transmitted, polarized light; DGR-6-883.75]

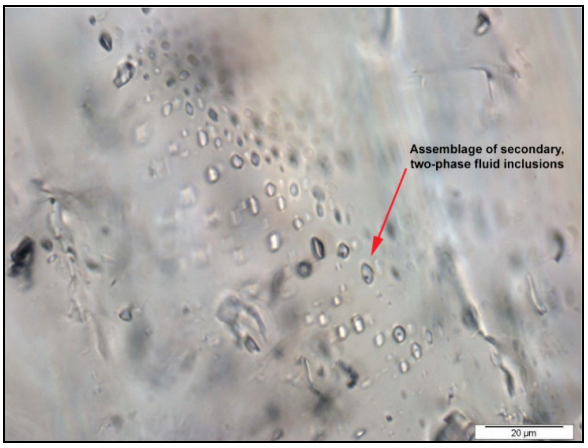


Figure A47. Assemblage of subhedral, equant secondary fluid inclusions uniformly with 5 vol% vapour, indicative of homogeneous entrapment. [Transmitted, polarized light; DGR-6-883.75]

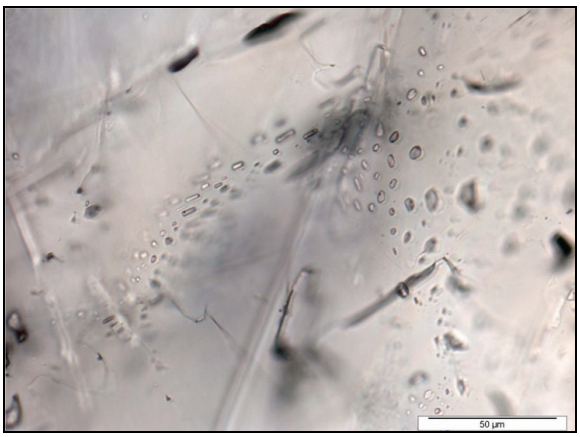


Figure A48. Two healed fractures marked by assemblages of secondary, subhedral, equant fluid inclusions, uniformly containing 5 vol% vapour. [Transmitted, polarized light; DGR-6-883.75]

SAMPLE DGR-6-886.91

Table A10. Paragenetic sequence and interpreted paleofluids in sample DGR-6.886.91. Column 2 lists the figures upon which the paragenetic sequence is based.

Minerals + Fluid Inclusions (phases at room *T*)	Fig. No. in Appendix 1	Vol% vapour	Vol% halite	Time stages → I	II	III	IV	V	VI	VII
				Wall rock	Vug+ Vein	Vug+ Vein	Vug+ Vein	Vug+ Vein	Vug+ Vein	Vug+ Vein
Dolomite matrix	-									
Calcite	A49									
Primary Liq+Vap	A50	Variable: 0-85	0-70							
Secondary Liq+Vap+Hal	A53, A54	Variable: 0-90	0-50							
Late secondary Liq+Vap	A51, A52	Uniform: 5	0-15							
Late secondary metastable-Liq	A53	Uniform: 0	0						?	?

In addition to the features given in Table A10, some of the secondary Liq+Vap inclusions also enclose crystals (Figs. A52-A54). No Raman signal was obtained owing to their small size and great depth within the thick-sections. The optical properties suggest anhydrite.

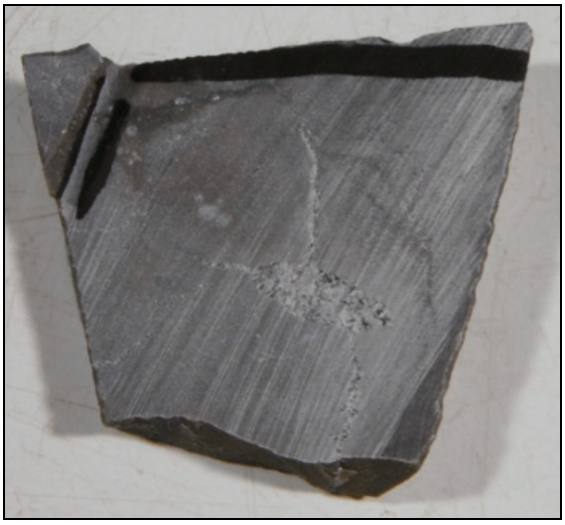




Figure A49. *Left*: Core sample showing area cut out for petrographic section. *Right*: Areas of calcite-filled vug cut out for microthermometry. [Macrophotos in reflected light; DGR-6-886.91]

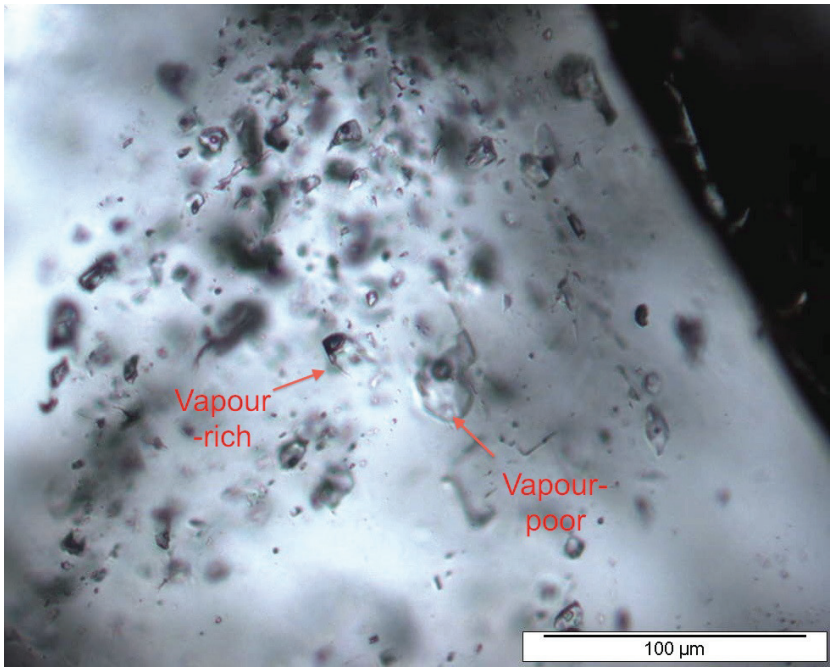


Figure A50. Assemblage of primary, subhedral to anhedral fluid inclusions in vug calcite. The volume fraction of vapour varies from 0% (liquid-only) to 85 vol%, indicating heterogeneous entrapment. [Transmitted, polarized light; DGR-6-886.91]

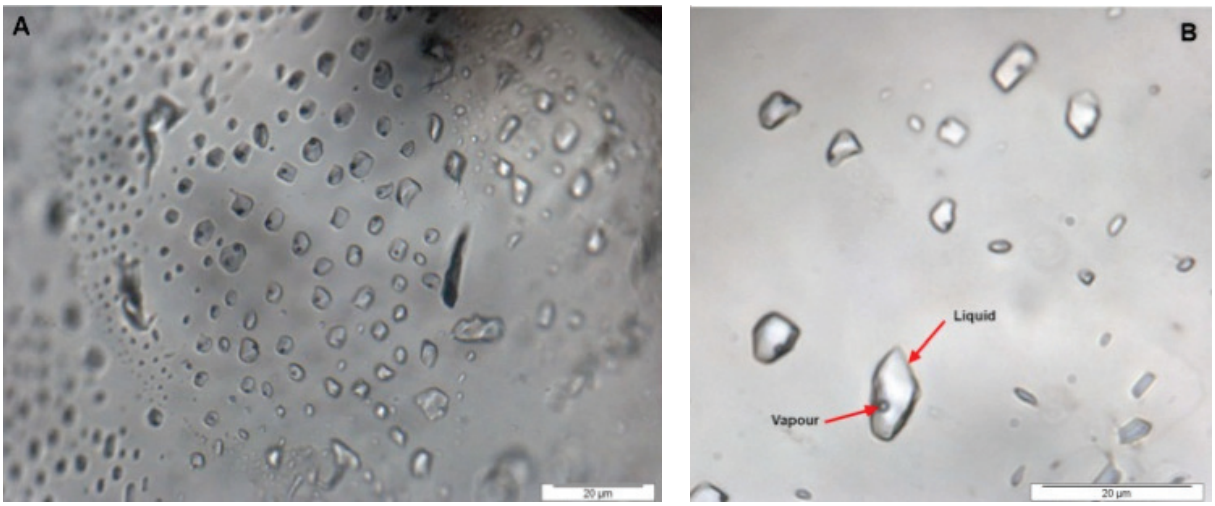


Figure A51. [A] Typical healed fracture containing an assemblage of secondary, liquid+vapour inclusions uniformly with ~5 vol% vapour. This indicates homogeneous entrapment. The inclusions are subhedral and equant (≤16 µm diameter). [B] Detail of [A]. [Transmitted, polarized light; DGR-6-886.91]

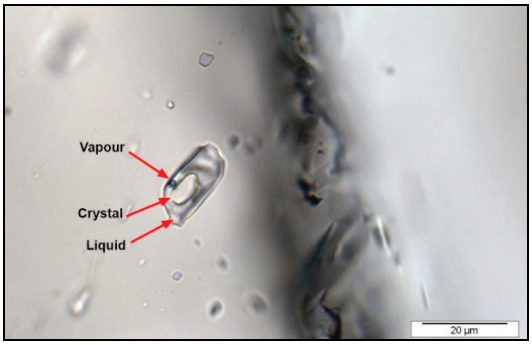


Figure A52. Secondary, subhedral fluid inclusion containing 5 vol% vapour and a transparent, birefringent crystal. This crystal is most likely anhydrite, but the inclusion lies too deep in the sample to obtain a Raman spectrum. [Transmitted, polarized light; DGR-6-886.91]

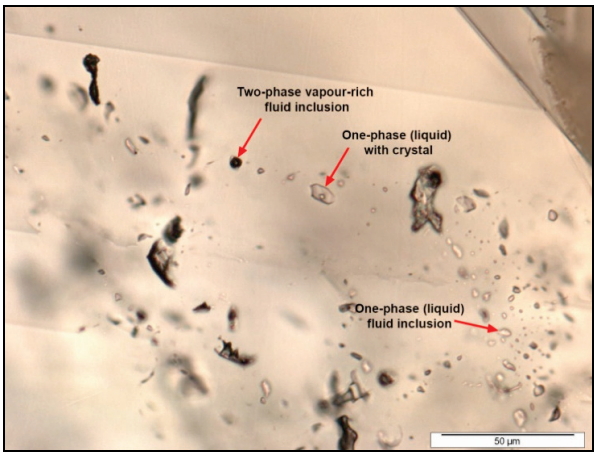


Figure A53. Two assemblages of secondary inclusions in calcite. Top: Subhedral inclusions in which the volume fraction of vapour varies from ~10% to ~90%, indicating heterogeneous entrapment. Bottom right: liquid-only inclusions, indicating homogeneous entrapment [Transmitted, polarized light; DGR-6-886.91]

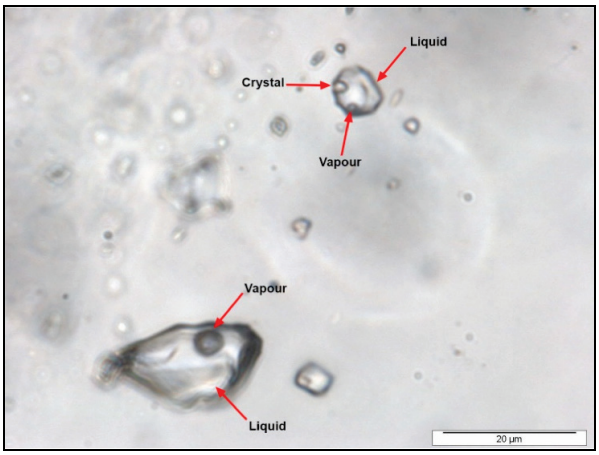


Figure A54. Calcite-hosted assemblage of subhedral, secondary fluid inclusions with variable volume fractions of vapour, indicating heterogeneous entrapment. Some of these inclusions contain a crystal, most probably anhydrite according to optical properties (too deep in section for Raman spectroscopy). [Transmitted, polarized light; DGR-6-886.91]

SAMPLE DGR-6-892.99

Table A11. Paragenetic sequence and interpreted paleofluids in sample DGR-6.892.99. Column 2 lists the figures upon which the paragenetic sequence is based.

Minerals + Fluid Inclusions (phases at room *T*)	Fig. No. in Appendix 1	Vol% vapour	Vol% halite	Time stages → I	II	III	IV	V	VI	VII
				Wall rock	Vug+ Vein	Vug+ Vein	Vug+ Vein	Vug+ Vein	Vug+ Vein	Vug+ Vein
Dolomite matrix	A55, A56									
Calcite	A55, A56									
Primary Liq+Vap ±Hal	A57-A61	Variable: 0-95								
Secondary Liq+Vap ±Hal	A65	Variable: 0-90	0-40							
Late secondary Liq+Vap ±Hal	A62B, A64	Uniform: 10	0-10							
Late secondary metast.-Liq	A62C, A63	Uniform: 0	0						?	?
Late secondary Oil+Vap	A66, A67	Uniform: 10	0						?	?

In addition to the features given in Table A11, some of the primary inclusions also enclose crystals (Figs. A60 and A61). No Raman signal was obtained from the crystals owing to their small size and great depth within the thick-sections. The optical properties suggest halite.

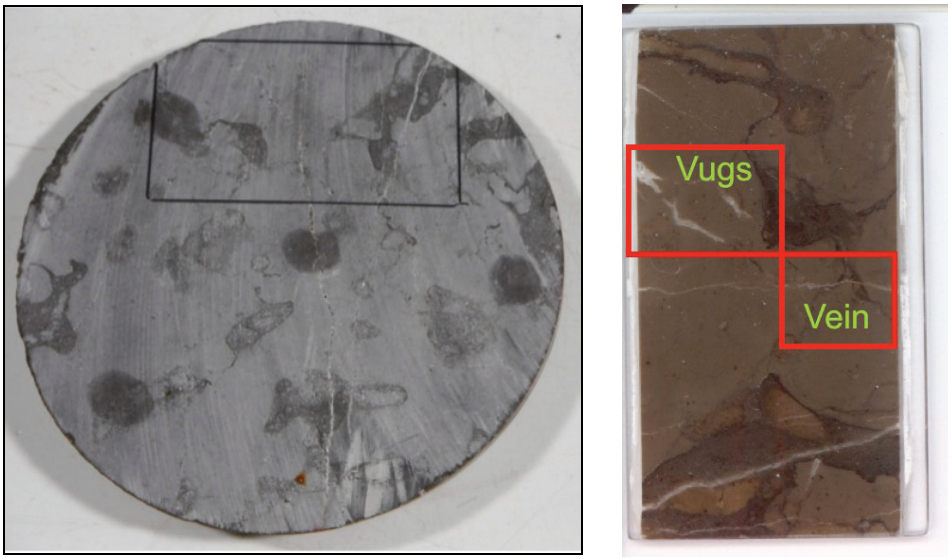


Figure A55. *Left*: Core sample showing area cut for petrographic section. *Right*: Areas of calcite-filled vug cut out for microthermometry. [Macrophotos in reflected light; DGR-6-892.99].

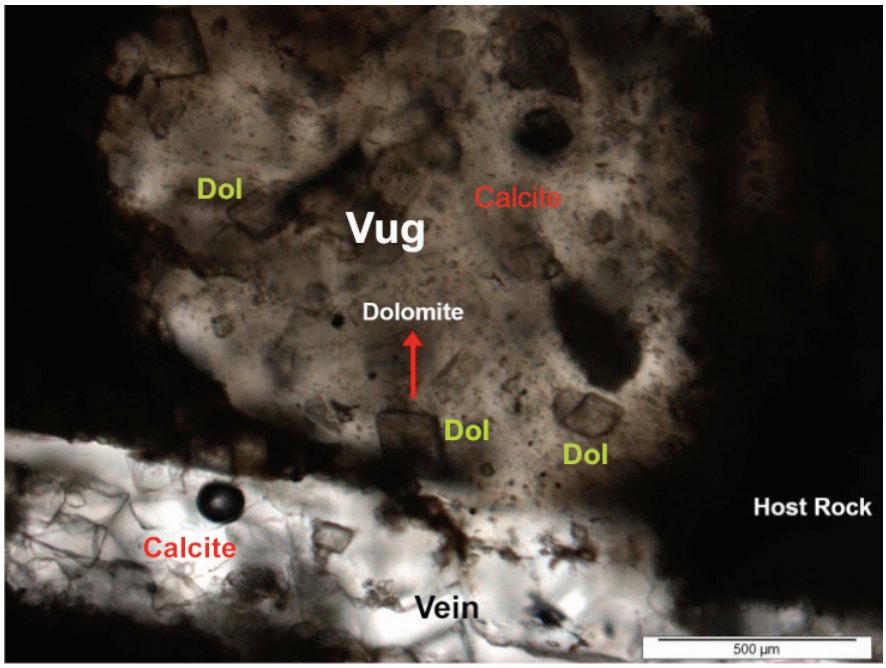


Figure A56. Timing relations between vug and vein. The vug contains small dolomite rhombs cemented by cloudy calcite, rich in fluid and solid inclusions. The vug is cross-cut by a younger vein of clear calcite. The large dark bubble in the vein is an artefact of sample preparation (air bubble trapped in the epoxy). [Transmitted, polarized light; DGR-6-892.99]

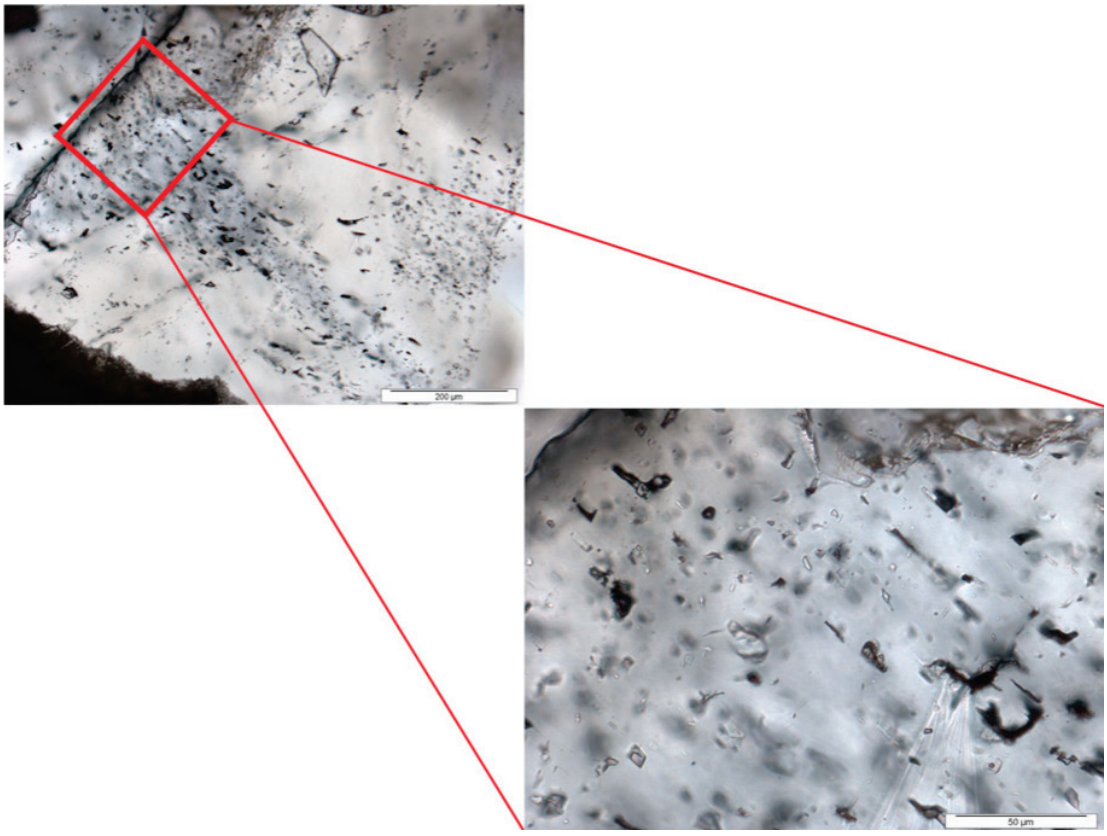


Figure A57. Vug calcite showing three-dimensional clouds of sub- to anhedral fluid inclusions, many of which are elongated parallel to the growth direction of the host crystal. This well-known texture demonstrates that the inclusions are primary, having been captured during growth of the host calcite crystal. The inclusions consist of vapour (almost opaque in this view) and liquid (clear). The volume fraction of vapour varies from ~0 (all liquid) to ~90%, indicating heterogeneous entrapment. [Transmitted, polarized light; DGR-6-892.99]

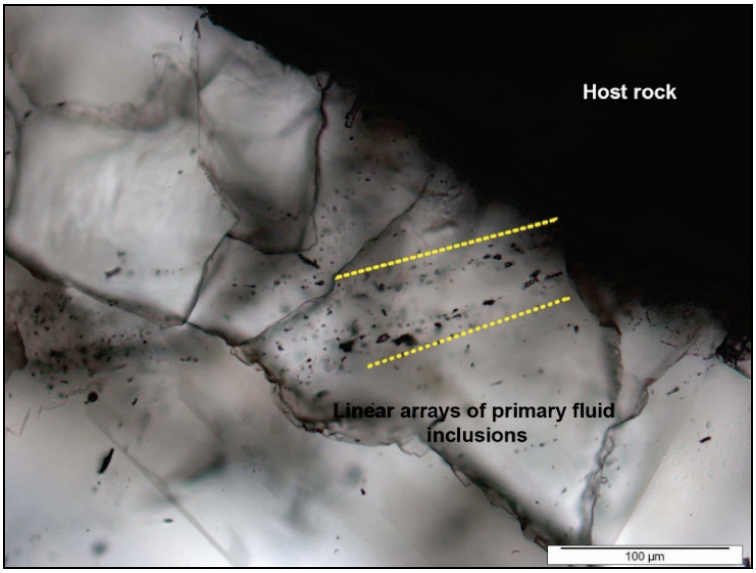


Figure A58. Linear arrays of fluid inclusions lying parallel to the growth direction of calcite within a vein. The arrays do not describe planar features but rather are distributed in three dimensions. This well-known texture demonstrates that the inclusions are primary, having been captured during growth of the host calcite. [Transmitted, polarized light; DGR-6-892.99]

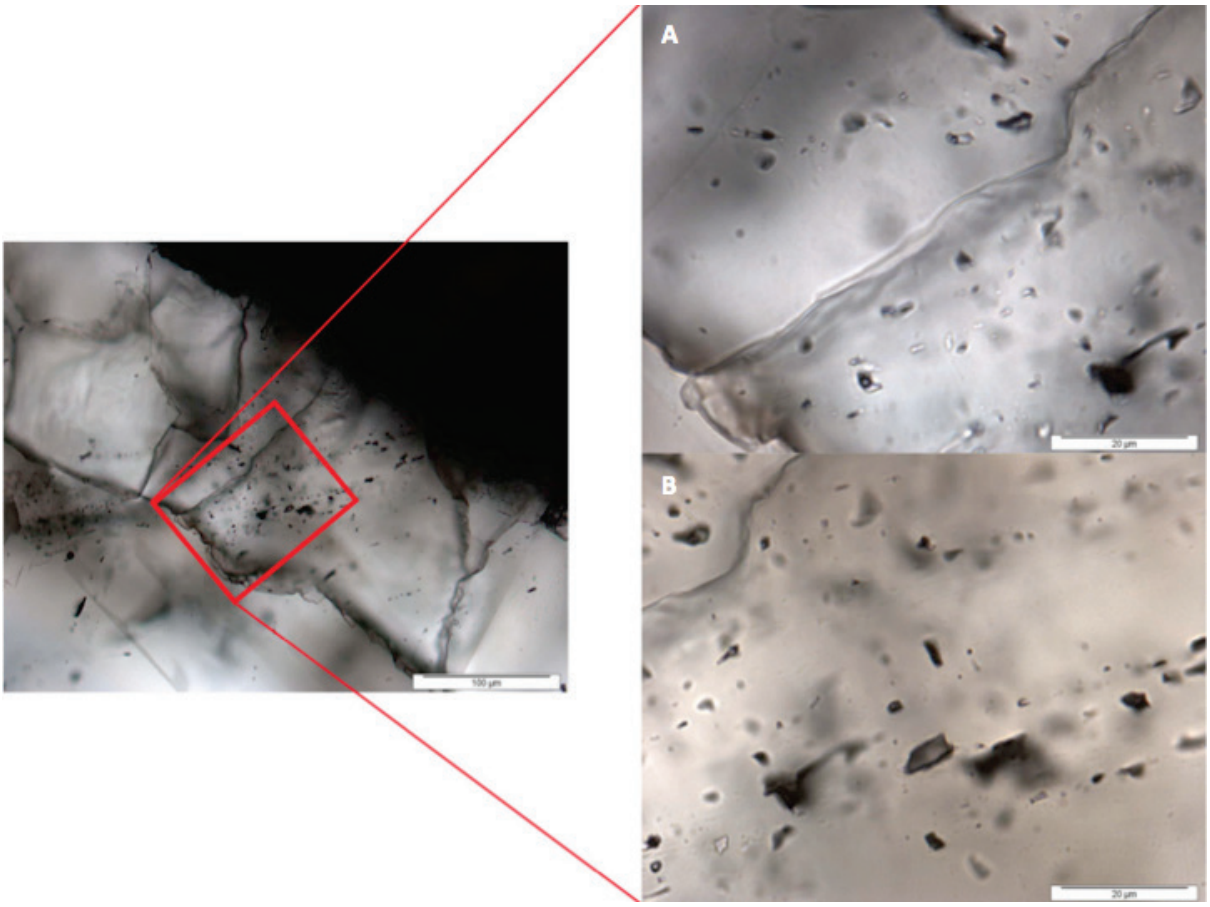


Figure A59. Close-up of Fig. A58. [A] and [B]: Assemblages of primary, anhedral fluid inclusions in vein calcite. The volume fraction of vapour varies from 0% to ~95%, indicating heterogeneous entrapment. [Transmitted, polarized light; DGR-6-892.99]

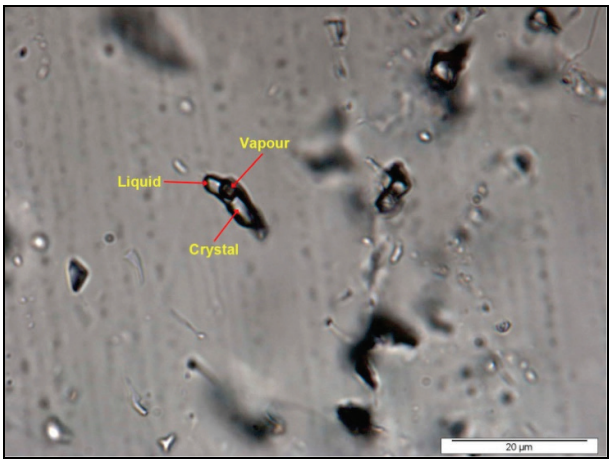


Figure A60. Elongated primary fluid inclusion (12 µm diameter) in calcite, containing ~25 vol% vapour. A small crystal is visible within the inclusion but it so far it has not been identified. [Transmitted, polarized light; DGR-6-892.99]

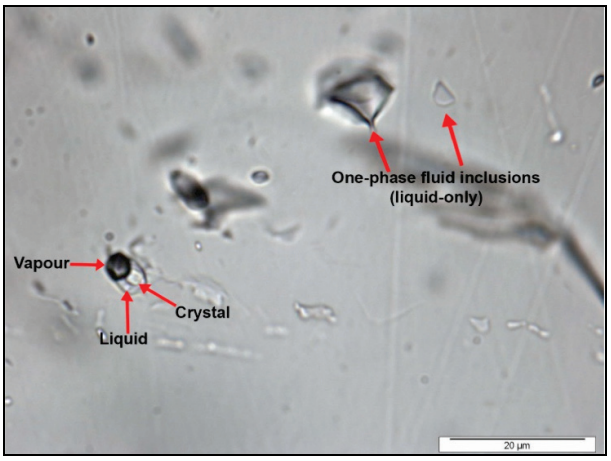


Figure A61. Detail of same assemblage as in Fig. A58, showing primary, anhedral fluid inclusions in vug calcite. Liquid-only as well as liquid+vapour inclusions are present. Some inclusions also contain transparent crystals, but they have not yet been identified. [Transmitted, polarized light; DGR-6-892.99]

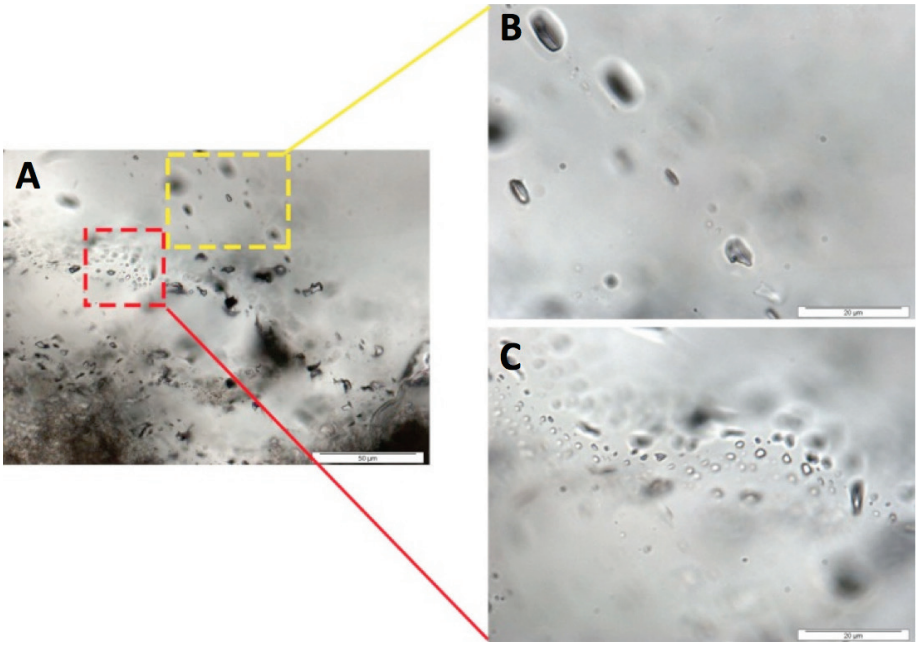


Figure A62. [A] Two healed, hairline fractures with different orientations in calcite. The fractures themselves are invisible but their traces are defined by arrays of secondary fluid inclusions with contrasting elongations. [B] Assemblage of elongated, liquid+vapour fluid inclusions with uniform volume fractions of vapour (~10%), indicating homogeneous entrapment. [C] Assemblage of metastable liquid-only inclusions, also indicating homogeneous entrapment. [Transmitted, polarized light; DGR-6-892.99]

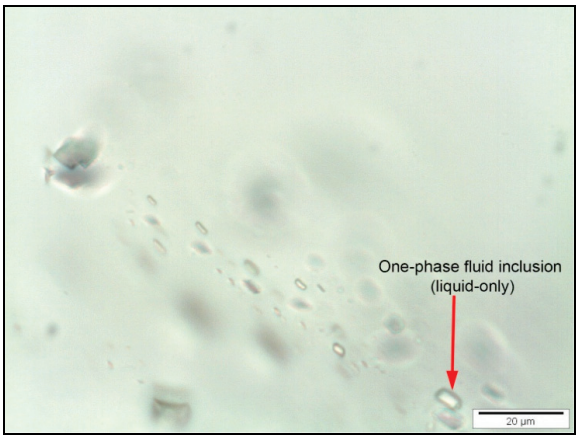


Figure A63. Assemblage of secondary, euhedral, metastable liquid-only inclusions in healed fractures in calcite. The lack of vapour in all the inclusions within the assemblage indicates homogeneous entrapment below 70 °C. [Transmitted, polarized light; DGR-6-892.99]

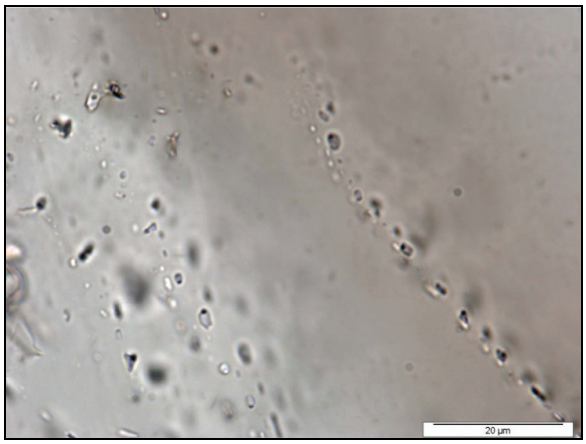


Figure A64. Assemblages of secondary subhedral, equant fluid inclusions in healed fractures in calcite. The volume fraction of vapour at room temperature is uniform within each assemblage at ~10%. [Transmitted, polarized light; DGR-6-892.99]

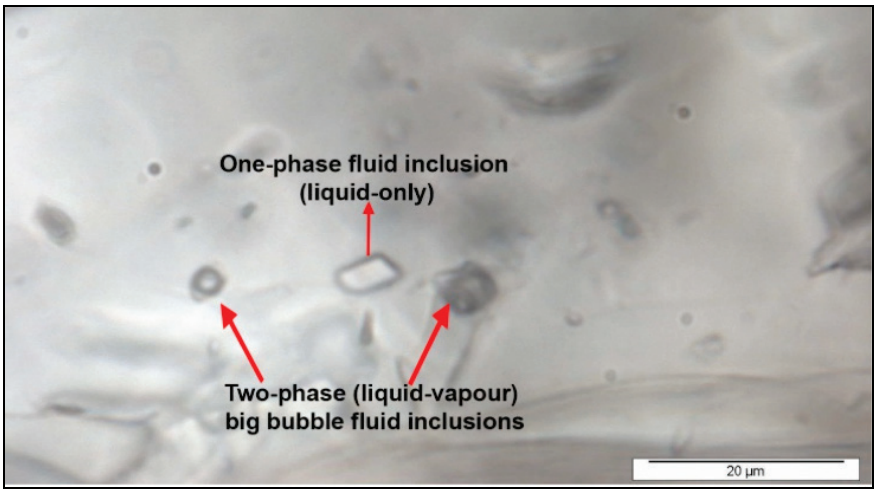


Figure A65. Assemblage of secondary, subhedral fluid inclusions in calcite. The volume fraction of vapour varies from 0% to ~90%, indicating heterogeneous entrapment. [Transmitted, polarized light; DGR-6-892.99]

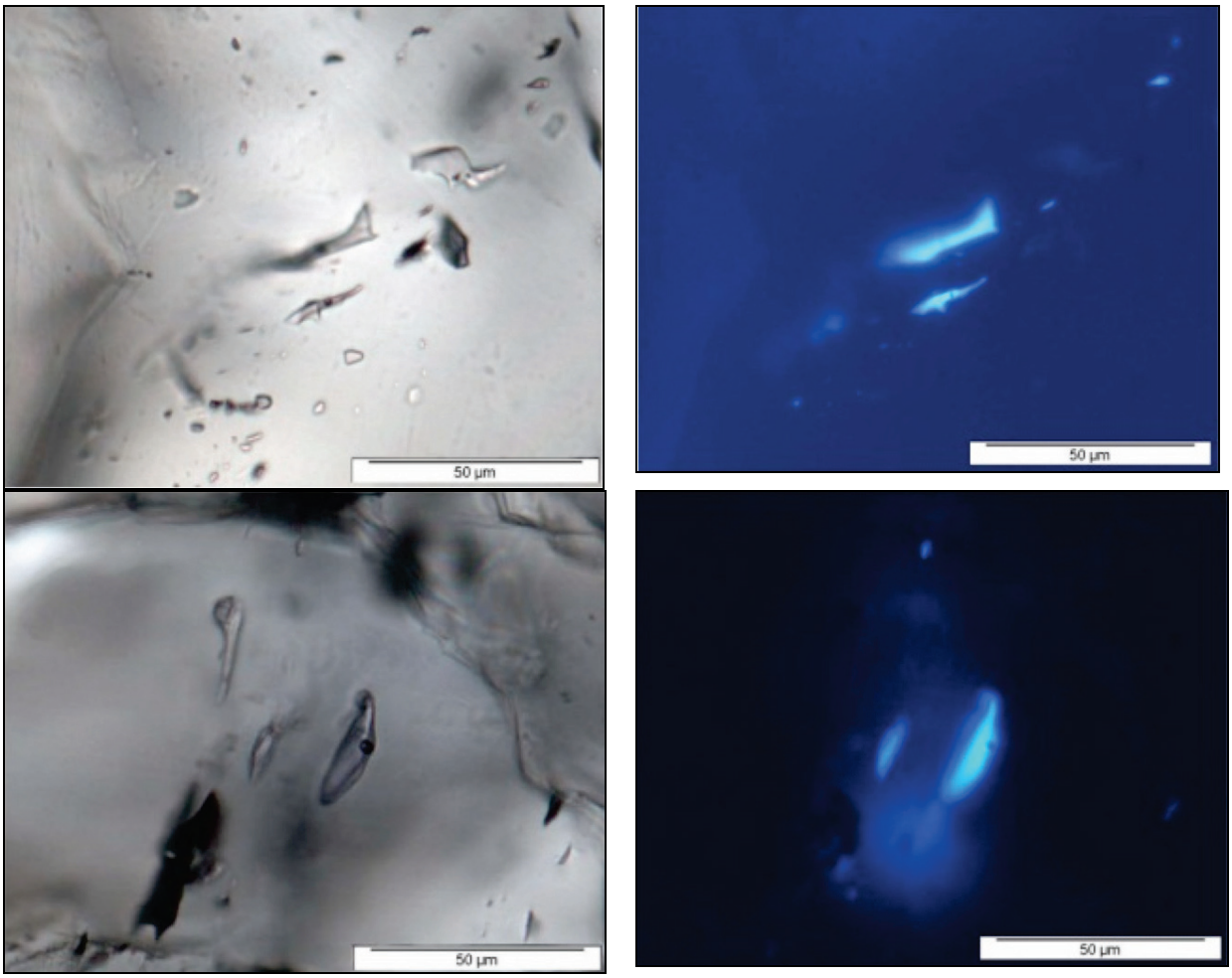


Figure A66. Assemblages of secondary hydrocarbon inclusions in healed fractures within calcite. At room temperature the vapour fraction is uniform at ~10 vol%. The liquid portion of the inclusions is rich in aromatic hydrocarbons, as indicated by the bluish-white UV fluorescence colour. The vapour bubbles are non-fluorescent, and presumably consist dominantly of methane. [*Left*: transmitted, polarized light; *Right*: UV epi-illumination; DGR-6-892.99].

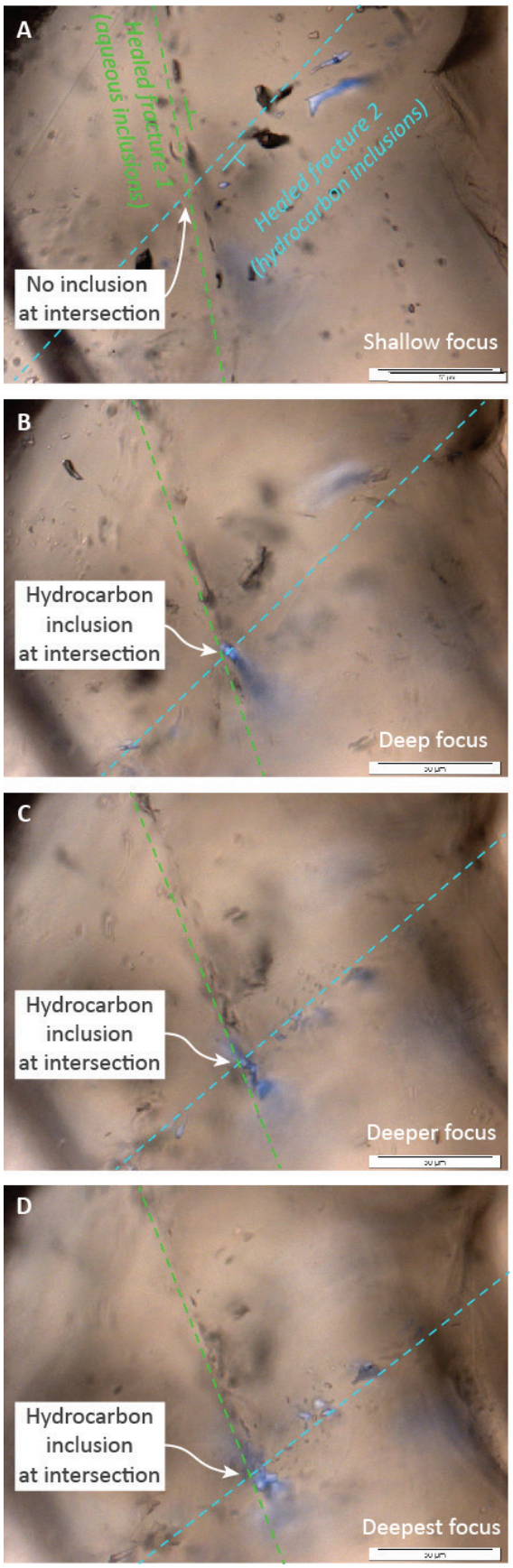


Figure A67. Interpretation of relative timing of secondary fluid inclusion generations in sample DGR-6-892.99 [simultaneous transmitted and UV epi-illumination]. For principle of method, see Fig. 1.

Traces of two healed fractures are visible, each marked by secondary fluid inclusions. *Green:* aqueous liquid+vapour inclusions with ~10 vol% vapour, within a fracture trace that strikes NNW-SSE and dips steeply to NNE. *Blue:* bluish fluorescent hydrocarbon inclusions in a fracture trace that strikes NE-SW and dips shallowly to SE.

[A] *Shallow focus level:* No inclusion is present at the intersection of the fracture traces, thus the relative ages of the fluid generations are ambiguous.

[B-D] *Deeper focus levels:* A hydrocarbon inclusion is present at the intersection of the fracture traces in each image, indicating that the hydrocarbon inclusions and their host fracture are younger than the aqueous inclusions and their corresponding host fracture.

SAMPLE DGR-4-818.36

Table A12. Paragenetic sequence and interpreted paleofluids in sample DGR-4-818.36. Column 2 lists the figures upon which the paragenetic sequence is based.

Minerals + Fluid Inclusions (phases at room *T*)	Fig. No. in Appendix 1	Vol% vapour	Vol% halite	Time stages → I	II	III	IV	V	VI	VII
				Wall rock	Vug+ Vein	Vug+ Vein	Vug+ Vein	Vug+ Vein	Vug+ Vein	Vug+ Vein
Dolomite matrix	A68, A69, A72									
Pyrite	A69									
Primary, unknown phases	A69									
Calcite	A68, A69, A72									
Primary Liq+Vap ±Hal	A74A,B	Variable: 0-90								
Early secondary Liq+Vap ±Hal	A71	Variable: 10-90	0-20							
Late secondary Liq+Vap ±Hal	A74C, A75	Uniform: 10	0-50							
Late secondary metast.-Liq	A70, A77	Uniform: 0	0						?	?
Late secondary Oil+Vap	A72, A73, A76	Variable: 5-80	0						?	?



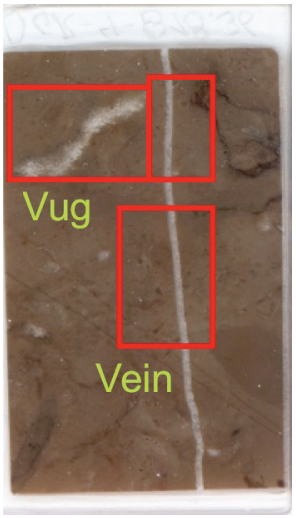


Figure A68. *Left*: Core sample showing area cut out for petrographic section. *Right*: Areas of calcite-filled vug cut out for microthermometry. [Macrophotos in reflected light; DGR-4-818.36]

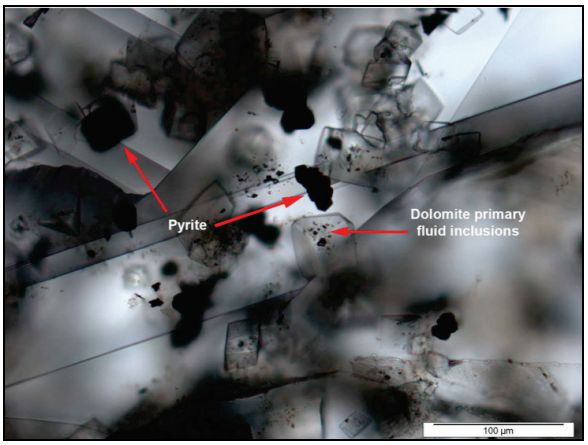


Figure A69. Vug containing pyrite crystals (opaque) and dolomite rhombs all enclosed by later, clear calcite. The dolomite crystals contain abundant primary fluid inclusions but they are too small to identify their phase contents [Transmitted, polarized light; DGR-4-818.36]

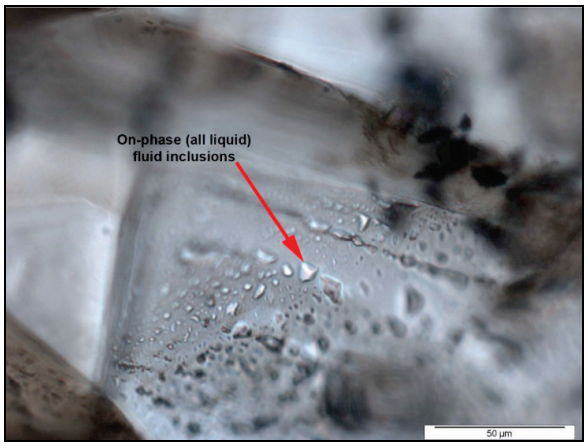


Figure A70. Assemblage of secondary, liquid-only inclusions, lying within a healed fracture in calcite. These inclusions correspond to a metastable state (stretched liquid). [Transmitted, polarized light; DGR-4-818.36]

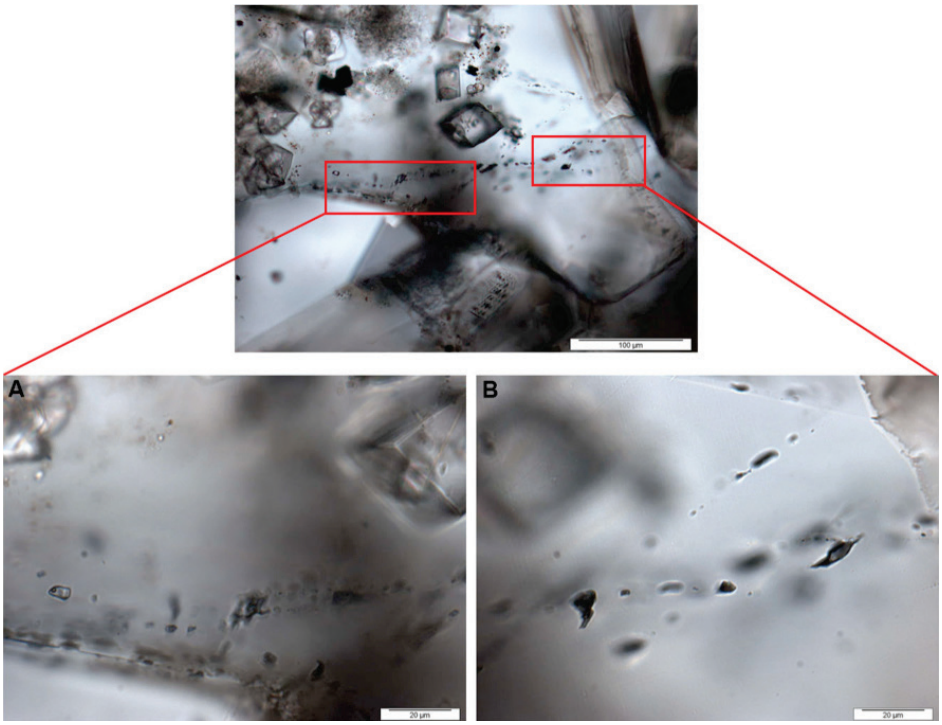


Figure A71. Secondary fluid inclusions in calcite. [A] Subhedral liquid+vapour inclusion with about 10 vol% vapour. [B] Secondary, anhedral, vapour-rich inclusion. [Transmitted, polarized light; DGR-4-818.36]

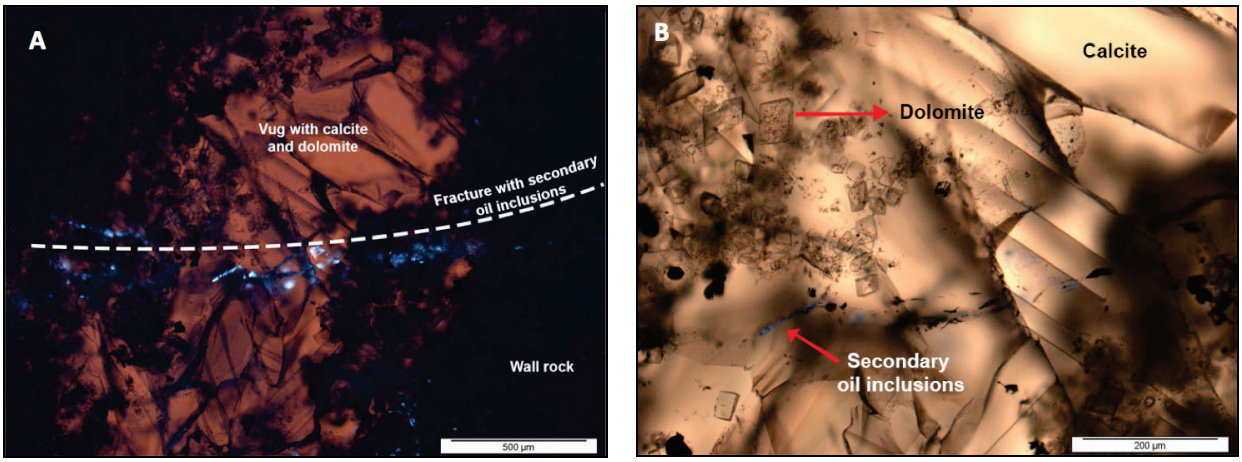


Figure A72. [A] Relation between the calcite-filled vug and the healed fracture containing secondary oil inclusions. The oil inclusions fluoresce bluish white in UV epi-illumination. [B] Detail of image A in simultaneous UV and transmitted light, showing that the fracture cross-cuts the calcite crystals. [DGR-4-818.36]

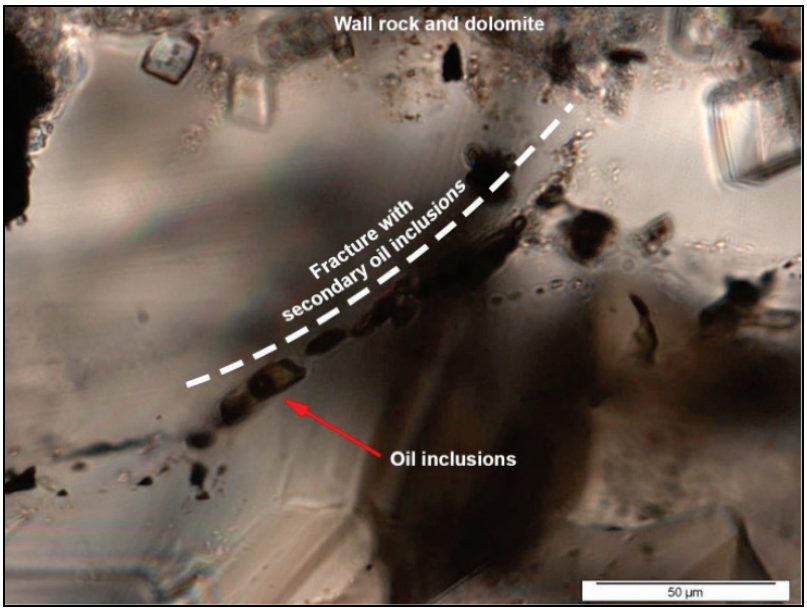
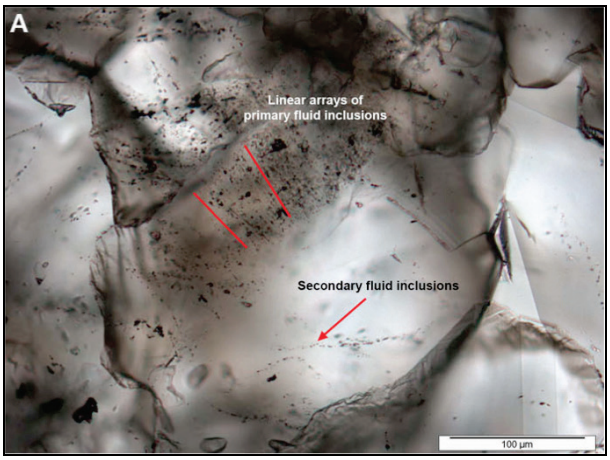
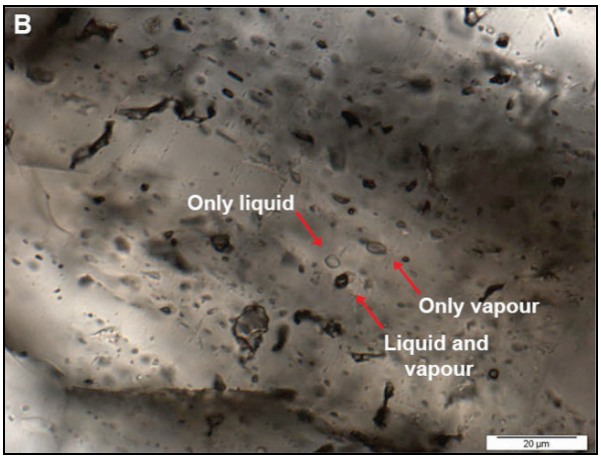


Figure A73. Euhedral, secondary oil inclusions at room temperature with ~33 vol% vapour and a diameter of ≤23 µm. The liquid portion has a distinct brownish tinge. [Transmitted, polarized light; DGR-4-818.36]





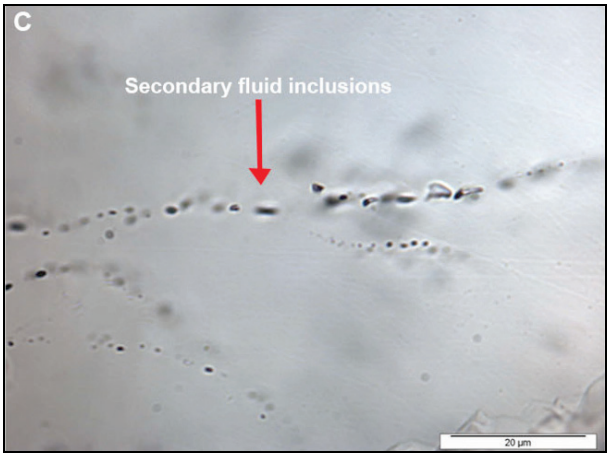


Figure A74.
[A] Vein calcite with linear arrays of primary fluid inclusions distributed in three dimensions, radiating out from an inclusion-free crystal core.
[B] Detail of the primary, anhedral fluid inclusions, showing variable fractions of vapour from 0% to 90%, indicating heterogeneous entrapment.
[C] Assemblage of secondary fluid inclusions arrayed within a healed fracture, all of which uniformly contain 10 vol% vapour.
[Transmitted, polarized light**;** DGR-4-818.36]

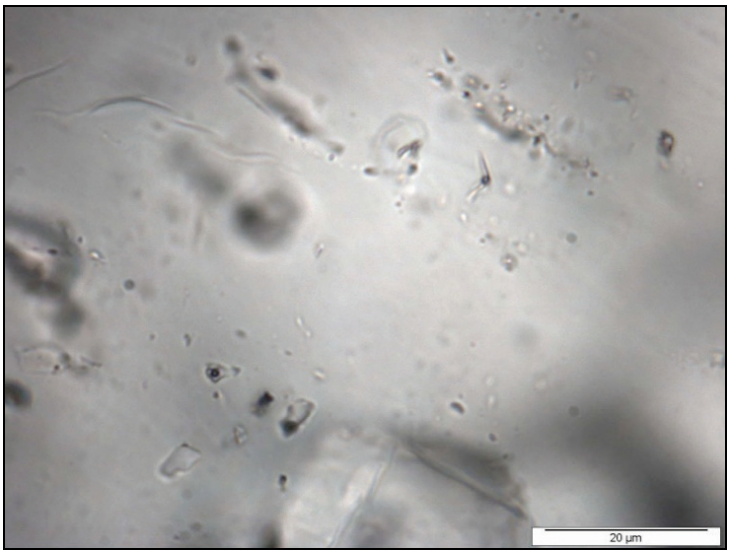


Figure A75. Assemblage of secondary, anhedral, liquid+vapour, fluid inclusions all with ~10 vol% vapour. The uniform phase proportions indicates homogeneous entrapment. [Transmitted, polarized light; DGR-4-818.36]

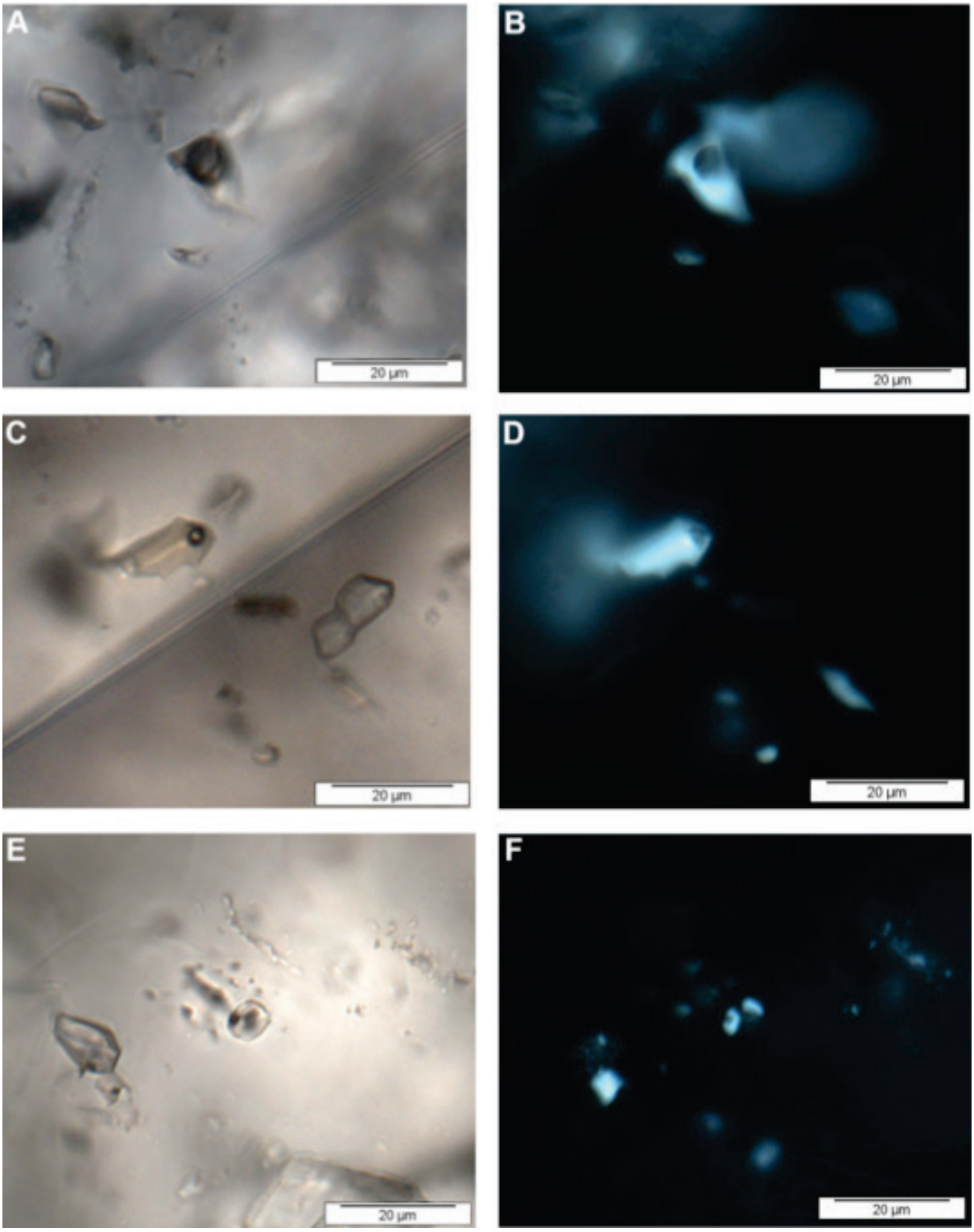


Figure A76. Secondary oil inclusions in healed fractures in calcite. At room temperature the volume fractions of vapour are highly variable, compare [A], [B] and [C]. [Transmitted, polarized light]. [B], [D] and [F] correspond to the same images of [A], [B] and [C] but under UV epi-illumination, showing bluish-white fluorescence of aromatic hydrocarbons. [DGR-4-818.36]

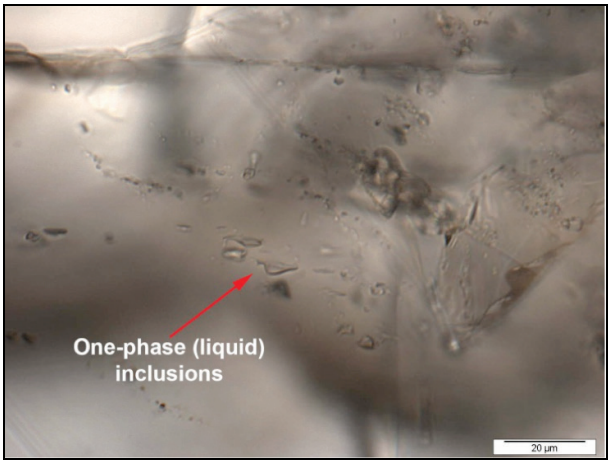


Figure A77. Assemblage of secondary, anhedral, liquid-only inclusions in calcite. [Transmitted, polarized light; DGR-4-818.36]

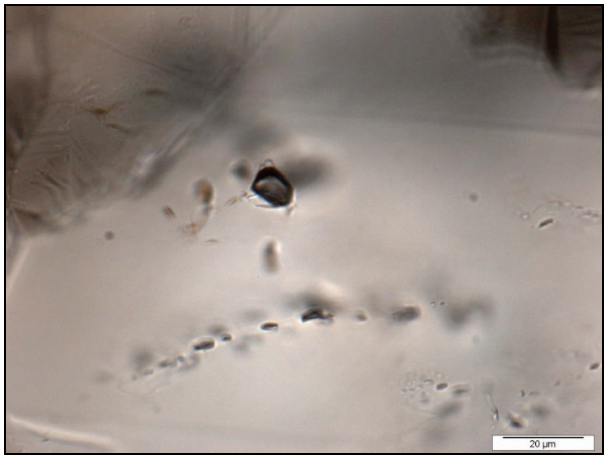


Figure A78. Primary fluid inclusion in calcite with a big vapour bubble of methane, identified by Raman spectroscopy. [Transmitted, polarized light; DGR-4-818.36]

SAMPLE DGR-4-829.53

Table A13. Paragenetic sequence and interpreted paleofluids in sample DGR-4-829.53. Column 2 lists the figures upon which the paragenetic sequence is based.

Minerals + Fluid Inclusions (phases at room *T*)	Fig. No. in Appendix 1	Vol% vapour	Vol% halite	Time stages → I	II	III	IV	V	VI	VII
				Wall rock	Vug+ Vein	Vug+ Vein	Vug+ Vein	Vug+ Vein	Vug+ Vein	Vug+ Vein
Dolomite matrix	A79									
Pyrite	-									
Dolomite (saddle habit)	A79									
Anhydrite	A79									
Primary Liq+Vap ±Hal	A80	Variable: 0-40	0-20							
Primary Liq+Vap ±Hal	A81	Variable: 0-90	0-30							
Secondary Liq+Vap ±Hal	A82	Uniform: 80	0							
Late secondary Liq+Vap ±Hal	A83	Variable: 0-85	0							
Late secondary Oil+Vap	A84, A85	Variable: 5-30	0						?	?

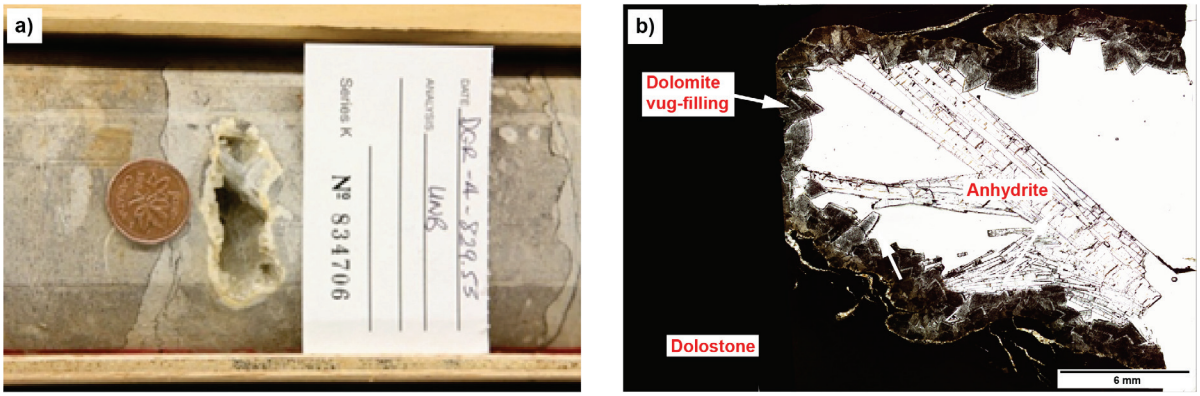


Figure A79. **a)** Photograph of core sample. **b)** Transmitted, polarized light microphotograph of a dolomite-anhydrite vug cut for microthermometry. The walls of the vug are lined with euhedral dolomite crystals which are overgrown by fibrous anhydrite, thus postdating the dolomite [DGR-4-829.53].

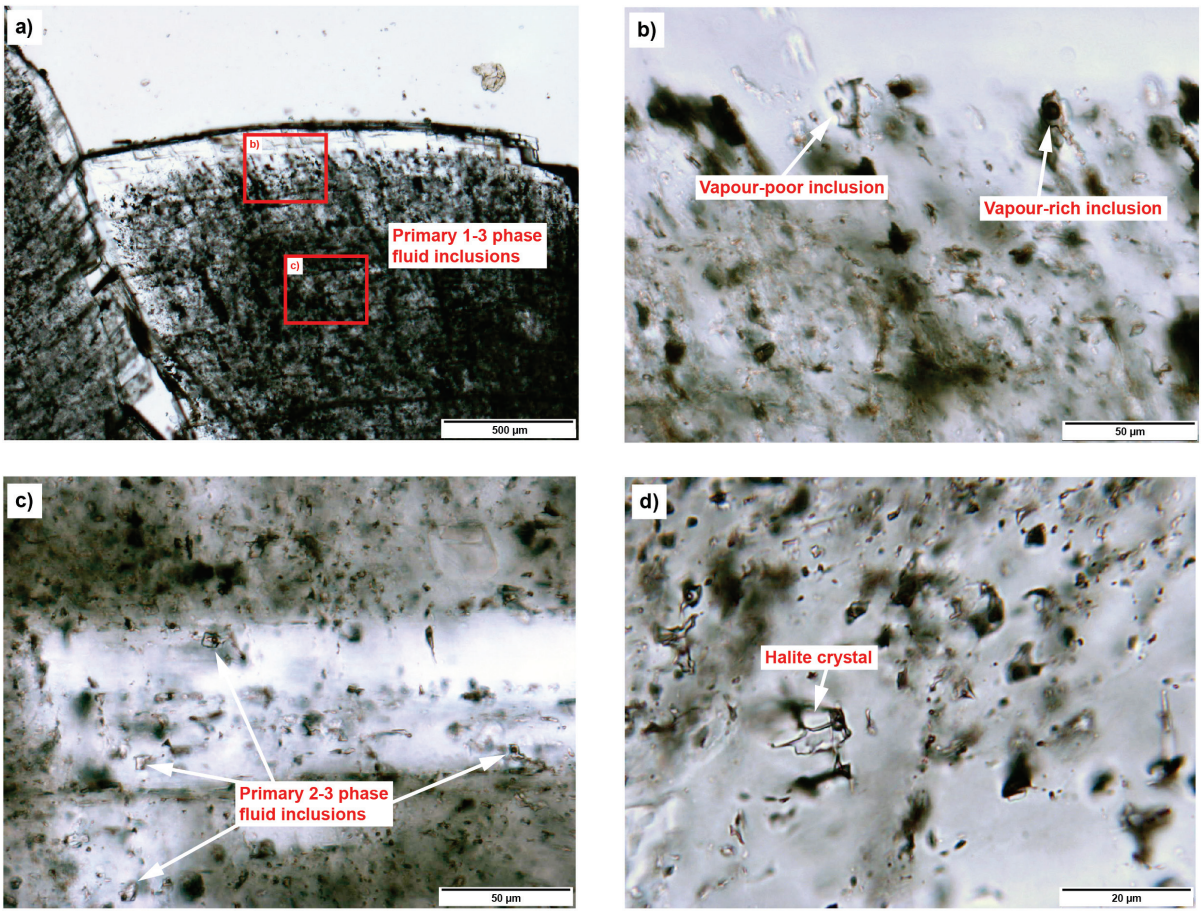


Figure A80. **a)** The euhedral dolomite crystals lining the walls of the vug commonly show a large inclusion rich-core, which is borderer by a slim, inclusion-free outer rim. **b)** The variable phase proportions of the primary inclusions within the inclusion-rich dolomite cores indicate heterogeneous entrapment. The vapour bubbles contain methane and carbon dioxide (identified by Raman-spectroscopy) **c)** Within the inclusion-rich dolomite cores distinct growth zones can be recognized (characterized by lower amounts of fluid inclusions). **d)** Several inclusions contain variable-sized halite crystals [Microphotographs in transmitted, polarized light; DGR-4-829.53].

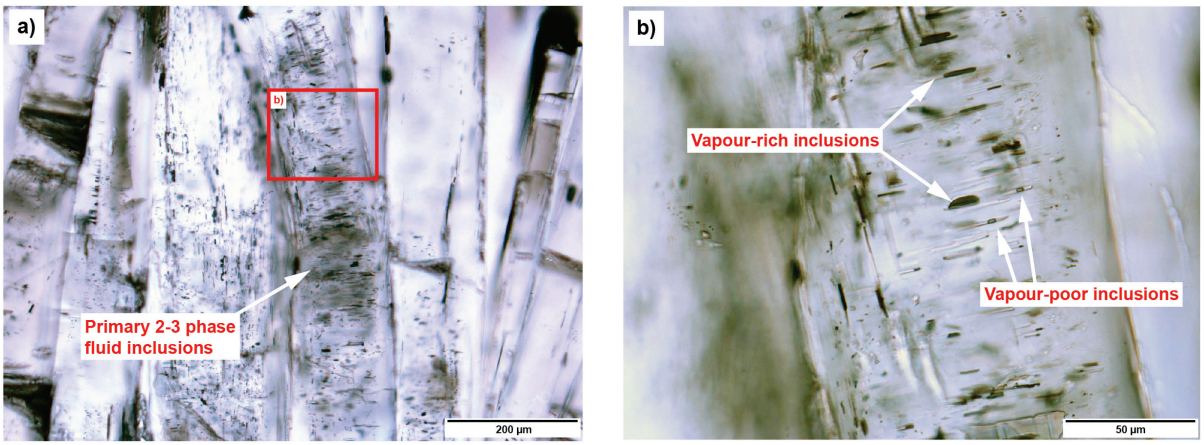


Figure A81. a) Primary inclusions within the fibrous anhydrite. **b)** The variable phase proportions of the primary inclusions indicate heterogeneous entrapment. **c)** Several inclusions contain variable-sized halite cubes [Microphotographs in transmitted, polarized light; DGR-4-829.53].

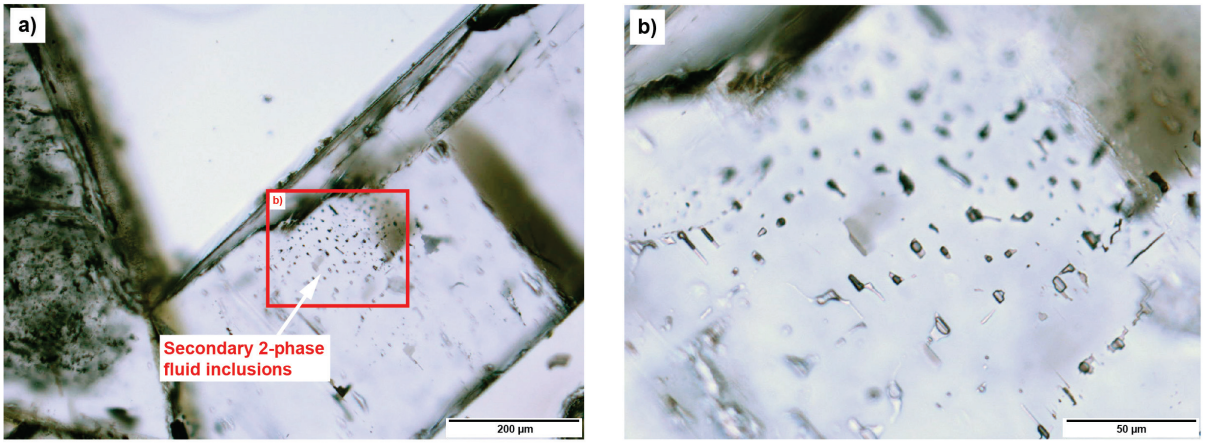


Figure A82. a) Planar array of secondary, liquid+vapour inclusions on a healed fracture within vug anhydrite. **b)** The inclusions show uniform phase proportions (~80 vol% vapour), indicative of homogeneous entrapment [Microphotographs in transmitted, polarized light; DGR-4-829.53].

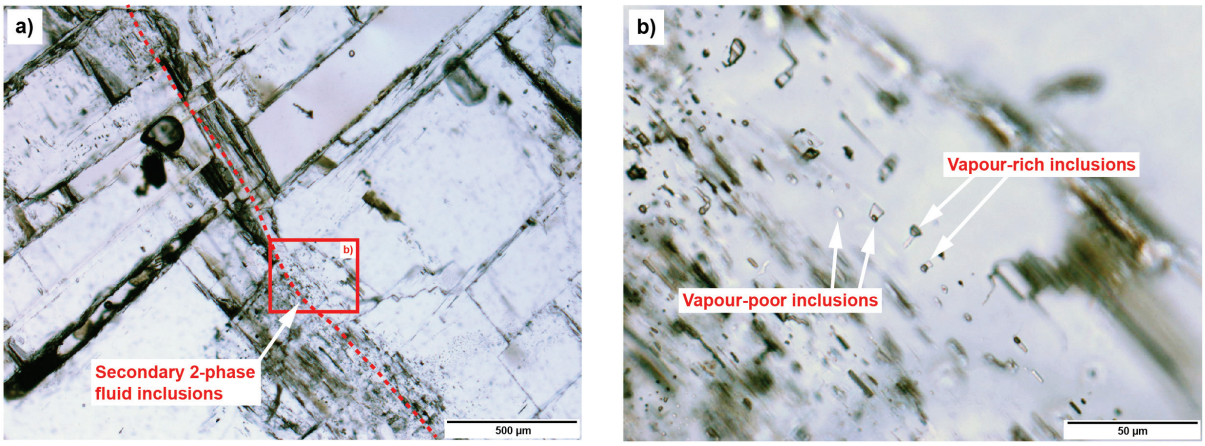


Figure A83. a) Planar array of secondary, liquid+vapour inclusions on a healed fracture within vug anhydrite. **b)** The inclusions show variable phase proportions, indicative of heterogeneous entrapment [Microphotographs in transmitted, polarized light; DGR-4-829.53].

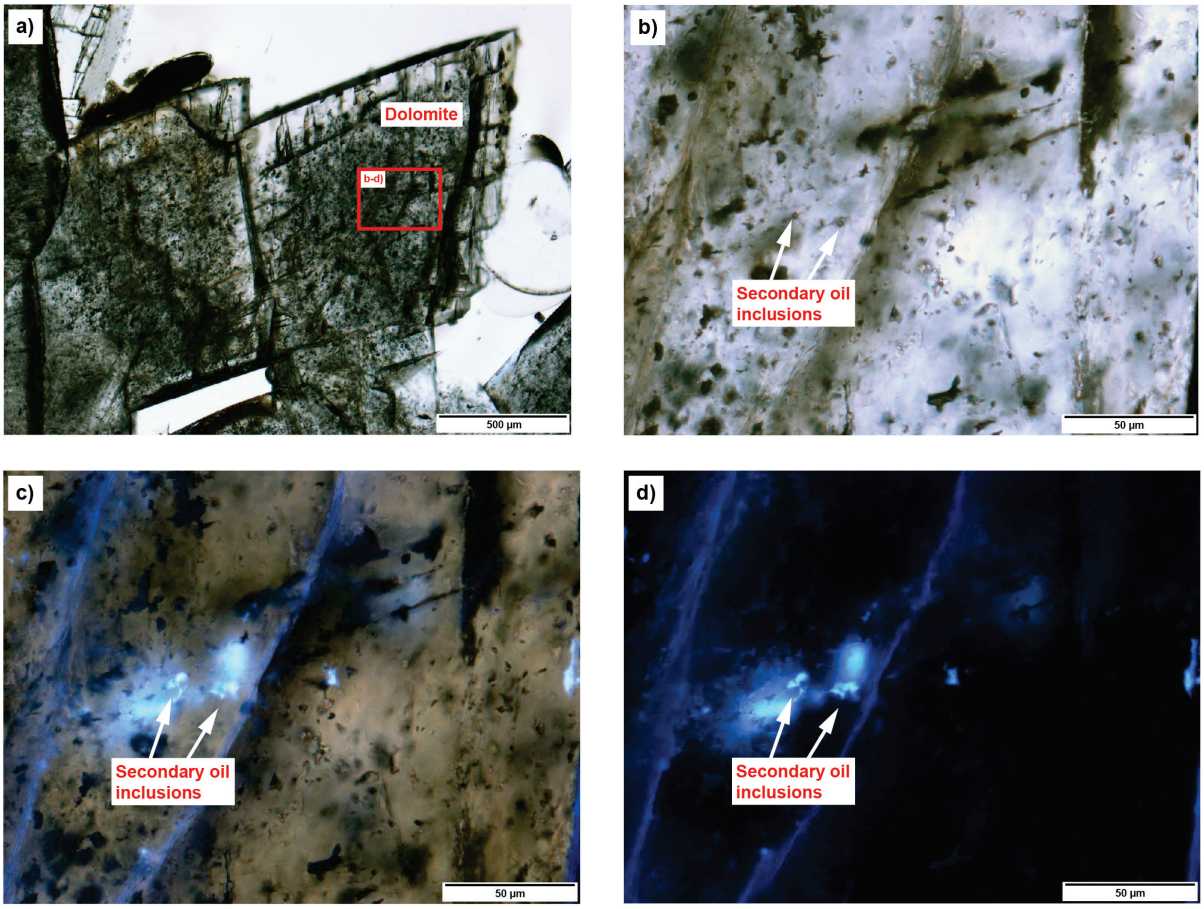


Figure A84. a,b) Healed fracture in dolomite containing secondary oil inclusions. **c)** Fluorescence of the oil inclusions in simultaneous transmitted and UV epi-illumination. **d)** Bluish-white UV fluorescence colour of the aromatic hydrocarbons [DGR-2-778.44].

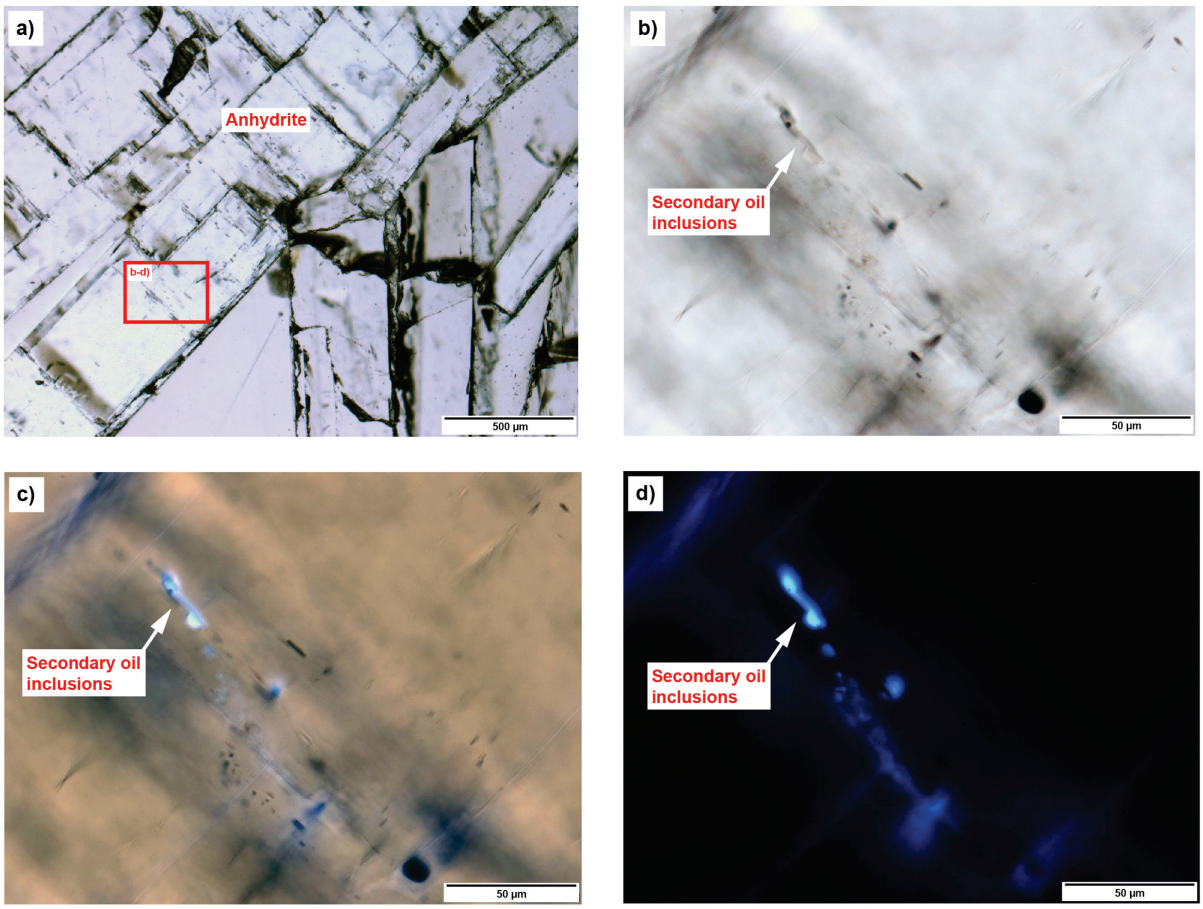


Figure A85. a,b) Healed fracture in anhydrite containing secondary oil inclusions. **c)** Fluorescence of the oil inclusions in simultaneous transmitted and UV epi-illumination. **d)** Bluish-white UV fluorescence colour of the aromatic hydrocarbons in the liquid portion of the inclusion. The vapour bubble is non-fluorescing and presumably contains dominantly methane [DGR-2-778.44].

SAMPLE DGR-2-844.31

Table A14. Paragenetic sequence and interpreted paleofluids in sample DGR-2-844.31. Column 2 lists the figures upon which the paragenetic sequence is based.

Minerals + Fluid Inclusions (phases at room *T*)	Fig. No. in Appendix 1	Vol% vapour	Vol% halite	Time stages → I Wall rock	II Vug+ Vein	III Vug+ Vein	IV Vug+ Vein	V Vug+ Vein	VI Vug+ Vein	VII Vug+ Vein
Dolomite matrix	A86									
Pyrite	-									
Dolomite (rhombic habit)	A86									
Calcite	A86									
Primary Liq+Vap ±Hal	A87	Variable: 0-15	0-40							
Early secondary Liq+Vap±Hal	A88	Variable: 0-70	0-35							
Late secondary Liq+Vap±Hal	A89	Uniform: 5	0-70							
Secondary metastable-Liq	A90	Uniform: 0	0						?	?
Late secondary Oil+Vap	A91	Variable: 0-70	0						?	?

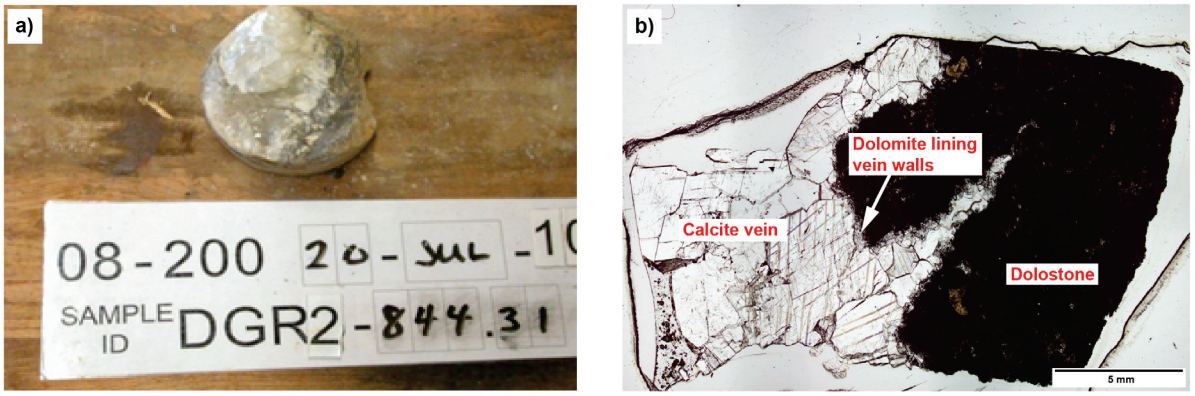
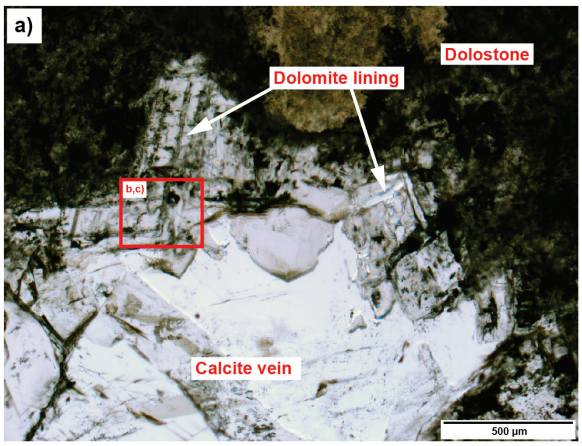
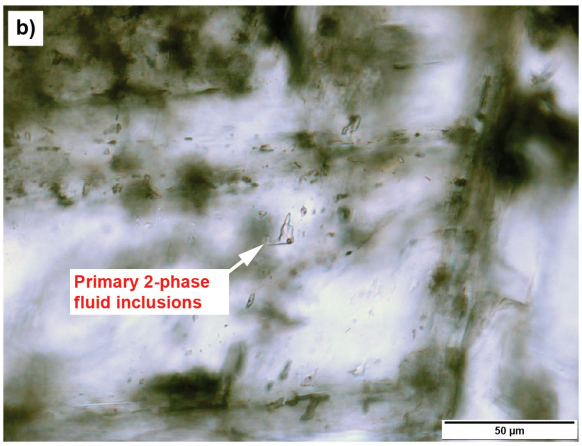


Figure A86. **a)** Photograph of core sample. **b)** Transmitted, polarized light microphotograph of calcite vein cut for microthermometry. The walls of the vein are lined with euhedral dolomite crystals which are overgrown by the calcite [DGR-4-829.53].





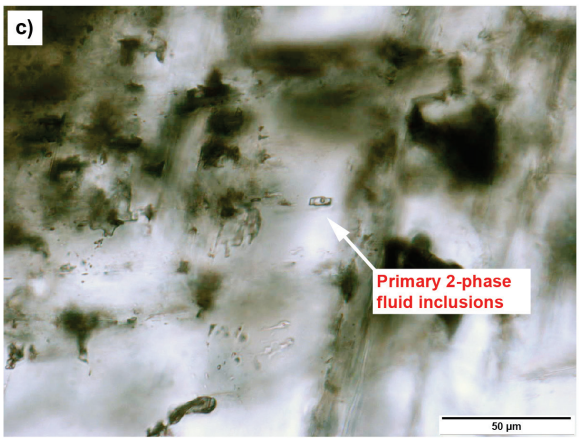


Figure A87. **a)** Paragenetic relationship between dolomitic rock matrix, dolomite lining the walls of the vein and the calcite vein infill. **b,c)** The phase proportions of primary inclusions in dolomite vary range from 0-15 vol% vapour, thus indicating heterogeneous entrapment. No primary inclusions were found in the calcite vein infill [Microphotographs in transmitted, polarized light; DGR-2-844.31].

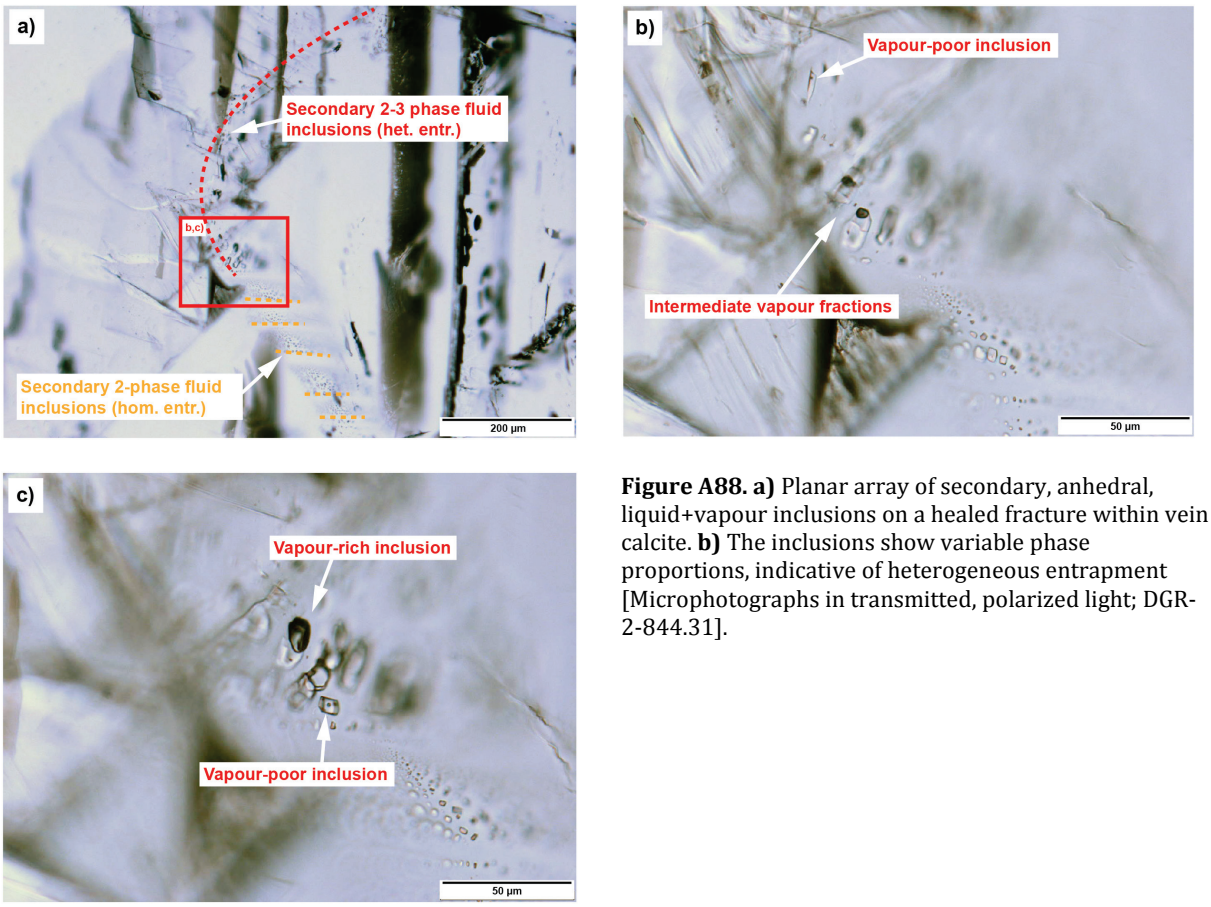


Figure A88. a) Planar array of secondary, anhedral, liquid+vapour inclusions on a healed fracture within vein calcite. **b)** The inclusions show variable phase proportions, indicative of heterogeneous entrapment [Microphotographs in transmitted, polarized light; DGR-2-844.31].

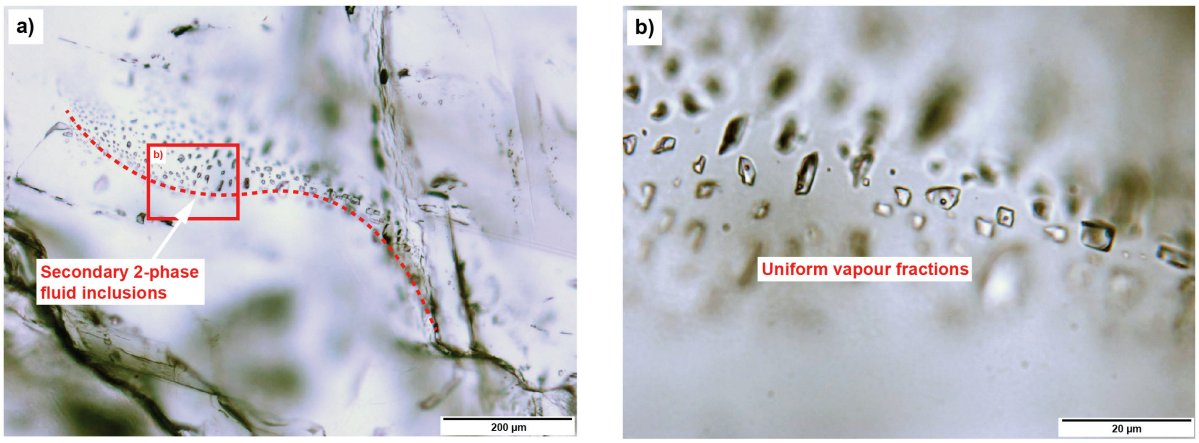


Figure A89. a) Planar array of secondary, liquid+vapour inclusions on a healed fracture within vein calcite. **b)** The inclusions show uniform phase proportions (~5 vol% vapour), indicative of homogeneous entrapment. **c)** Some of the inclusions contain variably sized halite crystals [Microphotographs in transmitted, polarized light; DGR-2-844.31].

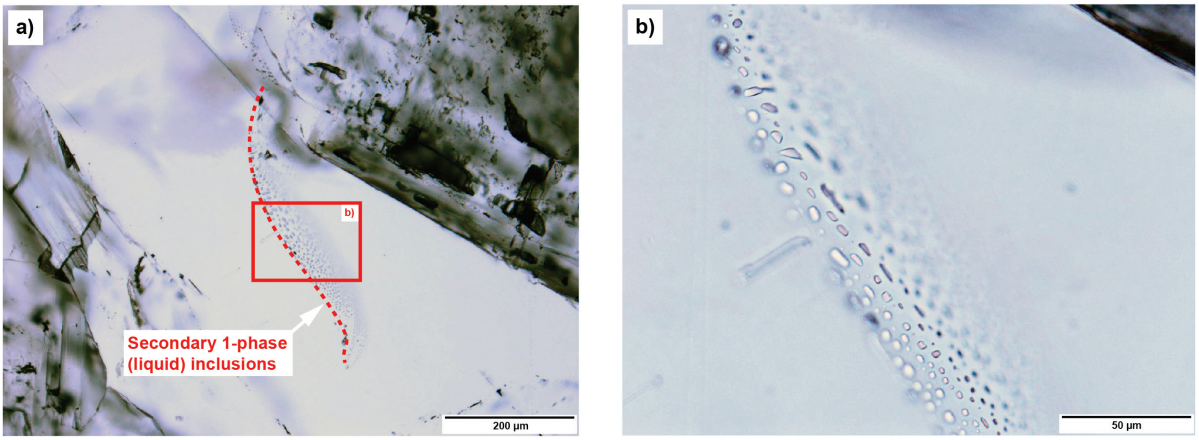


Figure A90. a,b) Planar array of secondary liquid-only inclusions (metastable stretched water) on a healed fracture in vein calcite [Microphotos in transmitted, polarized light; DGR-2-844.31].

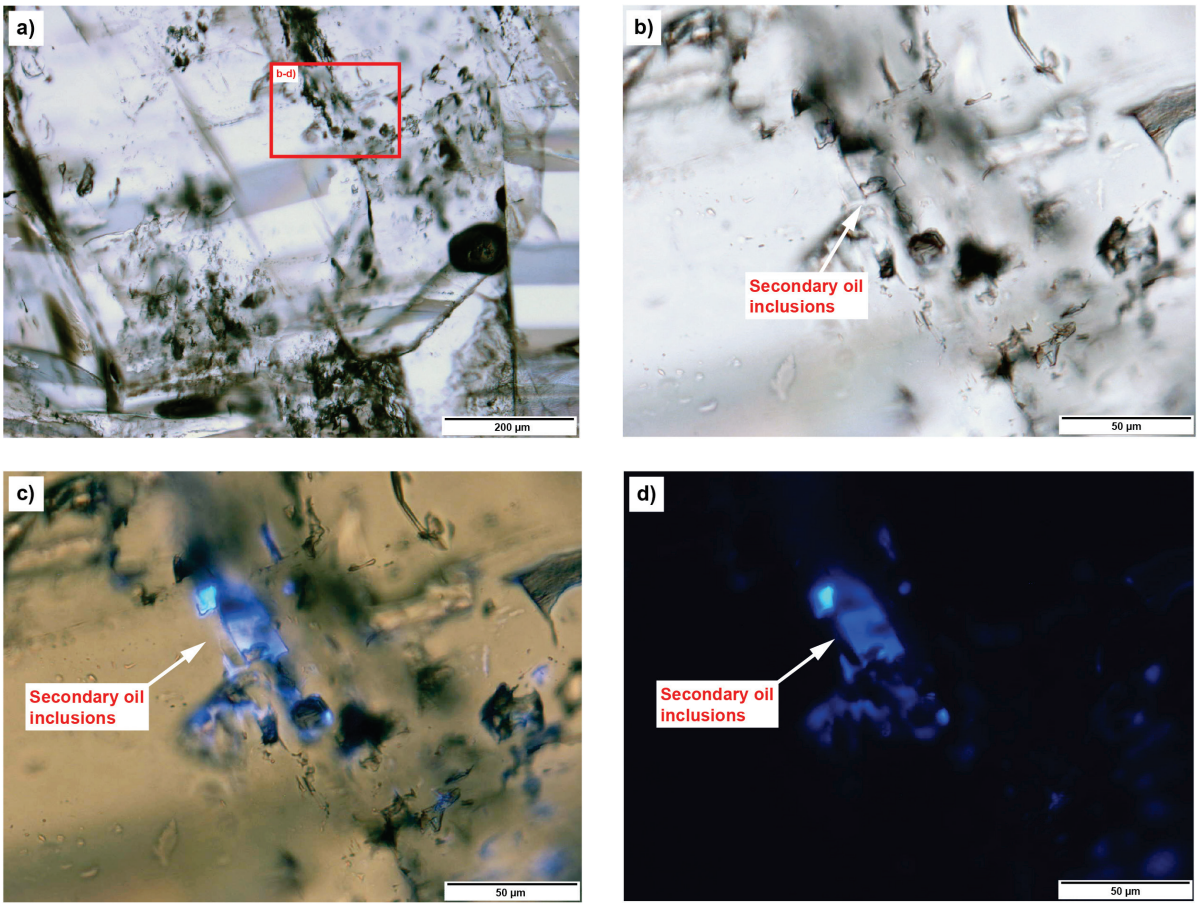


Figure A91. a,b) Healed fracture in vein calcite containing secondary oil inclusions. **c)** Fluorescence of the oil inclusions in simultaneous transmitted and UV epi-illumination. **d)** Bluish-white UV fluorescence colour of the aromatic hydrocarbons in the liquid portion of the inclusion. The vapour bubble is non-fluorescing and presumably contains dominantly methane [DGR-2-844.31].

SAMPLE DGR-2-847.42

Table A15. Paragenetic sequence and interpreted paleofluids in sample DGR-2-847.42. Column 2 lists the figures upon which the paragenetic sequence is based.

Minerals + Fluid Inclusions (phases at room *T*)	Fig. No. in Appendix 1	Vol% vapour	Vol% halite	Time stages →						
				I	II	III	IV	V	VI	VII
				Wall rock	Vug+ Vein	Vug+ Vein	Vug+ Vein	Vug+ Vein	Vug+ Vein	Vug+ Vein
Quartz sandstone matrix	A92									
Calcite	A92									
Early secondary Liq+Vap ±Hal	A93	Variable: 0-60	0-30							
Late secondary Liq+Vap ±Hal	A94	Uniform: 5	0-40							

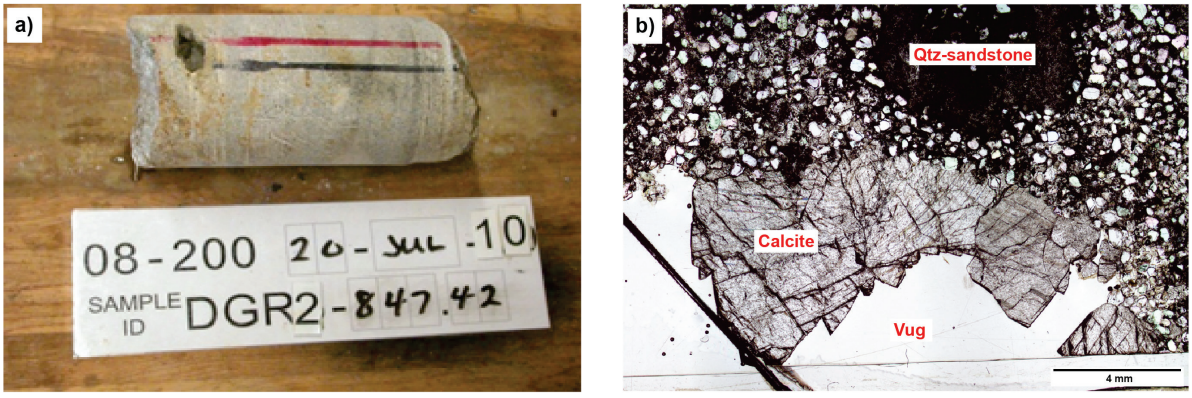
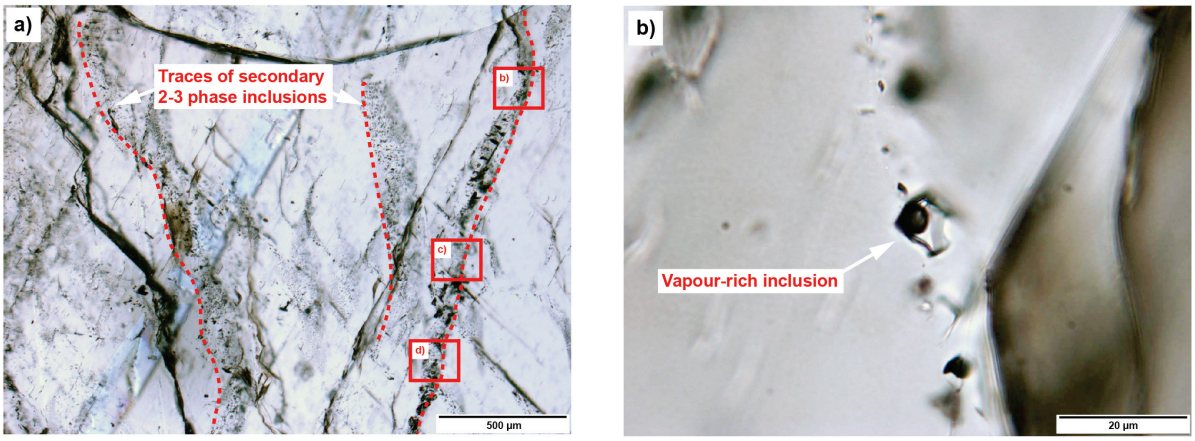


Figure A92. **a)** Photograph of core sample. **b)** Transmitted, polarized light microphotograph of calcite vug cut for microthermometry. The walls of the vein are lined with calcite crystals [DGR-2-847.42].



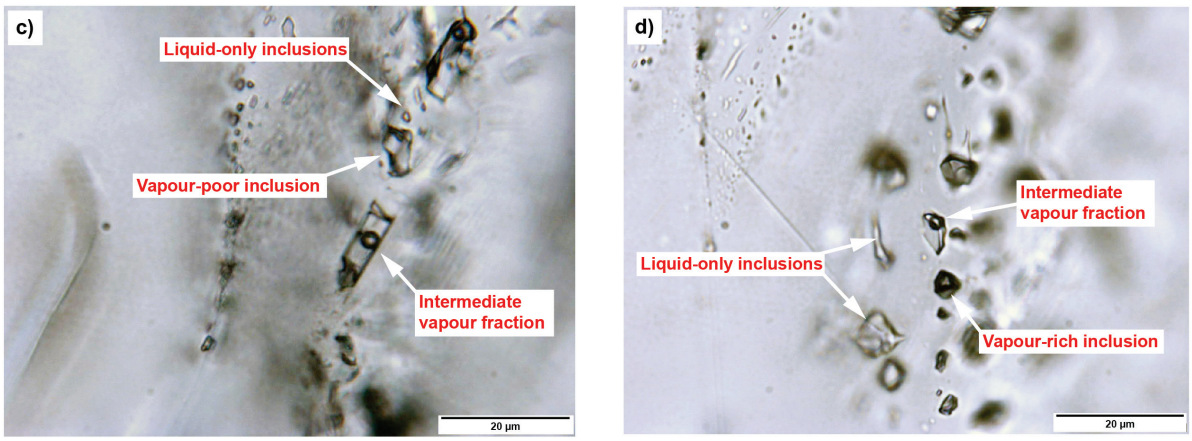


Figure A93. a) Planar arrays of secondary, anhedral, liquid+vapour inclusions on healed fractures within vug calcite. **b-d)** The inclusions show variable phase proportions, indicative of heterogeneous entrapment [Microphotographs in transmitted, polarized light; DGR-2-847.42].

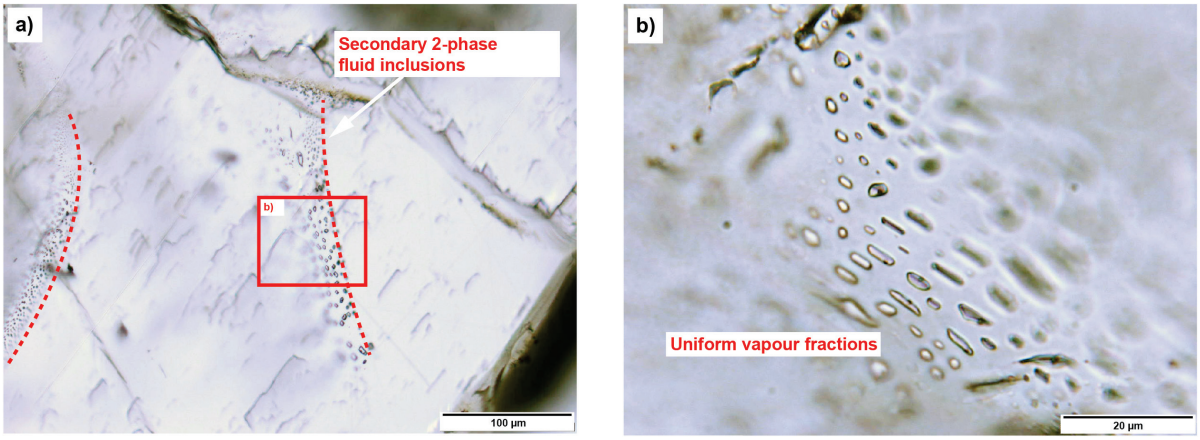


Figure A94. a) Planar arrays of secondary, subhedral, liquid+vapour inclusions on healed fractures within vug calcite. **b)** The inclusions show uniform phase proportions (~5 vol% vapour), indicative of homogeneous entrapment [Microphotographs in transmitted, polarized light; DGR-2-847.42].

SAMPLE DGR-2-850.01

Table A16. Paragenetic sequence and interpreted paleofluids in sample DGR-2-850.01. Column 2 lists the figures upon which the paragenetic sequence is based.

Minerals + Fluid Inclusions (phases at room *T*)	Fig. No. in Appendix 1	Vol% vapour	Vol% halite	Time stages → I	II	III	IV	V	VI	VII
				Wall rock	Vug+ Vein	Vug+ Vein	Vug+ Vein	Vug+ Vein	Vug+ Vein	Vug+ Vein
Quartz sandstone matrix	A95									
Dolomite (rhombic habit)	A95									
Pyrite	-									
Calcite	A95									
Primary Liq+Vap ±Hal	A96	Variable: 0-75	0-30							
Late secondary Liq+Vap ±Hal	A97	Uniform: 5	0-20							
Late secondary metastable-Liq	A97	Uniform: 0	0						?	?
Late secondary Oil+Vap	A98	Variable: 0-90	0						?	?

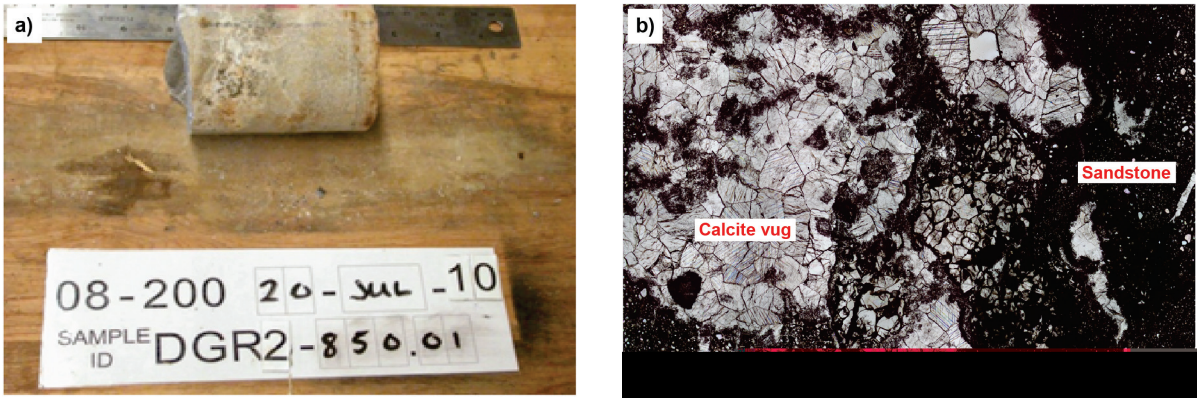


Figure A95. **a)** Photograph of core sample. **b)** Transmitted, polarized light microphotograph of calcite vug cut for microthermometry. The walls of the vug are lined with calcite crystals [DGR-2-850.01].

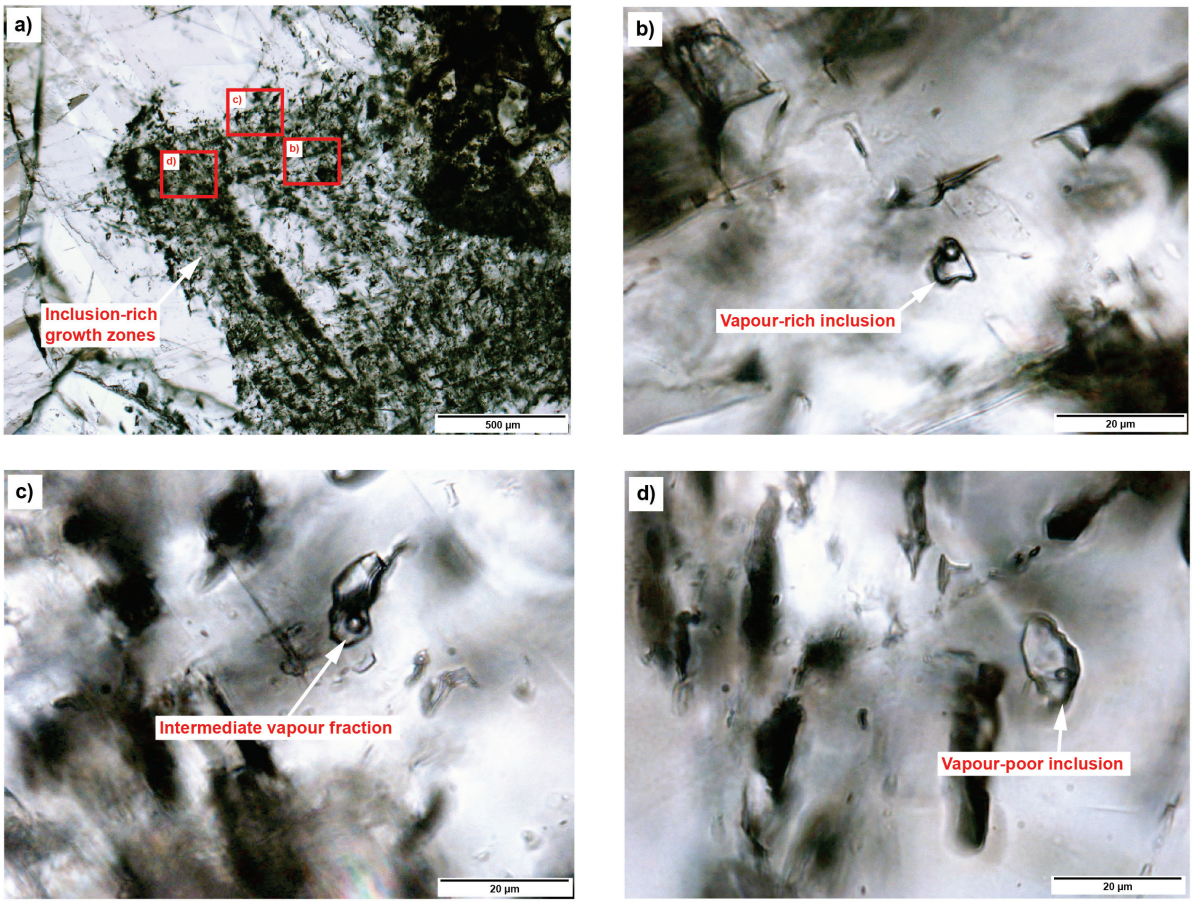
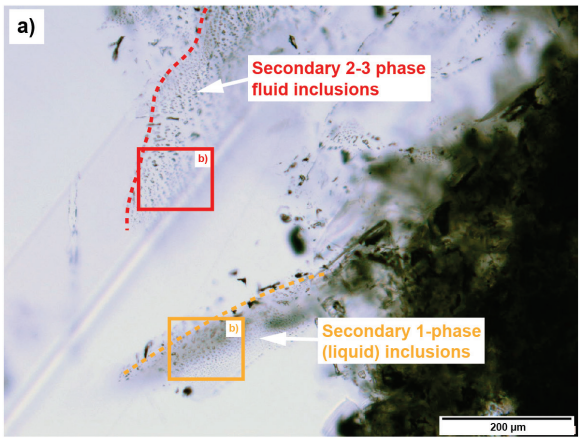
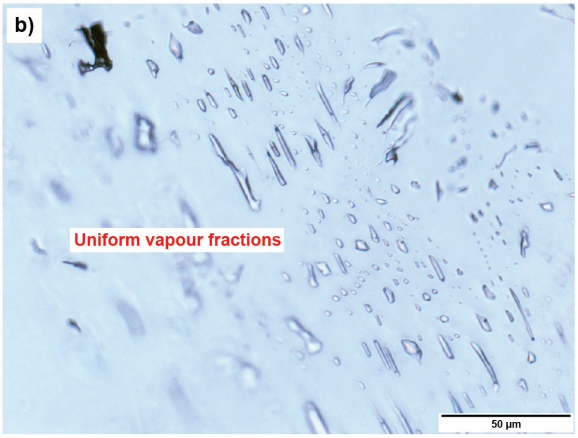


Figure A96. **a)** Relationship between fluid inclusions (dark specs) and calcite growth zonation reveals a primary origin of the inclusions. **b-d)** The variable phase proportions of the primary inclusions within the vug calcite indicate heterogeneous entrapment [Microphotographs in transmitted, polarized light; DGR-2-850.01].





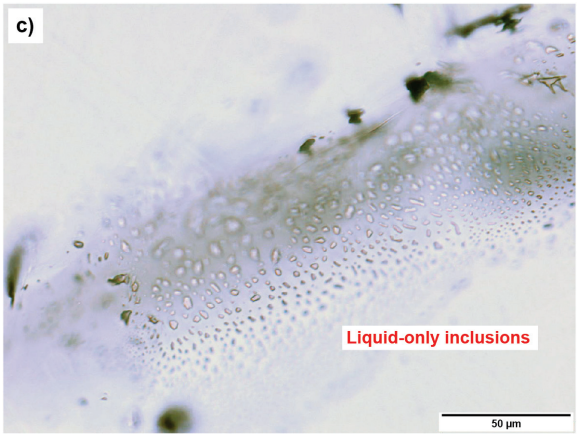


Figure A97. a) Planar arrays of secondary fluid inclusions on healed fractures within vug calcite. **b)** Liquid-vapour inclusions show uniform phase proportions (~5 vol% vapour), indicative of homogeneous entrapment. **c)** Liquid-only inclusions (metastable stretched water) [Microphotos in transmitted, polarized light; DGR-2-850.01].

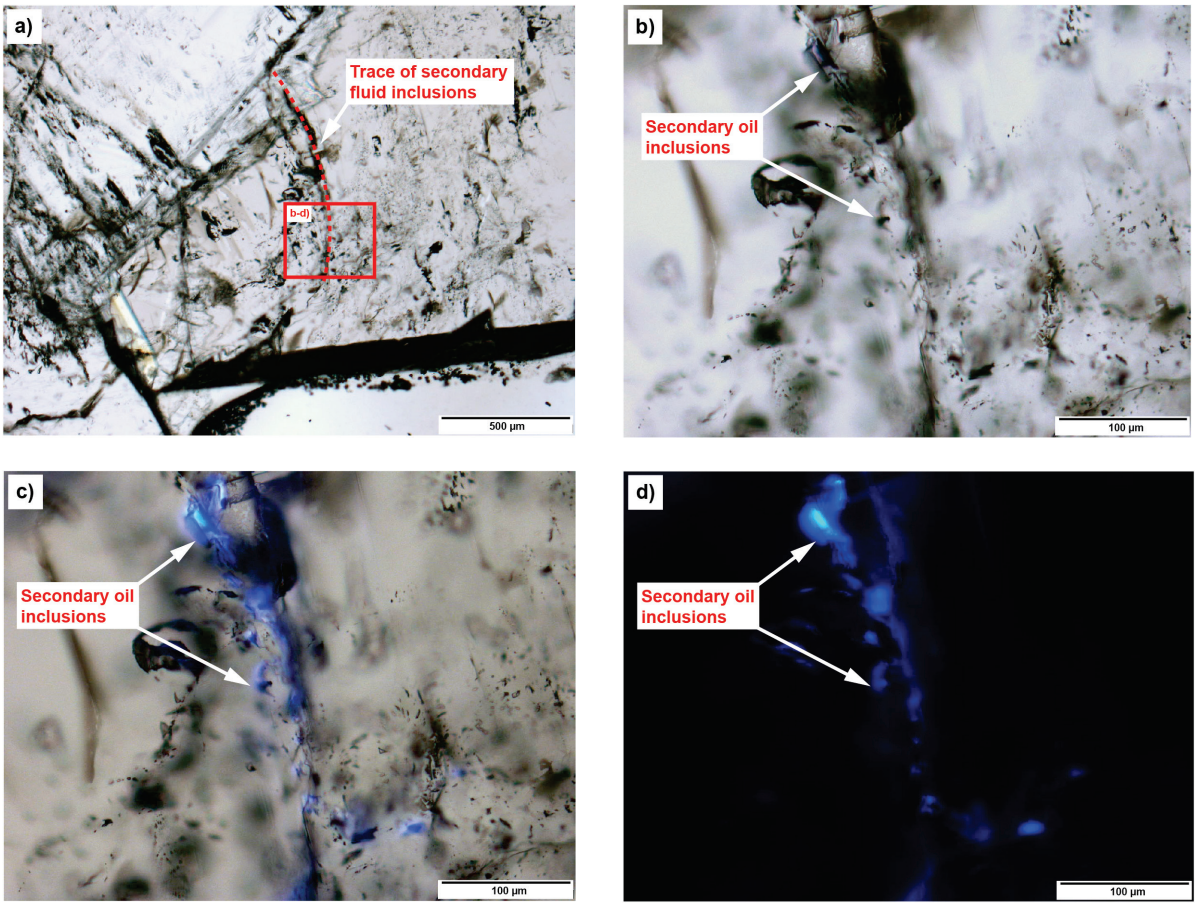


Figure A98. a,b) Healed fracture in vug calcite containing secondary oil inclusions. **c)** Fluorescence of the oil inclusions in simultaneous transmitted and UV epi-illumination. **d)** Bluish-white UV fluorescence colour of the aromatic hydrocarbons in the liquid portion of the inclusion [DGR-2-850.01].

SAMPLE DGR-2-853.72

Table A17. Paragenetic sequence and interpreted paleofluids in sample DGR-2-853.72. Column 2 lists the figures upon which the paragenetic sequence is based.

Minerals + Fluid Inclusions (phases at room *T*)	Fig. No. in Appendix 1	Vol% vapour	Vol% halite	Time stages → I Wall rock	II Vug+ Vein	III Vug+ Vein	IV Vug+ Vein	V Vug+ Vein	VI Vug+ Vein	VII Vug+ Vein
Quartz sandstone matrix	A99									
Calcite	A99									
Primary Liq+Vap (±Hal)	A100	Variable: 0-70	0-35							
Early secondary Liq+Vap (±Hal)	A101	Variable: 0-60	0-25							
Late secondary Liq+Vap (±Hal)	A102	Uniform: 5	0-20							
Late secondary metastable-Liq	-	Uniform: 0	0						?	?

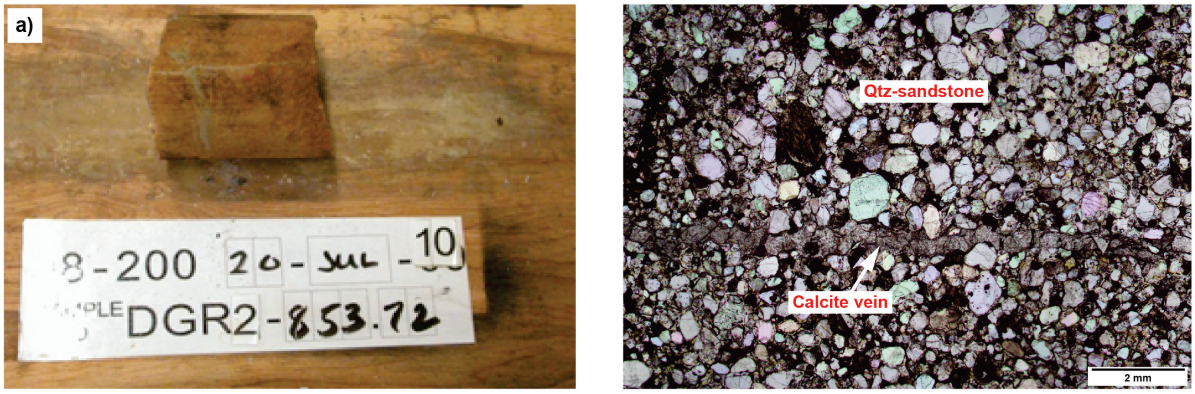


Figure A99. **a)** Photograph of core sample. **b)** Transmitted, polarized light microphotograph of calcite vein cut for microthermometry [DGR-2-853.72].

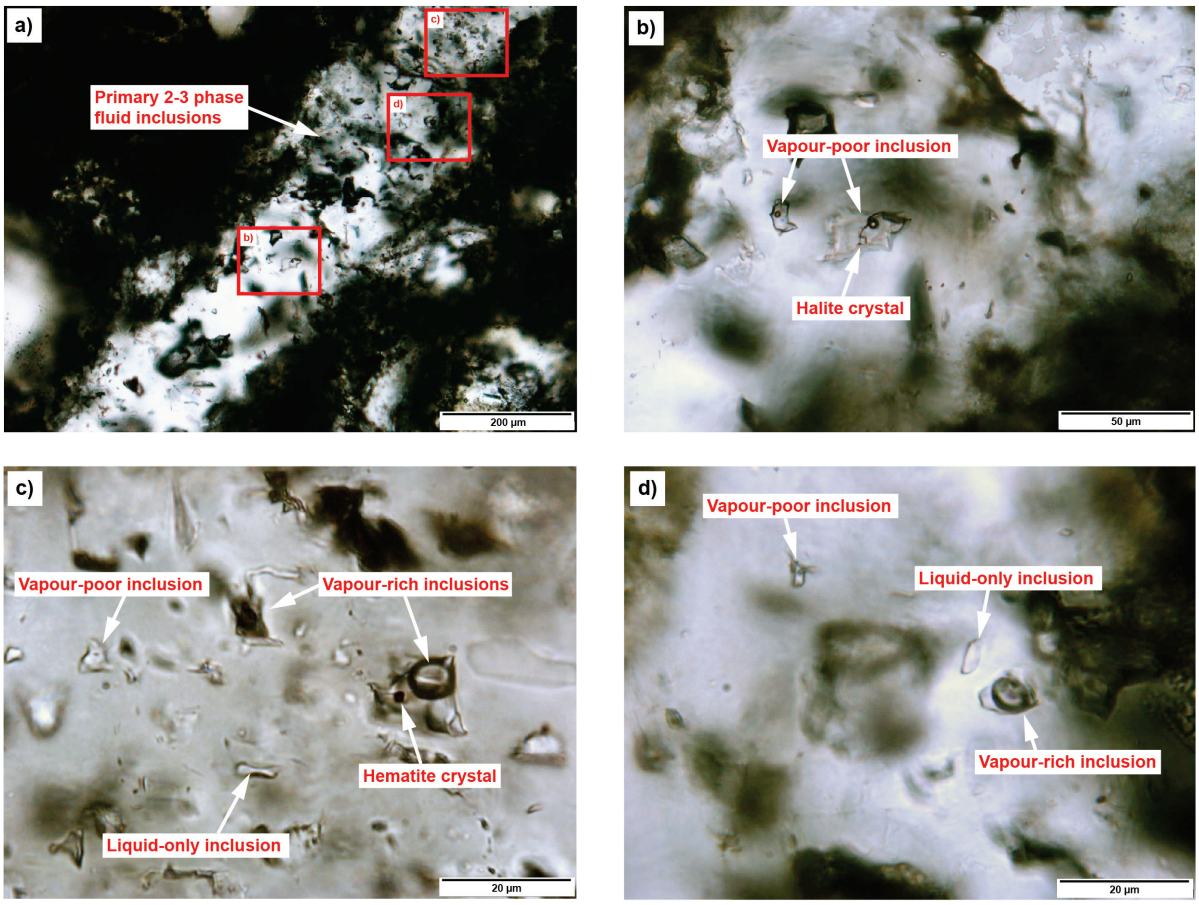


Figure A100. **a)** Primary liquid-vapour inclusions (dark specks) within vein calcite. **b-d)** The variable phase proportions of the primary inclusions indicate heterogeneous entrapment. Some of the inclusions contain accidentally trapped hematite crystals [Microphotographs in transmitted, polarized light; DGR-2-853.72].

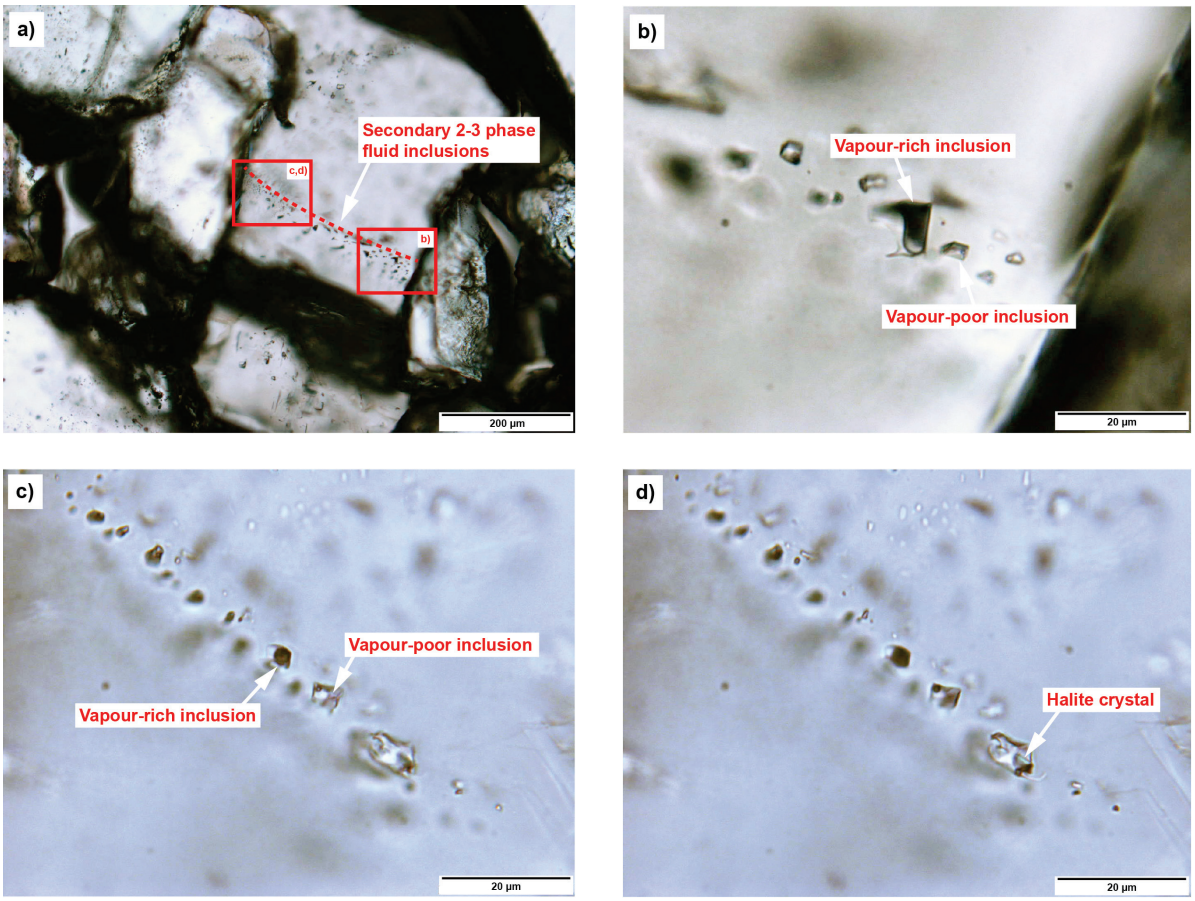


Figure A101. a) Planar array of secondary liquid+vapour inclusions on a healed fracture within vein calcite. **b,c)** The inclusions show variable phase proportions, indicative of heterogeneous entrapment. **d)** Some of the inclusions contain halite crystals [Microphotographs in transmitted, polarized light; DGR-2-853.72].

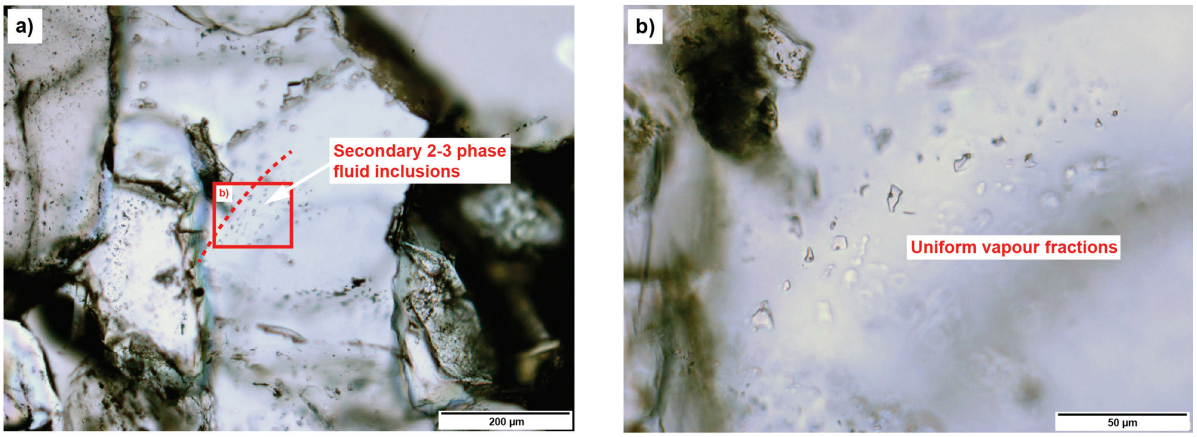


Figure A102. a) Planar array of secondary, liquid+vapour inclusions on a healed fracture within vein calcite. **b)** The inclusions show uniform phase proportions (~5 vol% vapour), indicative of homogeneous entrapment [Microphotographs in transmitted, polarized light; DGR-2-853.72].

APPENDIX B: PHASE BEHAVIOUR OF FLUID INCLUSIONS BELOW ROOM TEMPERATURE

B.1 Behaviour of high-salinity inclusions

The following photographs document a cooling-heating experiment for an inclusion in sample DGR 6-886.91 as an illustration of the typical metastable behaviour of high-salinity inclusions in the Bruce Site samples.

Figure B1a shows the liquid+vapour+halite inclusion within calcite at room temperature prior to cooling. No phase changes were visible upon initial cooling of the inclusions to –160 °C (compare Fig. B1a and B1b), a phenomenon which is typical of $CaCl_2$-rich brines. The state of the inclusion at –160 °C is something akin to a saline gel, in which hydration shells around the dissociated electrolytes hinder crystallization to stable salt-hydrates.

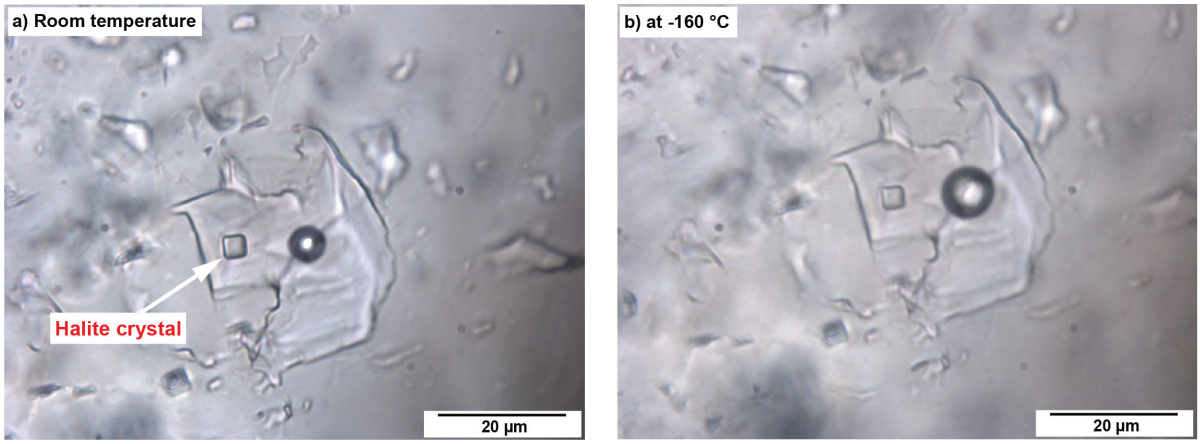


Figure B1. a) *Secondary 3-phase fluid inclusion with rectangular halite crystal at room temperature and* **b)** *at -160 °C. Upon cooling from room temperature to –160 °C, no phase change was observed. Inclusion in calcite in sample DGR-6-886.91.*

Upon heating to 95 °C, methane-hydrate-clathrate started to nucleate at the meniscus of the vapour bubble. Upon further heating, feathery crystals of clathrate grew radially into the surrounding brine and the vapour bubble steadily deformed (Fig. B2).

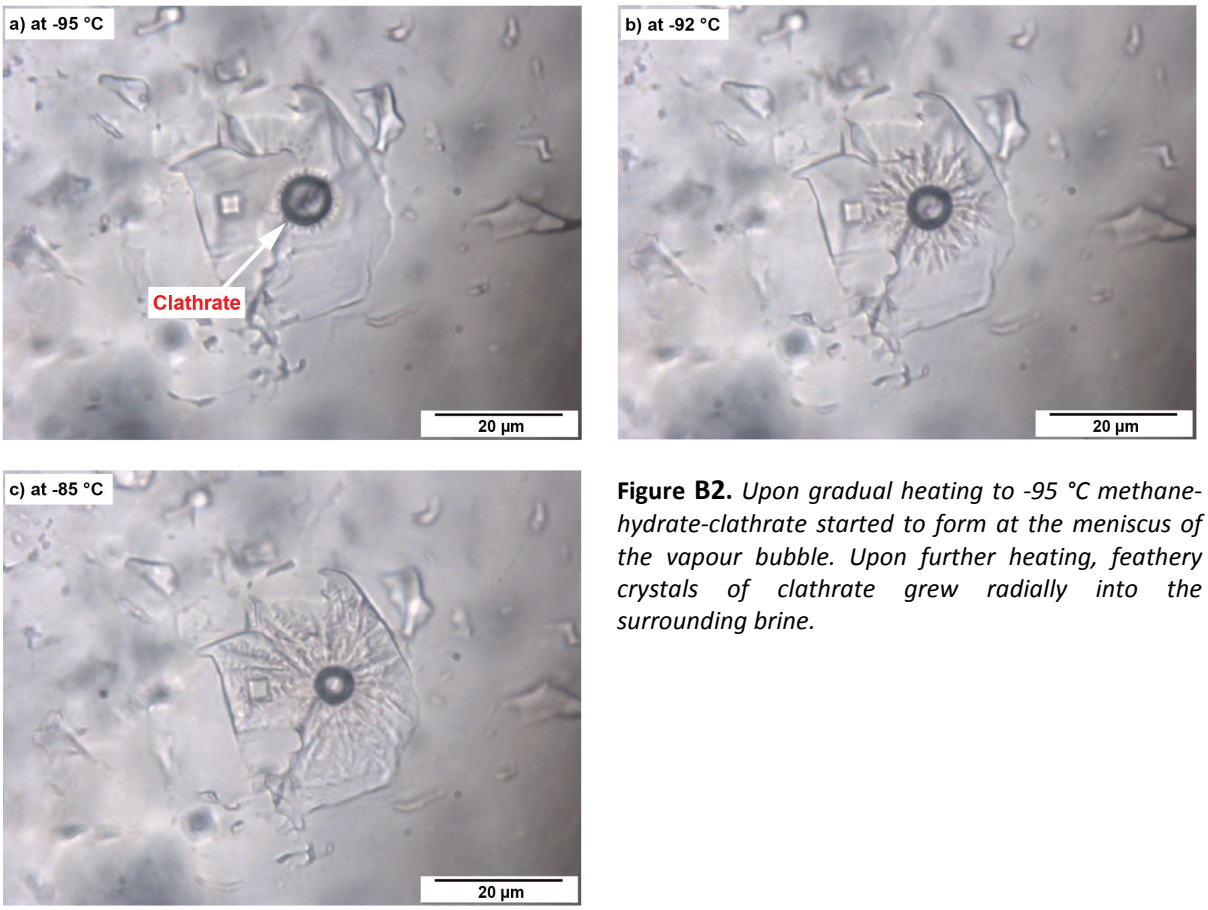


Figure B2. *Upon gradual heating to -95 °C methane-hydrate-clathrate started to form at the meniscus of the vapour bubble. Upon further heating, feathery crystals of clathrate grew radially into the surrounding brine.*

Heating the inclusion to approximately –65 °C causes the clathrate to begin to dissociate (Figs. B3a and B3b), individual clathrate crystals becoming fewer but coarser, elongated and prismatic (Fig. B3b and B3c) with the vapour bubble adopting its original spherical shape. Complete dissociation of the clathrate followed with further heating, leaving well rounded ice crystals in its place. At -42 °C, ice was the last remaining solid besides halite (Figs. 10c and d). However, this represents a metastable equilibrium. The halite typically shows no corrosion or reaction with the aqueous phase to form the more stable hydrohalite phase ($NaCl \cdot 2H_2O$).

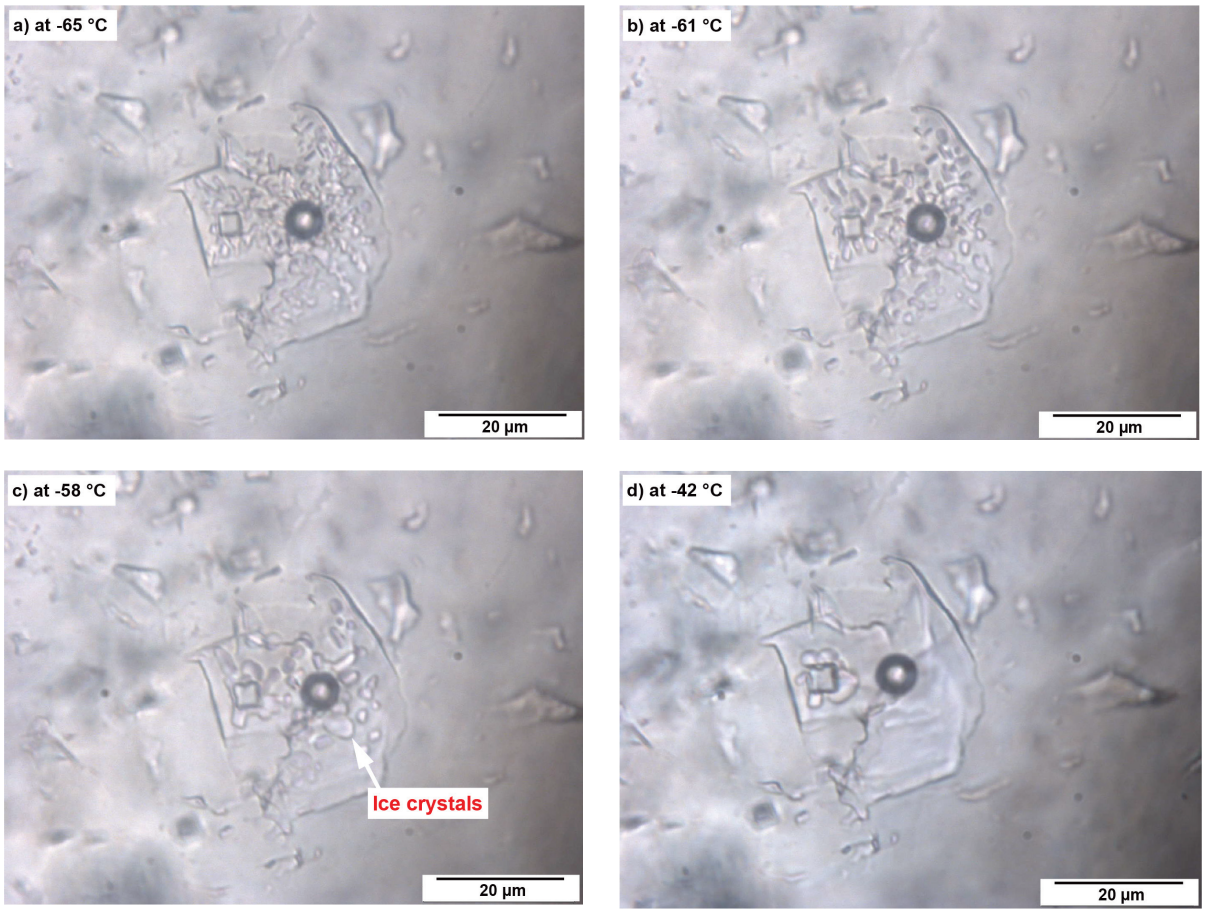


Figure B3. a) *At approximately -65 °C clathrate began to dissociate.* **b)** *Clathrate crystals coarsened and adopted elongated, prismatic shapes.* **c)** *Upon further heating the clathrate and gave way to well rounded ice crystals.* **d)** *At -42 °C ice was the only remaining solid phase beside halite, together in metastable equilibrium.*

The heating run was stopped when only one ice crystal remained (Fig. B4a). Subsequent cooling allowed this crystal to grow (Fig. B4b) until at approximately -70 °C it reached its maximum size and further cooling did not result in further growth. The remaining volume of the inclusion not occupied by the ice is filled with a highly saline, metastable gel (Fig. B4c). The halite still shows no sign of a reaction rim, however it appears to have increased slightly in size.

Renewed heating caused the ice to melt completely at -34 °C (this was recorded as T_m for this specific inclusion). Upon heating above room temperature the halite crystal started to decrease in size and the edges eroded, becoming rounded, which is indicative for its dissolution (Fig. B5a). Complete dissolution of the halite crystal occurred at 99 °C. Renewed cooling of the inclusion to –160 °C did not cause the halite crystal to reappear (Fig. B5b). This failure to re-nucleate halite is a common occurrence in $CaCl_2$-rich brine inclusions.

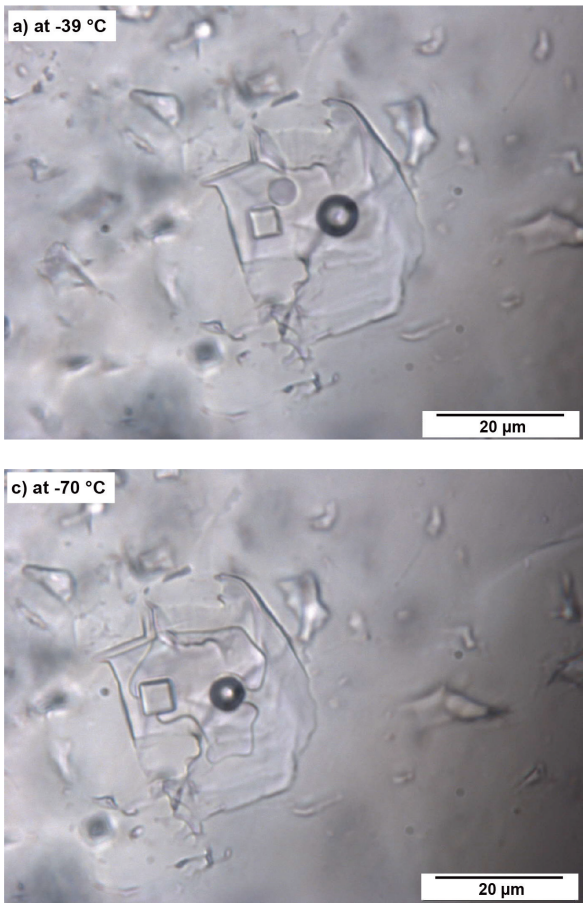


Figure B4. a) *Remaining ice crystal at -39 °C.* ***b)*** *Growth of the single ice crystal during renewed cooling.* ***c)*** *The ice crystal reaches its maximum size at approximately -70 °C. Further cooling does not result in further ice growth.*

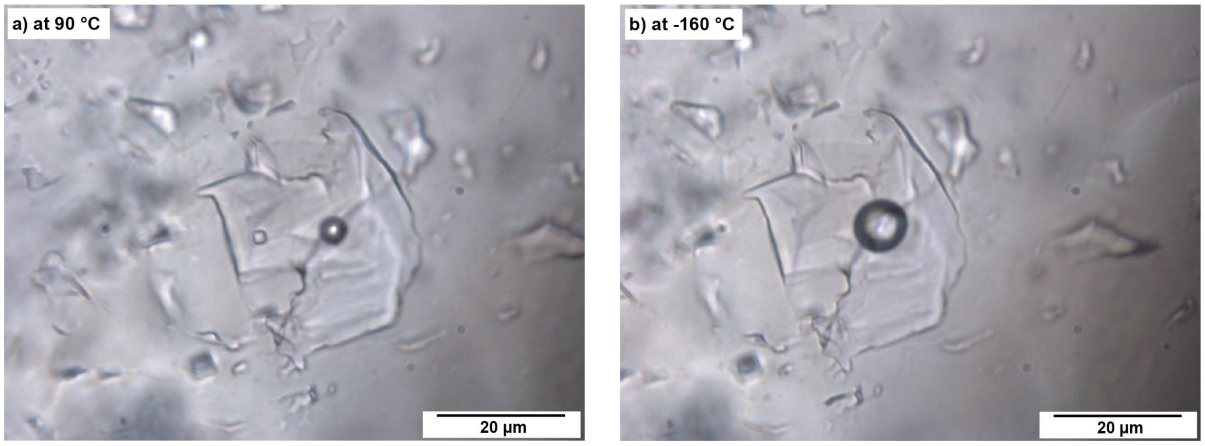


Figure B5. a) *Heating of the inclusion to +99 °C caused complete dissolution of the halite crystal.* ***b)*** *Upon renewed cooling to -160 °C the halite crystal did not reappear, a common effect of nucleation inhibition in complex $CaCl_2$-rich brines.*

However, heating the inclusion to -45 °C in the absence of halite resulted in nucleation of hydrohalite (see elongated, prismatic crystals with rounded edges in Fig. B6a and B6b). Upon further heating the hydrohalite crystals melted and finally disappeared at +17 °C (Figs. 13b and c). However, the expected equilibrium halite crystal did not reappear.

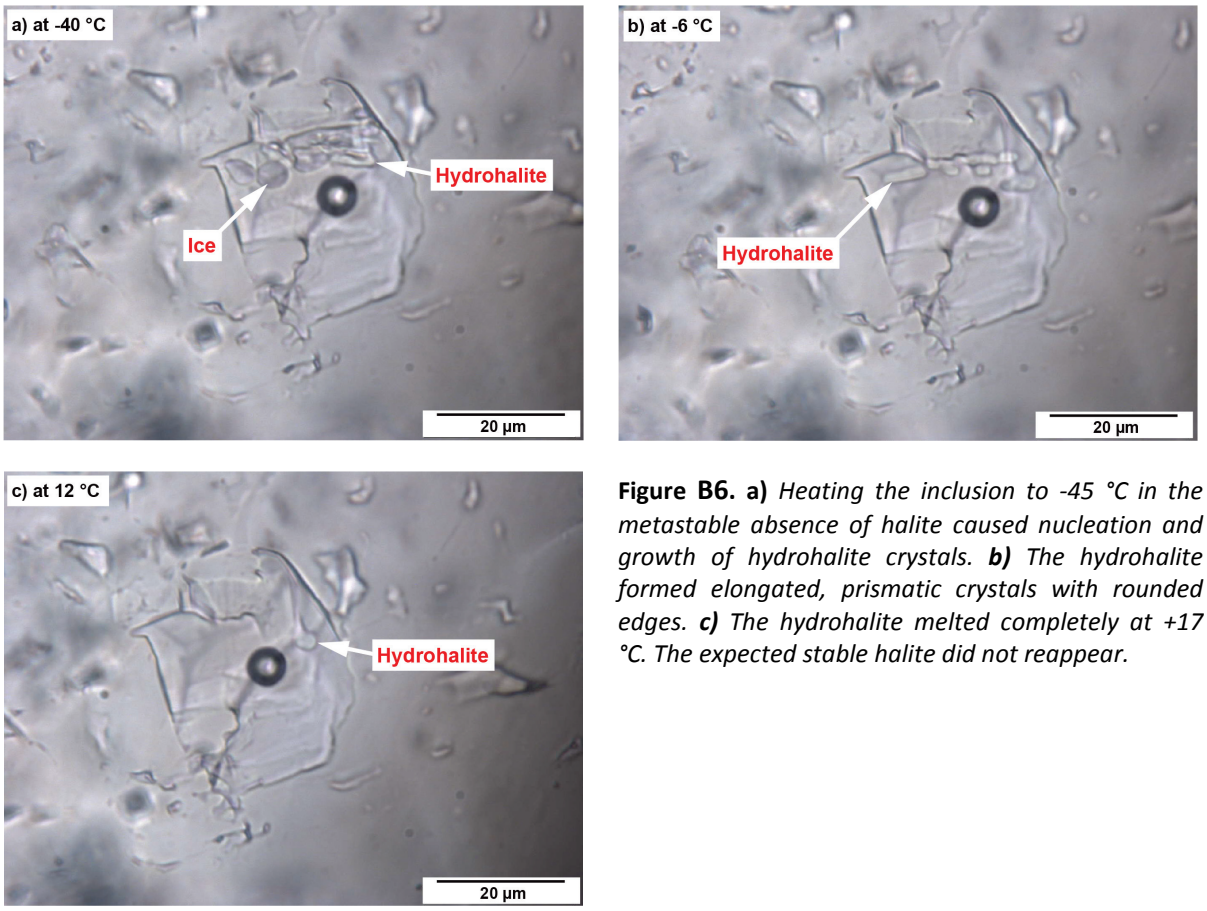


Figure B6. a) *Heating the inclusion to -45 °C in the metastable absence of halite caused nucleation and growth of hydrohalite crystals.* ***b)*** *The hydrohalite formed elongated, prismatic crystals with rounded edges.* ***c)*** *The hydrohalite melted completely at +17 °C. The expected stable halite did not reappear.*

B.2 Behaviour of low-salinity inclusions

During the cryogenic experiments the low-salinity inclusions behaved in a comparatively simple manner. An example is shown in Fig. B7 and described in the following.

Upon cooling to –42 °C the vapour bubble suddenly contracted owing to the volume increase as ice nucleated (Fig. B7a and B7b). The formation of the ice crystals themselves was not visible, as is typical for low-salinity inclusions. During further cooling to -60 °C the size of the bubble remained approximately constant (Fig. B7c), whereas during heating to -5 °C the vapour bubble steadily deformed and decreased in size, due to further growth of ice (Fig. B7d). Final melting of the ice was marked by the rapid sweeping of a solid/liquid meniscus across the inclusion within a very small temperature interval (0.1 to 0.2 °C). This contrasts with the slow melting of

rounded ice crystals observed in the high-salinity inclusions. The sweeping meniscus was accompanied by sudden expansion and movement of the vapour bubble as it regained its initial size and position in the inclusion (Fig. B7e).

The phase behaviour described above is typical of very dilute aqueous inclusions, and indeed of pure water inclusions (Diamond, 2003a), and so it is compatible with the very high ice-melting temperatures reported in Section 4.2.3 below.

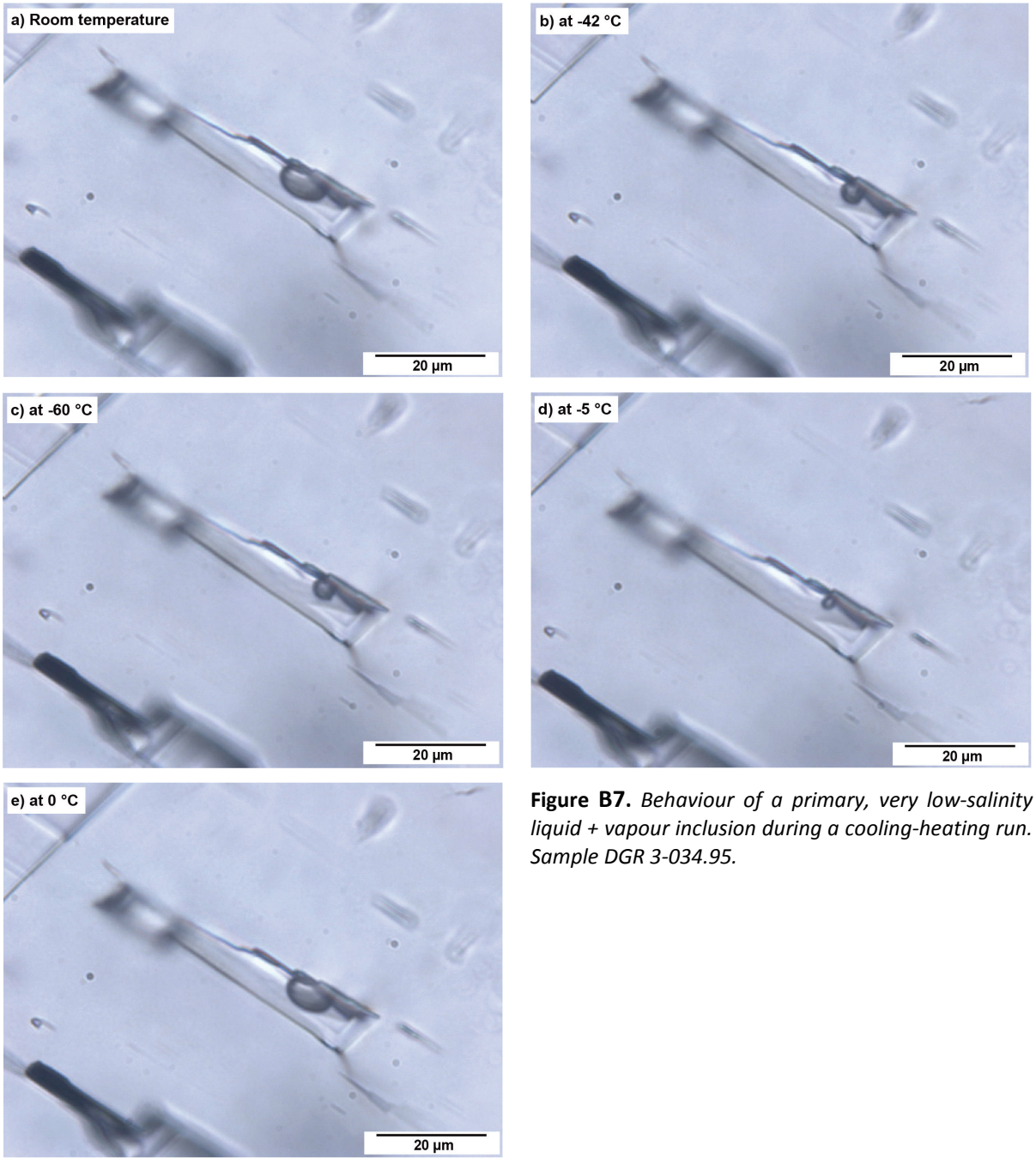


Figure B7. *Behaviour of a primary, very low-salinity liquid + vapour inclusion during a cooling-heating run. Sample DGR 3-034.95.*

APPENDIX C: ELECTRON MICROPROBE ANALYSES OF DOLOMITES

Electron microprobe analyses were performed on three samples, each containing rock-matrix dolomite and saddle dolomite (high-temperature hydrothermal dolomite, "HTD"). One of the samples had dolomite in vein fillings (Fig. C1), overgrown by saddle dolomite. The saddle and veins dolomites are assigned to stage II of the paragenetic sequence (Figs. 7 and 11).

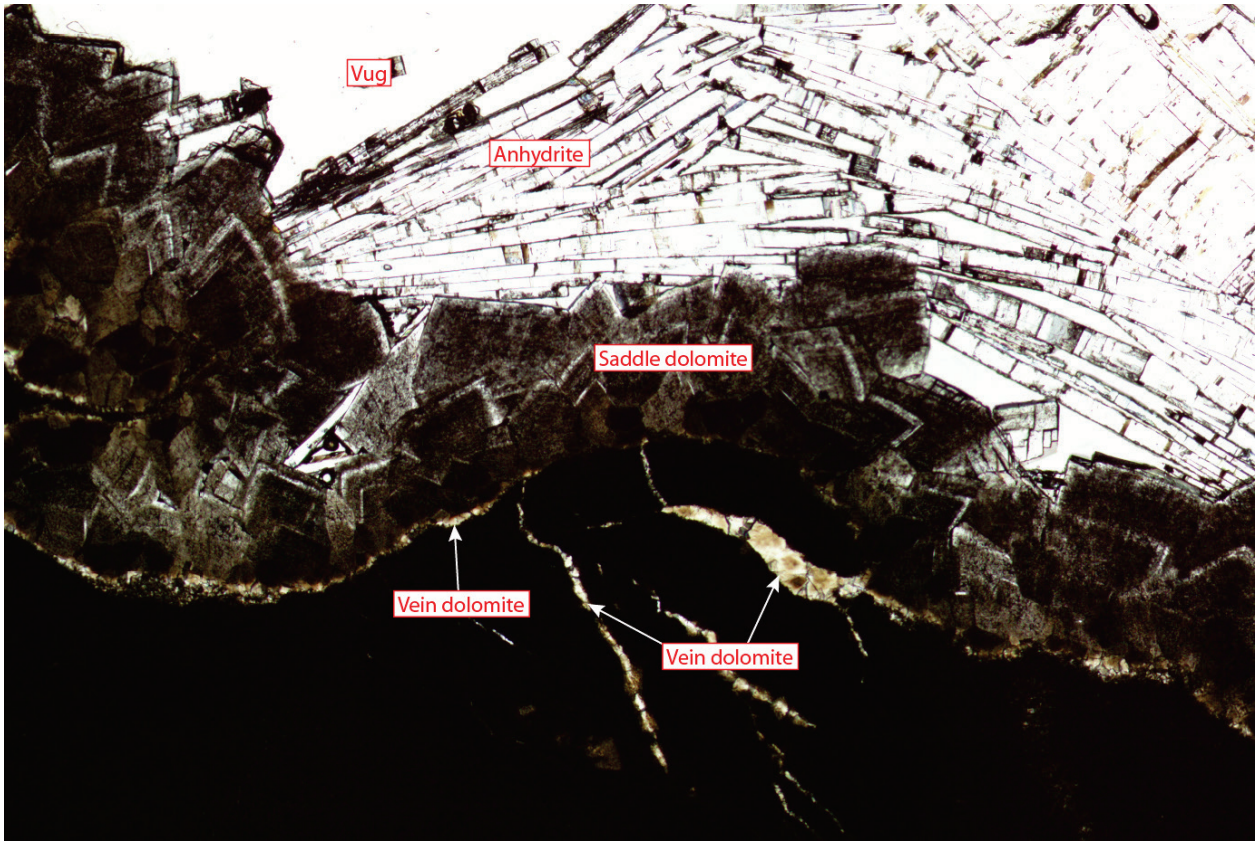


Figure C1. *Sample* DGR-4-829.53. *Close-up photograph of same scene illustrated in Fig. A79b, viewed in transmitted, polarized light. The dolomite filling in veinlets (termed "vein dolomite" in Table C1 is overgrown by the coarse saddle dolomite, and therefore it appears to be a precursor of the saddle dolomite generation. Both are assigned to Stage II of the paragenetic sequence in Figs. 7 and 11.*

Spot analyses of the elements Ca, Fe, Mg, Mn, Na, Sr were acquired on a JEOL JXA-8100 electron microprobe by Arthur Adams at the University of Bern. Beam conditions were 15 kV accelerating voltage, 10 nA current and 10 µm spot diameter. Carbonate minerals were used for standards.

Results in µg/g ("ppm") are given in Table C1 (this table extends over two pages in this report). Ratios of Mn/Fe are given in Fig. C2. The saddle dolomites are notably Fe-richer and mostly Mn-richer than the matrix dolomites. The "vein dolomites" have intermediate compositions between the saddle and matrix dolomites, in accord with their interpretation as an early phase of saddle dolomite (Fig. C1).

Table C1. Electron microprobe analyses of dolomites (continued on following page)

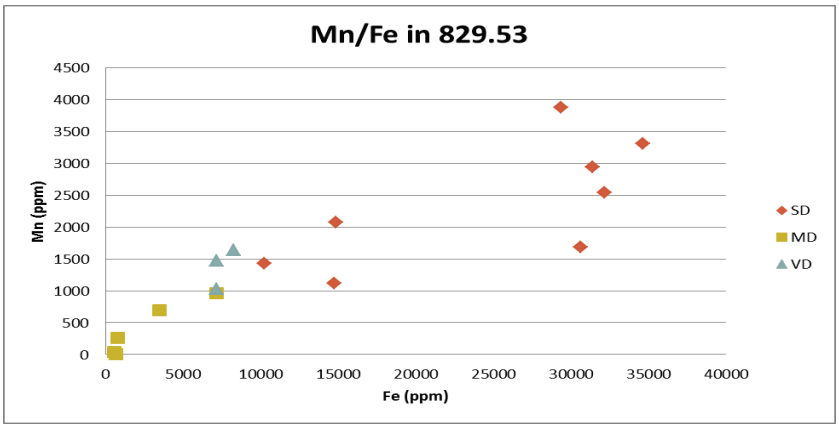
Dolomite type	Sample /Depth (m)	Formation	Analysis Number	Na (µg/g)	Mn (µg/g)	Ca (µg/g)	Mg (µg/g)	Fe (µg/g)	Sr (µg/g)	Total* (wt%)
Matrix	2-778.44	Coboconk	77844A4_re	214	228	219627	120600	3205	460	97.53
Matrix	2-778.44	Coboconk	77844A5	5	294	232063	112037	6658	0	98.26
Matrix	2-778.44	Coboconk	77844A6_re	228	0	246572	110952	638	769	100.37
Matrix	2-778.44	Coboconk	77844B1	65	174	224845	119093	2663	94	98.08
Matrix	2-778.44	Coboconk	77844B2	202	400	221914	122409	4412	644	99.04
Matrix	2-778.44	Coboconk	77844B3	177	143	225559	121987	3666	0	99.47
Matrix	4-829.53	Gull River	82953A5	634	38	233993	116078	547	0	98.97
Matrix	4-829.53	Gull River	82953A6	461	258	234779	112761	795	511	98.16
Matrix	4-829.53	Gull River	82953A7	793	0	239067	110409	675	457	98.41
Matrix	4-829.53	Gull River	82953B5	36	698	227846	117464	3450	206	98.56
Matrix	4-829.53	Gull River	82953B6	93	957	234207	109806	7136	791	98.42
Matrix	2-844.31	Gull River	84431B6	271	441	218269	127474	1311	37	99.16
Matrix	2-844.31	Gull River	84431B7	62	1631	219056	128439	1235	0	99.88
Matrix	2-844.31	Gull River	84431B8	45	1490	215982	125183	2304	244	98.20
Matrix	2-844.31	Gull River	84431B9	201	359	215768	129705	1349	277	99.32
Matrix	2-844.31	Gull River	8844A3	369	2241	218126	121987	2270	384	97.88
Matrix	2-844.31	Gull River	8844A4	53	503	218770	126148	1497	0	98.81
Matrix	2-844.31	Gull River	8844A5_re	432	325	217054	129042	1412	786	99.56
Saddle	2-778.44	Coboconk	77844A1	261	603	219056	106671	30937	0	98.31
Saddle	2-778.44	Coboconk	77844A2_re	185	657	215053	120359	13991	161	98.56
Saddle	2-778.44	Coboconk	77844A3_re	44	728	216483	119997	14691	0	98.91
Saddle	2-778.44	Coboconk	77844A6_te2	68	496	220413	116198	15779	0	98.74
Saddle	2-778.44	Coboconk	77844B4	27	304	220914	118248	12748	0	98.90
Saddle	2-778.44	Coboconk	77844B5	81	667	216769	118248	18888	0	99.23
Saddle	2-778.44	Coboconk	77844B6	207	744	213409	108178	33346	1232	98.14
Saddle	2-778.44	Coboconk	77844B6_te	0	462	212909	111615	30315	390	98.35
Saddle	2-778.44	Coboconk	77844B7	217	686	215839	116198	17722	428	98.16
Saddle	2-778.44	Coboconk	77844B8	35	601	213266	112158	32724	0	99.08
Saddle	2-778.44	Coboconk	77844B9	0	679	217698	112158	26972	0	99.01
Saddle	4-829.53	Gull River	82953A1	0	1118	214196	119273	14769	299	98.22
Saddle	4-829.53	Gull River	82953A2	0	2075	210336	120057	14846	874	97.83
Saddle	4-829.53	Gull River	82953A3	0	2945	210694	111193	31403	0	98.32
Saddle	4-829.53	Gull River	82953A4	125	1430	213409	120419	10260	0	97.52
Saddle	4-829.53	Gull River	82953B1	5	2542	215125	110048	32180	0	99.11
Saddle	4-829.53	Gull River	82953B2	324	3310	211051	110651	34668	115	99.05
Saddle	4-829.53	Gull River	82953B3	74	3880	209836	112218	29382	0	98.24
Saddle	4-829.53	Gull River	82953B4	143	1684	212409	110892	30626	323	98.31
Saddle	2-844.31	Cambrian	84431B1	183	2057	211122	117585	23474	0	98.86
Saddle	2-844.31	Cambrian	84431B2	227	1740	208478	118429	21298	0	97.99
Saddle	2-844.31	Cambrian	84431B3	0	2397	209907	116560	24019	0	98.33

Dolomite type	Sample /Depth (m)	Formation	Analysis Number	Na (µg/g)	Mn (µg/g)	Ca (µg/g)	Mg (µg/g)	Fe (µg/g)	Sr (µg/g)	Total* (wt%)
Saddle	2-844.31	Cambrian	84431B4	0	3064	209050	112761	32336	0	98.68
Saddle	2-844.31	Cambrian	84431B5	21	8402	211051	108721	29926	0	98.39
Saddle	2-844.31	Cambrian	8844A1	231	1686	212909	114510	20598	0	97.57
Saddle	2-844.31	Cambrian	8844A2	0	1901	212337	115113	22542	0	98.04
Vein	4-829.53	Gull River	82953A10	364	1472	233993	109203	7153	0	98.19
Vein	4-829.53	Gull River	82953A8	110	1639	234636	107334	8274	508	98.00
Vein	4-829.53	Gull River	82953A9	217	1025	236637	111012	7182	409	99.43

** Includes mass of C and O in dolomite stoichiometry*

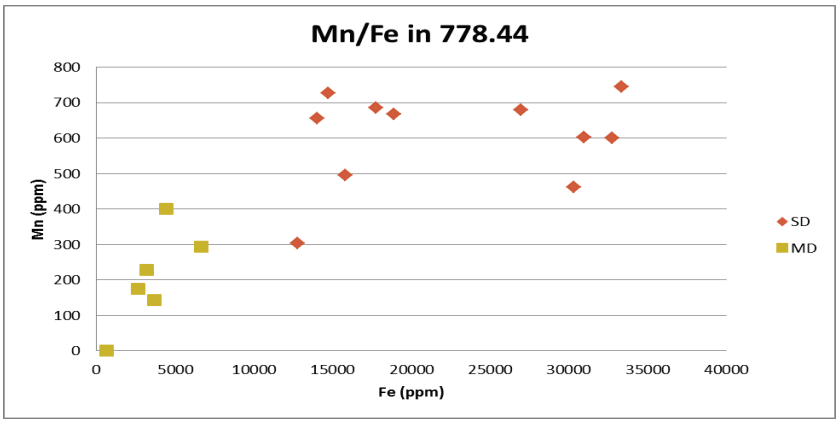
Sample 4-829.53

Gull River



Sample 2-778.44

Coboconk



Sample 2-844.31

Cambrian

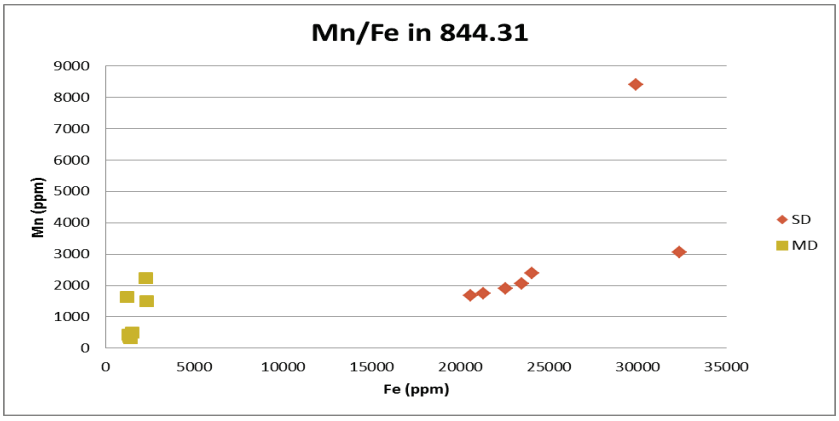


Figure C2. *Manganese and iron contents in three borehole samples. Date from Table C1. Units of concentration are µg/g ("ppm"). SD: Saddle dolomite (HTD); MD: Matrix dolomite; VD: Vein dolomite.*